Functionalization of Endohedral Fullerenes and Their Application in Quantum Information Processing

Guoquan Liu

St. Anne's College

A thesis submitted for the degree of *Doctor of Philosophy*

at the University of Oxford

Trinity Term 2011

Functionalization of Endohedral Fullerenes and Their Application in Quantum Information Processing

Guoquan Liu
St. Anne's College
Trinity Term 2011

The abstract of a thesis submitted for the degree of Doctor of Philosophy

Quantum information processing (QIP), which inherently utilizes quantum mechanical phenomena to perform information processing, may outperform its classical counterpart at certain tasks. As one of the physical implementations of QIP, the electron-spin based architecture has recently attracted great interests. Endohedral fullerenes with unpaired electrons, such as $N@C_{60}$, are promising candidates to embody the qubits because of their long spin decoherence time. This thesis addresses several fundamental aspects of the strategy of engineering the $N@C_{60}$ molecules for applications in QIP.

Chemical functionalization of $N@C_{60}$ is investigated and several different derivatives of $N@C_{60}$ are synthesized. These $N@C_{60}$ derivatives exhibit different stability when they are exposed to ambient light in a degassed solution. The cyclopropane derivative of $N@C_{60}$ shows comparable stability to pristine $N@C_{60}$, whereas the pyrrolidine derivatives demonstrate much lower stability. To elucidate the effect of the functional groups on the stability, an escape mechanism of the encapsulated nitrogen atom is proposed based on DFT calculations. The escape of nitrogen is facilitated by a 6-membered ring formed in the decomposition of the pyrrolidine derivatives of $N@C_{60}$. In contrast, the 4-membered ring formed in the cyclopropane derivative of $N@C_{60}$ prohibits such an escape through the addends.

Two $N@C_{60}$-porphyrin dyads are synthesized. The dyad with free base porphyrin exhibits typical zero-field splitting (ZFS) features due to functionalization in the solid-state electron spin resonance (ESR) spectrum. However, the nitrogen ESR signal in the second dyad of $N@C_{60}$ and copper porphyrin is completely suppressed at a wide range of sample concentrations. The dipolar coupling between the copper spin and the nitrogen spins is calculated to be 27.0 MHz. To prove the presence of the encapsulated nitrogen atom in the second dyad, demetallation of the copper porphyrin moiety is carried out. The recovery of approximately 82% of the signal intensity confirms that the dipolar coupling suppresses the ESR signal of $N@C_{60}$.

To prepare ordered structure of $N@C_{60}$, the nematic matrix MBBA is employed to align the pyrrolidine derivatives of $N@C_{60}$. Orientations of these derivatives are investigated through simulation of their ESR spectra. The derivatives with a $-CH_3$ or phenyl group derived straightforward from the *N*-substituent of the pyrrolidine ring are preferentially oriented based on their powder-like ESR spectra in the MBBA matrix. An angle of about 45^o is also found between the directors of fullerene derivatives and MBBA. In contrast, the derivatives with a $-CH_2$ group inserted between the phenyl group and the pyrrolidine ring are nearly randomly distributed in MBBA. These results illustrate the applicability of liquid crystal as a matrix to align $N@C_{60}$ derivatives for QIP applications.

Acknowledgement

When the DPhil is going to finish, I would like to thank all the people who have helped and supported me.

First of all, I shall thank Dr Kyriakos Porfyrakis, my primary supervisor. I have benefitted a lot from his expertise, as well as his enthusiasm to explore new knowledge. Through my DPhil course, he has generously offered immeasurable support to me. He taught me to operate HPLC, a machine with which I spent a significant portion of my time in the last four years. More importantly, I have greatly enjoyed the time with him, whenever in work or out of work. I would like to thank Dr Andrei N. Khlobystov, for his indispensible guidance in my project. He has been a great source of knowledge and has a profound understanding of fullerene chemistry. His critical thinking 'surprised' me, but he is right the person who would guide you to the right direction. I would also like to thank my two other supervisors, Prof. Andrew Briggs and Dr Arzhang Ardavan, for their inspiring comments and helpful discussions.

My sincere thanks go to Dr Maria del Carmen Gimenez-Lopez, for her help in acquisition of some of the NMR and MS spectra; to Martyn Jevric, for his contribution to prepare some precursors and the fun he brought to the group; to Dr Steven Karlen, for teaching me the chemistry of porphyrin; to Georgios Charalambidis and Athanassios G. Coutsolelos, for their kind provision of the porphyrin sample. I also wish to extend my gratitude to those who help me develop my research skills: Dr Simon Benjamin and Dr Jason Smith for their introduction course to QIP, Dr John Morton for his help in EasySpin, Dr Jeffrey Harmer for the training on using the EMX spectrometer and Dr Ilya Kuprov for teaching me how to perform quantum chemical calculations.

I owe my thanks to Rizvi Rahman for his kind offer to run excitation experiments on my samples, Vasileia Filidou for trying my samples in the pulsed-ESR spectrometer, Dr Simon Plant, Dr Yasuhiro Ito and Dr Jamie Warner for their helps in the chemistry lab. It was also a great pleasure to work with Benjamin Farrington, Yimin Wu, Hua Wu, Richard Brown, Mujtaba Zaka, Thomas Poulianitis and others in the dynamic QIP group.

I acknowledge the Oxford Supercomputing Centre for the provision of computing services, the Department of Materials for facilities and the Department of Chemistry for acquisition of spectra. In addition, I wish to acknowledge the financial support from China Oxford Scholarship Fund, William Louey Educational Fund, and St. Anne's College. Without their support, I would not be able to study in Oxford.

Finally, I have to thank all my family members and friends for their understanding and support. Especially, I should thank Zhidan Liu for her love and everything she has done for me.

Contents

Abbreviations and Acronyms

3-D	three dimentional
B3LYP	Becke, 3-parameter, Lee-Yang-Parr
BrPOT	2,4,6-*tris*-(4-bromophenoxy)-1,3,5-triazine
CC	coupled cluster
CI	configuration interaction
CuTPP	copper (II) tetraphenylporphyrin
CW	continuous wave
DCTB	*trans*-2-[3-(4-tert-butylphenyl)-2-methyl-2-propenylidene] malononitrile
DFT	density funtional theory
DMF	dimethylformamide
DMSO	dimethyl sulfoxide
EDMR	electrically detected magnetic resonance
EI	electron impact ionisation
EMF	endohedral metallofullerene
ESI	electrospray ionisation
ESR	electron spin resonance
GDIIS	geometry optimization by direct inversion of the iterative subspace
H_2TPP	tetraphenylporphyrin
HEG	homogeneous electron gas
HF	Hartree-Fock theory
hfc	hyperfine coupling constant
HOMO	highest occupied molecular orbital
HPLC	high performance liquid chromatography
IPR	Isolated pentagon rule
LDA	local density approximation
LUMO	lowest unoccupied molecular orbital

ABBREVIATIONS AND ACRONYMS

MALDI	matrix assisted laser desorption ionisation
MBBA	*N*-(4-Methoxybenzylidene)-4-butylaniline
MP	Moller-Plesset
MS	mass spectrometry
NMR	nuclear magnetic resonance
ODMR	optically detected magnetic resonance
PCC	pyridinium chlorochromate
PES	potential energy surface
PM3	Parameterized Model number 3
ppm	parts per million
QIP	quantum information processing
RF	radio frequency
RFO	rational function optimization
SCF	self-consistent field
SWNTs	single-walled nanotubes
TEMPO	2,2,6,6-tetramethyl-1-piperidinyloxy
TNT	trimetallic nitride template
UV-vis	ultraviolet-visable
XRD	X-ray diffraction
ZFS	zero-field splitting

List of Figures

LIST OF FIGURES

LIST OF FIGURES

LIST OF FIGURES

LIST OF FIGURES

LIST OF FIGURES

LIST OF FIGURES

List of Tables

LIST OF TABLES

Chapter 1

Quantum information processing and endohedral fullerenes

1.1 Overview of quantum information processing

The booming information technology has witnessed the success of Moore's Law over more than half a century. However, if the circuitry packed onto silicon chips continues to shrink as expected, it will soon reach the area where determinism of the classical theory becomes invalidated. In this context, quantum information processing (QIP) which incorporates quantum mechanics and information theory may provide a completely new route towards enhanced computation power. In 1985, Deutsch proposed a *universal quantum computer* based on both quantum mechanics and the Turing machine [1]. Such a quantum computer, in principle, has many remarkable properties not reproducible by any classical computers and may solve some problems effectively intractable to the latter.

Deutsch's proposal intrigued worldwide research interest, and significant progress has been achieved since then. In 1994, Peter Shor devised the *Quantum Fourier Transform* algorithm, known as Shor's algorithm [2]. This algorithm scales only polynomially with the size of the problem rather than exponentially as the classical *Fast Fourier Transform* does. As a straight application of Shor's algorithm, two extremely important problems in computation, factoring integers and finding discrete logarithms, could be efficiently resolved in a quantum computer [3]. Experimentally, Shor's algorithm has been demonstrated in a nuclear magnetic resonance (NMR) implemented quantum computer [4] and entangled photonic qubits (quantum bits) [5,6], by factoring 15 into 3×5.

1.1.1 Physical implementation of QIP

To build up a physical system for QIP, there are many realistic concerns to address. In 2000, DiVincenzo developed the so-called *DiVincenzo criteria*, which have been widely accepted as the general standards for any physical QIP systems [7]:

a. A scalable system with well characterized qubits;

b. The ability to initialize the qubits to a simple fiducial state, such as $|000...\rangle$;

c. Long relevant decoherence times, much longer than the gate operation time;

d. A 'universal' set of quantum gates;

e. A qubit-specific measurement capability.

Additionally, two other criteria, known as *DiVincenzo desiderata*, were also proposed in consideration of the transmission of quantum information:

f. The ability to interconvert stationary and flying qubits;

g. The ability to faithfully transmit flying qubits between specified locations.

To date, several physical systems for QIP have been suggested and explored, although none of them matches the *DiVincenzo criteria* comprehensively. These physical systems include NMR [8], ion traps [9], cavity quantum electrodynamics [10] and quantum dots [11]. Among them, NMR has provided a testbed for computing concepts and quantum algorithms since the beginning of physical implementation of QIP, and has so far hosted the most complex example of quantum algorithms [12].

In the NMR based QIP, qubits are embodied in the nuclear spins of a molecule [13-15]. The energy of a nuclear spin $I = 1/2$ is split into two levels in an applied magnetic field. A qubit can then be defined as a superposition of the two states:

$$|\psi\rangle = \alpha|0\rangle + \beta|1\rangle \tag{1.1}$$

where α and β are complex numbers satisfying $|\alpha|^2+|\beta|^2=1$. Under a measurement, the qubit gives rise to a result of $|0\rangle$ or $|1\rangle$ at the chance of $|\alpha|^2$ and $|\beta|^2$, respectively. A single qubit can be visualized on the surface of a Bloch sphere (Figure 1.1) when it is described in polar coordinates:

$$|\psi\rangle = \cos\frac{\theta}{2}|0\rangle + e^{i\varphi}\sin\frac{\theta}{2}|1\rangle \tag{1.2}$$

The superposition state of a nuclear spin could be relaxed from interactions with the environment. Two parameters are traditionally used in NMR to describe the relaxation rate: the spin-lattice relaxation time T_1, relating to the loss of θ; the spin-spin relaxation time or decoherence time T_2, relating to the loss of phase φ. In QIP, the decoherence time T_2 is particularly important because it determines the maximum number of quantum operations on a qubit.

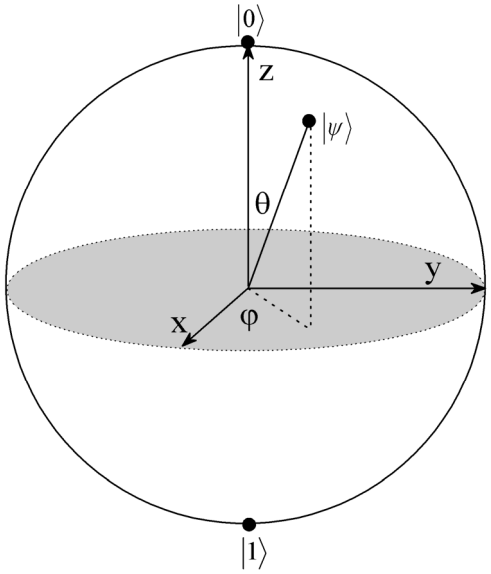

Figure 1.1: A qubit represented in the Bloch sphere.

Quantum operations in NMR are realized by applying radio frequency (RF) pulses in a specific sequence. One-qubit operations comprise of pulses at a resonant frequency with the spins [16-18]. Pulses of a pre-defined duration could move the qubit to a specific point on the Bloch sphere. A pulse that rotates the qubit with an angle of 180^o, for instance from $|0\rangle$ to $|1\rangle$, is a called a π pulse, and one that rotates with an angle of 90^o is called a $\pi/2$ pulse. Two-qubit operations are realized similarly to the one-qubit operations, but a spin-spin interaction is essential [19-22]. In NMR, such an interaction is provided by *J*-coupling, the spin-spin interaction mediated by bonding electrons joining the two nuclei.

The biggest challenge confronted by the NMR based QIP is the preparation of pure states. In NMR spectroscopy, ensemble of spins instead of single spin is used due to the limits of read-out techniques. Only pseudo-pure states can be initialized, which are statistical mixtures of pure states. Because NMR signal strength of the pseudo-pure states decreases exponentially with the number of spins, high polarization of nuclear spins is required for multiple-qubit system. However, the accessible temperature and magnetic field of NMR

restrict the extent of spin polarization given the small nuclear magnetic moments. Therefore, the number of qubits that can be processed in the NMR based QIP is fundamentally limited [23]. This intrinsic scalability drawback prompts the exploration of other physical systems.

Electron spins were recommended by Warren [24] as an alternative to nuclear spins for QIP. There are several significant benefits of using electron spins as qubits. Firstly, their bigger magnetic moment leads to larger energy separation in a magnetic field, which can enhance the spin polarization ratio under current experimental limits. Secondly, the gate operations are much faster than those for the nuclear spins. A typical electron spin rotation normally requires a pulse of about 10 ns, which is much shorter than the 10 μs for nuclear spins. In addition, the development in electrically detected magnetic resonance (EDMR) [25] and optically detected magnetic resonance (ODMR) [26] techniques may achieve more sensitive detection, even single qubit read-out in the future.

Because electron spin resonance (ESR) and NMR share the same principles, many well-developed concepts and techniques used in NMR based QIP could be readily transferred into the electron-spin based QIP. Loss and DiVincenzo proposed the implementation of a universal set of one- and two-qubit quantum operations using electron spins in quantum dots [27]. These operations can be realized by gating the tunnelling barrier between neighbouring quantum dots. Furthermore, a systematic scheme for the electron-spin based quantum computer was also developed. In this scheme, Loss *et al.* [28] addressed a series of questions required by quantum computing, including initialization, read-in, gate operations, read-out, coherence, switching times and precision. According to this scheme, a scalable and all-electronically controlled quantum computer can be envisioned and experimentally realized in quantum dots, by resorting to further breakthroughs in the semiconductor technology.

Despite its advantages, an inherent problem concerned in the electron-spin based QIP is the short decoherence time of most electron radicals. The information embodied by the

electron spin may decay completely before the processing or read-out is completed. Fortunately, the discovery of a family of new molecules, the endohedral fullerenes that possess unpaired electrons, sheds new light on the prospective of electron-spin based QIP [29-32]. Long decoherence time enough for thousands of quantum operations were observed in several endohedral fullerenes [33,34].

1.1.2 Fullerene based QIP

In 2002, Harneit proposed a scalable spin quantum computer based on endohedral fullerenes [35,36], in particular $N@C_{60}$ and $P@C_{60}$. As shown in Figure 1.2, the key points in Harneit's scheme include:

Firstly, qubits embodied by endohedral fullerenes are set and read-out via pulsed ESR. For the endohedral fullerenes of spins S=3/2, a coherent repopulation scheme suggested that large spin polarization could be achieved even at room temperature [37].

Secondly, qubit addressing is realized by local magnetic fields or field gradients (A-gate). Endohedral fullerenes usually exhibit different ESR spectrum because of the hyperfine splitting caused by electron-nuclear interaction. These different resonant frequencies could be utilized to achieve individual addressing.

Thirdly, qubit-qubit interaction (J-gate) is mediated by magnetic dipolar coupling, whose strength can be adjusted by controlling of its direction with respect to the magnetic field. The coupled spins then permit a straightforward way to implement a two-qubit operation (such as the controlled-NOT gate), via the execution of a sequence of ESR pulses. Many of the sequences have been already established in NMR based quantum computer [38], where the spin-spin interaction is provided by *J*-coupling.

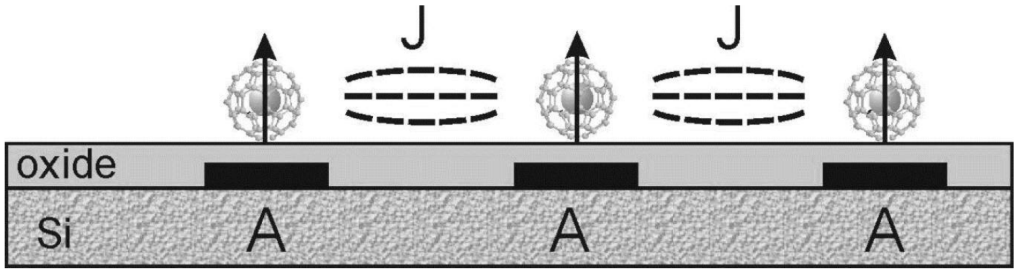

Figure 1.2: A scheme for endohedral fullerene based quantum computer proposed by Harneit. Reprinted from [35].

Harneit's scheme is in practice subject to several technological restrictions, especially the obstacle of single spin read-out. As a preliminary attempt, large molecular ensembles have to be used instead and therefore the control of spin-spin interactions has to be considered at the molecular level. Based on the rapidly developing fullerene chemistry, Harneit proposed molecular chains of endohedral fullerenes by following the key-lock principle. A realistic scheme for a hetero-endohedral dimer $N@C_{60}$-XY-$P@C_{60}$ was provided by Hirsch [39], with X, Y specially designed to react exclusively with each other (Figure 1.3). Such a dimer or chain structure can be further aligned to create ordered structure. This approach may eventually allow for realization of the quantum cellular automaton of the ABC-type [40], where three qubit units (for instance, there different endohedral fullerenes) are repeated to form a 1-D array (ABCABC …). In this scheme, the desired operations are achieved through *global control* of the whole array, and it is not needed to address the individual qubit.

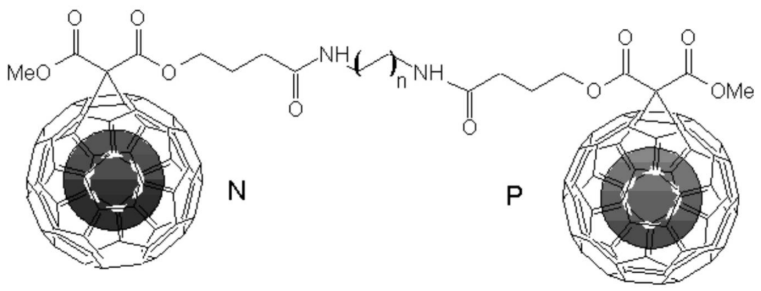

Figure 1.3: Schematic views of a hetero-endohedral dimer $N@C_{60}$-XY-$P@C_{60}$ constructed by the key-keyhole principle. Reprinted from [35].

Beyond $N@C_{60}$ and $P@C_{60}$, other endohedral fullerenes are also candidates for the electron-spin based QIP. A more generalized scheme included any spin-active metallofullerenes into the potential family of qubits [41]. Some metallofullerenes being both optically active and spin-active, such as $Er_3N@C_{80}$, offer the potential of much more sensitive optical addressing and optical read-out [42,43]. In terms of scalability, the endohedral fullerenes could be self-assembled into carbon nanotubes, forming one-dimensional fullerenes arrays or *peapod* structures [44,45]. The carbon nanotube is an excellent host because of its one-dimensional ballistic electron transport [46] and remarkably long spin coherence lengths [47]. Moreover, the nanotubes allow for fabrication of electrodes, which could be readily integrated into solid-state devices [48].

In all fullerene based QIP schemes, functionalization of endohedral fullerenes is essential. In Harneit's scheme, the functionalization provides the chemically linked fullerene dimers or chains. In the *peapod* scheme, the functionalization is essential to control the distance between the encapsulated fullerenes. As shown in Figure 1.4, such a control could be realized by adding functional groups of the specific length to the fullerenes. Thus, we are motivated to explore the functionalization of endohedral fullerenes, which would play a key role in the route toward a scalable fullerene based quantum computer.

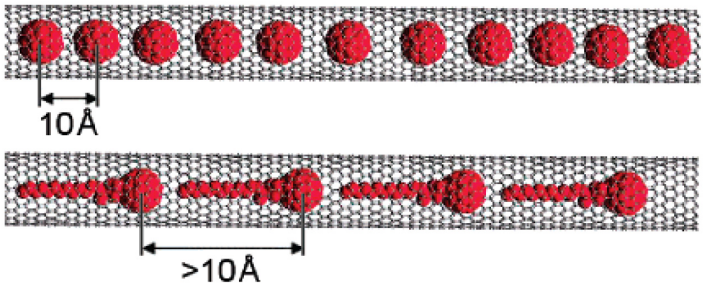

Figure 1.4: Schematic structure of a *peapod* structure (top) and a proposed method of increasing the inter-fullerene separation of peapod systems by use of a fullerene functionalized with a long alkyl chain (bottom). Reprinted from [49].

1.2 Functionalization of endohedral fullerenes

1.2.1 Endohedral fullerenes

Ever since the discovery of fullerene in 1985 [50], researchers have shown great interest in inserting atoms into the soccer-like cage regarding its considerable void size (0.4 nm to 1.0 nm across) and the perfect shield structure. Actually, it was just a few days after the discovery of C_{60} that La@C_{60} was detected by mass spectrometry [32]. Since then, the family of endohedral fullerenes has expanded in a remarkably rapid manner. Many fullerenes, including the non-IPR (isolated pentagon rule) fullerenes, could act as a host to enclose a variety of atoms. An incomplete list of these hosts includes C_{60}, C_{70}, C_{74}, C_{78}, C_{82} and C_{84}. Based on the number and nature of the encapsulated atoms, most of the endohedral fullerenes can be roughly divided into five groups:

Non-metallic Endohedral Fullerenes

In this group, only non-metallic atoms are encapsulated in a fullerene cage, such as He@C_{60}, H_2@C_{60}, N@C_{60}, P@C_{60}, N@C_{70} and P@C_{70}.

Mono-endohedral Metallofullerenes

Only one metallic atom is encapsulated into the carbon cage. Most of the monometallic endohedral fullerenes enclose group II or group III elements (including the Lanthanides), such as Gd@C_{82}, La@C_{82}, Y@C_{82} and Sc@C_{82}.

Multi-metallic Endohedral Fullerenes

Some cages accommodate more than one metal atoms, such as La_2@C_{72}, Sc_2@C_{74},Y_2@C_{82}, Er_2@C_{82} and Sc_3@C_{82}.

Trimetallic Nitride Template (TNT) Endohedral Fullerenes

Clusters consisting of three metal atoms and one nitrogen atom could be encapsulated in a fullerene cage as well. The metal atoms could be the same, as in $Sc_3N@C_{80}$, $Y_3N@C_{80}$; or different as in $ErSc_2N@C_{80}$, $Er_2ScN@C_{80}$ and $L_xLu_{3-x}N@C_{80}$ (L is one element from Sc, Er, Gd and Ho; x = 0, 1, 2).

Metal Carbide Endohedral Fullerene

This group encloses clusters of metal carbide. $Sc_2C_2@C_{84}$, which is originally claimed as $Sc_2@C_{86}$, has been later clarified by NMR [30]. Other metal carbide endohedral fullerenes include $Sc_2C_2@C_{82}$ and $Y_2C_2@C_{82}$.

Except for the non-metallic endohedral fullerenes of the first group, all those endohedral fullerenes of at least one metal atom are traditionally known as metallofullerenes (EMFs). Up to date, exploration of new endohedral fullerenes enclosing different atoms remains active in the fullerene field, in the purpose of searching for novel materials that may find applications in biomedicine or molecular electronics.

The electronic structure of endohedral fullerenes relies mainly on the nature of the atoms encapsulated in the carbon cage. In fullerenes with group V elements or inert gas atoms, such as $N@C_{60}$, $P@C_{60}$ and $He@C_{60}$, the encapsulated atoms are virtually independent from the cage and do not significantly perturb electronic structure of the original fullerene. In most EMFs, electrons are transferred from the metal atoms to the cage, which can be generally represented as $M^{n+}@(C_{2k})^{n-}$ (*n* spreads normally from 1 to 6).

1.2.2 Functionalization of EMFs

Although the chemistry of fullerenes is already well established, EMFs have not been studied as extensively as C_{60} in functionalization schemes. One of the reasons is that most

EMFs involve lower symmetry cages, such as C_{82} and C_{80}. Chemistry on these cages usually gives rise to a number of isomers and complex multiple adducts. Functionalization protocols applied on EMFs are summarized in Figure 1.5. These reactions include Diels-Alder [4+2] cycloadditions [51,52], [3+2] cycloadditions [53-56] and [2+1] cycloadditions such as the Bingel-Hirsch reaction [57-59]. In addition to these cycloadditions, free radical reactions and other miscellaneous schemes have been reported in the fluorinated derivative of trimetallic nitride template (TNT) metallofullerene $Sc_3N@C_{80}(CF_3)_{16}$ [60] and the chlorinated derivatives of the missing fullerenes $La@C_{74}(C_6H_3C_{l2})$ [61] and $La@C_{80}(C_6H_3Cl_2)$ [62]. In the chemistry of EMFs, the atoms encapsulated inside the carbon cage exert important effects on the reactivity and the addition pattern [63,64].

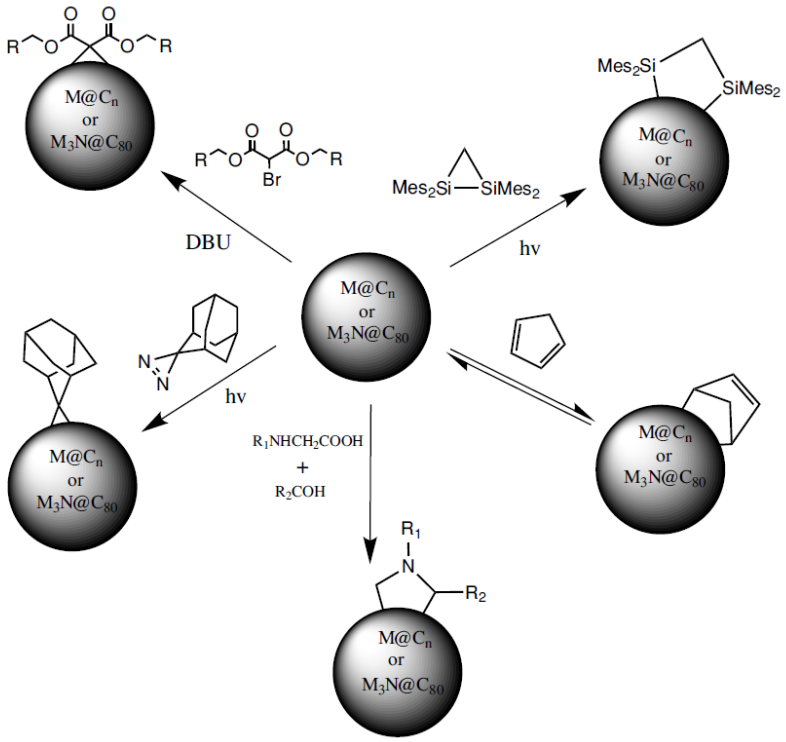

Figure 1.5: Chemical functionalization routes for EMFs. Reprinted from [65].

Further to covalent bonding, non-covalent interactions present an attractive route toward the assembly of arrays of endohedral fullerenes. These interactions include hydrogen-

bonding, van der Waals interactions, π-π stacking interactions and coordination chemistry. Porphyrins, cyclodextrins, calixarenes and other macrocycles can be complexed with fullerenes to create supramolecular arrays [66-68].

1.2.3 Derivatives of La@C_{82}

The three major spin-active EMFs, La@C_{82}, Y@C_{82} and Sc@C_{82} exhibit decoherence time long enough for QIP. T_2 greater than 200 μs has been recently achieved for all these fullerenes under optimized temperature and solvent [34]. However, only La@C_{82} has been widely explored in terms of chemistry.

With the symmetry of C_{2V}, there are 24 non-equivalent carbons and 19 non-equivalent [6,6] junctions in La@C_{82}. Therefore, several isomers were usually identified in the functionalization of La@C_{82} through analysis of ESR spectra. In the early reports, no structural details were resolved because of the lack of complete separation. The first functionalization on La@C_{82} was performed in 1995 by Akasaka e*t al*. [69]. Both disilirane [69,70] and digermirane [71] were functionalized into La@C_{82} through photochemical and thermal addition. A higher reactivity of La@C_{82} was observed in both additions compared with empty fullerenes. This finding is consistent with the theoretical calculations that La@C_{82}, as well as Y@C_{82} and Sc@C_{82}, are stronger electron donors and stronger electron acceptors than C_{60} and C_{70} [72]. In addition, the first derivative with a C-C bond derived from La@C_{82} was synthesized in the reaction of La@C_{82} with diphenyldiazomethane (Ph_2CN_2) [73].

Application of high performance liquid chromatography (HPLC) enables the complete separation of La@C_{82} derivatives. In 2002, 7 isomers of perfluoroalkylated La@C_{82} (La@C_{82}-(C_8F_{17})$_2$) were separated for the first time, although no structural information was revealed [74]. Later, Akasaka *et al.* made more progress in the [3+2] cycloaddition of

La@C_{82}. Pyrrolidine derivatives of La@C_{82} were firstly synthesized through addition of an azomethine ylide to La@C_{82} [75]. The addition was found to be efficient and relatively regioselective, where the two major derivatives, a monoadduct and a bisadduct, were separated with the abundance ratio of ~1:0.4.

Because of its open-shell structure, La@C_{82} is different from empty fullerenes in the Bingel-Hirsch reaction [76,77]. Among the 5 isomers of the monoadducts, only one preserves the unpaired electron of pristine La@C_{82}, while all the rest is spin-silent. The paramagnetic isomer possesses a cyclic moiety between the appended malonate group and the fullerene cage, analogous to the conventional Bingel-Hirsch adducts. In contrast, the 4 spin-silent isomers have a single bond linked between the appended group and the carbon cage. All the isomers were characterized by NMR techniques, and remarkably, the structure of one single bonded derivative was unambiguously determined by X-ray crystallographic analysis.

A highly regioselective reaction carried out on La@C_{82} is the carbene addition with 2-adamantane-2,3-[3H]-diazirine [78]. The exclusive derivative was characterized by single crystal X-ray diffraction. The La atom stays at a single site near the end of the molecule and its position remains surprisingly constant over a wide temperature range from 90 K to 293 K. This derivative should have an open structure, because the distance between the two sp^3 carbons (2.097 Å) is longer than a normal C-C bond of the fullerene cage (around 1.4 Å). Another highly regioselective reaction performed on La@C_{82} is the [4+2] cycloadditions with cyclopentadiene, where only one derivative was identified by both HPLC and ESR spectroscopy [79]. An additional advantage of this reaction is its reversibility, which could be employed to control addition pattern of the second reaction on La@C_{82}.

The exohedral groups may invoke significant electronic changes to La@C_{82}. In terms of spin properties, the effects of functionalization on La@C_{82} are summarized as follows:

Firstly, the unpaired electron of La@C_{82} can be quenched as a consequence of the functionalization. When a covalent bond is derived, only one electron is diverted away from the originally unpaired electron system of La@C_{82}. If the number of single bonds is odd, the derivative would have even number of electrons and become spin-silent. A typical example is the 4 diamagnetic monoadducts in the Bingel-Hirsch reaction of La@C_{82} [77]. Therefore, to reserve the open-shell structure in La@C_{82} derivatives, either an even number of single bonds or cycloadditions must be applied [69,78,79].

Secondly, a shift in the hyperfine coupling constant (hfc) of the encapsulated metal is usually observed in La@C_{82} derivatives. Because hyperfine coupling is the interaction between electron spins and nuclear spins, a shift in hfc to some extent reflects the electron density deviation induced by the addends. Larger hfc (1.5-1.9 G) is observed in all isomers of the disilirane and digermirane derivatives of La@C_{82} (hfc of La@C_{82} is 1.15 G) [69-71]. The hfc in pyrrolidine monoadduct is analogous (1.14-1.17 G) [73], but decreases in the carbene derivative (0.89 G) [78]. Additionally, it becomes slightly larger in the bisadduct of pyrrolidine derivative (1.2 G) [75], but significantly larger in bisadduct of perfluoroalkylated La@C_{82} (3.7-3.8 G) [74].

1.3 Endohedral nitrogen fullerenes

1.3.1 Electron spin properties

Endohedral fullerene N@C_{60} has attracted much attention because of its special molecular structure: a C_{60} cage enclosing atomic nitrogen [80,81]. The stability mechanism of the reactive nitrogen atom was investigated theoretically through quantum chemical calculations [82]. It was found that high energy barrier blocks nitrogen from bonding with or from

passing through the fullerene cage, which demonstrates that N@C_{60} is structurally, rather than chemically, inert due to the rigidity of the fullerene cage.

The spin-active ^{14}N@C_{60} has a spin system analogous to nitrogen atom. Three electron spins S = 3/2 are coupled to the ^{14}N nuclear spin I = 1, with the Hamiltonian in high field approximation of:

$$\hat{H} = \omega_e S_z - \omega_I I_z + \hat{S} \cdot \mathbf{A} \cdot \hat{I} \tag{1.3}$$

where $\omega_e = g\mu_B B_0 / \hbar$, $\omega_I = g_N \mu_N B_0 / \hbar$, μ_B is the Bohr magneton, μ_N is the nuclear magneton, B_0 is the magnetic field strength, and **A** is the hyperfine interaction tensor. The system results in a 12-level structure as shown in Figure 1.6. Although nine transitions are permitted according to the selection rules, the electron spin transitions $\Delta M_S = 1$ within the S=3/2 multiplet are nearly degenerate given their small difference of 26 KHz [83] that usually falls within the spectrometer resolution limits. Therefore, three distinct transitions due to electron-nuclear spin coupling are usually observed in the continuous wave (CW) ESR spectrum of N@C_{60}. Only when a high resolution spectrometer is applied, can the degeneracy be lifted and all nine transitions be resolved. In that case, line broadening caused by inhomogeneous magnetic field in the spectrometer falls short of the intrinsic linewidth and therefore the second order corrections take effects. The hyperfine coupling constant (hfc) of N@C_{60} is approximately 50% larger than that of the free nitrogen atom. This increase of hfc is explained by a compressing effect imposed by the carbon cage on the encapsulated nitrogen. Hyperfine interaction with ^{13}C nuclei in the carbon cage is also observed. However, based on the small hfc (34 kHz) [84], approximately only 2% of the electron wave function of nitrogen spreads onto the fullerene cage. This finding indicates that the unpaired electrons of N@C_{60} are highly localized on the nitrogen atom.

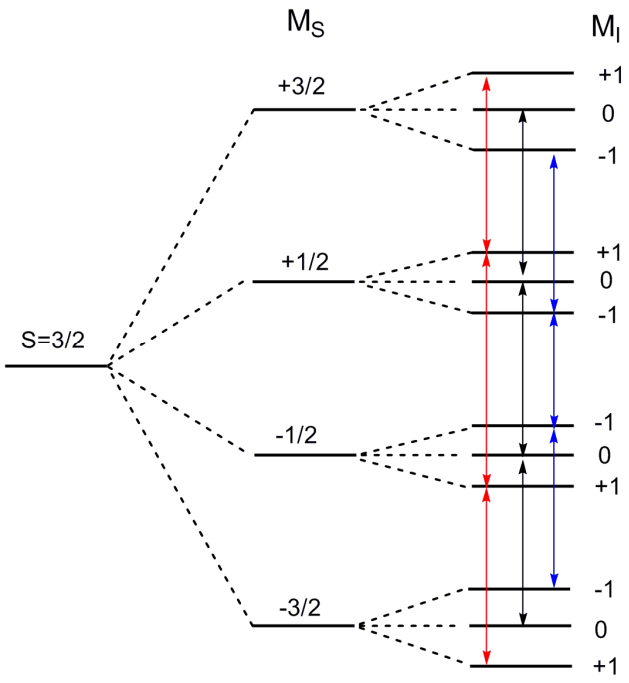

Figure 1.6: Energy level diagrams and the allowed transitions for $^{14}N@C_{60}$.

$N@C_{60}$ exhibits excellent magnetic properties because of the shielding effect provided by the carbon cage [80,84,85]. Because of its high symmetry, the relaxation pathways of electron spin are different in $N@C_{60}$. For most high spin ($S \geq 1$) systems, relaxation induced by fluctuating zero field splitting (ZFS) is usually the dominant mechanism. However, an Orbach relaxation mechanism, via the first excited vibrational state of the fullerene molecule, is found for $N@C_{60}$ by temperature dependence studies [33]. Remarkably, $N@C_{60}$ exhibits the longest decoherence time among any molecular radicals. The T_2 of 250 μs at 170 K allows more than 10^4 high fidelity quantum gate operations to be performed [33,86]. Moreover, its decoherence time reaches as long as 80 μs even at room temperature, which shows great prospect for practical applications.

Several recent experiments have demonstrated the feasibility of using $^{14}N@C_{60}$ or its isotopic brother $^{15}N@C_{60}$ as qubits in the electron-spin based QIP scheme. Firstly, high-fidelity one-qubit operations were successfully realized on the electron spins of $N@C_{60}$ by

applying composite pulses [87]. These high fidelity operations fall within the coherence time requirements for the application of quantum error correction, although they are still limited by pulse phase quality in the existing spectrometers. Secondly, coherence of the nuclear spin qubit was maintained for an arbitrary period through the *quantum bang-bang control* [88,89]. In this strategy, ultrafast phase gates on the nuclear spin are repeatedly applied by driving the coupled electron spins around a closed cycle. These fast phase shifts can lock the nuclear spin to a given state and effectively suppress its unwanted coupling to the environment. Finally, coherent state transfer between the electron spins and the nuclear spins has been recently achieved through a two-way transfer process with 88% fidelity [90]. This hybrid scheme provides a solution to effectively turn on or turn off interactions between two neighbouring electron spins.

1.3.2 Synthesis and purification

There are two well established methods to synthesize $N@C_{60}$: ion implantation and glow discharge, plus the newly reported method of electron cyclotron resonance. Ion implantation is the method through which $N@C_{60}$ was firstly discovered in 1996 [80], and remains as a method with relatively decent yield (10^{-4} to 10^{-5}). The glow discharge method uses high electrical field to ionize the nitrogen gas instead of an ion source [81], but its yield is usually an order of magnitude lower than for ion implantation. Electron cyclotron resonance is a new technique that generates plasmas by application of microwave radiation to a nitrogen gas in the presence of a magnetic field [91]. The N_2 was ionized and a yield of 3×10^{-4} for $N@C_{60}$ was reported under the optimized conditions. However, it is not clear whether this method can scale up and produce comparable amounts with the other two established methods.

In most applications of $N@C_{60}$, samples of large molar ratio of $N@C_{60}$ to C_{60}, or even pure $N@C_{60}$ are required. Therefore, multi-stage HPLC is usually employed to enrich

$N@C_{60}$ from the crude products. The enrichment process is labourious because of two obstacles: the very low production yields of $N@C_{60}$ for current methods, and the fact that C_{60} and $N@C_{60}$ are almost chemically identical. Nevertheless, an almost complete isolation of $N@C_{60}$ with a purity of higher than 99% has been achieved via a combination of multiple injections and recycling HPLC by several groups including ours [92-94].

1.3.3 Functionalization of endohedral nitrogen fullerene

$N@C_{60}$ resembles C_{60} in reactivity. All reactions performed on $N@C_{60}$ have been transferred from those well developed on C_{60}. However, functionalization of $N@C_{60}$ is practically restricted by two obstacles. The first one is the difficulty in producing the material at a scale normally required to carry out a chemical reaction. The second and equally formidable one is the lower thermal and photolytic stability of $N@C_{60}$. Because most reactions applied to C_{60} are either thermally- or photolytically-activated, $N@C_{60}$ is not as robust as C_{60} to survive these harsh conditions.

The reported derivatives of $N@C_{60}$ are summarized in Figure 1.7. These derivatives are functionalized with exohedral 3- to 6-membered ring groups. The cyclopropanated derivative **1** was the first derivative of $N@C_{60}$ synthesized through Bingel-Hirsch reaction [81] and the hexaadduct $N@C_{66}(COOC_2H_5)_{12}$ [95] was similarly obtained with excessive diethyl bromomalonate. The epoxide derivative **2** was oxidized from $N@C_{60}$ by H_2O_2 in the presence of MeO_3Re under ambient conditions for 12 hours [96].

The pyrrolidine derivatives were simultaneously synthesized by Franco *et al.* [97] and by our group [98] through the Prato reaction. Refluxing of $N@C_{60}$ with formaldehyde and *N*-methylglycine under the protection of nitrogen gas affords the derivative **4**. Following the same scheme, other pyrrolidine derivatives including derivatives **5** and **6**, can be synthesized

by using corresponding aldehydes. These Prato reactions afforded decent yields, for instance, a yield of 31% for derivative **5** [98].

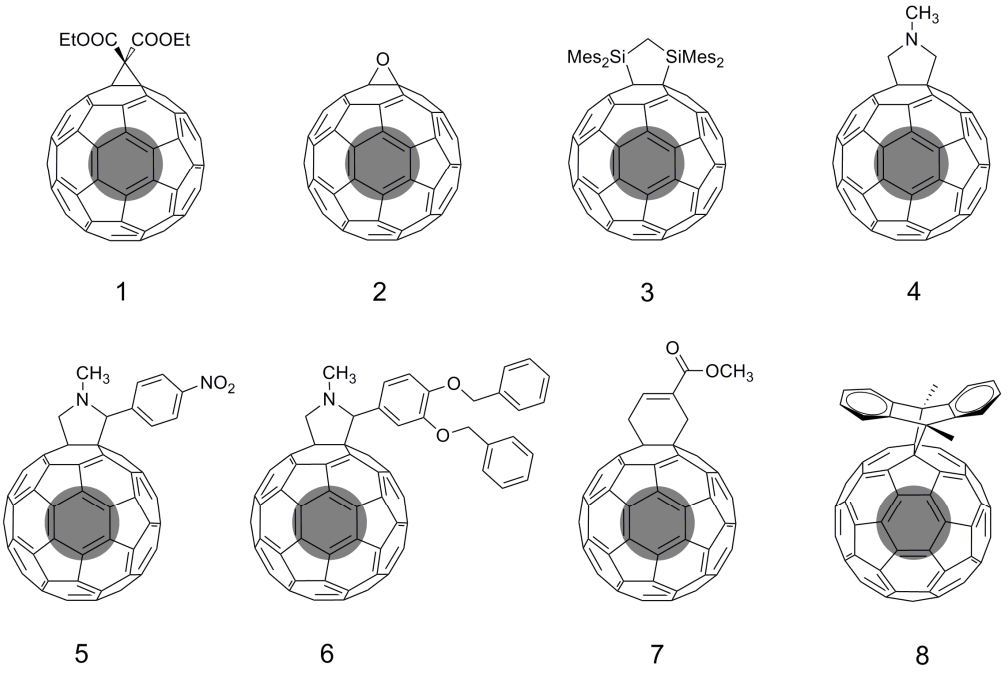

Figure 1.7: Schematic views of currently reported N@C_{60} derivatives.

Derivative **7** with a 6-membered ring group and derivative **8** with a bicyclic group were both achieved by following the established schemes for C_{60} [97]. In addition to these derivatives synthesized through thermally activated chemistry, derivatives from photochemical synthesis have been reported as well. Derivative **3** was a product of bis-silylation of N@C_{60} under ultraviolet excitation [99].

Compared with the wide scope of C_{60} derivatives, hardly any adducts with functional groups other than an exohedral ring have been reported for N@C_{60}. The reason is partly due to the limited amount of available N@C_{60} for chemistry, and therefore more work on the production and purification of N@C_{60} is necessary.

In terms of purity of these N@C_{60} derivatives, it is important to clarify that none of them was ever separated from the corresponding C_{60} derivatives. Up to date, all claimed reactions

on $N@C_{60}$ were actually performed on the $N@C_{60}/C_{60}$ mixture (usually with a molar ratio lower than 0.01). The restriction in purity of the starting materials gives rise to two major concerns in $N@C_{60}$ chemistry. The first one is the reactivity. It has been proved that the endohedral nitrogen atom in $N@C_{60}$ brings little modification to the electronic structure of the carbon cage [80,81]. Therefore, it is usually assumed that $N@C_{60}$ exhibits a similar reactivity to C_{60} in reactions. Although this assumption is partly supported by the successful transfer of reactions from C_{60} to $N@C_{60}$, it has not been proved yet by conclusive experimental results. In principle, such proof could be found by a comparison of the nitrogen filling ratio in the starting materials and that in the derivatives. However, the problem becomes complicated in practice because of the decomposition of $N@C_{60}$ in most reactions. Equal reactivity of $N@C_{60}$ and C_{60} was firstly reported in parallel with the doubtful claim that no change in nitrogen filling ratio was observed in the Bingel-Hirsch reaction [95]. In contrast, a significantly lower reactivity of $N@C_{60}$ was claimed in its photochemical reaction with disilirane [99]. Akasaka *et al*. found a higher nitrogen filling ratio for the unreacted $N@C_{60}/C_{60}$ than for the starting materials, and deduced a relative reactivity of $N@C_{60}$ to C_{60} equalling to 0.7 [99]. Due to the low purity of $N@C_{60}$ and the accuracy limits of quantitative ESR analysis, further work is necessary to fully understand the reactivity of $N@C_{60}$. Additionally, the instability of $N@C_{60}$ causes extra trouble when the nitrogen filling ratio is compared. In contrast to the earlier claims that all the electron spins were recovered after the reaction [95], obvious loss of spin signal was found in later studies [98,100].

The other concern in $N@C_{60}$ chemistry is the full characterization of $N@C_{60}$ derivatives. The presence of nitrogen in the derivatives can be hardly detected by mass spectroscopy due to both the low purity of $N@_{60}$ and its possible decomposition during the acquisition. Therefore, the existence of $N@C_{60}$ derivatives is currently established by ESR spectroscopy. Firstly, the corresponding C_{60} derivatives are purified and fully characterized by

conventional methods such as MS, NMR and UV-vis. Secondly, the reaction is transferred to $N@C_{60}/C_{60}$ mixture and the derivatives are accordingly isolated. Thirdly, the presence of $N@C_{60}$ derivative would be confirmed by the characteristic features in the solution ESR spectrum of the product mixture.

1.3.4 $N@C_{60}$ dimers

In Harneit's scheme for endohedral fullerenes based quantum computer [35], a hetero-endohedral dimer $N@C_{60}$-XY-$P@C_{60}$ was proposed based on the chemical key-keyhole principle. Although synthesis of the hetero-endohedral dimer has not been reported yet, some encouraging progresses have been made over the last decade.

Firstly, many fullerene dimers were synthesized with different bridging groups. To control the strength of dipolar coupling that is essential in QIP, it is important to tune the centre-to-centre distance between the two fullerene cages. Figure 1.8 shows some dimers of different separation distance [101]. The shortest distance of 9.4 Å corresponds to the directly bonded dimer. The longest distance of 14.8 Å corresponds to the dimer with a polycyclic bridge moiety. By following this strategy, the inter-fullerene spacing is modulated by at least 57%, and this is not the limit. Other chemical groups can afford even larger spacing between the fullerene cages [102].

Secondly, fullerene dimers with half-filled moiety have been synthesized as a preliminary step toward the final hetero-endohedral dimer. Three examples are shown in Figure 1.9. $N@C_{60}$-C_{60} (dimer **1**) was the first half-filled fullerene dimer [103], where the two fullerene moieties are joint by directly linked cycloaddition bond in the centre. Dimer **1** was prepared through a mechano-chemical synthetic approach, where mixtures of $N@C_{60}/C_{60}$ are milled together. However, the method affords low yields and lacks control of the dimer structure.

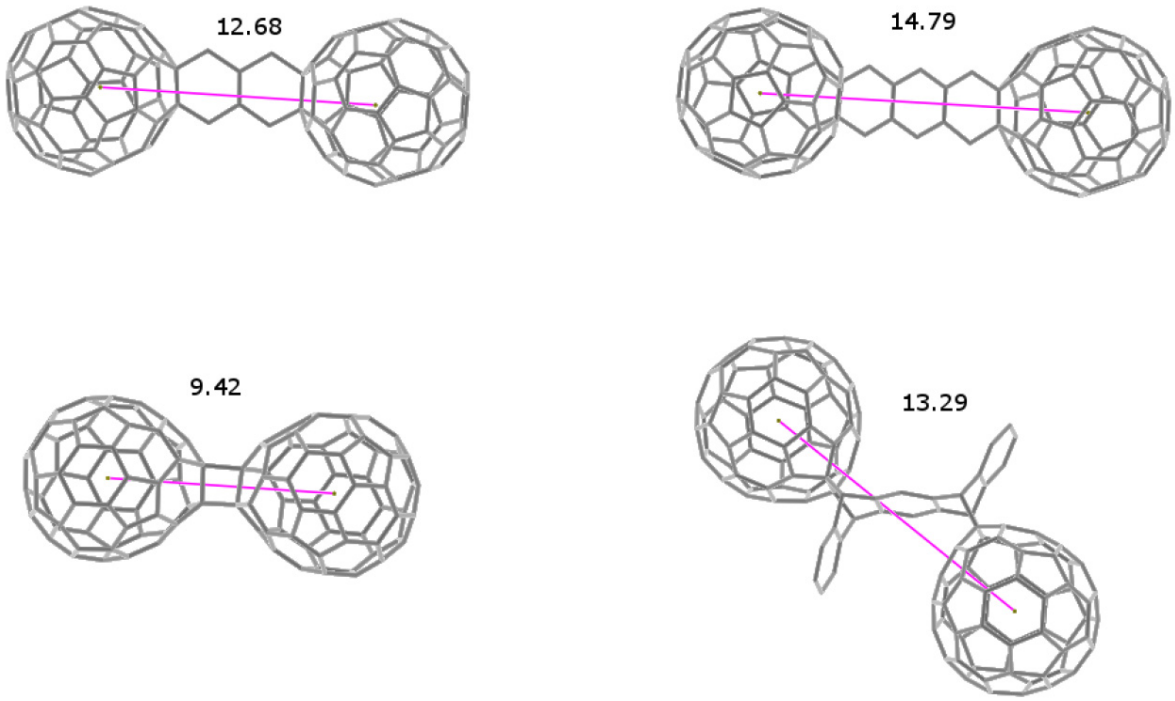

Figure 1.8: Comparison of the centre-to-centre distance between fullerene cages, for experimentally synthesized, covalently bonded dimers with a variety of bridge molecules. All distances are quoted in units of Å. Reprinted from [101].

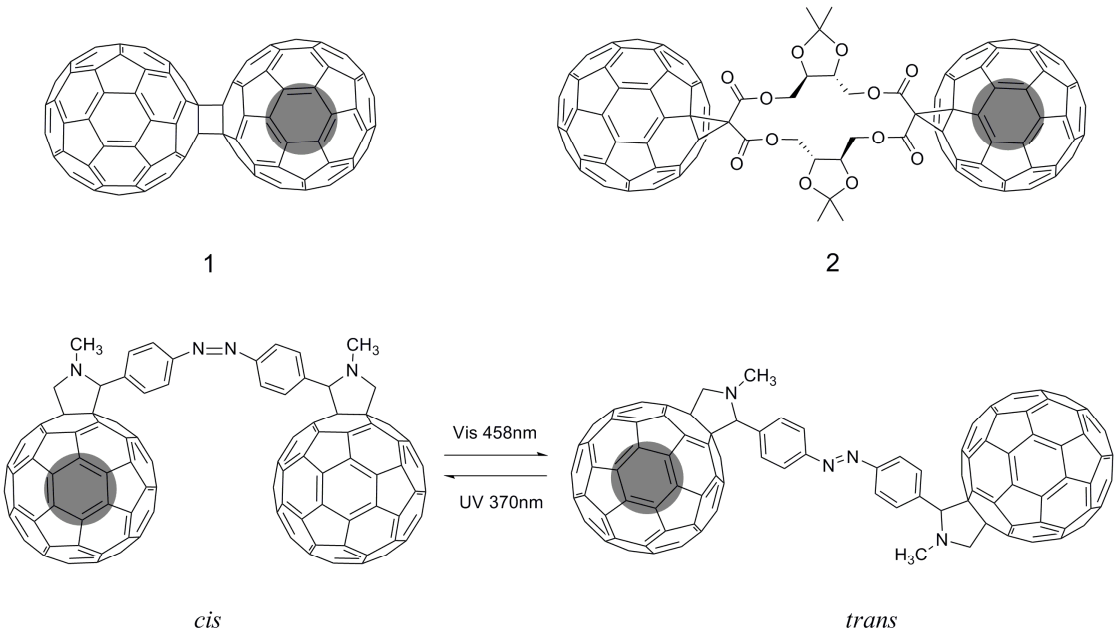

Figure 1.9: Schematic views of $N@C_{60}$-C_{60} dimers.

The $N@C_{60}$-C_{60} dimer joint by *cyclo*[2]malonate (dimer **2**) was recently produced through the Bingel-Hirsch reaction [100]. With the intention to prepare the hetero-fullerene dimer, a two-step strategy was adopted (Figure 1.10). In the first step, only one of the malonate groups was reacted with the fullerene to give the monomer as the dominant product. The remainder malonate group in the monomer was then reacted with another C_{60} fullerene (different fullerenes could be used to afford the hetero-fullerene dimer). With a decent yield for each step, a final yield of 18% was achieved.

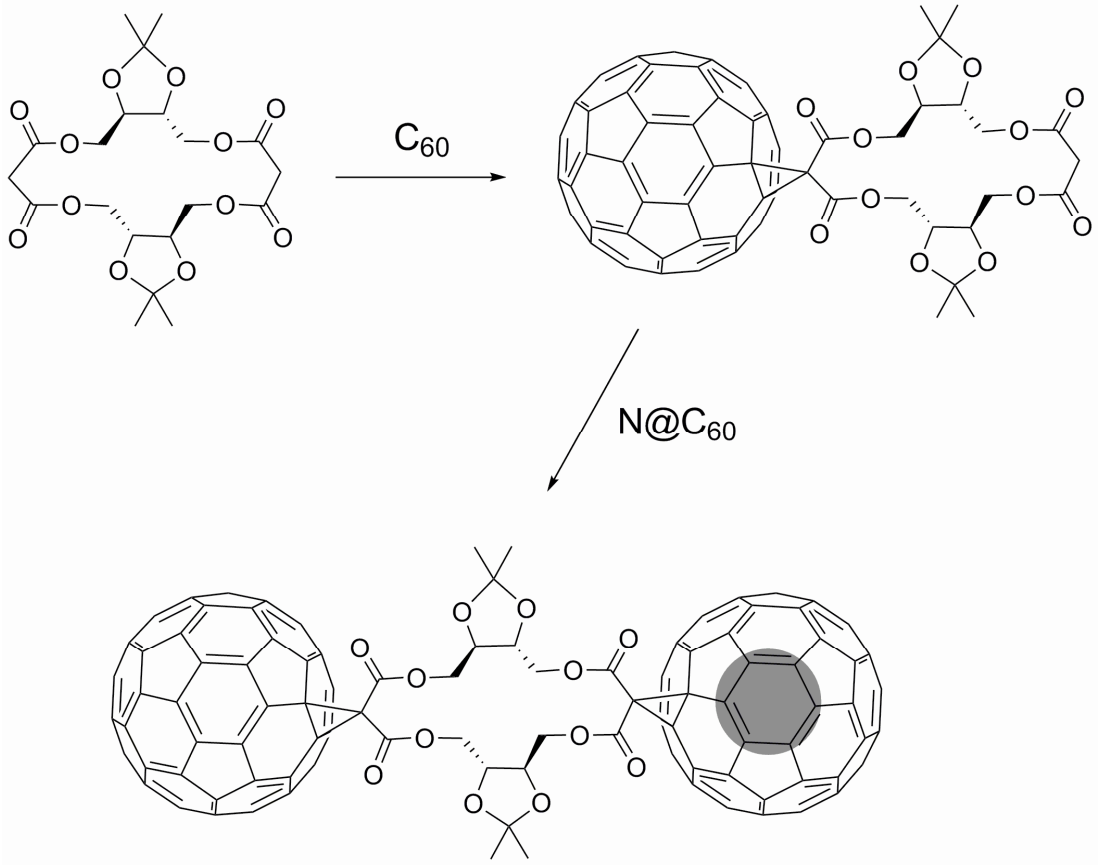

Figure 1.10: A two-step synthetic strategy for the $N@C_{60}$-C_{60} dimer. Adapted from [100].

Thirdly, the synthesis of dimer **3** marks another significant progress [104]. The $N@C_{60}$-azo-C_{60} dimer was prepared using bis-aldehyde 4, 4-azobenzaldehyde through the Prato reaction. When the scheme was firstly applied on C_{60}, the 2-day reaction afforded the C_{60}-azo-C_{60} dimer with a yield of 95%. Nevertheless, the reaction time was reduced to

approximately 2 hours when it was performed on $N@C_{60}/C_{60}$ in order to minimize the decomposition of encapsulated nitrogen atom. Under this condition, the 30% yield for the half-filled dimer $N@C_{60}$-azo-C_{60} is still higher than the overall yield for dimer **2**. Moreover, the two-step strategy could be similarly incorporated into this scheme to produce a hetero-fullerene dimer of $^{14}N@C_{60}$-azo-$^{15}N@C_{60}$.

Dimer **3** exhibits the photoisomerism features inherited from its azobenzene moiety. Upon irradiation with UV or visible light, the dimer can switch between the *trans*- and *cis*-configurations (Figure 1.9). The two isomers demonstrate different rotational correlation time τ_c. Using pulsed ESR techniques, τ_c = 37.2±1.6 ps was measured for the *trans*- and τ_c = 34.8±2.7 ps for the *cis*-isomer. The difference is consistent with the fact that the *trans*-isomer is bulkier in space than the *cis*-isomer. The photoisomerism of dimer **3** demonstrated in principle the feasibility of modulating the separation distance between the fullerene cages and hence the spin-spin interactions in the same molecule.

1.3.5 ESR spectroscopy of N@C_{60} derivatives

Due to its high sensitivity, ESR spectroscopy is not only a critical characterization technique, but also a powerful tool to study the spin properties of $N@C_{60}$ derivatives.

Hyperfine coupling A change in hyperfine coupling constant (hfc) reflects the electron density deviation induced by the addends. Hfc of the hexa-adduct $N@C_{66}(COOC_2H_5)_{12}$ is about 0.7% smaller than that of the pristine $N@C_{60}$ [95]. Such a change results from the enlargement of the carbon cage in the hexa-adduct, which is supported by analysis of the X-ray single crystal structure of $C_{66}(COOC_2H_5)_{12}$ [105]. The hfc decreases slightly in dimer **1** (in Figure 1.9) as well [103], but it remains nearly constant in derivatives **5**-**7** (in Figure 1.7) with 5- or 6-membered or bicyclic ring groups [97].

Fine structure Fine structure is observed in the ESR spectrum of all the known derivatives of N@C_{60}. In pristine N@C_{60}, the nitrogen atom is located exactly at the centre of C_{60} and its three *p* orbitals are degenerate due to the high symmetry of the cage. When functional groups are attached, the carbon cage would be distorted and the molecular symmetry is correspondingly lowered. Consequently, the degeneracy of the three *p* orbitals is removed in N@C_{60} derivatives and fine structure appears in their solid state ESR spectra. The spin Hamiltonian of N@C_{60} derivatives with zero field splitting (ZFS) term is then represented by:

$$\hat{H} = \omega_e S_z - \omega_I I_z + \hat{S} \cdot \mathbf{A} \cdot \hat{I} + \hat{S} \cdot \mathbf{D} \cdot \hat{S} \tag{1.4}$$

Where **D** is the ZFS tensor, and is traditionally converted to two parameters *D* and *E* by $D = 3z/2$ and $E = (y - x)/2$ (x, y, z are the eigenvalues of **D**).

The value of *D* is subject to the chemical structure of the N@C_{60} derivatives. It increases in order in the 3- (6.1 MHz) to 4- (14 MHz) and 5-membered rings fused derivatives (17.2 MHz), but decreases in the 6-membered ring fused derivative (16.2 MHz) [97]. This trend is related to the geometrical angle θ of the bond joining the functional group and the carbon cage (defined in Figure 1.11). The maximum *D* corresponds to the angle of 104°, which is close to the angle between the radial *p* orbital of the carbon atom and [6, 6] bonds in pristine fullerene (101.6°). In this geometry, the fullerene cage would be distorted to the maximum extent. As shown in Figure 1.11, the electron density of the encapsulated nitrogen is distorted to an elongated pear-shape in the 5-membered ring derivative, while it maintains a nearly spherical shape in the 3-membered ring derivative.

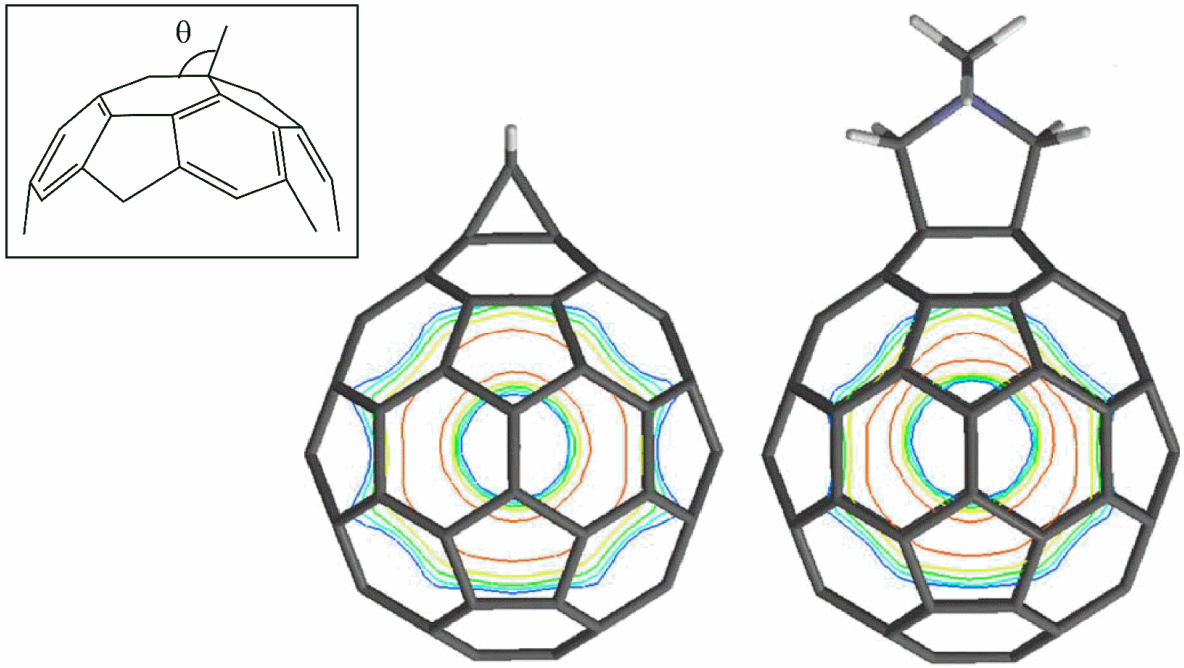

Figure 1.11: Calculated endohedral electron density in two $N@C_{60}$ derivatives. (a) A cyclopropanated derivative; (b) Pyrrolidine derivative **4**. Inset: angle between the appended bond and the [6, 6] bond. Reprinted from [97].

Linewidth and relaxation time Linewidth of $N@C_{60}$ derivatives is usually increased in the powder ESR spectra. The broadening might be attributed to either the anisotropic dipolar interaction between the nitrogen spins and protons of the addends, or the nonvanishing ZFS effects caused by matrix-induced cage distortion [95]. In a comparative experiment, Hirsch *et al*.[95] demonstrated that deuteration of the addends reduced significantly the linewidth measured in powder spectra. This observation indicates that the linewidth broadening of $N@C_{60}$ derivatives in powder spectra is mainly caused by the electron-nuclear dipolar interactions.

For $N@C_{60}$ derivatives in solution, the functional groups affect relaxation time of the nitrogen spins. As shown in Table 1.1, relaxation times in solution for all the derivatives are shorter than those for pristine $N@C_{60}$. In the pyrrolidine derivatives of $N@C_{60}$, the 'outer'

transitions usually decay faster than the 'inner' one [98]. To account for this difference, fluctuating ZFS was proposed as the dominant relaxation mechanism in $N@C_{60}$ derivative solutions [98]. With this approach, the molecular correlation time and the ZFS parameters could be simultaneously deduced from the relaxation behaviour.

Table 1.1： Relaxation and correlation time of $N@C_{70}$, $N@C_{60}$ and derivatives of $N@C_{60}$ at room temperature. (a is cited from [95], b from [98] and c from [104].)

	Solvent	T_1 (μs)	T_2 (μs)	τ (ps)
[a]$N@C_{60}$	toluene	120±2	50±1	11
[a]$N@C_{70}$	DCM	133±5	40±5	15
[a]$N@C_{61}(COOC_2H_5)_2$	toluene	78±5	13±2	25
[a]$N@C_{66}(COOC_2H_5)_{12}$	toluene	116±3	24±2	20
[b]$N@C_{69}H_{10}N_2O_2$	CS_2	8.0±0.4 (inner) 26.9 ±1.2 (outer)	12.3±0.7 (inner) 2.8±0.3 (outer)	31.4±2.5
[c]$N@C_{60}$-azo-C_{60} (*trans*-)	CS_2	15.9 (inner) 55.7 (outer)	24.7 (inner) 4.6 (outer)	37.2±1.6
[c]$N@C_{60}$-azo-C_{60} (*cis*-)	CS_2	14.8 (inner) 51.0 (outer)	22.9 (inner) 4.6 (outer)	34.8±2.7

1.3.6 Further prospects on $N@C_{60}$ derivatives for QIP

Several fundamental aspects have to be addressed when $N@C_{60}$ derivatives are considered for QIP. Firstly, stability of the encapsulated nitrogen is the above-all concern in any applications of $N@C_{60}$. The unique spin properties of $N@C_{60}$ would be lost, had the endohedral nitrogen atom escaped from the fullerene cage. For the $N@C_{60}$ derivatives, the stability might be further affected by the functional group.

Secondly, spin-spin interactions between endohedral fullerenes have to be investigated in order to achieve the two-qubit operations. Synthesis of hetero-endohedral dimers (for instance, $^{14}N@C_{60}$-$^{15}N@C_{60}$) is essential, but it remains a huge experimental challenge because of the restrictions of availability in starting materials. In addition to the efforts to

produce adequate $N@C_{60}$, exploration of $N@C_{60}$ derivatives with other spin-active groups could provide preliminary insights on the spin-spin interactions before the synthesis of $^{14}N@C_{60}$-$^{15}N@C_{60}$ is eventually achieved.

Chapter 2

Methodology

This chapter provides an overview of the experimental techniques used through the thesis, and the quantum chemical calculations that underpin the experimental results.

2.1 Experimental techniques

2.1.1 Ion implantation

There are two well-established methods to synthesize $N@C_{60}$: ion implantation and glow discharge. The $N@C_{60}$ used in this work was produced using the ion implantation method [80]. Figure 2.1 shows a schematic representation of the ion implantation apparatus in our laboratory. In a typical operation, approximately 1 g of C_{60} is put into the effusion cell inside the vacuum chamber, which is evacuated at a pressure of ~10^{-6} Torr. The effusion cell is heated at around 500 °C. Under these conditions, the C_{60} is continuously sublimed inside the chamber and condensed onto the water-cooled copper target, which is located at 45 ° angle to both the effusion cell and the nitrogen ion source. Simultaneously, the resultant C_{60} film is bombarded with N^+ ions produced by the ion source. Those ions of appropriate

energy are then encapsulated by the fullerene cage. Typical values for the beam energy and beam current are set to be 40 eV and 500 μA, respectively [106].

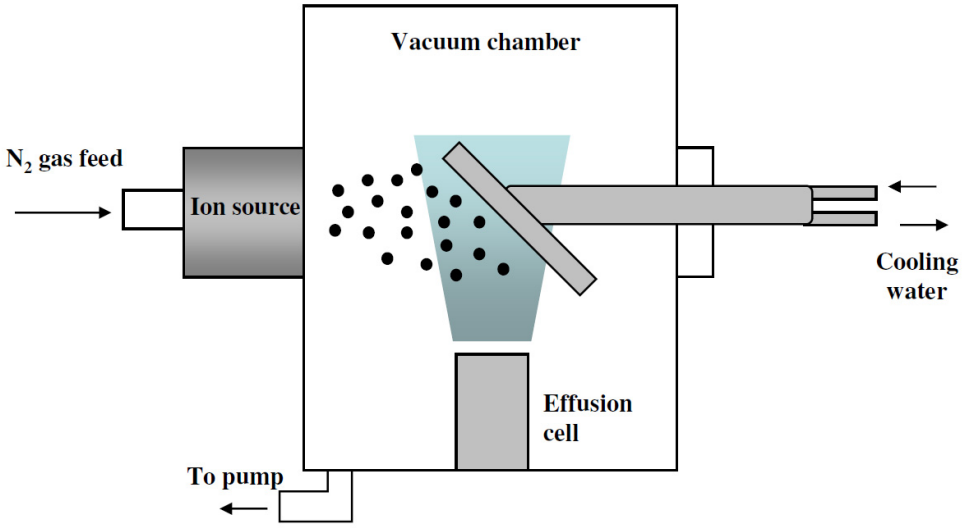

Figure 2.1: Schematic representation of the ion implantation apparatus used for production of N@C_{60}. Based on the schematic drawing in [107].

At the end of the implantation operation, the copper target will be covered with a fullerene wafer several tens of micrometers thick. The wafer is subsequently extracted by an organic solvent such as CS_2 or toluene, and the solution is filtered after being ultrasonicated for about half an hour. Normally between 60% and 70% of the soot could be dissolved by CS_2, and the insoluble solid comprises polymerized fullerenes and destroyed fullerene cages. The filtered solution is measured by ESR spectroscopy to estimate the yield. The ratio of N@C_{60}/C_{60} in the crude sample falls in the range of 10^{-4} to 10^{-5}, which normally requires post-processing to enrich N@C_{60} for further experiments.

2.1.2 High performance liquid chromatography

High performance liquid chromatography (HPLC) is a chromatographic technique especially useful in the separation and purification of fullerenes and their derivatives. It offers the

advantage of greatly reduced operation times, high reliability and integrated preparative and analytical functions.

The core principle of HPLC is the same as other forms of liquid chromatography. The eluent (a solvent or a mixture of different solvents) is the mobile phase and carries the sample through a column filled with solid stationary phase (powder or gel). The compounds in the sample interact differently with the stationary phase, resulting in different retention times when they pass through the column. The compounds are then separated out into different fractions according to the retention times. Depending on nature of the stationary phases, these interactions are governed by molecular weight, size, polarity, or structural isomerism. [108].

HPLC incorporates extra functional components, such as a pump and a detector, compared to standard column chromatography. The pump provides a steadily high pressure that drives the eluent through the column in a short time. The detectors, usually connected to a computer, can quantify the compounds that pass through the column and provide real time monitoring of the processing. The detection methods include traditional UV-vis absorption and fluorescence, as well as new techniques such as chemiluminescence, mass spectrometry and proton nuclear magnetic resonance (NMR) [108]. Furthermore, the HPLC apparatus also provide a 'recycling' function that could re-inject the sample eluted from the column immediately into the column for another pass. This function is essential for the separation of compounds of very similar structures, which stand closely in retention time in one pass. For instance, $N@C_{60}$ usually differs from its counterpart C_{60} in retention time by less than half a minute. Several 'recycling' passes could widen this gap to make an effective cut-off of their otherwise overlapping peaks. This is the reason why the enrichment process of $N@C_{60}$ is laborious and time-consuming.

The densely packed column is the most important component of HPLC. In our laboratory, the main columns used for separation of fullerenes are Buckyprep, Buckyprep-M, 5PBB and 5PYE. These columns, with the trade mark of Cosmosil® (Naclai Tesque, Japan), are categorized to the normal phase chromatography operating with a polar stationary phase (silica) and less polar mobile phase (usually toluene). The silica in these columns is functionalized with different molecular groups to suit the separation of specific fullerenes. Details of the stationary phase of these columns are shown in Figure 2.2. The average silica sizes are 5 μm in all the four columns.

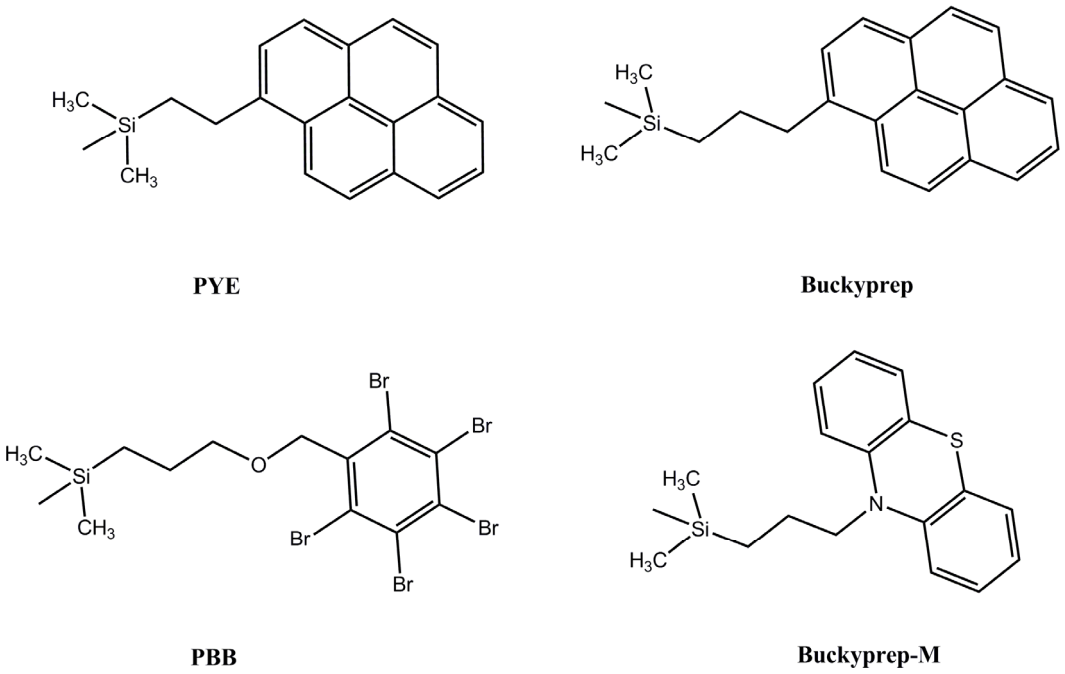

Figure 2.2: Stationary phases of the four commonly used HPLC columns for separation of fullerenes

The 5PYE column, with silica gel chemically bonded with 2-(1-pyrenyl)ethyl group, is widely used for separation of compounds with similar structure, such as isomers. The other three columns, Buckyprep, Buckyprep-M and 5PBB, were developed especially for preparative separation of fullerenes. The Buckyprep column, with 3-(1-pyrenyl)propyl groups bonded to silica gel, can be used to separate a variety of fullerenes including higher

fullerenes and metallofullerenes. The 5PBB column with pentabromobenzyl groups is useful for preparative separation of fullerenes, and is particularly efficient for the enrichment of $N@C_{60}$. Buckyprep-M column, with phenothiazinyl groups, is a newly developed column for separation of metallofullerenes. This column is also very effective for separation of functionalized fullerenes.

2.1.3 Mass spectrometry

Mass spectrometry (MS) is an analytical technique used to determine the molecular weight through measuring the mass-to-charge ratio (m/z) of charged particles [109]. It is widely used to identify new species of fullerenes and endohedral fullerenes. In an operation of MS, the sample is firstly vaporized and converted into ionized molecules or fragments. The ions are subsequently separated in an electromagnetic field according to their masses. Finally, the ions are analyzed (normally quantitatively) in the detector and the ion signal is processed into mass spectrum.

Several different techniques are used to create molecular ions: electrospray ionisation (ESI), electron impact ionisation (EI) and matrix-assisted laser desorption ionisation (MALDI). The ionisation technique must be carefully chosen in consideration of its applicability to the subject molecules. For instance, ESI is usually used for analysis of molecules with medium to high polarity, such as amino, aldehyde and carboxylate compounds. MALDI has been traditionally used for analysis of large biomolecules. In this technique, laser pulses are used to simultaneously vaporize and ionize the molecules. The matrix is essential because it prevents the sample from direct exposure to laser and therefore keeps the molecules intact. For analysis of fullerene derivatives, MALDI with *trans*-2-[3-(4-tert-butylphenyl)-2-methyl-2-propenylidene] malononitrile (DCTB) as the matrix is widely applied.

2.1.4 Ultraviolet-visible spectroscopy

Ultraviolet-visible spectroscopy (UV-vis) refers to absorption spectroscopy in the ultra-violet, visible and near infra-red spectral region. In the present work, the absorption spectroscopy was performed with a JASCO V-570 UV/VIS/NIR spectrophotometer. The sample is irradiated with light in visible and the adjacent ranges, and it absorbs photons of the incident beam when the wavelength matches an electronic transition in the molecule. Transitions measured in this way are those from the ground states to the excited states. For organic compounds, the electronic transitions occur normally in three types of electrons: σ electrons of the *s* orbital, π electrons of the *p* orbital and *n* electrons of the lone pair. Possible transitions include $\sigma \rightarrow \sigma^*$, $\pi \rightarrow \pi^*$, $n \rightarrow \sigma^*$ and $n \rightarrow \pi^*$. Most fullerenes possess unique optical absorption spectrum that is usually used as 'fingerprinting' for identification.

In addition to qualitative application, UV-vis is also used for quantitative analysis. The Beer-Lambert law manifests the relation of absorbance with the sample concentrations:

$$A = -\log_{10}(I / I_0) = \varepsilon \cdot l \cdot c \tag{2.1}$$

where A is the absorbance, I_0 is the intensity of the incident light at a specific wavelength, I is the intensity of light transmitted through the sample, ε is the molar extinction coefficient, l is the path length of the sample and c is the concentration of the sample. At a given temperature, pressure and wavelength, ε keeps constant as a fundamental molecular property. Therefore, equation 2.1 establishes the foundation for quantitative analysis. In practice, equation 2.1 is only applicable to samples at low concentrations where intermolecular interactions are negligible.

2.1.5 Nuclear magnetic resonance spectroscopy

Nuclear magnetic resonance (NMR) spectroscopy is a powerful technique for structural characterization of organic molecules [109]. It applies to molecules containing nuclei of non-zero nuclear spin. Under an external magnetic field, angular momentum of a nuclear spin is quantized and each state is ascribed with a magnetic quantum number, *m*. C and H are the two common elements in most organic molecules, and both ^{13}C (with a natural abundance of 1.1%) and ^{1}H have a spin number $I = 1/2$. For such a spin 1/2 system, two quantum states are expected in the magnetic field: $m = +1/2$ and $m = -1/2$. The energy gap between the two states is given by:

$$\Delta E = \gamma \hbar B \tag{2.2}$$

where γ is the *magnetogyric ratio* (different for ^{13}C and ^{1}H) and B is the strength of the magnetic field experienced by the spin. A resonance takes place when the radiation frequency satisfies:

$$h\nu = \Delta E \tag{2.3}$$

The magnetic field B experienced by the nucleus relates to both the external magnetic field and the local magnetic environment resulting from variations of electron distribution. According to both equation 2.2 and 2.3, the local magnetic environment is ultimately revealed by a shift of the resonance frequency. To exclude the instrumental dependence, chemical shift, δ, is traditionally used to describe such a shift:

$$\delta = \frac{\nu_0 - \nu_{TMS}}{\nu_s} \tag{2.4}$$

where ν_0 is the resonant frequency, ν_{TMS} is the resonant frequency of tetramethylsilane (TMS, used as internal standard) and ν_s is the spectrometer frequency. The unit of δ is taken as parts per million (ppm) when all these frequencies are measured in Hz. Owing to the accumulation

of NMR database, the relation between δ and the local structure has been well understood for most organic groups.

Corresponding to the two nuclear spins ^{1}H and ^{13}C, ^{1}H NMR and ^{13}C NMR are the two most frequently used NMR techniques in organic chemistry.

^{1}H NMR

In ^{1}H NMR, the chemical shift δ of most protons falls in the range of 0-11 ppm. Each proton of different environment exhibits one resonant peak and integrals of the peaks are proportional to the number of protons. Peaks of the isolated protons or of the chemically equal protons (for instance, protons bonded to the same carbon without steric difference) are singlet. Spin-spin coupling of adjacent protons results in multiplets, and the coupling constant J determines the spacing between the split peaks. The multiplicity is given by the number of the adjacent protons plus one (the $n+1$ rule), whereas intensity of these splitting follows the combinations rule (1:1, 1:2:1, 1:3:3:1, …). Application of these rules, when combined with the chemical shifts, can provide valuable information on the molecule's composition.

^{13}C NMR

In ^{13}C NMR, chemical shift δ of carbons falls in a wider range of 0-220 ppm. Because of the low natural abundance of ^{13}C, ^{13}C NMR requires greater sample quantities and longer acquisition times in general. For the same reason, spin-spin coupling is in practice negligible in ^{13}C NMR spectra due to the very low chance of having two adjacent ^{13}C nuclei (1.1%×1.1%).

2.1.6 Electron spin resonance spectroscopy

Electron spin resonance (ESR) spectroscopy is a technique for analysis of compounds with one or more unpaired electrons [109]. The principle of ESR is analogous to NMR, but the spins in focus are unpaired electrons instead of nuclear spins. In practice, ESR and NMR techniques tend to be mutually exclusive for a specific compound. The molecules that are spin-active in ESR exhibit bad or no NMR spectra, and *vice versa*.

Angular momentum of an electron spin is quantized in applied magnetic field in the same way to a nuclear spin, and a resonance takes place if the electromagnetic frequency matches the energy gap between the two levels:

$$h\nu = \Delta E = g\ \mu_B B_0 \tag{2.5}$$

where g is the electron spin g-factor, μ_B is the Bohr magneton and B_0 is strength of the applied magnetic field. Because the energy gap for electron spins is usually larger than that for the nuclear spins, microwave irradiation instead of radio frequency (RF) is required to invoke a resonance in ESR. In addition, this larger energy gap leads to more sharpened population contrast between the two states according to the Maxwell-Boltzmann distribution. ESR is therefore a more sensitive technique than NMR.

Whereas the local environment of a nuclear spin is characterized by chemical shifts in NMR, the local environment of an electron spin is revealed by the g-factor. For a free electron, $g_e = 2.0023$, and for other unpaired electrons in a compound the value varies. The g-factor in its full meaning describes the electron Zeeman interaction (the interaction between an electron spin and the applied magnetic field), and is given by a 3×3 matrix. This matrix is usually symmetric and could be transformed into the diagonal form:

$$g = \begin{bmatrix} g_{xx} & 0 & 0 \\ 0 & g_{yy} & 0 \\ 0 & 0 & g_{zz} \end{bmatrix} \tag{2.6}$$

In addition to the Zeeman interaction, the electron could couple to a nuclear spin, which is described by hyperfine interaction. This coupling usually gives rise to the splitting of ESR peaks.

There are two kinds of ESR techniques: continuous-wave (CW) ESR and pulsed ESR. In CW ESR, the irradiation frequency is fixed (for instance, 9.5 GHz for the X band ESR spectrometer) and the magnetic field B_0 is swept to change the energy gap to match the resonance condition defined in equation 2.5. In pulsed ESR, microwave pulses with certain duration at the resonant frequency are applied to rotate the spin state.

In the present work, CW ESR technique is applied to study electron spins in endohedral nitrogen fullerene and its derivatives. The two applied spectrometers are a Magnettech MiniScope MS100 and a Bruker EMX. Both spectrometers are operated at X-band (9-10 GHz). In a measurement, the main operation parameters include modulation of the applied magnetic, power of the microwave, scanning range and scanning rate of the magnetic field. These parameters must be tuned and optimized according to the specific sample.

2.2 Quantum chemical calculations

Quantum chemical calculations rely ultimately on the solution (or at least in an approximation) of the Schrodinger equation [110]. Following the Born-Oppenheimer approximation, the nuclei are assumed to be stationary with respect to the electrons. Therefore the many-body Schrodinger equation in its time-independent and non-relativistic form is:

$$\hat{H}\Psi\ (r_1, r_2, ...r_n) = E\Psi\ (r_1, r_2, ...r_n) \tag{2.7}$$

and the Hamiltonian is:

$$\hat{H} = -\frac{1}{2}\sum_{i}^{n}\nabla_i^2 - -\sum_{i}^{n}\sum_{I}^{N}\frac{Z_I}{r_{iI}} + \sum_{i<j}^{n}\frac{1}{r_{ij}} + \sum_{I<J}^{N}\frac{Z_I Z_J}{R_{IJ}} \tag{2.8}$$

where Ψ is the electronic wavefunction with the eigenvalues of E, r_i is the coordinate of the electron i, R_I is the coordinate of the nucleus I, and Z_I is the charge of the nucleus on R_I.

2.2.1 Density functional theory

Solution of the equation 2.7 is not currently feasible for molecules with tens of electrons. Therefore, two main routines have been developed to simplify the problem through making further approximation. The first one is the Hartree-Fock theory (HF) and the post-Hartree-Fock series including Moller-Plesset (MP), configuration interaction (CI) and coupled cluster (CC). The other routine is the density functional theory (DFT), which provides the correlation energy in a more computationally efficient way than the post Hartree-Fock methods [110].

The electronic wavefunction in equation 2.7 is dependent on 3n variable (each electron requires three coordinates). An interesting question is whether it is essential to solve this equation if only the ground state energy is concerned. The answer, which was proved by Hohenberg and Kohn in 1964, is no. The two Hohenberg-Kohn theorems build up the theoretical foundation for DFT. The first theorem states that the external potential or the Hamiltonian could be completely determined by the total electron density ρ(r) which is dependent on just three variables. The second theorem states that the electron density obeys the variational theorem that the energy corresponding to any given electron density is greater than or equal the exact energy of that system. In order to calculate the energy via DFT, Kohn and Sham proposed a functional in the form of:

$$E[\rho(\mathrm{r})] = T_e[\rho(\mathrm{r})] + V_{ne}[\rho(\mathrm{r})] + V_{ee}[\rho(\mathrm{r})] + E_{xc}[\rho(\mathrm{r})] \tag{2.9}$$

When the system is treated as a non-interaction system of n "orbitals" ψ_i, the first term in equation 2.9 is known as kinetic energy of these orbitals:

$$T_e[\rho(\mathrm{r})] = -\frac{1}{2}\left\langle \psi_i \middle| \nabla^2 \middle| \psi_i \right\rangle \tag{2.10}$$

with the electron density:

$$\rho(\mathrm{r}) = \sum_i^n \left|\psi_i(\mathrm{r})\right|^2 \tag{2.11}$$

$V_{ne}[\rho(\mathrm{r})]$ is the nuclear-electron attraction, and the electron-electron interaction term is treated as classical Coulomb interaction or Hartree energy:

$$V_{ee}[\rho(\mathrm{r})] = \frac{1}{2}\iint \frac{\rho(\mathrm{r}_1)\rho(\mathrm{r}_1)}{\left|\mathrm{r}_1 - \mathrm{r}_2\right|}\mathrm{d}\mathrm{r}_1\mathrm{d}\mathrm{r}_2 \tag{2.12}$$

$E_{xc}[\rho(\mathrm{r})]$, the exchange-correlation functional, is introduced to correct the error induced by non-interacting kinetic energy and the classical treatment of electron-electron interaction. It is the development of approximations for E_{xc} that has led to the large and rapidly expanding family of DFT modelling. In pure DFT, two classes of approximations are widely used: the local density approximation (LDA) [111] and the generalized gradient approximation (GGA) [112]. E_{xc} in LDA depends solely upon the local electron density:

$$E_{xc} = \int \rho(\mathrm{r})\varepsilon_{xc}(\rho)\mathrm{d}\mathrm{r} \tag{2.13}$$

This functional is generally decomposed into two terms, an exchange part and a correlation part. The exchange part is usually derived from the homogeneous electron gas (HEG) model. In particular, the exchange energy density ε_x of a constant electron density is:

$$\varepsilon_x(\rho) = -C\rho^{1/3} \tag{2.14}$$

However, general analytic forms of the correlation energy for HEG are unknown. Therefore, quantum Monte Carlo simulations and various other approaches have generated several different correlation functionals.

In GGA, the functional depends on both the electron density and its gradient. A typical form for a GGA functional is:

$$E_{xc} = \int \rho(\mathrm{r}) \varepsilon_{xc}(\rho, \nabla\rho) \mathrm{dr} \tag{2.15}$$

The GGA improves significantly the binding energy of molecules in comparison to the LDA. A number of functionals within the GGA family have been developed. Especially, the meta-GGA, as an extension of GGA, incorporates the Laplacian of the electron density or the local kinetic energy density.

In addition to the pure DFT functionals, the adiabatic connection approach allows for the construction of hybrid functionals to incorporate a part of the HF exchange term:

$$E_{xc} = aE_x^{HF} + bE_{xc}^{GGA} \tag{2.16}$$

where the coefficients *a* and *b* are either fit to the experiment data or to a system whose exact results are already known.

The functionals utilized in the present work is the widely used hybrid method B3LYP [113,114], which includes the Becke's exchange functional and the LYP correlation functional:

$$E_{xc}^{B3LYP} = (1-a)E_x^{LSDA} + aE_x^{HF} + b\Delta E_x^B + (1-c)E_c^{LSDA} + cE_c^{LYP} \tag{2.17}$$

Typical values for the coefficients are $a = 0.20$, $b = 0.72$ and $c = 0.81$, which are fitted from a set of atomization energies, ionisation potentials, proton affinities and total atomic energies. Although B3LYP, as well as other hybrid DFT functionals, possesses decidedly empirical flavour, it is widely applied in quantum chemical calculations due to its success in accurate prediction of chemical structures and properties [115-118].

2.2.2 Geometry optimization

Geometry optimization is essential for quantum chemical calculations. In the potential energy surface (PES), equilibrium geometries are the local minima and transition states correspond to saddle points [119]. Geometry optimization is therefore the process to find these minima or saddle points on the PES.

A minimum point on the PES must satisfy two criteria. The first derivatives must be zero and eigenvalues of the second derivative matrix or Hessian matrix must be positive. If one or more eigenvalues are negative in the Hessian matrix, the point is not a minimum but a saddle point. On the other hand, the transition state is a maximum along the reaction path and a minimum in all other directions. Its first derivatives must be zero as well, but one eigenvalues of the Hessian matrix must be negative. Those saddle points with more than one negative eigenvalues are not transition states. The eigenvector of the only negative eigenvalue represents the direction along the reaction path.

A variety of algorithms for geometry optimization have been developed in quantum chemical calculations [119]. In the modelling program Gaussian 03 [120], two algorithms are available for modelling methods with analytic gradients (for instance, the DFT). The first one is the rational function optimization (RFO) that controls the step size by minimizing a rational polynomial approximation of the surface. The other one is the GDIIS approach, or geometry optimization by direct inversion of the iterative subspace. Compared with RFO, GDIIS is less sensitive to the quality of the Hessian. It is therefore recommend for use with large systems and molecules with flat PES [121].

In the present work, GDIIS was used for all optimizations to local minima, and RFO was applied to all optimizations to transition states.

2.2.3 Population analysis

Mulliken population was calculated in order to analyze the electron and spin density distribution [122]. The Mulliken population is an orbital-based method, the contribution of a pair of orbitals to the total electron density is:

$$N_{\mu\nu} = P_{\mu\nu} \cdot S_{\mu\nu} = \sum_{i=1}^{N} c_{\mu i}^{*} c_{\nu i} \cdot \int \varphi_{\mu}^{*}(\mathrm{r}) \varphi_{\nu}(\mathrm{r}) d^{3}\mathrm{r} \tag{2.18}$$

where φ is the basis function, and $P_{\mu\nu}$, $S_{\mu\nu}$ are the density matrix and overlap matrix, respectively. If both φ_{μ} and φ_{ν} are located on the same atom, the density $N_{\mu\nu}$ would be assigned to a given atom. Otherwise, N_{μ} would be equally assigned to the two atoms on which φ_{μ} and φ_{ν} are located. After the assignment of all the electrons, the Mulliken charge is defined as the difference between the gross atomic population and the atomic number:

$$Q_A = Z_A - N_{\mu\nu}^{\mu\in A,\nu\in A} - \frac{1}{2} N_{\mu\nu}^{\mu\in A,\nu\in B} \tag{2.19}$$

where Q_A is the atomic number. In an open shell system, the atomic spin can be similarly calculated by a summation of differences between the α and β electrons.

2.2.4 Frequency and thermochemical analysis

For the structure at a stationary point, either a local minimum or a transition state, vibrational frequency can be determined from the second derivatives of the energy in the mass-weighted coordinates. While the local minimum has only real frequencies, the transition state must have one imaginary frequency that corresponds to the only negative eigenvalue in its Hessian matrix.

Thermochemical quantities, such as enthalpy and free energy, are calculated by consideration of the contributions from translational, electronic, rotational and vibrational motion [123]. In the Gaussian 03 program, sum of electronic and thermal enthalpies, and

sum of electronic and thermal free energies, are simultaneously calculated when a frequency analysis is performed. Because all the elements are the same on both sides of a reaction, which cancels out all the atomic information, the enthalpy of reaction could be simply obtained by:

$$\Delta_r H^0(298K) = \sum(\varepsilon_0 + H_{corr})_{products} - \sum(\varepsilon_0 + H_{corr})_{reac\,tan\,ts} \tag{2.20}$$

where ε_0 is the total electronic energy and H_{corr} is the thermal correction to enthalpy. Similarly, the Gibbs free energy of reaction could be calculated by:

$$\Delta_r G^0(298K) = \sum(\varepsilon_0 + G_{corr})_{products} - \sum(\varepsilon_0 + G_{corr})_{reac\,tan\,ts} \tag{2.21}$$

where G_{corr} is the thermal correction to Gibbs free energy.

Chapter 3

Synthesis of N@C_{60} derivatives

This chapter focuses on the synthesis of fullerene derivatives and their characterization by UV-vis, MS, NMR and ESR. Further experiments with these derivatives will be discussed in the following chapters.

3.1 General strategy

Because of the low yield of N@C_{60} and the laborious course of enrichment, all claimed functionalization of N@C_{60} in this work actually refers to reactions performed on N@C_{60}/C_{60} mixtures with the molar ratio ranging from 10^{-4} to 10^{-3}. Before the use of N@C_{60}/C_{60} mixtures, all the reaction conditions were firstly optimized with C_{60} to guarantee their reliability. Only after the object derivatives of C_{60} were successfully separated and characterized, was the reaction transferred to the N@C_{60}/C_{60} mixture. Derivatives of N@C_{60} are hardly distinct from their counterparts of C_{60} in HPLC traces, especially when the Buckyprep M column is used. Therefore, they were separated in the same route with which the latter were separated in HPLC. The resultant product is a mixture of N@C_{60} derivatives

and C_{60} derivatives with a molecular ratio normally smaller than that of the starting materials. In the absence of other characterization techniques, the existence of N@C_{60} derivatives in the mixture was exclusively confirmed by ESR technique. In all the performed reactions, no noticeable difference in reactivity between N@C_{60} and C_{60} has ever been observed.

In consideration of the instability of N@C_{60}, special precautions were made to reduce the decomposition of N@C_{60}. Light was strictly excluded during the reaction and was avoided to the maximum extent in all the processing. Gentle reaction conditions, such as short time and low temperature, were employed whenever applicable.

3.2 Cyclopropane derivatives

The cyclopropane derivatives of C_{60} were synthesized according to the Bingel-Hirsch reaction scheme shown in Figure 3.1 [124]. A peak at 432 nm in the UV-vis absorption spectrum indicates a 1,2-addition across the [6, 6] junction in fullerenes (Figure 3.2).

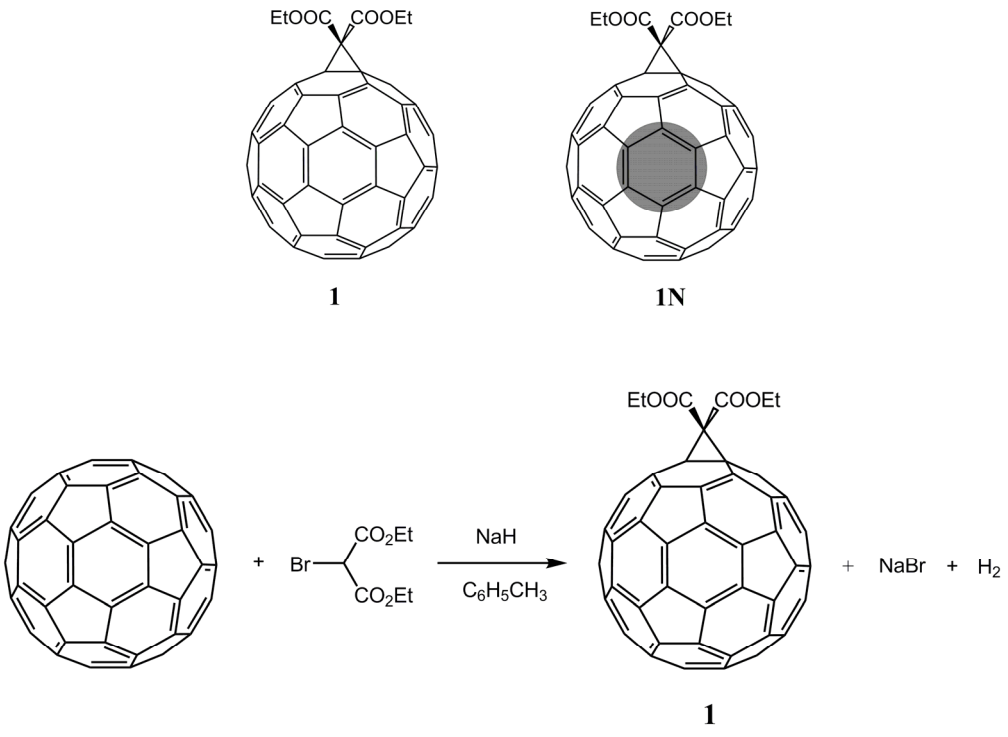

Figure 3.1: Schematic views of the cyclopropane derivatives of C_{60} (**1**) and N@C_{60} (**1N**), and the Bingel-Hirsch reaction scheme.

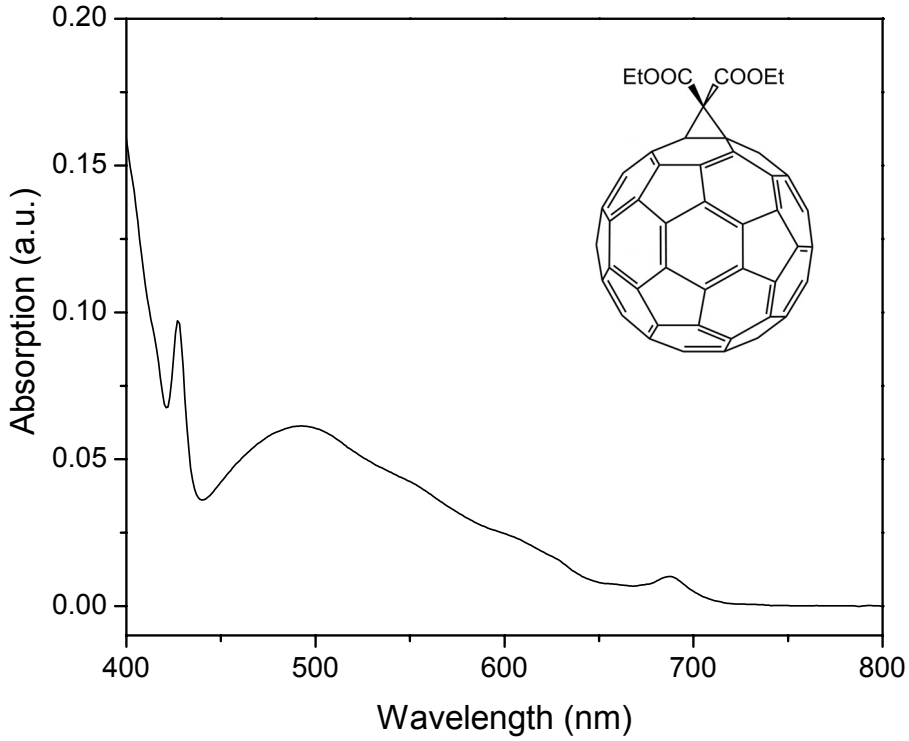

Figure 3.2: UV-vis absorption spectrum of derivative **1** in toluene.

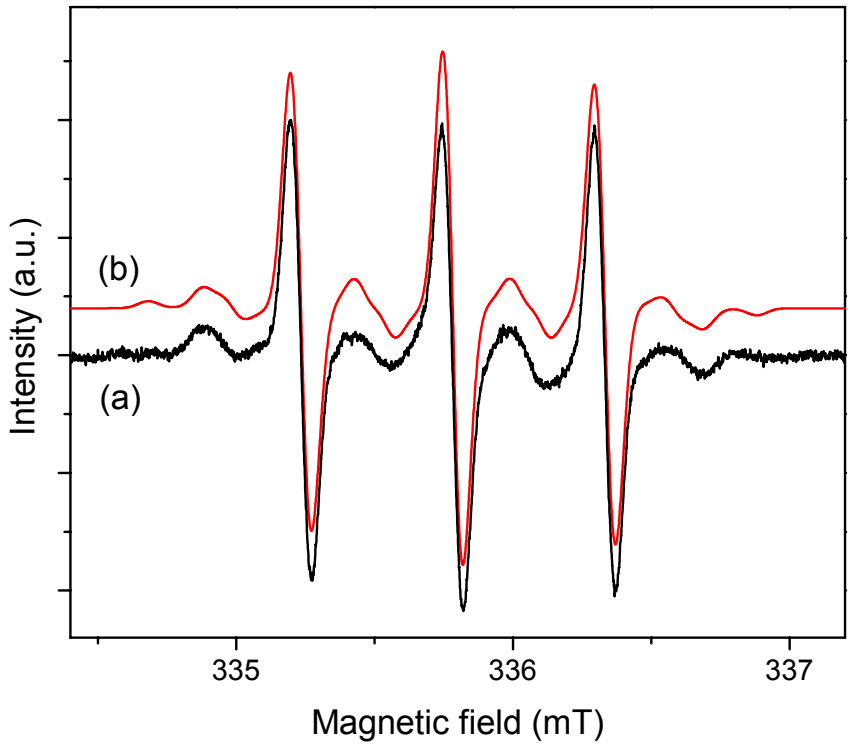

Figure 3.3: Experimental ESR spectrum of derivative **1N** in toluene at 77 K (a) and the simulation spectrum (b) (ZFS parameters D = 8.2 MHz, E = 0.5 MHz).

The corresponding N@C_{60} derivative **1N** was synthesized following the same procedure but using N@C_{60}/C_{60} (1/1000) as the starting material. **1N** shows similar ESR spectrum to pristine N@C_{60} in solution at room temperature, where the fast tumbling effect averages out the anisotropic features. ZFS effects due to symmetry breaking of the N@C_{60} are revealed by the ESR spectra measured in frozen solution. As shown in Figure 3.3, simulation of the frozen solution ESR spectrum gives $D = 8.2$ MHz and $E = 0.5$ MHz, which are consistent with a previous report [95].

Although the reaction was carried out in dark and at room temperature, only 55% of the spins were preserved in the product based on spin counting. The loss rate agrees with a recent report on the synthesis of N@C_{60} dimer through Bingel-Hirsch reaction, where approximately 50% of the spins were retained [100]. The significant loss of spins could be explained from the reaction mechanism of the Bingel-Hirsch reaction [125]. As shown in Figure 3.4, a carbanion of the malonate is generated after deprotonation by the strong base NaH, which attacks a [6, 6] junction of C_{60} and forms the intermediate state **1.1**. Subsequently, the carbanion on the fullerene displaces bromine in a nucleophilic aliphatic substitution and closes the cyclopropane ring. In the reaction, the carbanion of the intermediate state **1.1** is stabilized by the wide conjugation structure of fullerene. However, it is likely in this intermediate state (**1N.1**) that the encapsulated nitrogen atom escape from the carbon cage during the functionalization of N@C_{60}. The lone pair of electrons on the fullerene cage could react with the active encapsulated nitrogen atom, leading to a subsequent flip-out of the encapsulated nitrogen and the spin-quench as proposed in the decomposition of N@C_{60} [126].

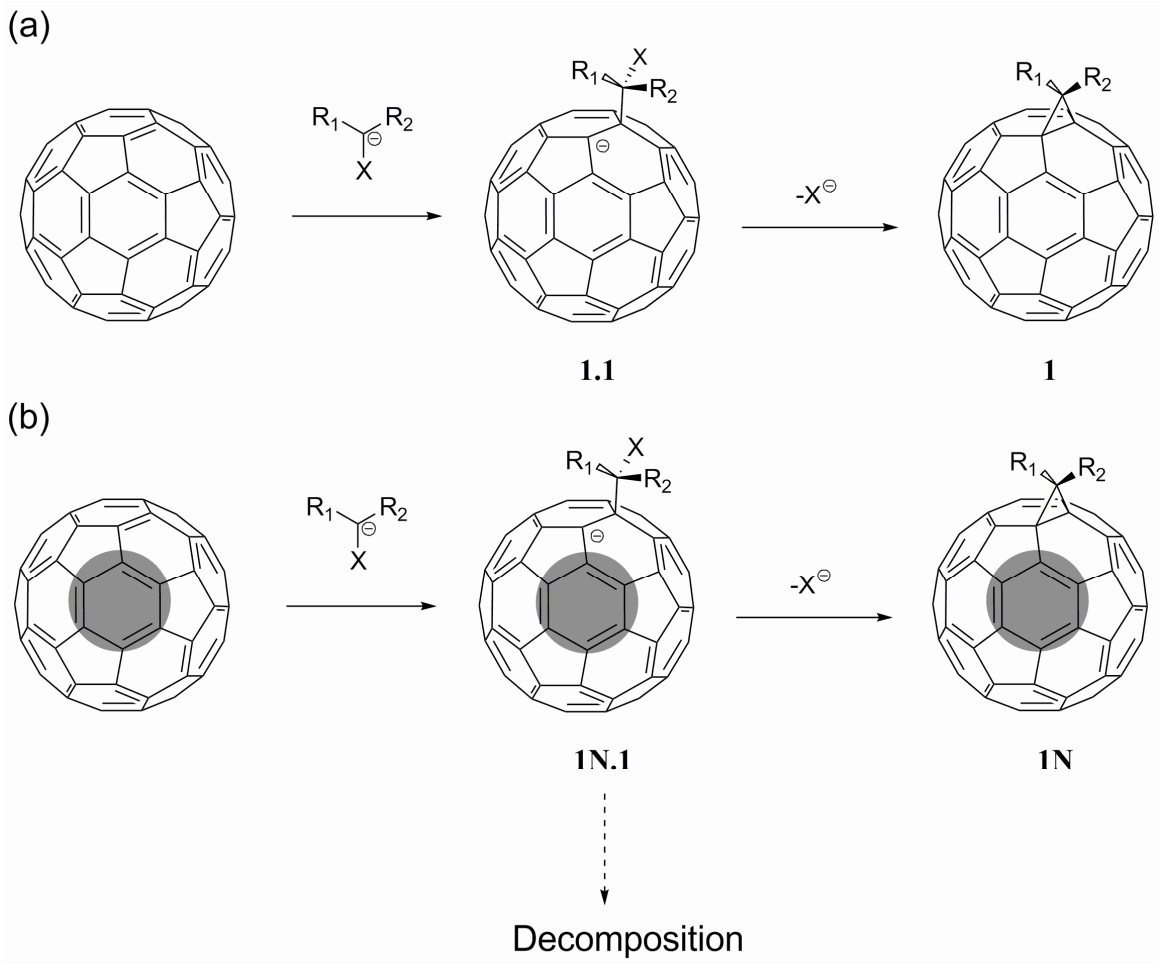

Figure 3.4: Reaction mechanism of the Bingel-Hirsch reaction for (a) C_{60} (adapted from [125]) and (b) N@C_{60}.

3.3 Pyrrolidine derivatives

The Prato reaction provides a convenient route to incorporate required chemical groups into the fulleropyrrolidine derivative [127]. As shown in Figure 3.5, a large family of fulleropyrrolidine derivatives could be synthesized by applying different amino acid and aldehyde [128-133]. The pyrrolidine derivatives of N@C_{60} concerned in this work are listed in Figure 3.6.

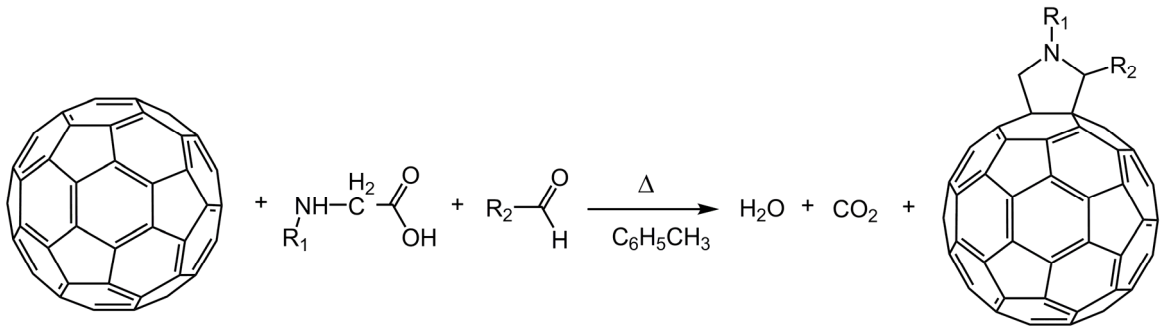

Figure 3.5: The generalized scheme for synthesis of fulleropyrrolidine (Prato reaction).

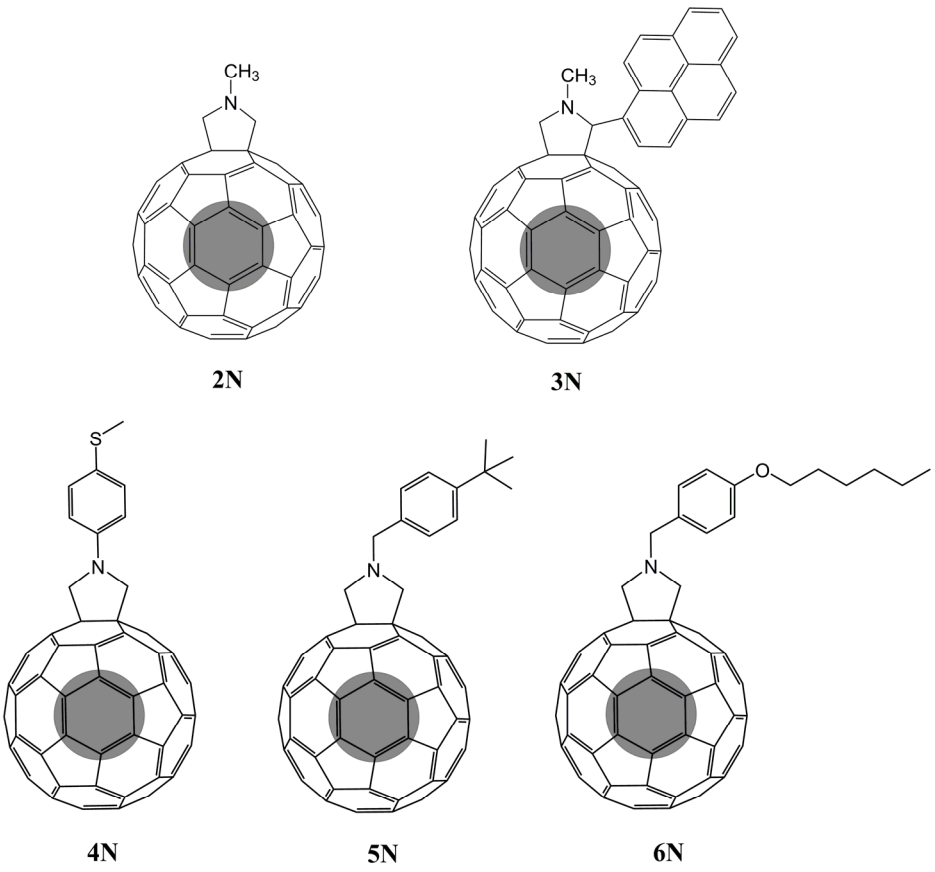

Figure 3.6: Schematic views of pyrrolidine derivatives of N@C_{60}. Their non-filled counterparts (derivatives **2**-**6**) are omitted for simplicity.

3.3.1 Synthesis of pyrrolidine derivatives of C_{60}

Derivatives **2** and **3** were synthesized according to the scheme shown in Figure 3.7. Derivative **2** was well studied before [127,134,135], and derivative **3** has just been recently reported [136].

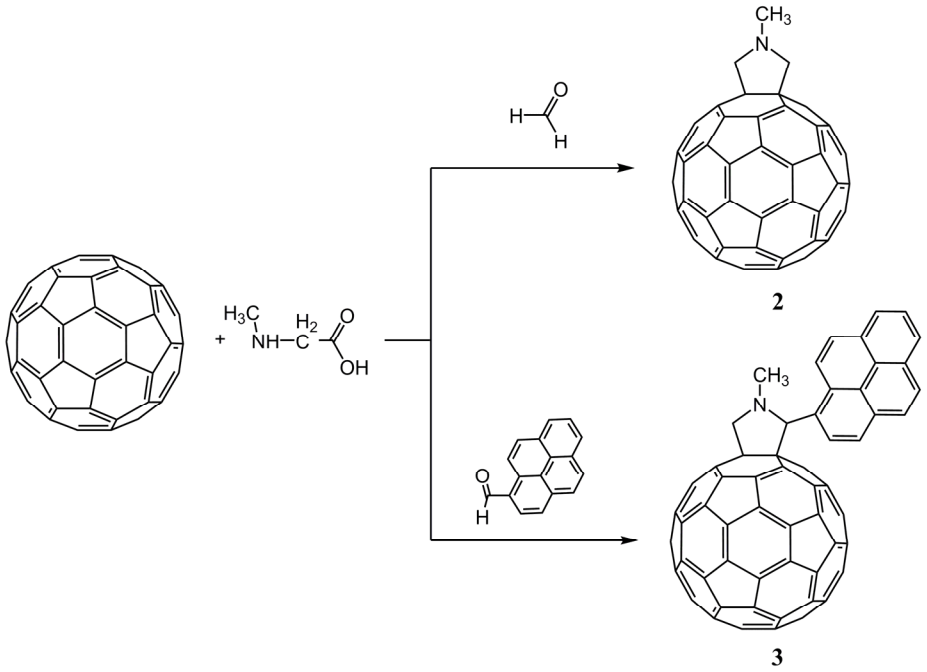

Figure 3.7: Scheme for the synthesis of derivatives **2** and **3**.

Derivatives **4**, **5** and **6** were newly synthesized in the present work, bearing groups of various length and degrees of flexibility at the α position to the *N*-substituent. The synthetic schemes are shown in Figure 3.8 (Precursors **4a**-**6a** were provided by Dr. Martyn Jevric in University of Nottingham).

Derivative **2** was purified by column chromatography, and it exhibits very close retention time to pristine C_{60} in HPLC traces (Buckyprep M, toluene as eluent). All the other pyrrolidine derivatives were readily purified by HPLC. For instance, the HPLC traces of derivative **3** are shown in Figure 3.9. The monoadduct is readily separated from pristine C_{60}, with a retention time approximately 1.2 min earlier than the latter. At least four bisadducts are identified as well, which elute even earlier than the monoadduct. Recycling mode HPLC could further purify the product for characterization and experiments.

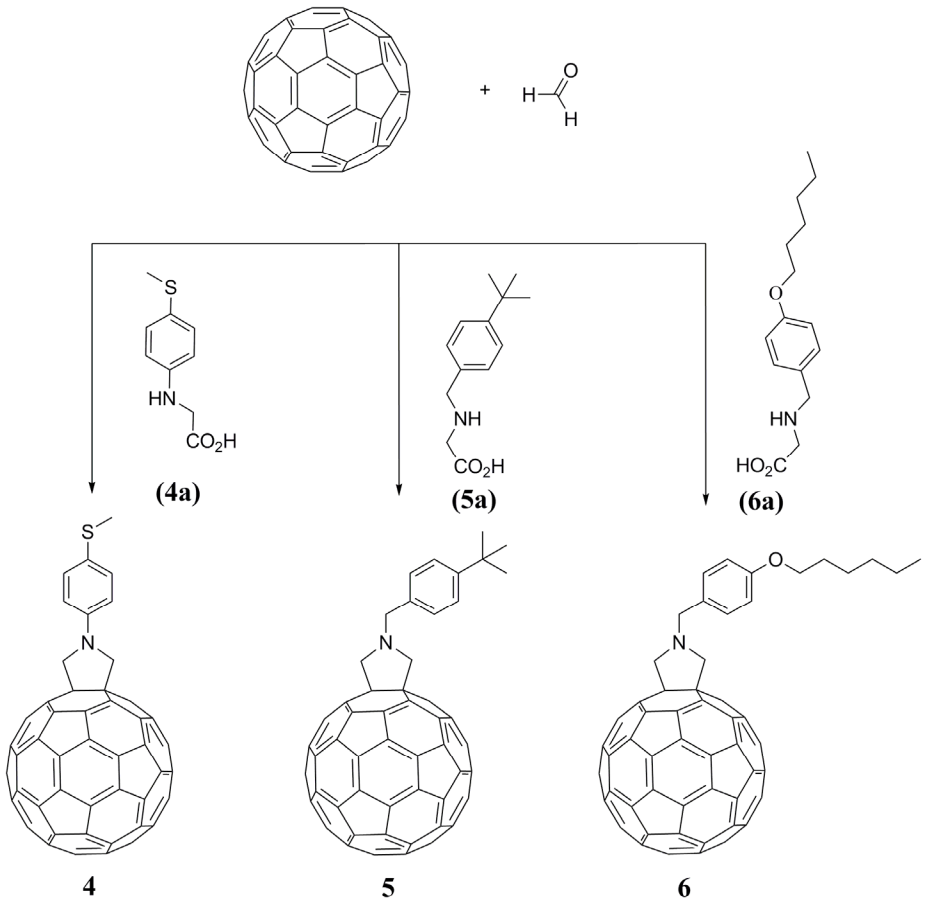

Figure 3.8: Scheme for synthesis of derivatives **4**, **5** and **6**.

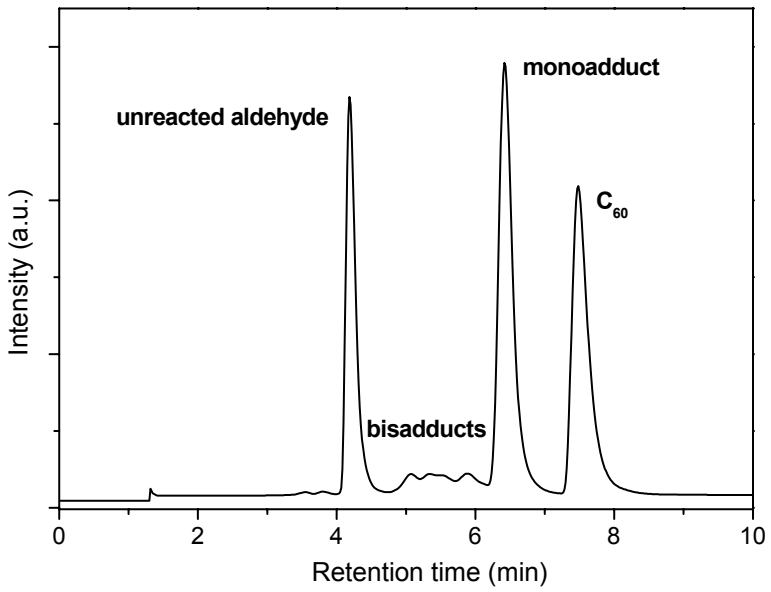

Figure 3.9: HPLC traces of the resultant mixture from the synthesis of derivative **3** (Buckyprep M, 20mm × 250mm, toluene eluent, 17 mL/min).

NMR spectra of derivatives **2** and **3** are consistent with previous reports [127,136]. The ^{13}C NMR spectrum of derivative **4** is shown in Figure 3.10. The resonance relating to sp^3 carbon atom corresponds to the $–CH_3$ bonded to the sulphur. The four carbon atoms of the pyrrolidine are divided into two groups: the two $-CH_2$ atoms (δ = 63.97 ppm) and the two sp^3 carbon atoms of fullerene (δ = 70.43 ppm). There are 16 resonances arising from sp^2 carbons of the fullerene (δ = 135-155 ppm). The ^1H NMR of derivative **4** consists of four resonances (Figure 3.11): the $–CH_3$ protons, the four identical protons of the pyrrolidine ring and two sets of protons of the phenyl ring. These findings indicate that derivative **4**, similar to derivative **2** [127], has a C_{2v} symmetry.

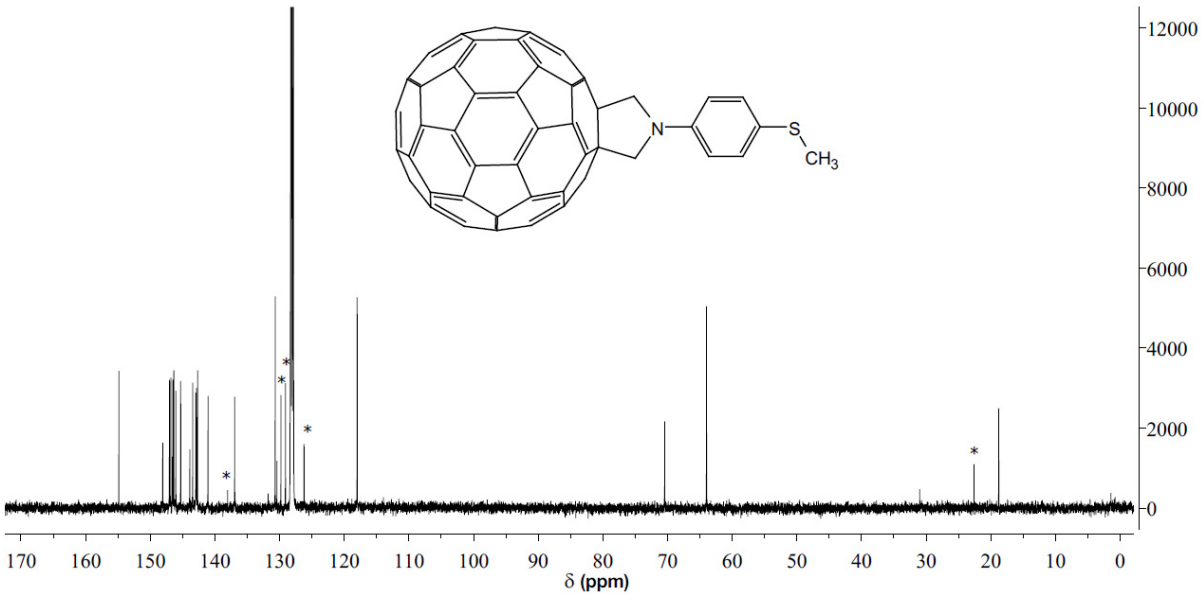

Figure 3.10: ^{13}C NMR spectrum (125 MHz, CS_2, C_6D_6 used as insert) of derivative **4**. Peaks arising from remnant toluene are marked (*).

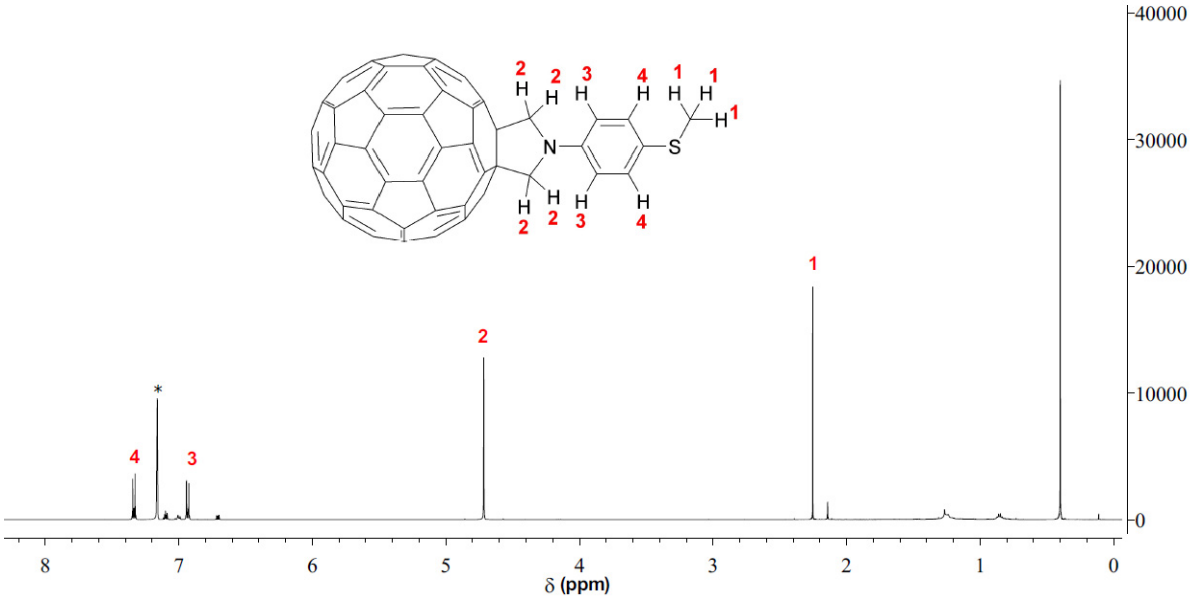

Figure 3.11: ^{1}H NMR spectrum (500MHz, CS_2/C_6D_6=1:1) of derivative **4**. Peaks arising from C_6D_6 is marked (*).

NMR spectra of derivative **5** (refer to section 3.5) and derivative **6** (Figure 3.12 and Figure 3.13) confirm that they have the same C_{2v} symmetry.

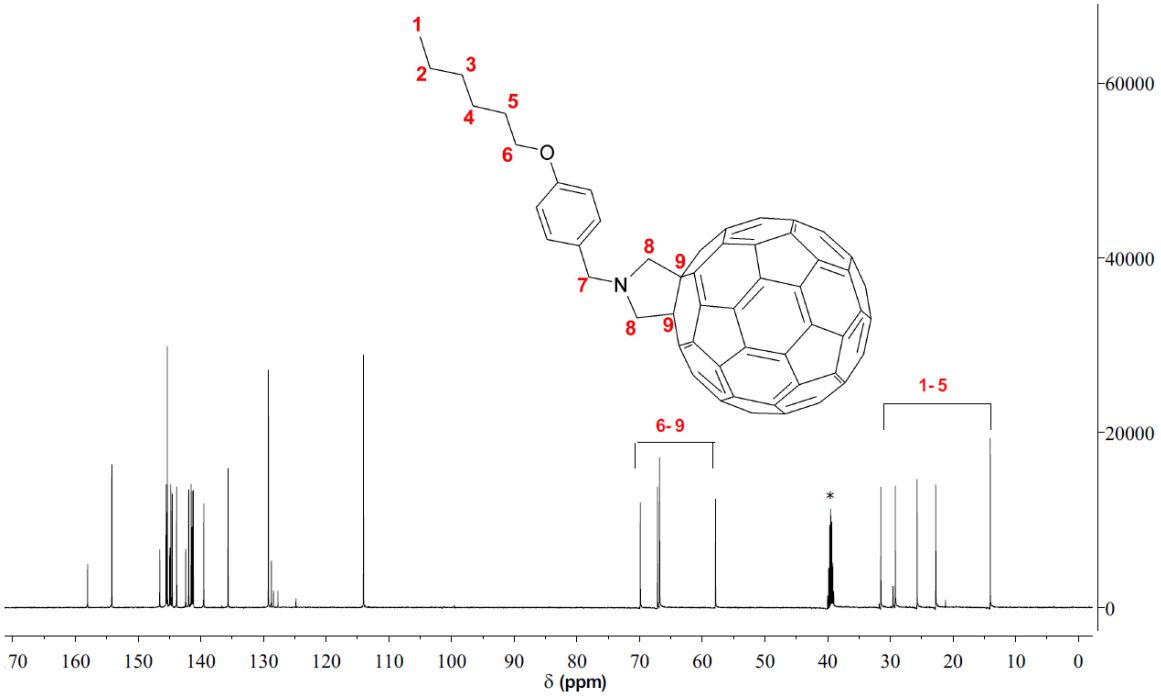

Figure 3.12: ^{13}C NMR spectrum (125 MHz, CS_2, DMSO-d_6 used as insert) of derivative **6**. Peaks arising from DMSO-d_6 are marked (*).

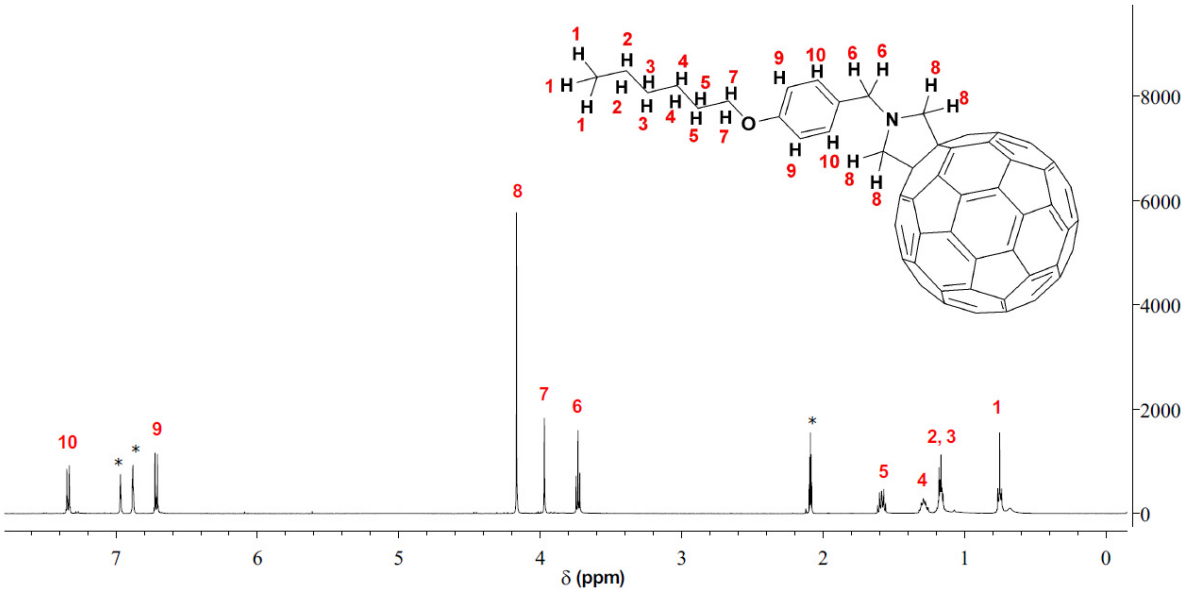

Figure 3.13: ^{1}H NMR spectrum (500MHz, CS_2/toluene-d_8=5:1) of derivative **6**. Peaks arising from toluene-d_8 are marked (*).

3.3.2 Synthesis of pyrrolidine derivatives of N@C_{60}

The N@C_{60} derivatives **2N-5N** were synthesized and purified in the same procedures to derivatives **2-5**, respectively. Their identity is confirmed by the ZFS effects observed in frozen solution ESR spectra (Figure 3.14) and their ZFS parameters are listed in Table 3.1. The small difference in *D* and *E* for all derivatives demonstrates a negligible effect of the functional groups attached to the *N*-substituent of pyrrolidine on the encapsulated nitrogen electron spins.

Table 3.1: Best fit ZFS parameters for pyrrolidine derivatives of N@C_{60}. The estimated uncertainties are 0.2 MHz.

	D (MHz)	*E* (MHz)
2N	16.2	0.5
3N	16.8	0.6
4N	16.3	0.4
5N	16.3	0.6
6N	16.3	0.3

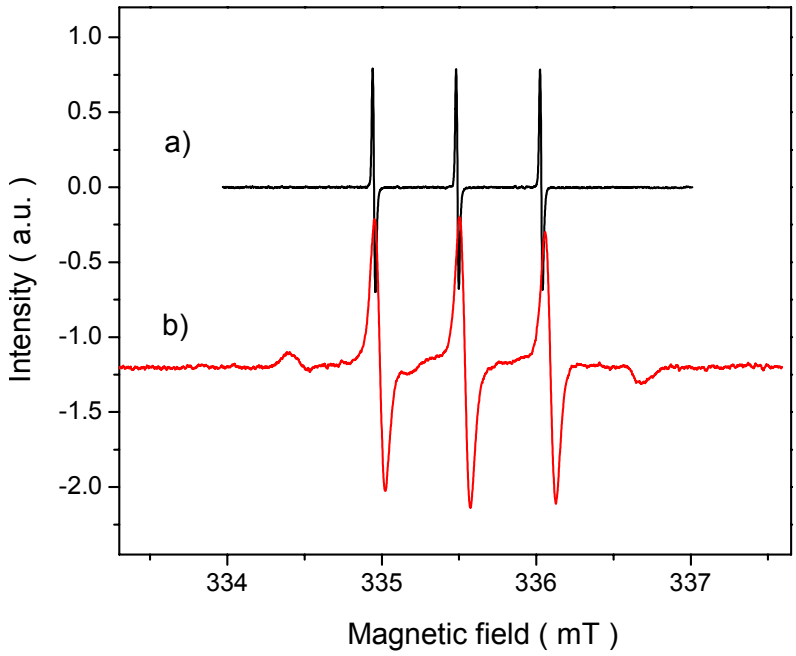

Figure 3.14: ESR spectra of derivative **2** in toluene at room temperature (a) and 77 K (b).

Spin loss was also observed in these Prato reactions although special care was taken to exclude light. For instance, approximately 66% of the nitrogen spins was retained in the synthesis of derivative **3N**. This spin surviving rate is very encouraging, with respect to the 55% in the Bingel-Hirsch reaction to synthesize derivative **1N**. The encapsulated nitrogen atom may escape from the carbon cage through an intermediate state in the Bingel-Hirsch reaction (Fig. 3.4), but it should follow a different decomposition mechanism in the Prato reaction. As shown in Figure 3.9, the pyrrolidine derivatives are formed through the 1,3-dipolar cycloaddition, where the azomethine ylide attacks a [6, 6] junction of C_{60} [137,138]. The transition state in the course of the cycloaddition should not significantly affect stability of the encapsulated nitrogen atom given its transient nature. Therefore, spin loss in the Prato reaction mainly results from thermal decomposition of N@C_{60} and its derivatives in high temperature solutions. This conclusion is further supported by the previous finding that only 70% of pristine N@C_{60} could survive the two-hour refluxing in toluene [106], the same conditions that are used for Prato reaction.

The Prato reaction is a better option than the Bingel-Hirsch reaction in functionalization of N@C_{60} in consideration of stability of the encapsulated nitrogen atom. Because spin loss in the Bingel-Hirsch reaction is determined by its reaction mechanism, it is unlikely to reduce the loss ratio by adjusting reaction conditions. In contrast, the Prato reaction leaves much room for improvement of this ratio. Although the reaction temperature has to be kept at 110°C, other conditions could be optimized to reduce the reaction time without sacrificing the yield. For instance, the use of highly soluble amino acid or aldehyde could significantly shorten the reaction time. In the synthesis of derivatives **5N** and **6N**, 40 min or an even shorter period could afford decent yields. Under these conditions, the spin loss ratio is less than 15%.

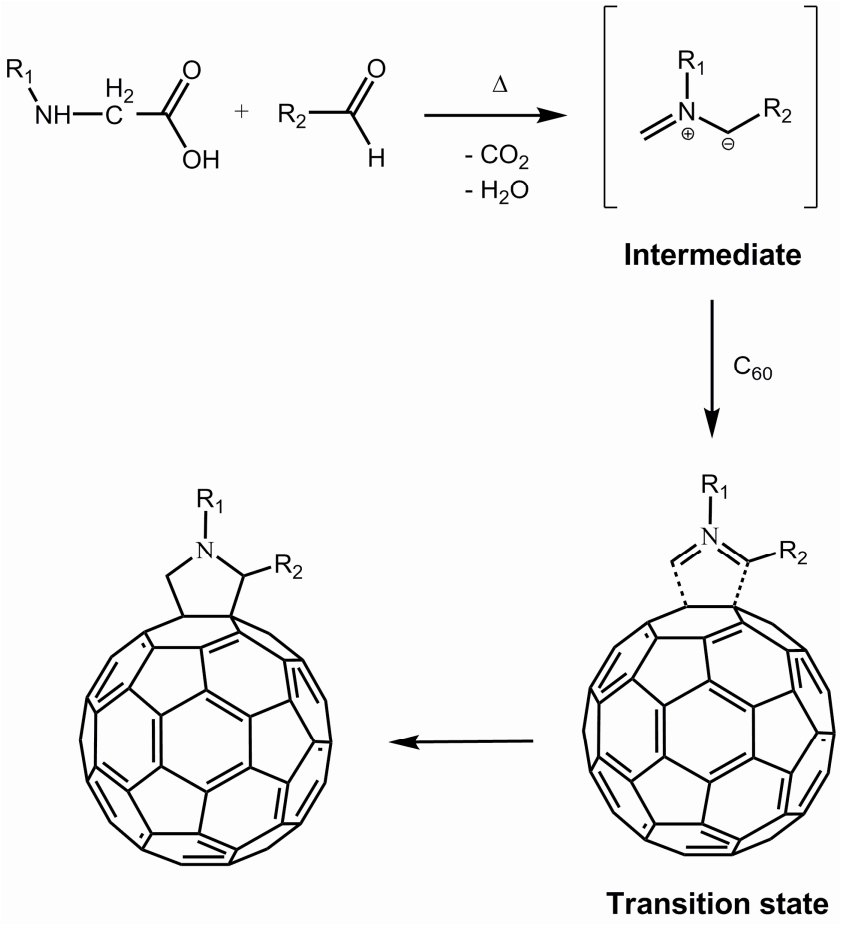

Figure 3.15: Mechanism of Prato reaction through azomethine ylide.

3.4 Dyads of N@C_{60}-porphyrin

Dyads of C_{60}-porphyrin have been long studied as photo-induced charge transfer systems for applications in photovoltaic energy conversion and molecular devices [139-143]. In the present work, two such dyads were synthesized to investigate the spin-spin interactions. As shown in Figure 3.16, dyads **7** and **8** were obtained by following the Prato reaction scheme. Dyad **8** could be alternatively synthesized through metallation of dyad **7**. But this option was excluded in consideration of the simplicity to synthesize the metalloporphyrin (**8a**) [144].

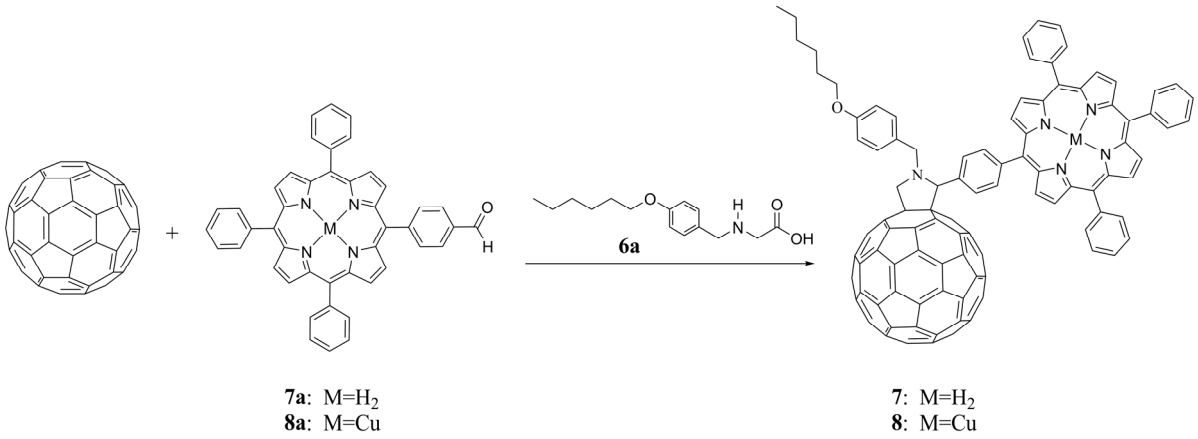

Figure 3.16: Scheme for synthesis of dyads **7** and **8**.

3.4.1 Synthesis of porphyrin-aldehyde

As shown in Figure 3.17, the synthesis of porphyrin-aldehyde **7.a** starts from the porphyrin-acid **7.1** (precursor **7.1** was supplied by Prof. A. G. Coutsolelos, in University of Crete in Greece). The acid group in **7.1** was firstly reduced to an alcohol group in **7.2** by $LiAlH_4$, and subsequently oxidized to the aldehyde group in **7.a** by pyridinium chlorochromate (PCC), which prevents a full oxidation of the alcohol to the carboxyl acid.

The three porphyrin compounds were easily separated by flash column chromatography. The porphyrin-alcohol and porphyrin-aldehyde were characterized by ^{1}H NMR [145,146]. While the alcohol group in derivative **7.2** is confirmed by the resonance at δ = 5.09 ppm of

the two protons in *–CH_2OH*, the aldehyde group in derivative **7a** is confirmed by the resonance δ = 10.41 ppm (refer to section 3.5). Additionally, the electron-withdrawing aldehyde group changes the chemical environment of the protons in the pyrrole-*NH* and in the 5-phenyl ring, in a more significant way than the alcohol group. The pyrrole-*NH* protons of **7a** are split into three sets, and the four protons in the 5-phenyl ring become different to their counterparts in the 10,15,20-phenyl rings.

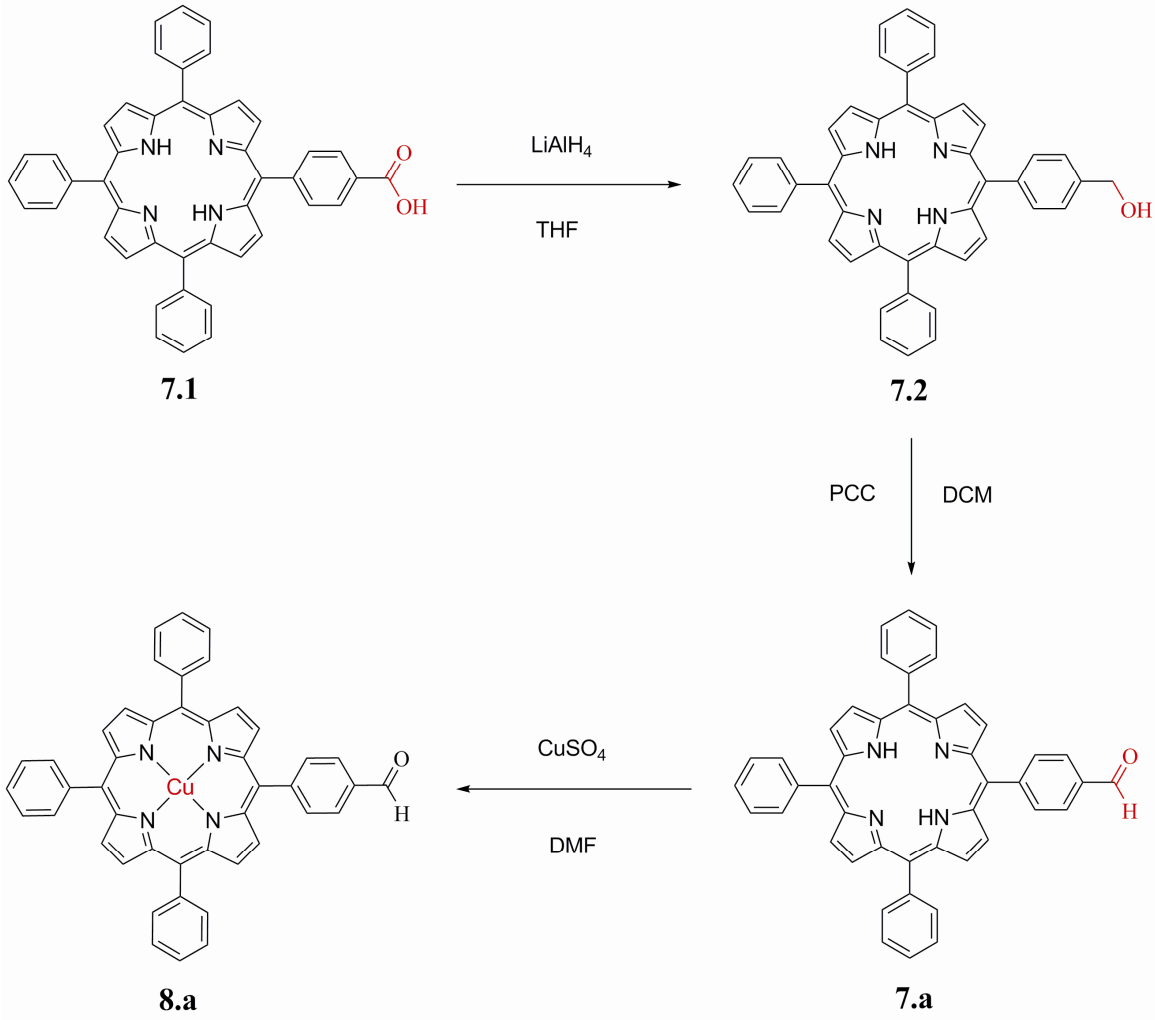

Figure 3.17: Scheme for synthesis of porphyrin aldehyde **7.a** and **8.a**.

The derivative **8a** was synthesized from **7a** through metallation in dimethylformamide (DMF) [144]. The substitution of protons by copper is readily monitored by optical absorption spectroscopy (Figure 3.18) [147-149], and further confirmed by MALDI-MS

(Figure 3.19) [150]. Due to its similarity to derivative **7a**, no purification was performed except passing the crude product through a silica pad to remove the polar molecules. Purity of the resultant product is demonstrated by the facts that no features ascribed to **7a** are identified in both the optical absorption and MALDI-MS spectra.

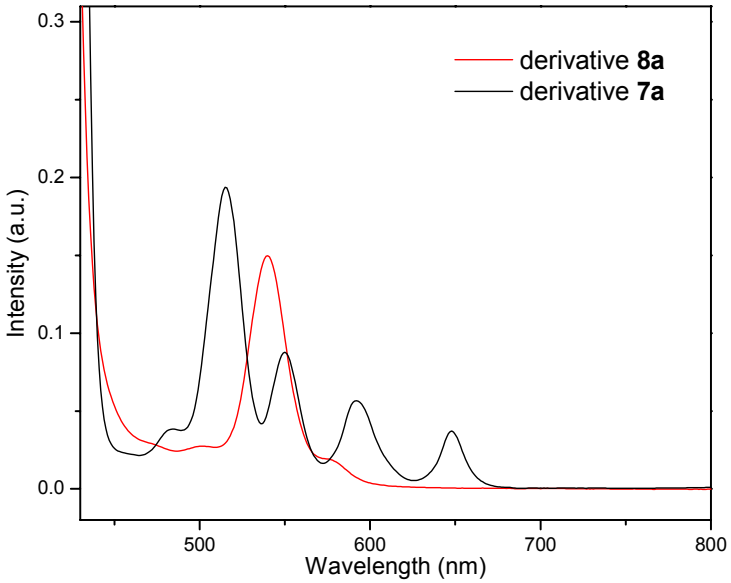

Figure 3.18: Optical absorption spectra of the porphyrin-aldehyde in acetone. Red trace is for derivative **8a**; black trace is for derivative **7a**.

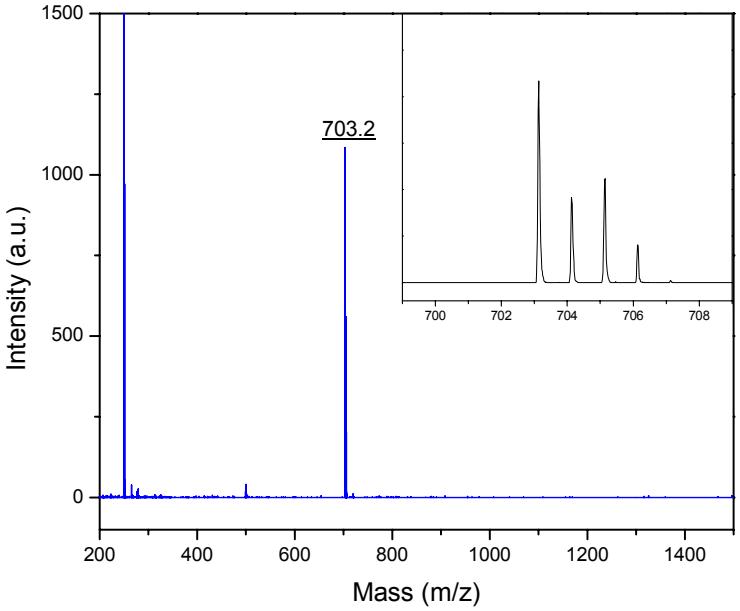

Figure 3.19: MALDI mass spectrum of derivative **8a** (the inset shows the corresponding isotropic distribution in the molecular ion peak).

3.4.2 Synthesis of fullerene-porphyrin dyads

To increase the solubility of the dyads, amino acid **6a** was used to introduce a phenyl group with long alkyl chain at the α-position to the *N*-substituent (Figure 3.16). The reaction time could be reduced to 15 min (2 h for derivative **2**), owing to the high solubility of both the aldehyde and the amino acid in toluene. The desired dyads (monoadduct) were then separated from the unreacted fullerene and bisadducts by HPLC.

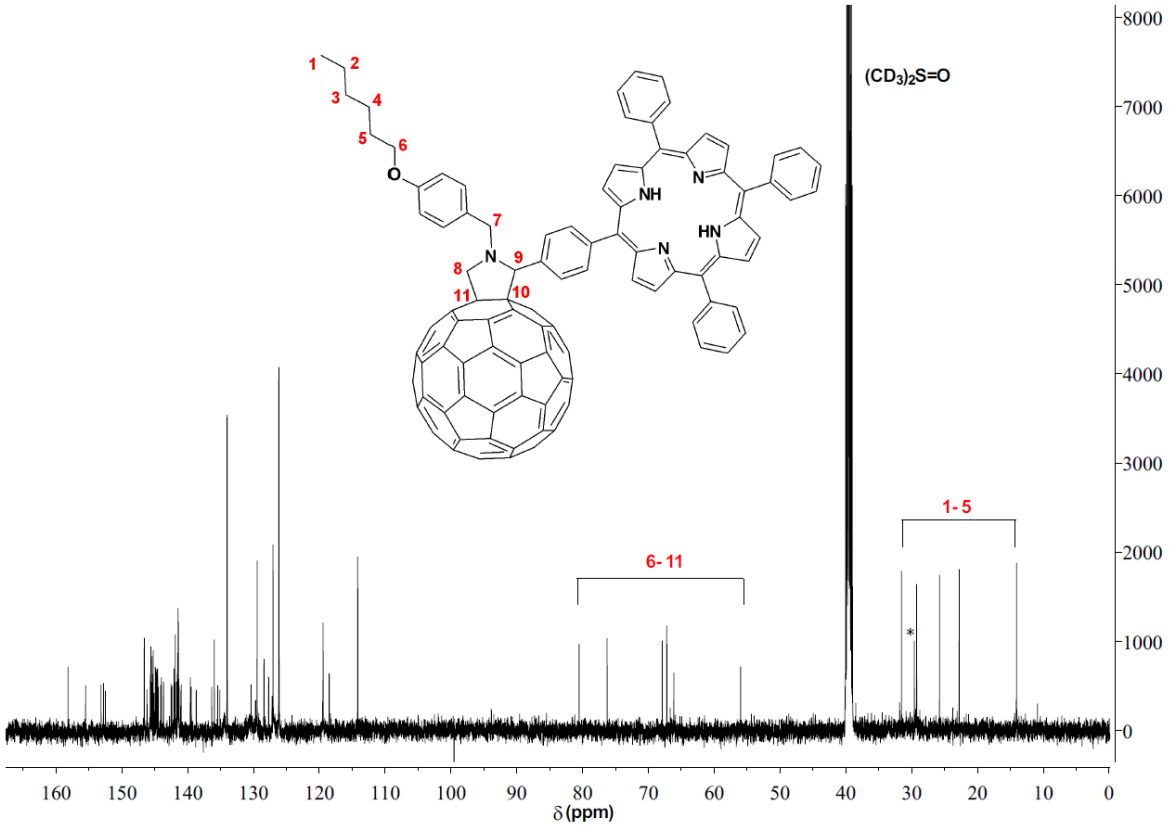

Figure 3.20: ^{13}C NMR spectrum (125.8 MHz, CS_2/C_6D_6=1:1) of dyad **7**. Minor impurity is marked (*).

The ^{13}C NMR spectrum of dyad **7** is shown in Figure 3.20. Five resonances arising from the alkyl chain (carbon 1-5) are identified in the carbon sp^3 ranges. With respect to derivative **6**, the presence of porphyrin at position 2 of the pyrrolidine ring changes the symmetry of fullerene cage in dyad **7** from C_{2v} to C_1. Firstly, all the 58 carbon sp^2 atoms of the fullerene cage become distinct. Secondly, the four carbon atoms of the pyrrolidine ring

become non-equivalent [151]. Consequently, six resonances are observed in the middle region (δ = 50-85 ppm) of the spectrum, in contrast with the four resonances for derivative **6** (Figure 3.12).

The lowered symmetry of derivative **7** is also supported by its ^{1}H NMR spectrum shown in Figure 3.21. Whereas the four pyrrolidine protons in derivative **6** are equivalent, the three protons in dyad **7** give rise to one singlet and two sets of doublets. This germinal coupling indicates that the two protons (H9) bonded to the same carbon atom are non-equivalent. The reason is that they are locked on either side of the heterocycle, and are therefore magnetically different [132,152] because of the asymmetric presence of porphyrin. A similar effect is also found on the methylene group connecting the pyrrolidine and phenyl ring (H7), where two doublets are observed [151].

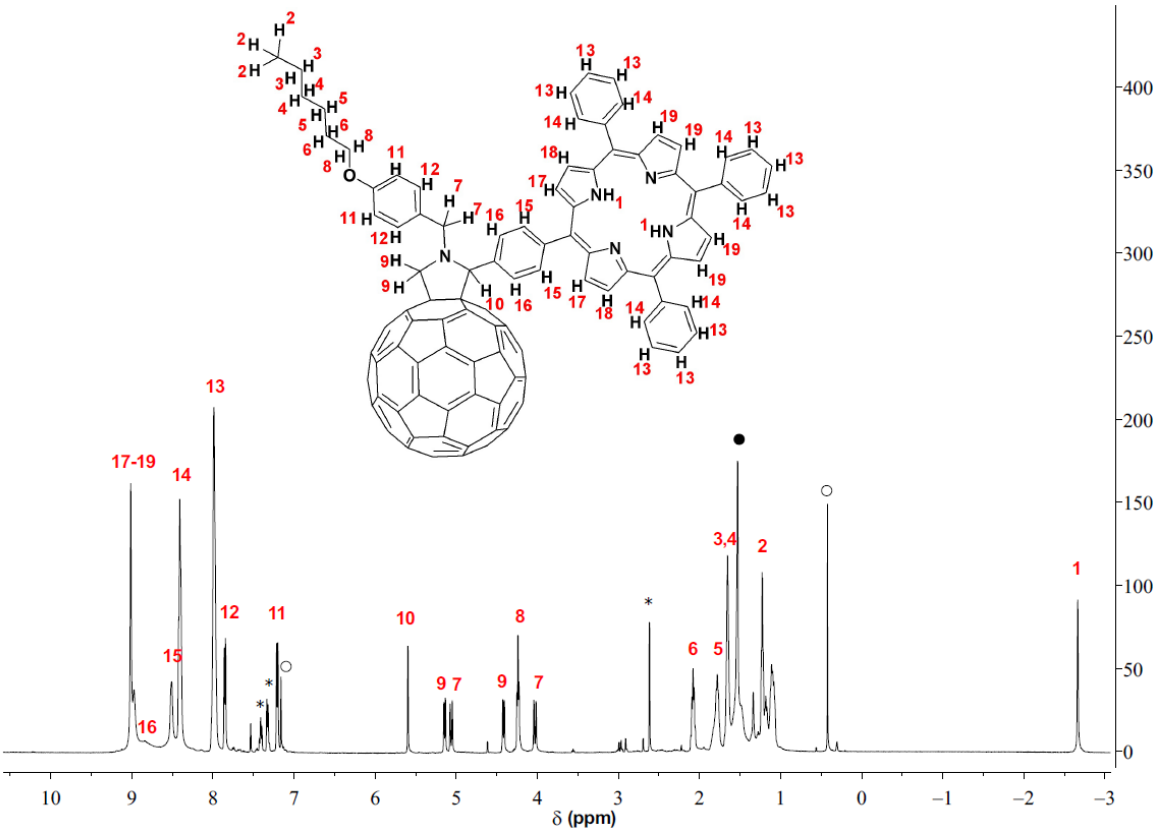

Figure 3.21: ^{1}H NMR spectrum (500 MHz, CS_2 with C_6D_6 as inset) of dyad **7**. Peaks arising from remnant toluene are marked (*); C_6D_6 is marked (○); water is marked (●).

A complete separation of dyad **8** (and **8N**) from dyad **7** (and **7N**) was achieved by a recycling mode HPLC (Figure 3.22). This operation effectively removed the residual dyad **7** (and **7N**) in the dyad **8** (and **8N**) sample resulting from contamination of **7a** in **8a**.

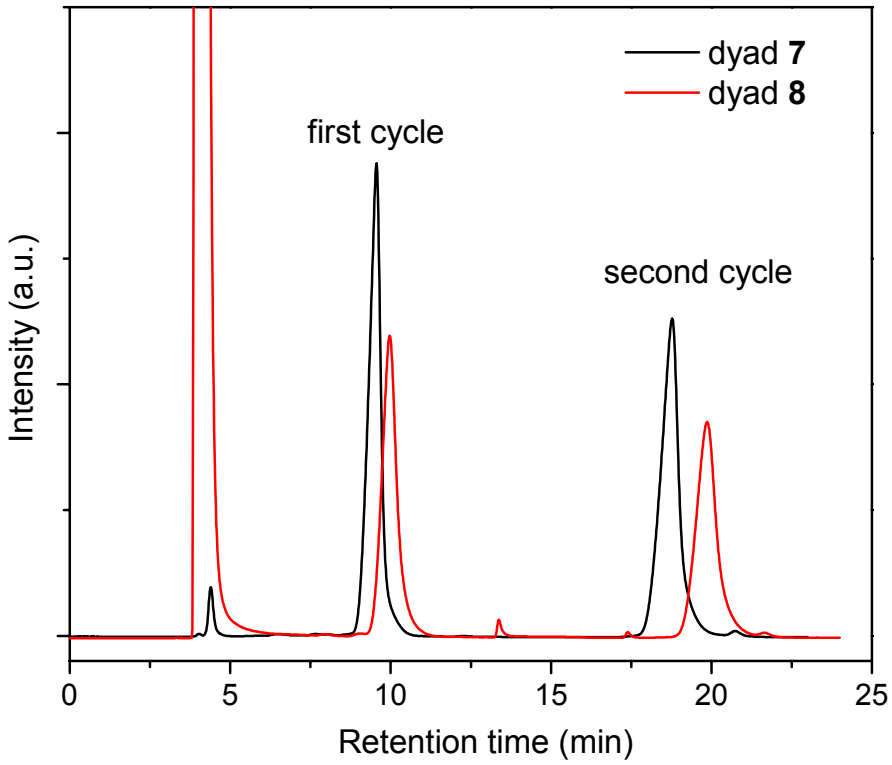

Figure 3.22: HPLC traces of dyads **7** and **8**, (5PBB column, toluene as eluent, 18 ml/min).

Dyad **8** was characterized by mass spectrometry and optical absorption spectroscopy. As shown in Figure 3.23, the peak at *m/z* = 1628 and its isotopic distribution are consistent with the calculations for dyad **8**. The minor peak at *m/z* = 721.4 is ascribed to the fragmentation of C_{60}.

UV-vis absorption spectrum for both dyads is the combination of individual fullerene and porphyrin. As shown in Figure 3.24, the peak centred at 310 nm is ascribed to absorption of C_{60} in both dyads, and the peaks between 390-680 nm are characteristic of porphyrins. The peak at 432 nm, a common feature for pyrrolidine derivatives of C_{60}, is completely overlapped by the features of porphyrin with much larger extinction coefficient [147,153].

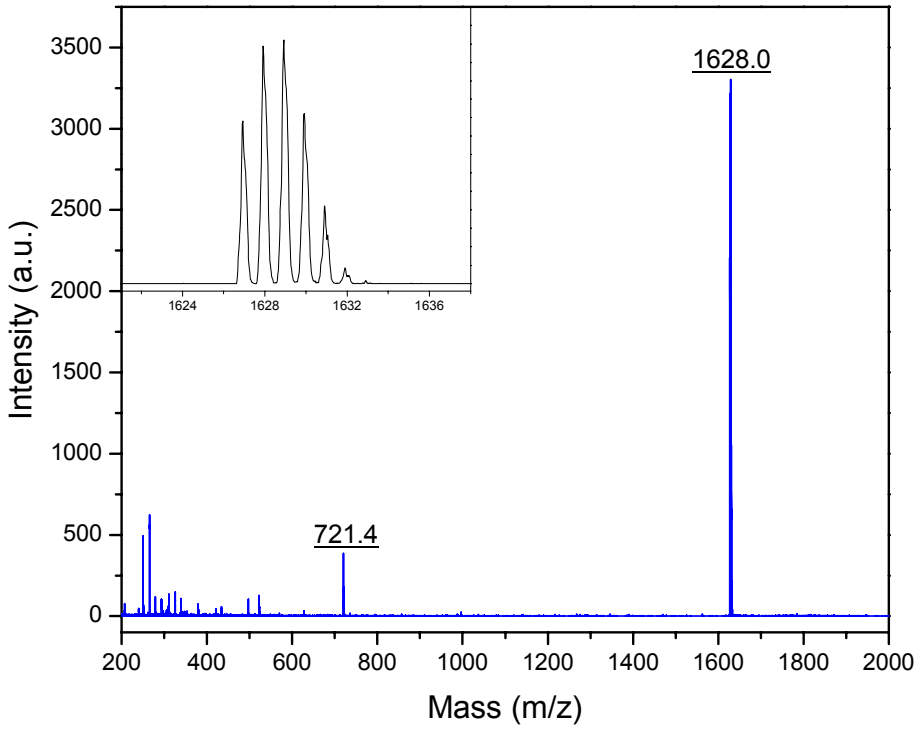

Figure 3.23: MALDI mass spectrum of dyad **8** (the inset shows the corresponding isotropic distribution).

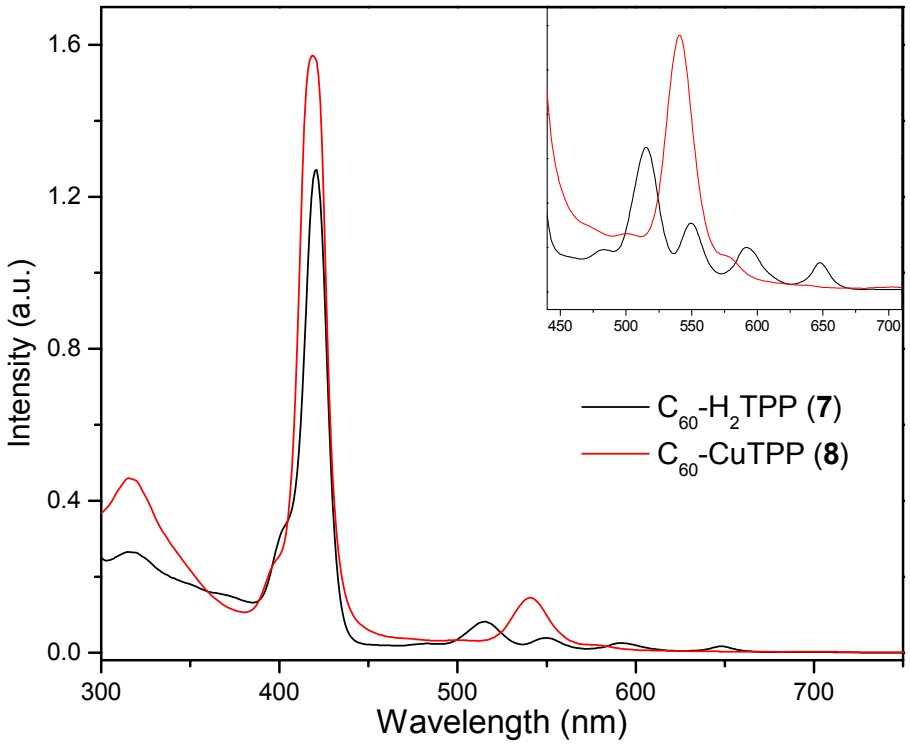

Figure 3.24: Optical absorption spectra of the porphyrin-aldehyde in toluene. Red trace is for dyad **7**; black trace is for dyad **8**. The inset shows the enlarged spectra in the range of 450-700 nm.

The dyads of N@C_{60}-porphyrin (**7N** and **8N**) were synthesized by following the exact procedures for dyads **7** and **8**, respectively. Details of the ESR characterization of these two dyads will be discussed in Chapter 5.

3.5 Synthesis and characterization details

Diethyl (1,2-methanofullerene C_{60})-61,61-dicarboxylate (1)

21.8 mg of C_{60} (0.03 mmol) was dissolved in 25 ml toluene; 0.072 mg of NaH (0.3 mmol) and 10.8 mg of diethyl bromomalonate (0.045 mmol) was added into the solution under nitrogen gas. After stirring for 6 h at room temperature, the reaction was quenched by one drop of 2N H_2SO_4. The crude product was purified by column chromatography (silica, toluene/hexane=1:1) (R_f = 0.5, toluene) to give the mono-adduct product in 40% yield. MALDI-MS 878.23 *m/z* $[M]^-$. ^{1}H NMR (500 MHz, $CDCl_3$): δ=1.50 (t, *J*=7.13 Hz, 6H), 4.58 (q, *J*=7.14 Hz, 4H) ppm.

***N*-methyl-C_{60} fulleropyrrolidine (2)**

2 was synthesized according to the literature [127]. MALDI-MS 778 *m/z* $[M]^-$. UV–vis (toluene) λ_{max}: 433 nm.

***N*-Methyl-2-pyrenyl-C_{60} fulleropyrrolidine (3)**

50.0 mg of C_{60} (0.07 mmol), 12.5 mg of sarcosine (0.14 mmol) and 64.0 mg of 1-pyrenecarboxaldehyde (64.0 mg, 0.28 mmol) were dissolved in 75 mL of toluene in a 150 mL two-neck flask equipped with a magnetic stirrer under nitrogen gas. The mixture was heated and stirred for 120 min at 110 °C using an oil bath. After cooling to room temperature, the brown mixture was filtered, evaporated and redissolved in toluene. Purification through recycling mode HPLC (Buckyprep M, toluene) afforded the title compound as a dark brown

powder (23.9 mg, 35%). MALDI-MS 977.41 *m/z* $[M]^-$. ^{1}H NMR (500 MHz, CS_2/toluene-d_8=5:1): δ= 2.78 (s, 3H), 4.42 (d, *J*=9.5 Hz, 1H), 5.03 (d, *J*=9.5 Hz, 1H), 6.08 (s, 1H), 7.86-8.07 (m, 6 H), 8.22 (d, *J*=8.2 Hz, 1H), 8.68 (d, *J*=9.5 Hz, 1H), 8.87 (d, *J*=8.1 Hz, 1H) ppm. In accordance with a previous report [136], minor signals ascribed to a second thermodynamically rotamer due to restricted rotation of the bulky pyrene ring are observed in the ^{1}H NMR as well: δ= 2.84 (s, 3H), 4.28 (d, *J*=9.5 Hz, 1H), 5.08 (d, *J*=9.4 Hz, 1H), 5.58 (s, 1H), 7.86-8.09 (m, 6 H), 8.17 (d, *J*=8.0 Hz, 1H), 10.39 (d, *J*=9.5 Hz, 1H) ppm.

***N*-[4-(methylsulfanyl)phenyl]-C_{60} fulleropyrrolidine (4)**

Similar to the synthetic procedures for **3**, a mixture of C_{60} (50 mg, 0.07 mmol), paraformaldehyde (13.5 mg, 0.42 mmol) and **4a** (42 mg, 0.21 mmol) in degassed toluene (100 mL) was allowed to react for 40 min at 110 ºC. Purification of the resultant mixture by HPLC (Buckyprep M, toluene) afforded the pure title compound as a brown solid (19 mg, 30%). MALDI-MS 885 *m/z* $[M]^-$. Elemental analysis for CHN found (expected) %: C 93.60 (93.55), H 1.12 (1.25), N 1.53 (1.58). UV–vis (toluene) λ_{max}: 432 nm. HPLC: 6.95 min. ^{1}H NMR (500 MHz, CS_2/C_6D_6=1:1): δ= 2.25 (s, 3H), 4.72 (s, 4H), 6.93 (d, *J*=8.8 Hz, 2H), 7.34 (d, *J*=8.8 Hz, 2H) ppm. ^{13}C NMR (125 MHz, CS_2, C_6D_6 used as insert): δ=154.85, 148.07, 147.04, 146.83, 146.58, 146.52, 146.35, 146.04, 145.29, 143.89, 143.44, 142.95, 142.84, 142.68, 141.06, 136.94, 130.68, 130.41, 129.79, 129.08, 126.21, 118.00, 70.43, 63.97, 18.77 ppm.

***N*-[(4-tert-butylphenyl) methyl]-C_{60} fulleropyrrolidine (5)**

Following the synthetic procedures for **4**, **5a** was reacted with C_{60} and paraformaldehyde to afford the title compound as a brown solid (yield 35%). MALDI-MS 909 *m/z* $[M]^-$. Elemental analysis for CHN found (expected) %: C 96.33 (96.34), H 2.00 (2.10), N 1.47

(1.54). UV–vis (toluene) λ_{max}: 432 nm. HPLC: 5.65 min. ^{1}H NMR (500 MHz, CS_2/toluene-d_8=5:1): δ= 1.21 (s, 9H), 4.03 (s, 2H), 4.20 (s, 4H), 7.28(d, *J*=8.5 Hz, 2H), 7.42 (d, *J*=8.4Hz, 2H) ppm. ^{13}C NMR (125 MHz, CS_2, DMSO-d_6 used as insert): δ= 154.18, 149.38, 146.56, 145.56, 145.36, 145.22, 144.98, 144.82, 144.58, 143.88, 142.43, 141.96, 141.57, 141.40, 141.22, 139.55, 135.68, 134.12, 128.41, 127.97, 127.70, 125.07, 124.83, 69.93, 66.93, 58.10, 33.59, 30.96, 30.82 ppm.

***N*-{[4-(hexyloxy)phenyl]methyl}-C_{60} fulleropyrrolidine (6)**

Following the synthetic procedures for **4**, **6a** was reacted with C_{60} and paraformaldehyde to afford the title compound as a brown solid (yield 38%). MALDI-MS 953 *m/z* $[M]^-$. Elemental analysis for CHN found (expected) %: C 94.42 (94.42), H 2.52 (2.43), N 1.36 (1.47). UV–vis (toluene) λ_{max}: 432 nm. HPLC: 5.46 min. ^{1}H NMR (500 MHz, CS_2/toluene-d_8=5:1): δ= 0.78 (t, *J*=5.9 Hz, 3H), 1.10-1.37 (m, 6H), 1.61 (m, 2H), 3.77 (t, *J*=6.0 Hz, 2H), 4.0 (s, 2H), 4.20 (s, 4H), 6.75 (d, *J*=8.7, 2H), 7.37 (d, *J* =8.8 Hz, 2H) ppm. ^{13}C NMR (125 MHz, CS_2, DMSO-d_6 used as insert): δ= 158.04, 154.18, 146.53, 145.52, 145.34, 144.95, 144.78, 144.55, 143.85, 142.40, 141.93, 141.54, 141.37, 141.18, 139.51, 135.64, 129.20, 128.72, 114.04, 69.89, 67.14, 66.82, 57.89, 31.52, 29.58, 29.21, 25.74, 22.75, 14.06 ppm.

***meso*-5-((4-formylphenyl)-10,15,20-triphenylporphyrin (7a)**

7.a was produced by oxidization of *meso*-5-((4-hydroxymethylphenyl)-10,15,20-triphenyl-porphyrin **(7.2)**, which was synthesized by reduction of *meso*-5-(4-benzoic acid)-10,15,20-triphenylporphyrin (**7.1)**.

7.2: to a solution of *meso*-5-(4-benzoic acid)-10,15,20-triphenylporphyrin (**7.1**) (47 mg, 0.07 mmol) in dry THF (20 ml), $LiAlH_4$ (12 mg, 0.28 mmol) was added. The solution was stirred at room temperature for about 30 min and was then quenched by EtOAc. The crude

product was purified by column chromatography (silica, EtOAc, R_f = 0.95) to afford **7.2** in the yield of 65%. ESI-MS 645.3 *m/z* $[M]^+$. ^{1}H NMR (500 MHz, $CDCl_3$): δ= 8.86 (8H, s), 8.24-8.23 (8H, m), 7.82-7.75 (11H, m), 5.09 (2H, s), -2.75 (2H, s) ppm.

7.a: To a solution of **7.2** (31 mg, 0.048 mmol) in dry DCM (20 ml), pyridinium chlorochromate (22 mg, 0.096 mmol) was added. The solution was stirred at room temperature for about 60 min and 20 mL silica gel was added. The crude product was purified by column chromatography (silica, DCM with 0.1% Et_3N, R_f = 0.75) to afford **7.a** in the yield of 90%. ESI-MS 643.2 *m/z* $[M]^+$. UV–vis (acetone): 482, 515, 550, 592, 648 nm. ^{1}H NMR (500 MHz, $CDCl_3$): δ= 0.41 (1H, s), 8.90 (2H, d, *J*=4.7Hz), 8.88 (4H, s), 8.80 (2H, d, *J*=4.7Hz), 8.43 (2H, d, *J*=8.0Hz), 8.31 (2H, d, *J*=8.1Hz) 8.25-8.23 (4H, m), 7.83- 7.72 (9H, m) -2.75 (2H, s) ppm.

***meso*-5-((4-formylphenyl)-10,15,20-triphenylporphyrinato copper (II) (8a)**

8a was synthesized according to the Adler procedures [144]. To a solution of **7a** (20 mg, 0.03 mmol) in DMF (5 ml), anhydrous $CuSO_4$ (52 mg, 0.33 mmol) was added. The mixture solution was allowed to reflux for about 10 min, and completion of the reaction was checked by UV-vis absorption spectroscopy. The resultant solution was cooled in an ice-water bath, and chilled distilled water was then added. The precipitate was filtered and washed with water to afford the title compound in the yield of 92%. MALDI-MS 703.2 *m/z* $[M]^-$. UV–vis (acetone): 501, 540, 579 nm.

C_{60}-H_2TPP dyad (7)

Similar to the synthetic procedures for **3**, a mixture consisting of C_{60} (22 mg, 0.03 mmol), **7a** (29.0 mg, 0.045 mmol) and **6a** (16.0 mg, 0.06 mmol) in degassed toluene (100 mL) was allowed to react for 15 min at 110 ºC. Purification of the resulting mixture by HPLC (5PBB,

toluene) afforded the pure title compound in the yield of 28%. MALDI-MS 1566.7 *m/z* $[M]^-$. UV–vis (toluene): 317, 421, 483, 515,550, 591,647 nm. ^{1}H NMR (500 MHz, CS_2, C_6D_6 used as insert): δ= 9.01 (6H, broad s), 8.97 (2H, m), 8.83 (2H, broad s), 8.51 (2H, broad s), 8.41 (6H, broad s), 7.99 (9H, broad s), 7.86 (2H, d, *J*=6.7 Hz), 7.21 (2H, d, *J*=6.5 Hz), 5.60 (1H, s), 5.14 (1H, d, *J*=8.7 Hz), 5.06 (1H, d, *J*=12.8 Hz), 4.42 (1H, d, *J*=8.9 Hz), 4.24 (2H, t, *J*=5.6 Hz), 4.03 (1H, d, *J*=13.6 Hz), 2.08 (2H, m), 1.78 (2H, m), 1.65 (4H, m), 1.23-1.08 (3H, m), -2.66 (2H, s) ppm. ^{13}C NMR (125 MHz, CS_2, DMSO-d_6 used as insert): δ=158.18, 155.50, 153.16, 152.78, 152.49, 146.59, 146.17, 145.66, 145.59, 145.50, 145.44, 145.41, 145.25, 145.08, 144.90, 144.75, 144.73, 144.69, 144.61, 144.55, 144.54, 144.46, 144.09, 144.01, 143.70, 143.65, 142.50, 142.30, 142.06, 142.02, 141.93, 141.89, 141.67, 141.58, 141.51, 141.47, 141.45, 141.41, 141.34, 141.28, 141.05, 140.97, 139.60, 139.59, 139.45, 138.69, 136.34, 135.95, 135.43, 135.11, 134.00, 130.36, 129.45, 128.40, 127.69, 127.03, 126.14, 119.48, 119.42, 118.49, 114.16, 80.53, 76.27, 67.88, 67.20, 66.13, 55.99, 31.54, 29.24, 25.76, 22.77, 14.05 ppm.

C_{60}-CuTPP dyad (8)

Following the synthetic procedures for **7**, **8a** was reacted with C_{60} and **6a** to afford the title compound in the yield of 25%. MALDI-MS 1628 *m/z* $[M]^-$. UV–vis (toluene): 316, 419, 501, 541, 581 nm.

To summarize, the endohedral fullerene derivatives discussed in this chapter are listed in Table 3.2. Effects of the two different pendant groups on the photochemical stability of N@C_{60} in **1N**-**3N** will be discussed in Chapter 4. Studies on the spin-spin interactions in the fullerene-porphyrin dyads **7N** and **8N** will be discussed in Chapter 5. Finally, orientations of derivatives **2N** and **4N**-**6N** in an anisotropic matrix will be discussed in Chapter 6.

Table 3.2: Summary of the synthesized fullerene derivatives and the corresponding chapters where further studies are discussed.

Derivatives	Schematic views	Relevant chapters
1N	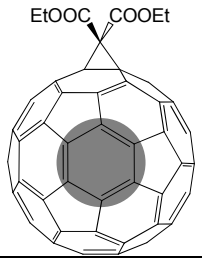	Chapter 4
2N	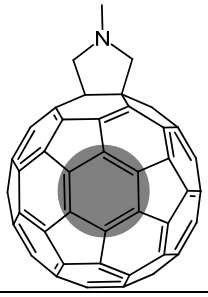	Chapter 4 and Chapter 6
3N	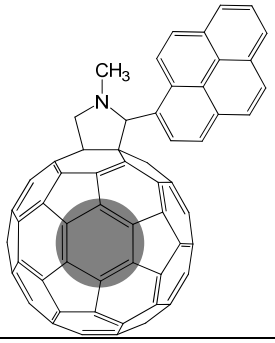	Chapter 4
4N	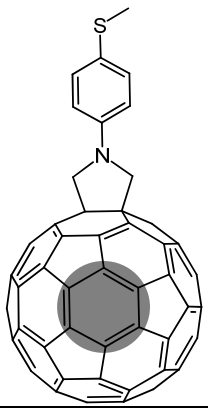	Chapter 6

5N	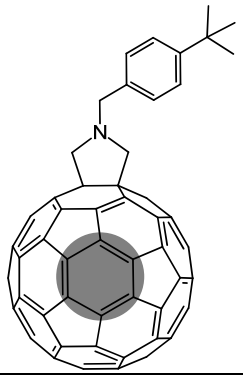	Chapter 6
6N	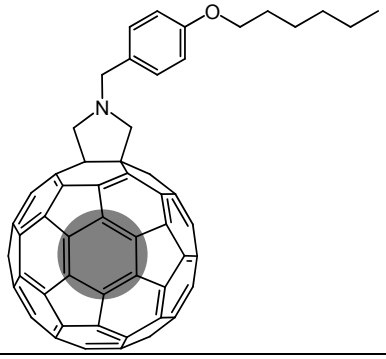	Chapter 6
7N	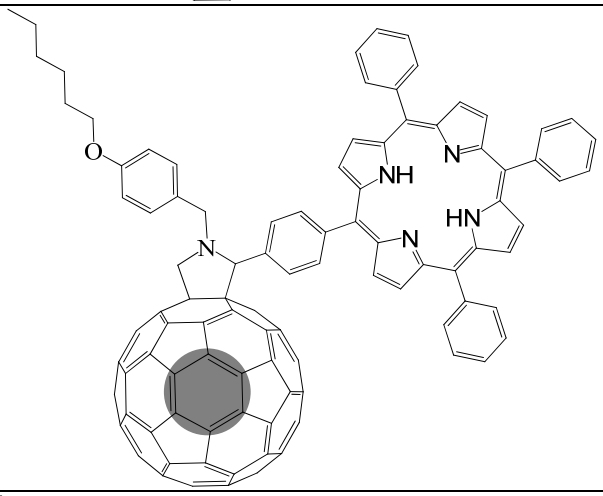	Chapter 5
8N	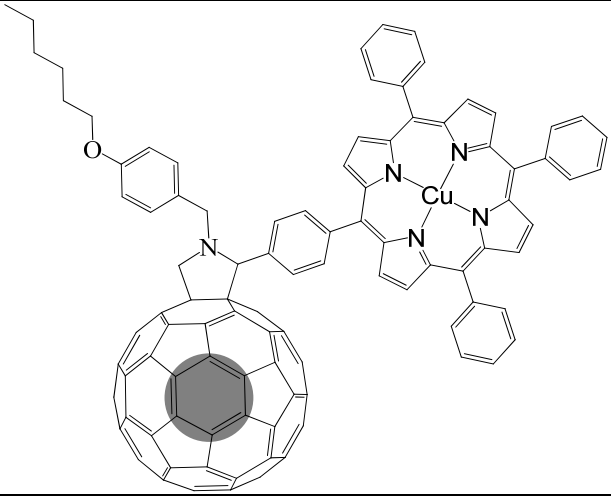	Chapter 5

Chapter 4

Photochemical stability of N@C_{60} derivatives: effects of the pendant groups

The excellent magnetic properties of N@C_{60} depend completely on its unique molecular structure where the atomic nitrogen is encapsulated by C_{60} cage. Due to its reactive nature, the encapsulated nitrogen would escape from the fullerene cage under some conditions. Stability of the encapsulated nitrogen is therefore a fundamental issue in any applications of N@C_{60}. However, because of restrictions in the sample amount, very limited studies on the stability of N@C_{60} and its derivatives have been carried out up to date. In this chapter, photochemical stability of the N@C_{60} derivatives is explored and effect of the functional groups on stability is studied, in order to illustrate the necessary practices that must be adopted during processing of N@C_{60} derivatives.

4.1 Introduction

4.1.1 Stability of pristine N@C_{60} and its derivatives

It has been widely observed that N@C_{60} is stable under ambient conditions, and no loss of ESR signal intensity is found after several months' storage in dark [96,107]. But this molecule becomes less stable when it is exposed to higher temperatures. A powder sample of N@C_{60} decayed at 520 K with a loss of more than 90% of its original ESR signal intensity after 10 min of heating (Figure 4.1a) [107]. The temperature dependence study found that 500 K is a critical point for N@C_{60} (Figure 4.1b), above which it starts to decay significantly [126].

Two other endohedral fullerenes bearing the group-V element, N@C_{70} and P@C_{60}, are thermally less stable than N@C_{60}. N@C_{70} and P@C_{60} started to decay at 450 K and 400 K, respectively [126]. An Arrhenius plot of the decay rates with temperature gives the activation energy for the escape of the encapsulated atom. As shown in Table 4.1, N@C_{60} exhibits the largest activation energy among the three pristine endohedral fullerenes.

Stability of N@C_{60} derivatives varies with the nature of the addends. Opposite trends in stability were reported in two different types of N@C_{60} derivatives. Firstly, the cyclopropane derivatives of N@C_{60} demonstrates enhanced thermal stability with respect to pristine N@C_{60}, and the stability increases with the number of addends [126]. As shown in Figure 4.1c, the monoadduct decays at a slightly higher temperature than pristine N@C_{60}, and the hexaadduct does not decay measurably until 570 K. Order of their decay temperature (from lower to higher) is consistent with their ranking in the activation energy for decay (Table 4.1): pristine N@C_{60} < the monoadduct < the hexaadduct. Secondly, the epoxide derivative N@C_{60}O is more vulnerable to both thermal heat and light excitation than pristine N@C_{60}

[96]. The powder sample of N@C_{60}O decayed at 373 K with a half-life time of approximately 3 d, and the sample in a degassed solution decayed at room temperature under the excitation of ambient light with a half-life time of approximately 2 d.

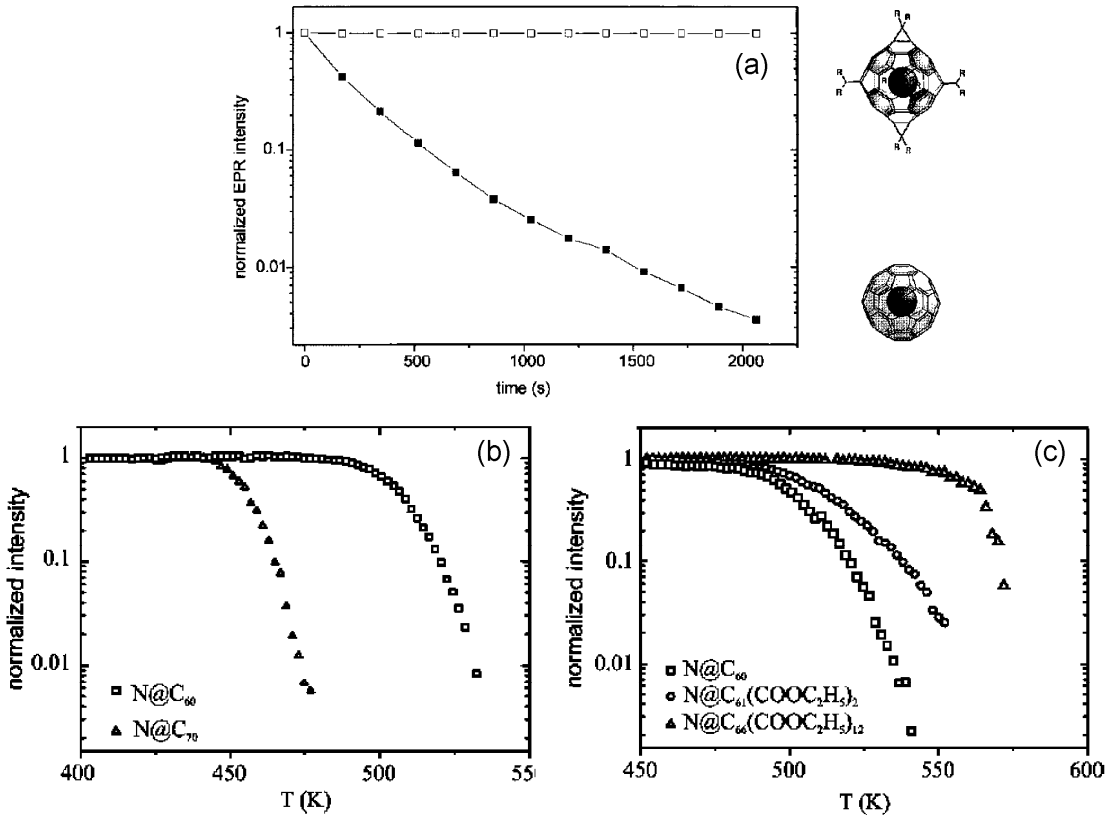

Figure 4.1: Thermal stability of endohedral fullerenes. (a) ESR intensity decay of N@C_{60} (solid squares) and its deuterated hexaadduct N@C_{66}(COOEt)$_{12}$ (open squares) heated at 520 K over time, R denotes $COOCD_2CD_3$ in the schematic view of the hexaaduct. (b) ESR intensity decay curve of N@C_{60} (squares) and N@C_{70} (triangles) under a heating rate of 2 K per 82 second. (c) ESR intensity decay curves of the monoadduct N@C_{61}(COOEt)$_2$ and hexaadduct N@C_{66}(COOEt)$_{12}$ under a heating rate of 2 K per 82 second. Reprinted from [126] and [107].

Table 4.1: Activation energy for the escape of the encapsulated atoms in endohedral fullerenes. [a] Estimated from the temperature of the main decay step [126].

	Activation energy (eV)
N@C_{60}	1.57
N@C_{70}	1.39
P@C_{60}	~1.2[a]
N@C_{61}(COOEt)$_2$	~1.6[a]
N@C_{66}(COOEt)$_{12}$	~1.8[a]

In addition to the thermal stability investigation, the surviving ratio of N@C_{60} after functionalization indicates its stability in chemical reactions. In early reports, a 100% surviving ratio was claimed in the synthesis of cyclopropane derivatives of N@C_{60} [81,95,97]. However, it was found later that only 60-70% of the nitrogen spins were preserved in a 2 h refluxing in the Prato reaction (373 K) and only 50% survived in the Bingel-Hirsch reaction (273 K) [98,100]. Conditions in these two reaction schemes were relatively mild compared with the heating at 500 K under which the pristine N@C_{60} starts to decay. Therefore, that stability of N@C_{60} could be significantly affected by factors other than temperature.

4.1.2 Escape mechanism for the encapsulated nitrogen atom

It is generally believed that loss of ESR signal intensity in N@C_{60} and its derivatives is caused by escape of the encapsulated nitrogen atom from the fullerene cage. However, the exact escape process is very speculative due to the very limited sample amount and the extreme difficulty in detection of the intermediates generated in the decay. From the experimental perspective, there are mainly two well-established facts on the stability of N@C_{60}. Firstly, N@C_{60} starts to decay at a much lower temperature than other endohedral fullerenes. For instance, He@C_{60} starts to decay at about 900 to 1150 K [154]. Secondly, stability of N@C_{60} derivatives varies with the nature of the addends (refer to section 4.1.1) [96,126]. Based on these two facts, two assumptions could be accordingly drawn. The first one is that the highly active nitrogen atom is chemically involved in the extrusion process [82,126]. The escape process of nitrogen in N@C_{60} is definitely different from that of the inert helium in He@C_{60}, for which a *window* mechanism is proposed (Figure 4.2). The trapped helium escapes through a larger ring after one or more bonds of the fullerene cage are broken up [155]. The critical decay point of 1000 K for He@C_{60} is therefore the

temperature at which the fullerene cage starts to decompose. Alternatively, the host fullerene cage determines the stability of He@C_{60}. The second assumption is that the addends are chemically engaged in the escape process of the encapsulated nitrogen [96].

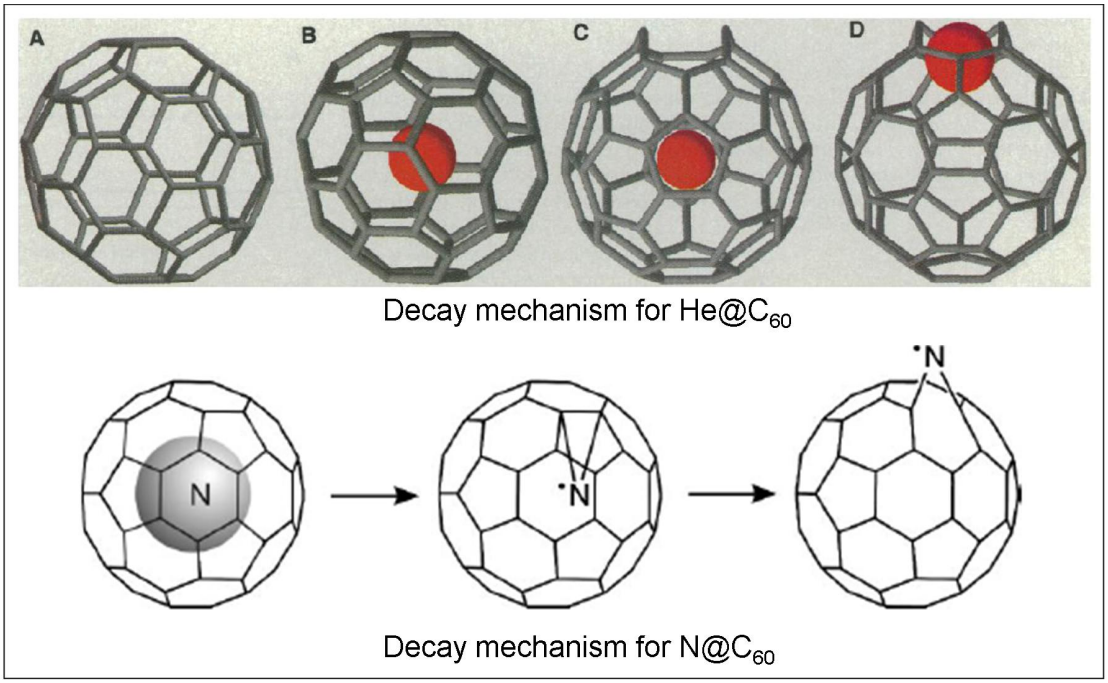

Figure 4.2: Proposed mechanism for the escape of helium in He@C_{60} (upper half, reprinted from [155]) and escape of nitrogen in N@C_{60} (lower half, reprinted from [126]). Red ball denotes the helium atom.

Based on the first assumption, a mechanism involving chemical bonding of the encapsulated nitrogen to the fullerene cage was proposed for the decay of pristine N@C_{60} [126]. As illustrated in Figure 4.2, the nitrogen atom bonds firstly to the fullerene cage from the inner side, and then swings out of the cage through breaking the carbon-carbon bond. The azo-bridge intermediate becomes spin-silent when the unpaired electron is quenched by either solvent molecules or radicals. This proposal was also supported by theoretical calculations [82]. Escape of the encapsulated nitrogen atom through a bond of the fullerene cage is energetically favourable over a straightforward pass through the centre of a 5- or 6-membered ring. Additionally, the enhanced thermal stability of the cyclopropane derivatives of N@C_{60} was explained by the blocking of double bonds by the addends.

Based on the second assumption, a mechanism to account for the lower stability of N@C_{60}O was proposed (Figure 4.3) [96]. The epoxide ring opens upon heating or photoexcitation and the encapsulated nitrogen atom bonds to the two radicals on the carbon cage. An azo-bridge intermediate is formed, similar to the intermediate in the decay mechanism of pristine N@C_{60} (Figure 4.2). The 4-membered ring C–O–C–N transfers to the outer side of the fullerene cage with a flip of the nitrogen, which leads to an exohedral 4-membered ring C–C–O–N.

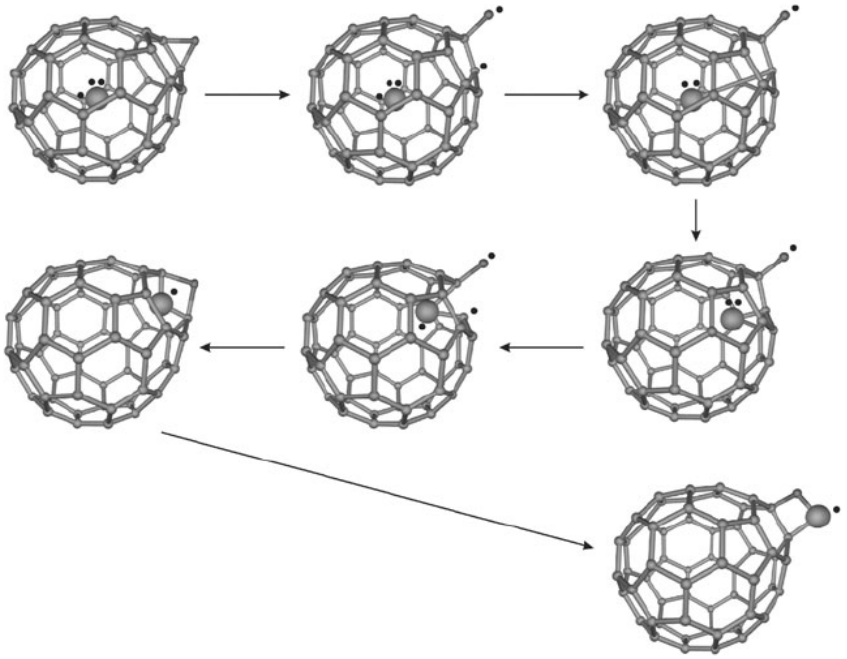

Figure 4.3: A proposed mechanism for loss of encapsulated nitrogen in N@C_{60}O, black dots denote the unpaired electrons. Reprinted from [96].

Pyrrolidine derivatives and cyclopropane derivatives are currently the two main families of N@C_{60} derivatives. Similar to N@C_{60}O, the pyrrolidine derivatives demonstrated a significant decay of ESR intensity under exposure to ambient light at room temperature (300 K). Such sensitivity to light makes it necessary to investigate their photochemical stability.

4.2 Experimental and modelling parameters for the stability studies

Fullerene derivatives investigated in this chapter

Synthesis and characterization of molecules **1(N)-3(N)** (Figure 4.4) were discussed in chapter 3.

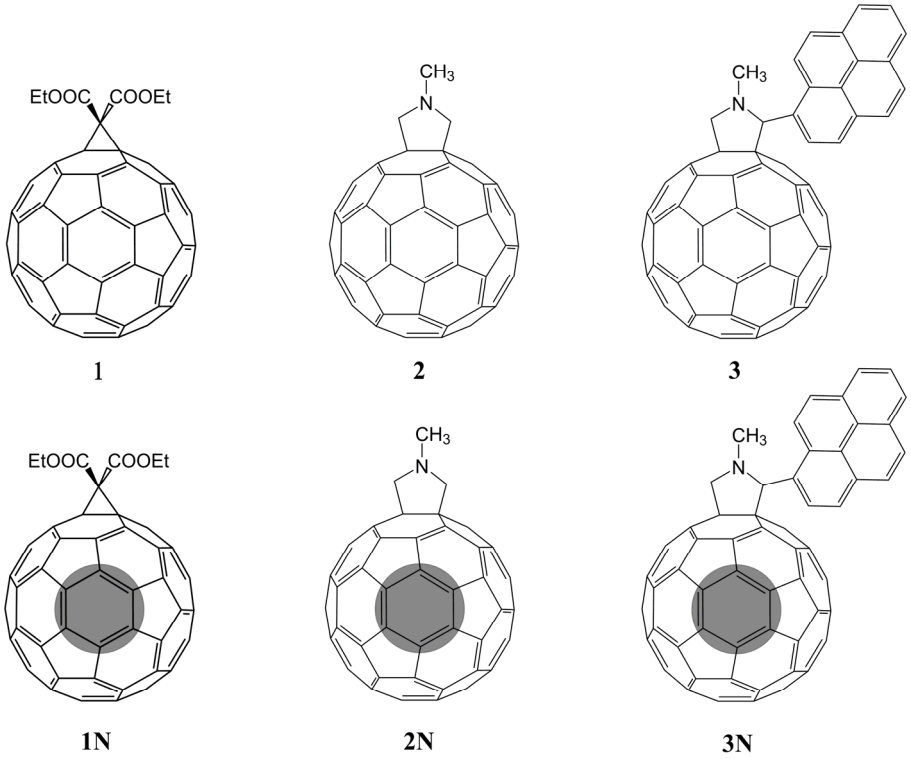

Figure 4.4: Schematic views of C_{60} derivatives and the corresponding N@C_{60} derivatives.

Photochemical stability monitored by CW ESR

Pristine N@C_{60} or its derivatives were dissolved in CS_2 or toluene (approximately 5×10^{-4} M). 0.1 ml of the solution was degassed and sealed off in a standard ESR tube. The ESR tubes were placed 1.5 meters vertically below three 18 W lamps (colour code 840, Philips TL-D) for different time durations. Stability of the endohedral fullerenes was monitored by measuring their ESR signal intensity at room temperature.

Density functional theory calculations

Hybrid DFT calculations were carried out with the Gaussian03 programme [120] at the spin-unrestricted B3LYP level. Split-valence 6-31G basis set was used for all elements with additional *d* and *p* polarization functional applied to N. Full geometry optimization was carried out by means of energy gradient techniques. Thermal energy calculation was performed with temperature and pressure set to be 273.15 K and 1 bar, respectively. Molecular structure and spin density distribution are visualized using GaussView [156]. All calculations were set to be in the gas phase.

4.3 Photochemical stability of N@C_{60} derivatives

4.3.1 Effect of the pyrrolidine group

The pyrrolidine derivative **2N** shows similar stability to pristine N@C_{60} in a degassed solution when it is stored in the dark, with a less than 10% loss of ESR signal intensity over a period of 40 d (Figure 4.5). However, it became vulnerable when exposed to ambient light, and significant spin loss was observed in a short time of exposure (less than 1 h). To determine the decomposition rate, time-dependence studies on its ESR signal intensity were carried out. Given the negligible interactions between endohedral fullerenes in solution (the filling ratio of encapsulated nitrogen is less than 0.1%), a first order reaction model is expected for the decay behaviour:

$$\ln A = -kt + \ln A_0 \tag{4.1}$$

where A is the ESR signal intensity of the sample under light, A_0 is the original signal intensity before exposure to light, t is the exposure time and k is the rate constant. The rate constant k is reflective of both molecular structure and experimental conditions. In a degassed solution where the effect of O_2 is excluded, possible experimental conditions

affecting *k* include: intensity and frequency distribution of light, temperature and solution concentration. When all experimental conditions are set the same, the rate constant *k* will exclusively reveal the intrinsic effects of the derivative groups on the stability of the encapsulated nitrogen atom.

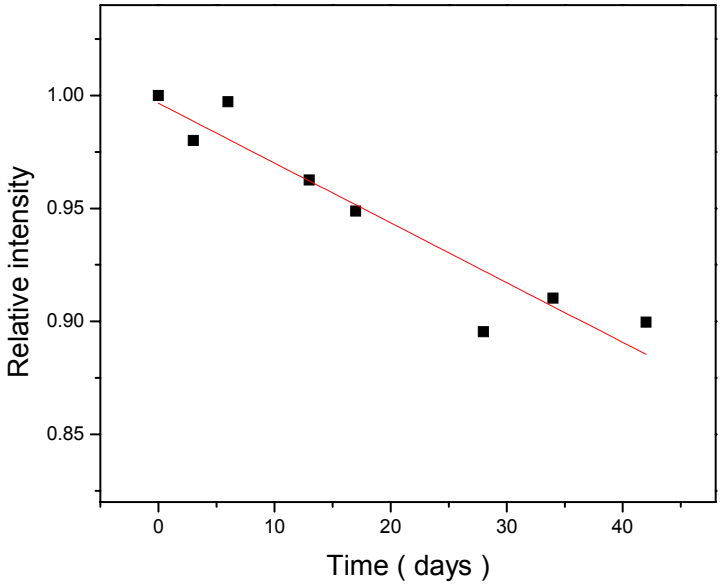

Figure 4.5: ESR intensity of derivative **2N** in degassed CS_2, sealed in an ESR tube and stored in dark.

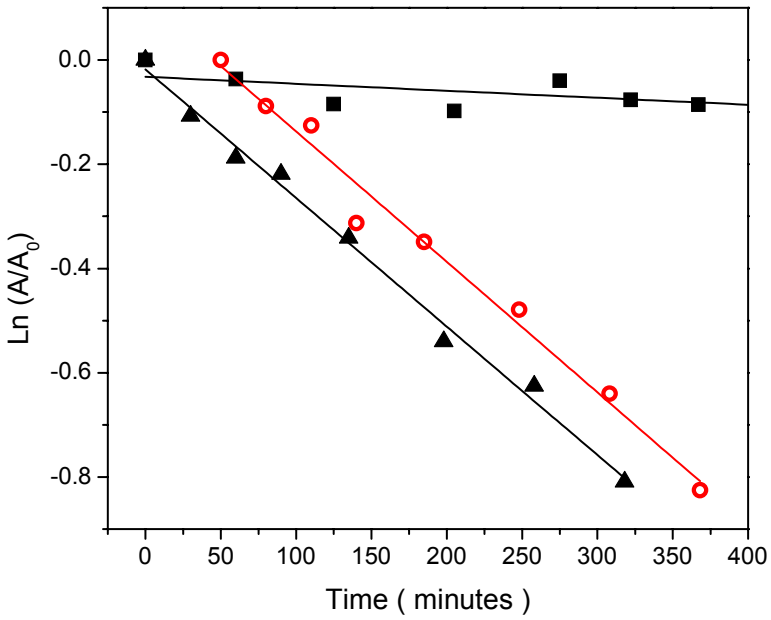

Figure 4.6: Time dependence of the relative intensity of ESR signal (A/A_0) for samples in degassed CS_2 exposed to ambient light at room temperature: N@C_{60} (squares), derivative **2N** (triangles), derivative **3N*** (circles). * Data points have been horizontally shifted for clarity.

As shown in Figure 4.6, ESR signal losses of both derivative **2N** and pristine N@C_{60} fit well the first order reaction kinetics of decomposition (equation 4.1). The calculated rate constants and half-life times are listed in Table 4.2. Decomposition rate constant for derivative **2N** is approximately 17 times higher than that for pristine N@C_{60}. Alternatively, half-life time of the encapsulated nitrogen atom in derivative 2N is only 280 min when exposed to light, much shorter than the 4951 min in pristine N@C_{60}. The significant difference suggests a key role of the pyrrolidine group in changing the stability of encapsulated nitrogen atom.

Table 4.2: Rate constant (k) and half-life time ($t_{1/2}$) for light induced decay of endohedral fullerenes in degassed CS_2 at room temperature.

	k (min^{-1})	$t_{1/2}$ (min)
Pristine N@C_{60}	0.00014 (7)	4951
Derivative **1N**	0.00017 (6)	4077
Derivative **2N**	0.00247 (9)	280
Derivative **3N**	0.0026 (1)	266

To further clarify the role of the pyrrolidine group, a pyrene chromophore was introduced at α position of the pyrrolidine ring (derivatives **3** and **3N**). As demonstrated in the UV-vis absorption spectra (Figure 4.7 left), derivative **3** shows the characteristic absorption peak at 433 nm reported for pyrrolidino-fullerenes [127,132]. Pyrene and C_{60} have distinct features in the UV-vis range of absorption. When they are chemically linked in derivative **3**, no electronic interaction between them was observed in the ground state based on the fact that the absorption spectrum of derivative **3** is just a superposition of that of derivative **2** and pyrene [157,158]. However, energy transfer from pyrene to fullerene takes place under excitation [136,159]. A comparison of the fluorescence intensity shows that more than 90%

of the excited singlet state of pyrene is quenched in fluorescence spectra of derivative **3** (Figure 4.7 right). Similar quenching phenomena were observed in mixtures of pyrene and C_{60} in solution. But the quenching effect in derivative **3** is more efficient than that in a C_{60}/pyrene =1/1 mixture in solution, and comparable to that in a mixture with C_{60}/pyrene =4/1 (inset in Figure 4.7 right). The enhanced intra-molecular energy transfer efficiency is not surprising considering the short link between pyrene and C_{60} in derivative **3**.

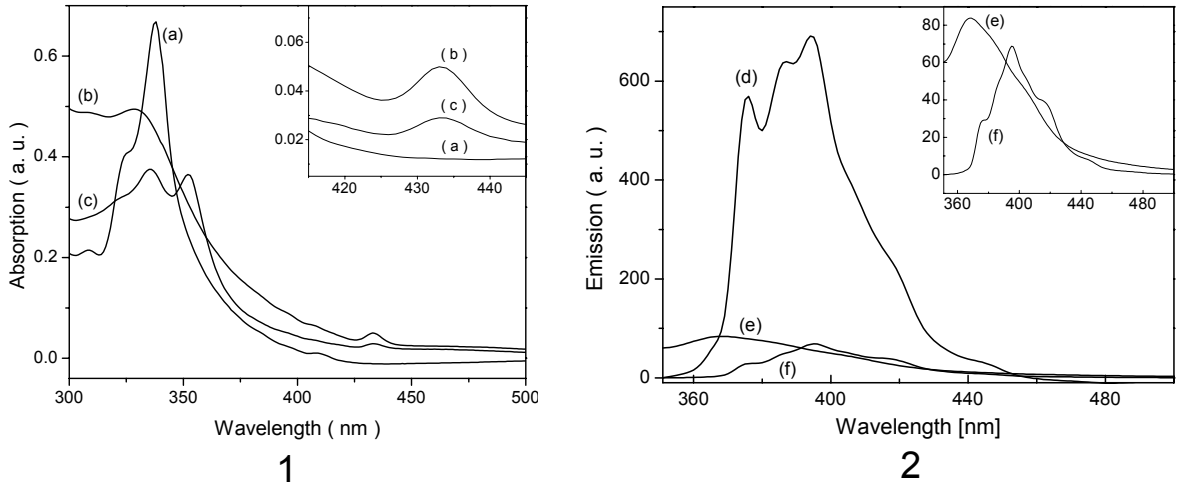

Figure 4.7: UV-vis absorption spectra (Left) of (a) mixture of pyrene and C_{60} (molar ratio 1/1), (b) derivative **2**, (c) derivative **3**. Fluorescence spectra (Right) of (d) pyrene, (e) derivative **3**, (f) mixture of pyrene and C_{60} (molar ratio C_{60}/pyrene= 4/1). (All samples were measured in toluene at room temperature.)

Although efficient energy transfer from pyrene to fullerene cage was observed in derivative **3** under excitation, derivative **3N** shows a comparable photochemical stability to derivative **2N** (Figure 4.6). The rate constant for derivative **3N** is 0.0026, indistinguishable from that for derivative **2N** (Table 4.2). This result indicates a negligible effect of the intra-molecular energy transfer. Therefore, it could be concluded that alteration of the C_{60} cage structure induced by the pyrrolidine group is the dominant reason for the increased decomposition rate of pyrrolidine derivatives of N@C_{60} under these experimental conditions.

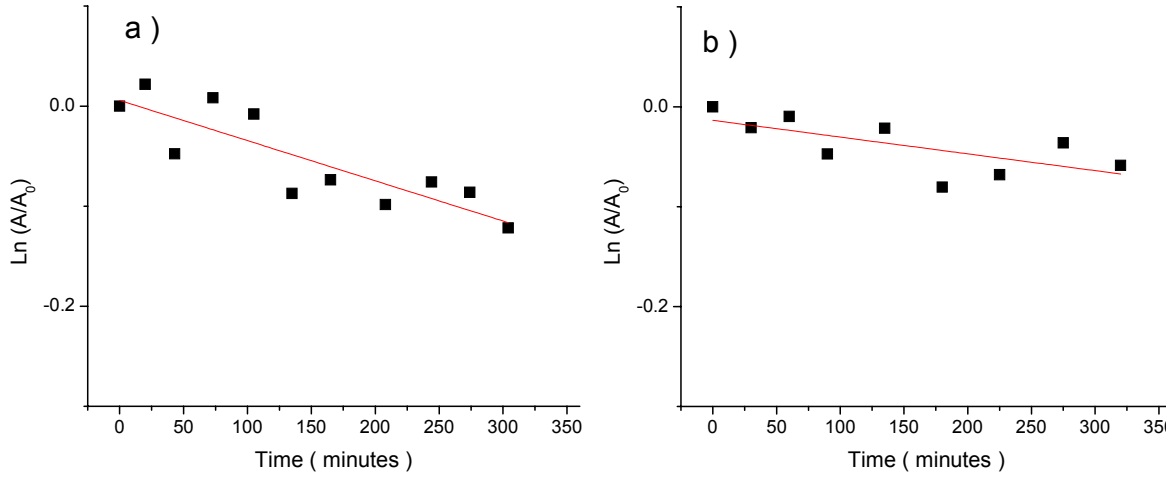

Figure 4.8: Time dependence of the relative intensity of ESR signal (A/A_0) for derivative **2N** in non-degassed CS_2 (a) and derivative **1N** in degassed CS_2 (b) when exposed to ambient light at room temperature.

In addition, the effect of oxygen on the photochemical stability were also examined. It was found that oxygen slowed down significantly the spin loss rate (Figure 4.8a). For derivative **2N** exposed to light in an air-saturated solution, the decay rate constant *k* was measured to be 0.00040 (8) min^{-1}, much lower than that measured in a degassed solution. Especially, when pristine N@C_{60} is exposed to light in an air-saturated solution, no decay of ESR intensity was detected over 6 h within the experimental accuracy.

4.3.2 Effect of the cyclopropane group

Photochemical stability of cyclopropane derivative of N@C_{60} was studied to compare effects of different functional groups on the stability of encapsulated nitrogen atom. As shown in Figure 4.8b and Table 4.2, the cyclopropane derivative **1N** shows a remarkably higher photochemical stability than the pyrrolidine derivatives **2N** and **3N** under the same conditions. The decay rate constant for derivative **1N** is 0.00017 min^{-1}, close to that for pristine N@C_{60}. This observation is consistent with previous findings that cyclopropane derivatives of N@C_{60} showed slightly higher thermal stability than pristine N@C_{60} [126].

Therefore, the cyclopropane group does not change the stability of the encapsulated nitrogen atom as much as the pyrrolidine group does in derivatives **2N** and **3N**.

4.4 DFT modelling of the escape mechanism

As discussed in the decay of N@C_{60}O (Figure 4.3), any functional groups attached to C_{60} cage can affect and may even engage in the escape process of the encapsulated nitrogen atom in N@C_{60} derivatives. However, it is currently not feasible to experimentally study the intermediates formed in decay of N@C_{60} because of restrictions in sample amounts. Therefore, quantum chemical calculations, such as DFT modelling, are necessary tools to explore the escape mechanism of encapsulated nitrogen atom in N@C_{60} and its derivatives. In the previous report [82], both semi-empirical (HF/PM3) and DFT calculations (B3LYP/D95*//PM3) were performed to determine the intermediate states and transition states in the decay process of N@C_{60} (Figure 4.9). Although these calculations are very instructive, higher-level calculations are required considering the much higher computing capacity today.

In our calculations, larger basis sets 6-31G and 6-31G(d, p) were employed. Based on the DFT calculations, escape mechanisms were proposed for both the pyrrolidine and cyclopropane derivatives of N@C_{60} (specifically, derivatives **2N** and **1N**). The intermediates and transition states identified in the decay process were compared with their counterparts in that of pristine N@C_{60}, in order to qualitatively account for the different photochemical stability observed for N@C_{60} derivatives.

4.4.1 Escape mechanism for the pyrrolidine derivatives of N@C_{60}

An escape mechanism incorporating the active engagement of the pyrrolidine group is proposed (Figure 4.10) for the decay of pyrrolidine derivatives of N@C_{60}. The derivative is

first excited into a triplet state upon absorption of light and subsequent intersystem crossing. The C1-C2 bond bearing the functional group would then break, and the two carbon atoms C1 and C2 bond to the endohedral nitrogen to form a covalent azo-bridge (Figure 4.10b). Dissociation of the C1-C2 bond is favoured over other bonds of the fullerene cage due to its elongation and the trend to release its σ strain induced by deviation from the ideal sp^3-hybridisation geometry. Next, the endohedral nitrogen swings out from the broken cage through an inversion of the 6-membered ring (Figure 4.10c). The free radical on the exohedral nitrogen atom is then quenched by either solvent molecules or O_2, which ends the escape process of the encapsulated nitrogen.

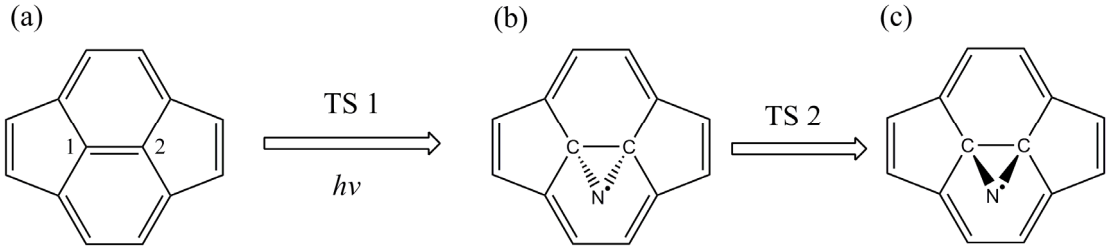

Figure 4.9: Proposed decay mechanism for pristine N@C_{60} through a [6, 6] bond. (a) Endohedral minimum state; (b) Endohedral bonding state; (c) Exohedral bonding state. TS stands for transition state.

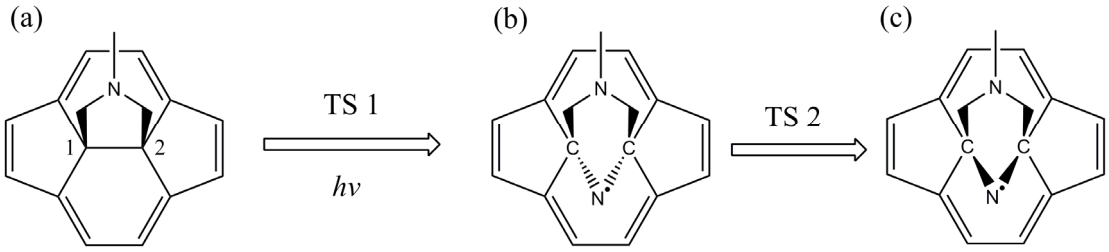

Figure 4.10: Proposed decay mechanism for a pyrrolidine derivative of N@C_{60}. (a) Endohedral minimum state; (b) Endohedral bonding state; (c) Exohedral bonding state. TS stands for transition state.

Although the proposed decay mechanism for N@C_{60} derivatives is similar to that for pristine N@C_{60} (Figure 4.9), the lower photochemical stability of the former indicates the possibility of major differences in their decay process. Therefore, the two intermediates

depicted in Figure 4.10b and Figure 4.10c, with their counterparts in Figure 4.9b and Figure 4.9c for comparison, are theoretically explored with DFT calculations.

4.4.1.1 Endohedral minimum state

Both previous experiments and theoretical calculations have shown that in the endohedral minimum state of pristine N@C_{60} [84,160,161], the nitrogen atom stays exactly in the centre of the fullerene cage. The *3p* electrons of nitrogen in pristine N@C_{60} are symmetrically distributed inside the carbon cage, resulting in nearly negligible ZFS effects. However, the fullerene cage is modified to incorporate the addends in N@C_{60} derivatives. For instance, the two carbon atoms baring the addend in derivative **2N** are pulled out of surface of the fullerene cage, and the C1-C2 bond, as well as other bonds in proximity, is elongated (Figure 4.11 and Table 4.3). Accordingly, the encapsulated nitrogen atom deviates from the centre of the fullerene cage in derivative **2N**, with a larger distance to the C1 carbon when compared that in pristine N@C_{60}. The distorted distribution of the nitrogen electron density gives rise to the ZFS effects of D = 16.2 MHz for derivative **2N** in its frozen solution.

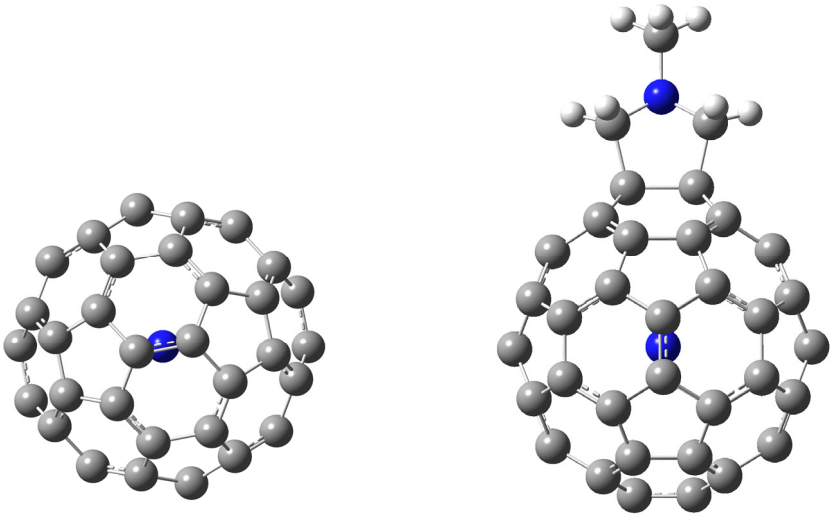

(a) (b)

Figure 4.11: Optimized geometry of the endohedral minimum state of N@C_{60} (a) and derivative **2N** (b).

Table 4.3: Some of the optimized bond lengths (Å), bond angles (°) and dihedral angles (°) in derivative **2N** and the intermediate states.

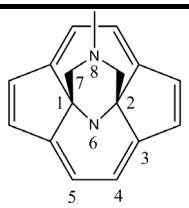

	Endohedral minimum state (Figure 4.10a)	Endohedral bonding state (Figure 4.10b)	Exohedral bonding state (Figure 4.10c)	Transition state (Figure 4.14c)
1-2	1.615	2.441	2.467	2.544
2-3	1.531	1.549	1.567	1.583
3-4	1.379	1.426	1.423	1.437
4-5	1.482	1.578	1.584	1.595
1-7	1.558	1.534	1.601	1.571
1-6	3.856	1.371	1.376	1.332
7-8	1.454	1.466	1.504	1.477
1-6-2	24.18	125.76	127.32	145.50
6-1-7	179.21	116.75	91.13	102.89
3-2-6	66.63	92.26	92.84	91.54
2-3-4	124.41	120.50	118.51	118.66
1-7-8	104.06	108.34	104.41	107.33
6-1-2-7	179.34	179.74	87.26	141.42
6-1-2-4	62.45	59.96	51.83	15.16

4.4.1.2 Endohedral bonding state

The encapsulated nitrogen forms a covalent azo-bridge inside the fullerene cage upon breaking of a [6,6] bond of the fullerene cage. In the endohedral bonding state for pristine N@C_{60}, the original double bond C1-C2 changes into a single bond when the azo-bridge is formed, with the bond length close to a [5,6] bond on the fullerene cage ((Figure 4.12a and Table 4.4). The C1-N6 bond is shorter than a normal C-N bond, indicating a conjugation of

electrons of the nitrogen with carbon atoms. As shown in Figure 4.12b, density of the nitrogen spins spreads over to C1, C2 and the nearby carbon atoms. Although the conjugation could lower its energy, bonding of the nitrogen to the fullerene cage still increases energy of the system. A reaction enthalpy of 40.6 kcal/mol is obtained by taking the endohedral minimum state as the reactant. This value is slightly larger than the 34 kcal/mol in previous literature calculated at the B3LYP/PM3 level [82], probably due to the enhanced bonding strength of the fullerene at a higher modelling level. The main reason for this energy increase in the endohedral bonding state is that the relatively rigid fullerene cage prevents a normal geometry of sp^3 hybridization for the endohedral addition, and results in geometrical distortion of the azo-bridge structure (Table 4.4).

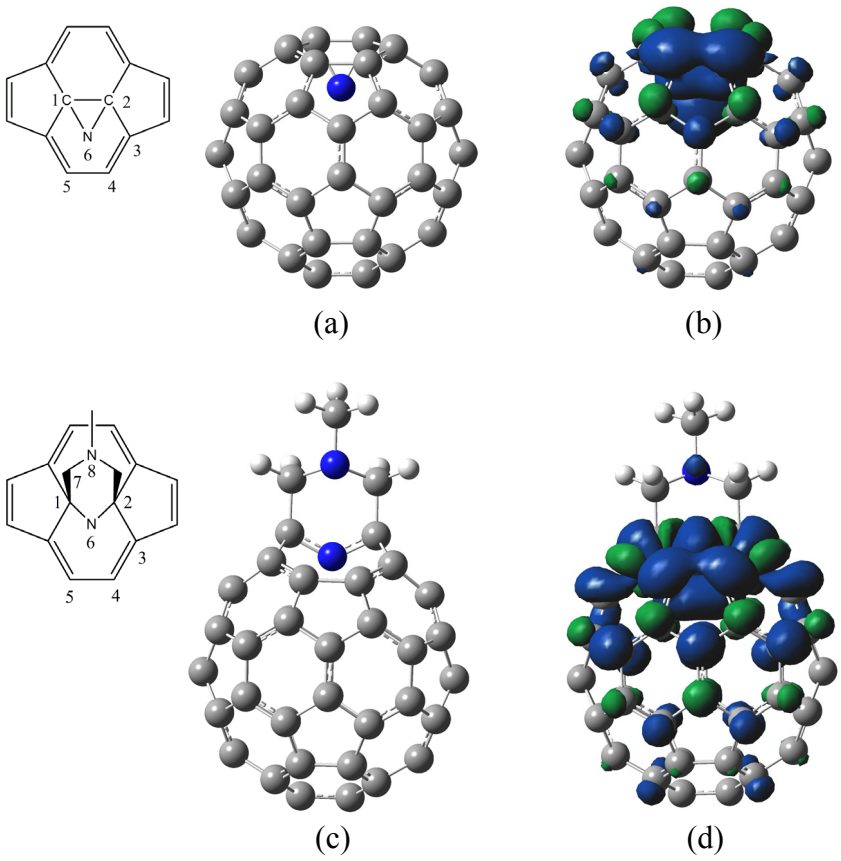

Figure 4.12: Optimized geometry and spin density distribution of the endohedral bonding state of pristine N@C_{60} (a, b) and derivative **2N** (c, d).

Table 4.4: Some of the optimized bond lengths (Å), bond angles (°) and dihedral angles (°) of pristine N@C_{60} and the intermediate states.

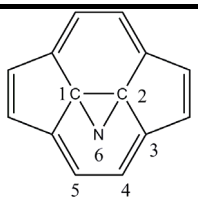

	Endohedral minimum state (Figure 4.9a)	Endohedral bonding state (Figure 4.9b)	Exohedral bonding state (Figure 4.9c)	Transition state (Figure 4.14a)
1-2	1.40	1.45	1.59	2.28
2-3	1.460	1.49	1.50	1.44
3-4	1.40	1.40	1.39	1.46
4-5	1.46	1.53	1.48	1.54
1-6	3.57	1.54	1.45	1.37
1-6-2	22.60	56.21	66.11	112.56
3-2-6	78.53	96.25	125.45	100.34
6-1-2-4	69.14	74.58	114.29	67.31

This intermediate state in the decay of derivative **2N** is structurally different from its counterpart in pristine N@C_{60}. As shown in Figure 4.12c, a 6-membered ring is formed upon the breaking of the original 5-membered pyrrolidine ring. The initial single bond C1-C2 is cleaved with the distance between the two carbon atoms increased to 2.44 Å (Table 4.3), resulting in a fulleroid cluster. The endohedral nitrogen lies in a plane defined by the carbon atoms (C1, C2 and C7) and its electrons are conjugated with those of the latter. The shorter C1-N6 bond (1.37 Å), as well as the broader distribution of nitrogen spins over the carbon cage (Figure 4.12d), point to a more stable structure than its counterpart in pristine N@C_{60}. Furthermore, the 6-member ring releases the bond strain that would be imposed by a 3-membered azo-bridge structure in N@C_{60}. Therefore, the intermediate state is calculated to

be 19.2 kcal/mol higher in enthalpy than the endohedral minimum state of derivative **2N**, only half of the 40.6 kcal/mol for pristine N@C_{60}.

No spin-active intermediates were detected by ESR spectroscopy in the decay of both pristine N@C_{60} and derivative **2N**. There are two possible reasons. Firstly, a very small portion of such intermediate exists in the system, and its lifetime may be shorter than the response time of an ESR spectroscopy (at the order of 10^{-10} s). Secondly, their ESR spectra may be broadened out because of the wide distribution of nitrogen spin over the carbon cage. Therefore, no ESR evidence of the intermediate states has been ever found in our investigation and previous reports [107,126].

4.4.1.3 Exohedral bonding state

From the endohedral bonding state, the encapsulated nitrogen swings out of the fullerene cage and forms an exohedral azo-bridge with the C1 and C2. For pristine N@C_{60}, this intermediate state reduces the σ strain of the fullerene cage (Figure 4.13a), and is energetically favourable over both the endohedral bonding state and the endohedral minimum state.

In the exohedral bonding state for derivative **2N** (Figure 4.13c), the nitrogen flips out of the hexagonal ring and changes conformation of the 6-member ring. Most bond lengths and bond angles of this exohedral state are close to those of the endohedral bonding state. But a change of the bond angle 6-1-7 from 116.8^o to 91.3^o distorts the C1 and C2 slightly further from the ideal sp^3-hybridisation geometry (Table 4.3). This intermediate state is 8.7 kcal/mol higher in energy than its endohedral bonding state, in contrast to the more stabilized exohedral bonding state for pristine N@C_{60}.

For the exohedral bonding state for pristine N@C_{60}, quenching of the free radical on the exohedral nitrogen would bring the escape process of the encapsulated nitrogen atom and the

spin loss into an end. A similar quenching process may take place for the exohedral bonding state for derivative **2N**. However, other development routines could not be excluded given the complex structure of this intermediate. The flipped nitrogen N6 may migrate to form bonds with other carbons such as C3 and C4. Alternatively, the unpaired electron on the flipped nitrogen N6 could transfer to the nitrogen of the initial pyrrolidine ring N8 through cleavage of the C1-C7 bond.

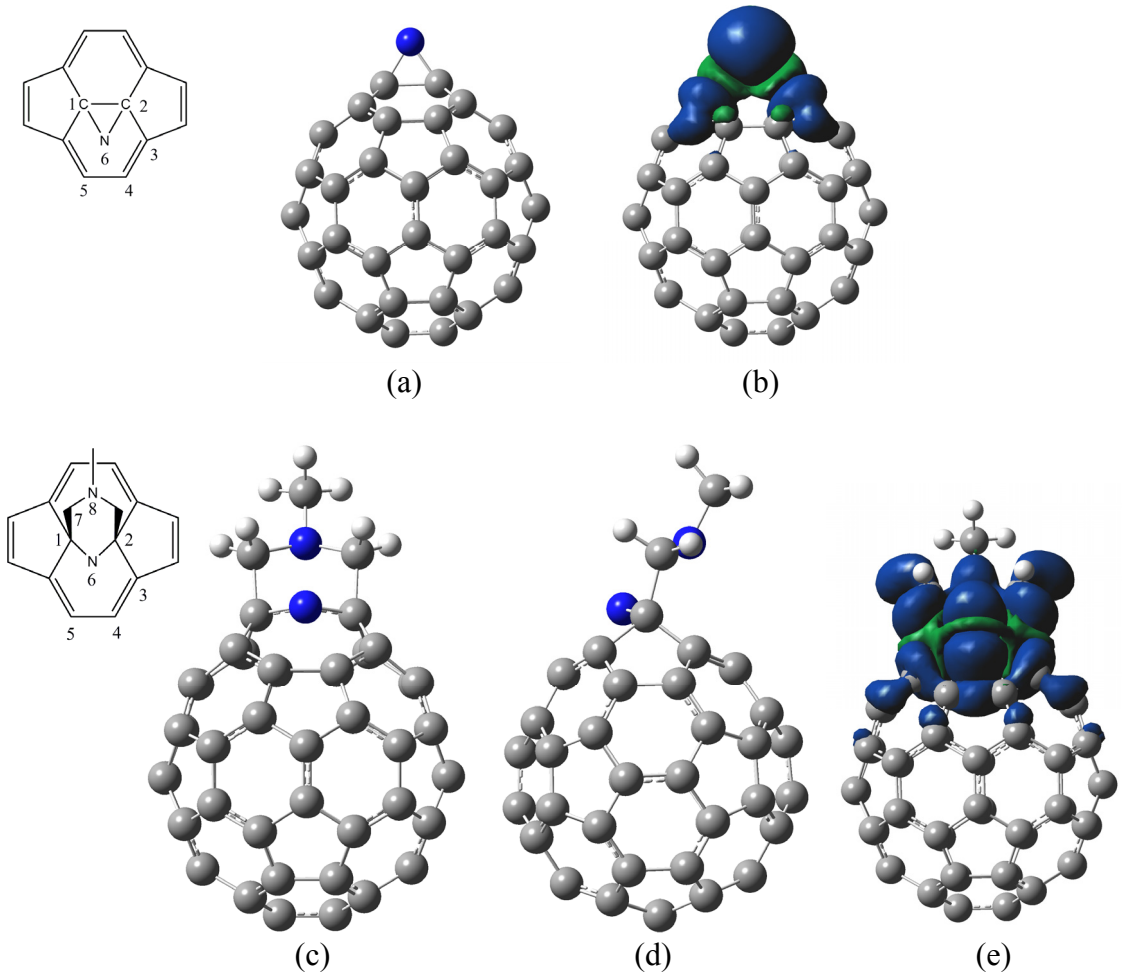

Figure 4.13: Optimized geometry and spin density distribution of the exohedral bonding state of pristine N@C_{60} (a, b) and derivative **2N** (c-e)*. * c and d are the views from two different perspective.

4.4.1.4 Transition states

Transition states reveal both the reaction routes and the activation energy of a chemical reaction. The transition state by definition is a structure with only one negative eigenvalues

in its Hessian matrix. Regarding the escape process, as shown in Figure 4.9 and Figure 4.10, the energy of the transition state 1 determines the activation energy for the formation of the endohedral bonding state (the first step); the energy of the transition state 2 determines the activation energy for the formation of the exohedral bonding state (the second step). In the previous report [82], identification of transition state 1 was achieved with the UHF/PM3 method but failed with the B3LYP/PM3 method. Our calculation at the B3LYP/6-31G level also failed to obtain this transition state for both pristine N@C_{60} and derivative **2N**. The change in the spin multiplicity from 4 (the endohedral minimum state) to 2 (the endohedral bonding state) results in difficulty for DFT modelling. However, search for the transition state 2 from the endohedral bonding state to the exohedral bonding state was achieved where the two intermediates have the same spin multiplicity.

Significant differences are identified between the transition state 2 for derivative **2N** and pristine N@C_{60}. Structural features of the transition state for pristine N@C_{60} (Table 4.4 and Figure 4.14a) includes: the nitrogen atom stays in the C_2 axis; the C1-C2 bond is broken with a distance of 2.3 Å between the two carbon atoms; the angle of 1-6-2 (112.6^o) is close to the ideal geometry of a sp^2-hybridisation state of the nitrogen atom; and the C1-N6 is shortened from 1.54 Å in the endohedral bonding state to 1.37 Å. The vibration mode with the negative frequency directs the encapsulated nitrogen out along the C_2 axis, indicating a straight escape course of the encapsulated nitrogen atom through the C1-C2 bond.

In the transition state for derivative **2N** (Figure 4.14c), the two nitrogen atoms stretch out in opposite directions of the plane defined by carbon atoms of the 6-membered ring, resembling the chair conformation of a cyclo-hexane. As shown in Table 4.3, the distance between C1 and C2 is 2.54 Å, and the dihedral angle 6-1-2-4 (15.2^o) indicates that the encapsulated nitrogen nearly stays in the plane of the hexagon (C1-C2-C3-C4-C5).

Conjugation of the encapsulated nitrogen with other parts of the derivative is demonstrated by the spin density distribution in Figure 4.14d. The vibration mode with the negative frequency demonstrates a completely different escape course for the encapsulated nitrogen: it swings out through the hexagon (C1-C2-C3-C4-C5) in a circular trajectory with C1-C2 as the rotation axis. An effort to search for a similar transition state for pristine N@C_{60} ended up with breaking the fullerene cage probably because the hexagon is too narrow for the encapsulated nitrogen atom to pass through. This supports again that the straight ejection is the most likely escape route in pristine N@C_{60}.

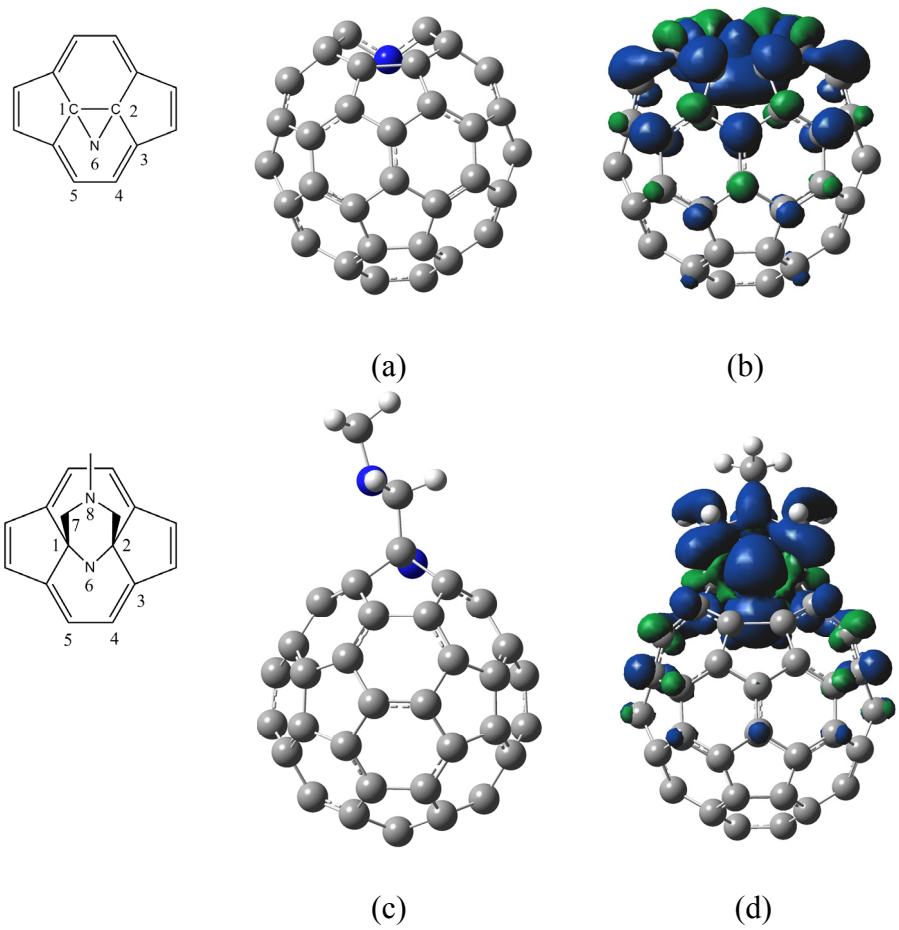

Figure 4.14: Optimized geometry and spin density distribution of the transition state 2 for N@C_{60} (a, b) and derivative **2N** (c, d) from endohedral bonding state to exohedral bonding state.

In terms of energy, the transition state for pristine N@C_{60} is 103.8 kcal/mol higher than its endohedral minimum state, in contrast to 40.5 kcal/mol for this transition state for derivative **2N** (Table 4.5). For derivative **2N**, a similar straight escape routine to that in pristine N@C_{60} could in principle takes place through bonds other than C1-C2. However, this straight escape routine should be energetically disfavoured with respect to the escape routine through the pyrrolidine ring. Therefore, the swinging escape through the C1-C2 bond would be the major decay route for the encapsulated nitrogen in derivative **2N**.

Table 4.5: Calculated reaction enthalpy (starting with the endohedral minimum) of intermediates and transition states in the decay of N@C_{60} (kcal/mol). (a) Refer to [5]. (b) Transition state from endohedral minimum state to the endohedral bonding state. (c) Transition state from endohedral bonding state to exohedral bonding state.

	$\Delta_r H^0$	$\Delta_r H^{0\,(a)}$	$\Delta_r H^{0\,(a)}$
	UB3LYP/6-31G	UHF/PM3	UB3LYP/PM3
transition state 1[(b)]	-	51.2	-
endohedral bonding state [6,6]	40.6	22.1	34.2
transition state 2 [(c)]	103.8	63.1	66.8
exohedral bonding state [6,6]	-44.8	-78.4	-47.5

According to the semi-empirical calculation (UHF/PM3) for decay of pristine N@C_{60} [82], activation energy for the first step (51.2 kcal/mol) is higher than that for the second step (41.0 kcal/mol). However, our calculation at the higher level (UB3LYP/6-31G) showed that energy of the transition state 2 was significantly underestimated and activation energy of 63.3 kcal/mol has been found for the second step. Because of the failure to identify the transition state 1 in our DFT calculations, it is impossible to make a conclusion on the decisive step with current knowledge. But we inclined to consider the second step as the decisive one in the decay of pristine N@C_{60}, based on the high energy level of the transition state 2 (103.8 kcal/mol).

On the contrary, we proposed that the first step determined the decay rate of derivative **2N**. The pyrrolidine ring favours the inversion of the encapsulated nitrogen and results in very low activation energy (21.4 kcal/mol) for the second step. This proposal is partially supported by the fact that O_2 remarkably lowers down the decay rate of derivative **2N**. O_2 is an effective quencher of triplet states [162-164], and its presence would suppress the first step in the decay process. Therefore, the observation of significantly reduced decay rate indicates a decisive role of the first step.

To summarize the escape mechanism, energy profiles for the decay process of both pristine N@C_{60} and derivative **2N** are compared in Figure 4.15. With respect to the pristine N@C_{60}, the lower energy barrier for the decay of derivative **2N** is consistent with its lower photochemical stability. From the structural perspective, two points facilitate escape of the encapsulated nitrogen in the pyrrolidine derivatives of N@C_{60}. Firstly, the attachment of derivatives changes the hybridisation state of C1 and C2 into sp^3 that favours their endohedral bonding with the encapsulated nitrogen atom. The elongated C1-C2 bond is also easier to be cleaved than other [6,6] double bonds of the fullerene. Secondly, the 6-membered ring formed in the decay process facilitates the inversion of the encapsulated nitrogen atom. The hexagonal windows opened up by the 6-membered ring provide adequate space for the encapsulated nitrogen to pass through. With an energy barrier of just 21.4 kcal/mol, evolution of the endohedral bonding state to the exohedral bonding state in derivative **2N** are readily accessible under ambient conditions.

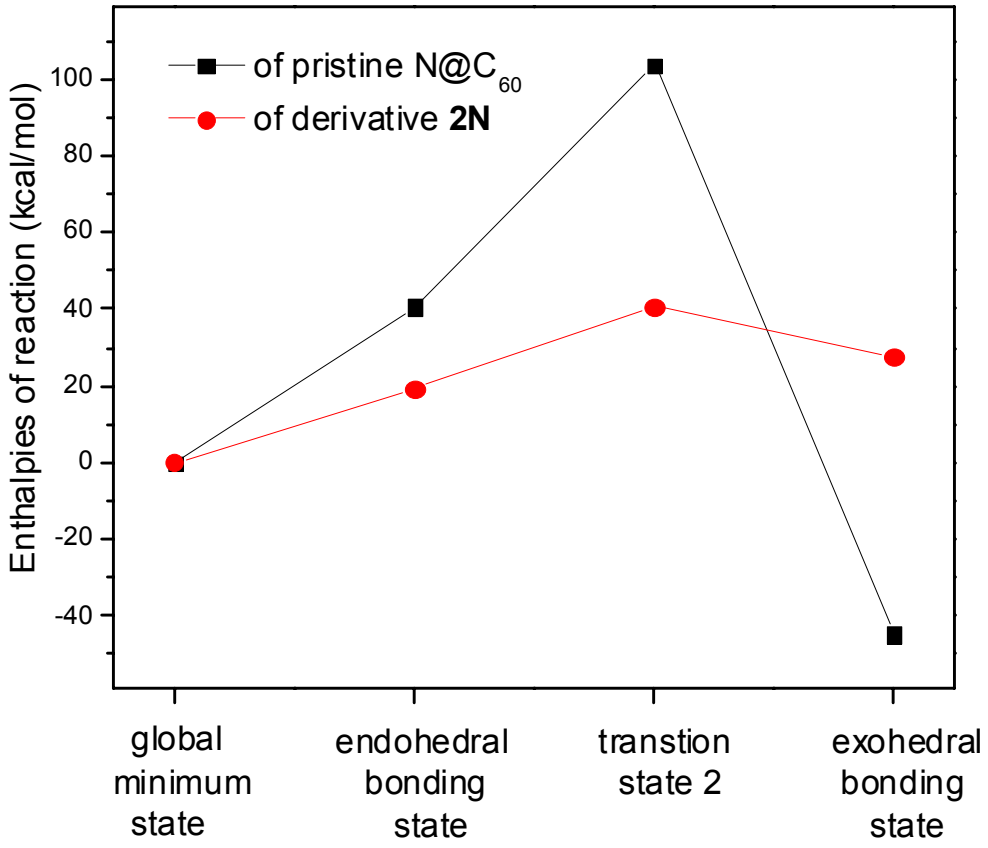

Figure 4.15: Reaction enthalpies $\Delta_r H^0$ (298 K) in the decay process of pristine N@C$_{60}$ and derivative **2N**.

4.4.2 Escape mechanism for the cyclopropane derivative of N@C$_{60}$

DFT calculations for the escape process in cyclopropane derivative of N@C$_{60}$ was carried out in a similar manner to that for the pyrrolidine derivative **2N**. In the endohedral minimum state for derivative **1N**, the fullerene cage is distorted by the addend (Figure 4.16a and Table 4.6). The C1-C2 bearing the addend exhibits longer bond length than any other carbon-carbon bonds of the fullerene cage. The encapsulated nitrogen deviates from the centre of the fullerene cage and moves apart from the addend. Based on their ZFS parameters, the distortion induced by a cyclopropane addend should be less apparent than a pyrrolidine addend.

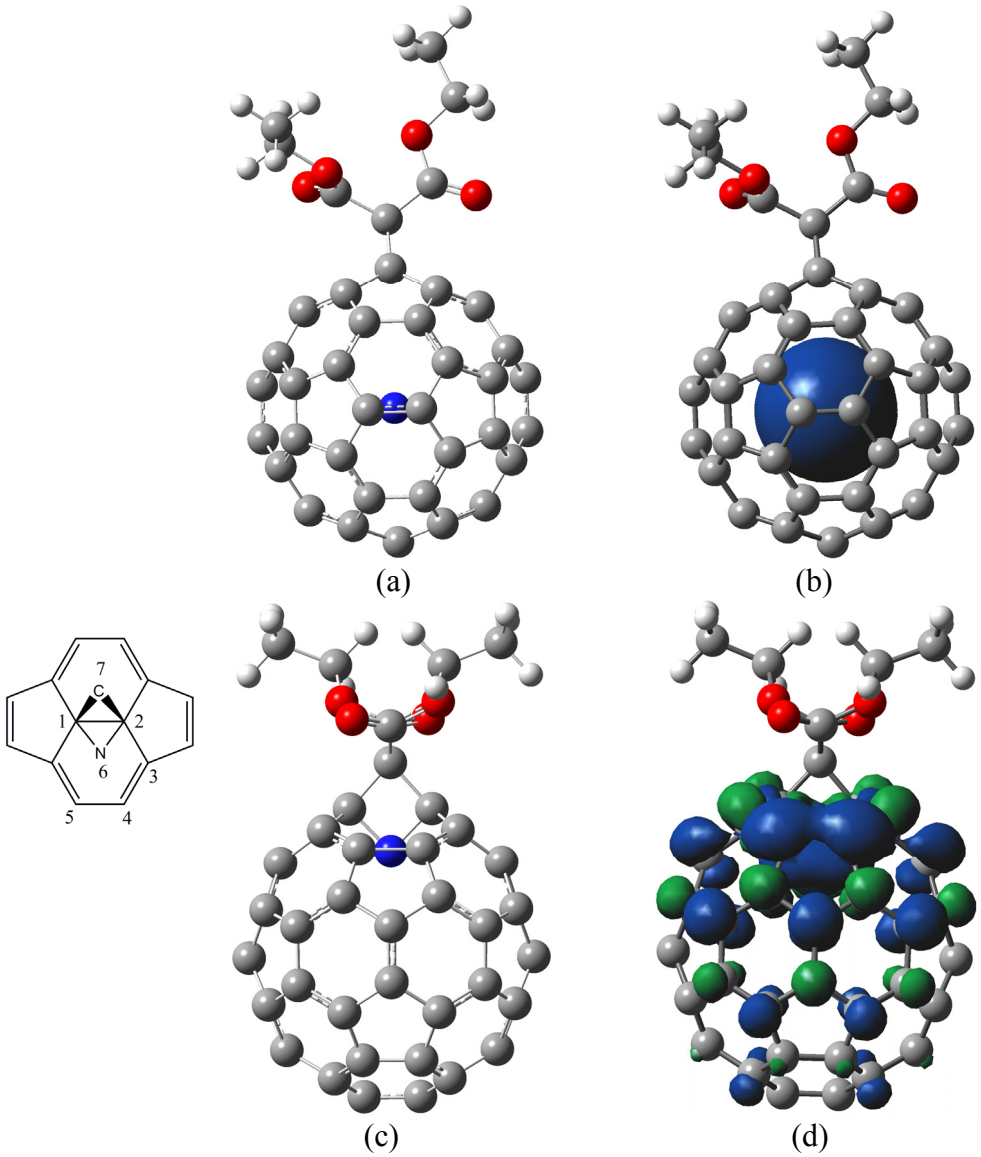

Figure 4.16: Optimized geometry and spin density distribution of the endohedral minimum state (a, b) and endohedral bonding state (c, d) of derivative **1N**.

The reaction enthalpy from the endohedral minimum state to the endohedral bonding state is 33.6 kcal/mol, which is just between that for derivative **2N** and pristine N@C_{60}. This result is consistent with the geometrical alterations in its endohedral bonding state. As shown in Table 4.6, the C1-C2 bond is completely cleaved with a distance of 2.04 Å between C1 and C2, and the C1-N6 bond is 1.47 Å. The cyclopropane ring is enlarged to incorporate the covalent bonding of nitrogen to form a 4-membered ring. The C1-C7 bond is slightly elongated and the angle 1-7-2 is significantly increased from 62.9^o to 83.1^o to match the

increased C1-C2 distance. Similar to the endohedral bonding state for both pristine N@C_{60} and derivative **2N**, a portion of the nitrogen spins is distributed over the carbon cage (Figure 4.16b). Therefore, the 3-membered cyclopropane ring weakens the C1-C2 bond and stabilizes the endohedral bonding state, but its effect is less significant than that of the pyrrolidine ring.

Table 4.6: Some of the optimized partial bond lengths (Å), bond angles (o) and dihedral angles (^{o}) of derivative **1N** and its intermediate state.

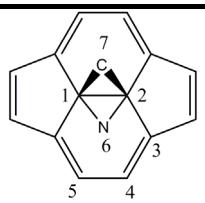

	Endohedral minimum state	Endohedral bonding state (Figure 4.17a)
1-2	1.588	2.04
2-3	1.499	1.51
3-4	1.386	1.43
4-5	1.474	1.58
1-6	3.754	1.47
1-7	1.520	1.54
1-6-2	24.42	87.65
3-2-6	71.54	91.62
1-7-2	62.91	83.21
6-1-2-4	64.84	66.21

Search for the exohedral bonding state for derivative **1N** failed to find any stable intermediate states with the flipped nitrogen atom bonding to C1 and C2. In addition, no transition state similar to that for pristine N@C_{60} and derivative **2N** were identified. Considering the restricted space and structural rigidity of the 4-membered ring, neither a straightway ejection nor swinging of the encapsulated nitrogen would take place through the

C1-C2 bond. Therefore, the endohedral bonding state in derivative **1N** either marks an end of the escape process (Figure 4.17) or would just reverse to the endohedral minimum state.

As discussed previously, derivative **1N** shows comparable photochemical stability to pristine N@C_{60} (Table 4.2), as well as slightly enhanced thermal stability. In addition, the increase of number of addends further improves the thermal stability [10]. This trend is explained well by the proposed mechanism. Firstly, inversion of the encapsulated nitrogen is restricted by the narrow and rigid 4-membered ring in the endohedral bonding state, and further blocked by the addends R due to the steric hindrance effect (Figure 4.17). The cyclopropane derivative could decay through bonds other than C1-C2 in a similar manner to pristine N@C_{60}. This explains the similar photochemical stability of derivative **1N** to pristine N@C_{60}. Secondly, the blocking of the C1-C2 bond by the cyclopropane addends reduces the chance of the fullerene cage in an attack from the encapsulated nitrogen. An increase in the number of addends would further reduce the chance and enhance the stability.

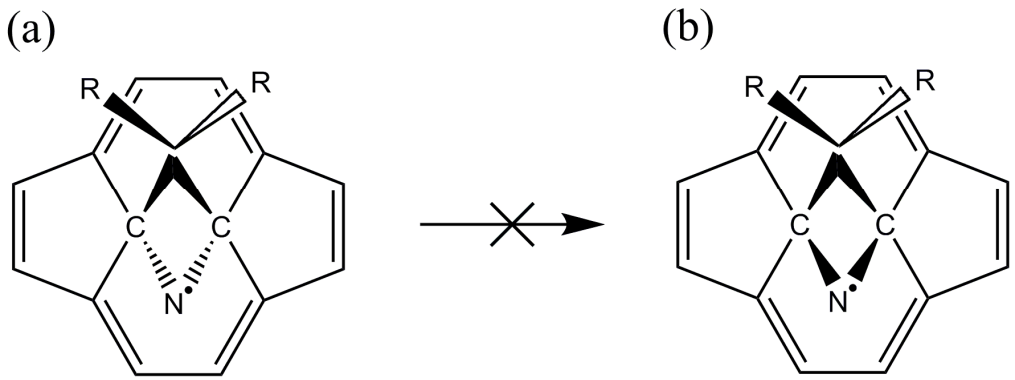

Figure 4.17: The hindered inversion of encapsulated nitrogen atom in the cyclopropane derivative of N@C_{60}. (a) Endohedral bonding state; (b) Exohedral bonding state. R=$COOC_2H_5$.

4.5 Conclusions

Photochemical stability of derivatives of N@C_{60} was investigated by ESR techniques in this chapter. All the derivatives are very stable when they are stored in dark. The pyrrolidine derivatives in a degassed solution are more sensitive to ambient light than pristine N@C_{60}.

Described by a first order decay model, the half-life time of derivative **2N** is only 280 min, in contrast to the 4077 min of pristine N@C_{60}. It is the pyrrolidine structure that determines the photochemical stability. An introduction of the pyrene chromophore to the peripheral pyrrolidine ring does not significantly change the stability of encapsulated nitrogen, although energy transfer from pyrene to C_{60} takes place efficiently in the excited state. In contrast, the cyclopropane derivative of N@C_{60} shows a comparable stability to pristine N@C_{60}. Furthermore, the presence of O_2 could effectively slow down the photo-activated decay rate of pyrrolidine derivatives of N@C_{60}.

DFT calculations were carried out to investigate the escape process in pristine N@C_{60} and its derivatives. A mechanism involving bonding of the encapsulated nitrogen atom to the two carbons bearing the addends and subsequent swinging out was proposed. The attachment of addends stabilizes the endohedral bonding state in both pyrrolidine and cyclopropane derivatives, but more effectively in the former. While the encapsulated nitrogen swings out through the window opened up by the pyrrolidine ring, it is ejected in a straight trajectory in pristine N@C_{60}. The 6-membered ring formed in the decay of pyrrolidine derivatives facilitates the inversion of the encapsulated nitrogen, which explains its lower photochemical stability. For the cyclopropane derivatives, no inversion of the encapsulated nitrogen could take place through the C1 and C2 bond restricted by the narrow and rigid 4-membered ring. The major decay route in cyclopropane derivative of N@C_{60} is similar to that for pristine N@C_{60}. Therefore, blocking of the C1-C2 bond by the cyclopropane addends may enhance the stability of the encapsulated nitrogen. The understanding on the stability of N@C_{60} derivatives is vital for any future development or applications of these endohedral fullerenes.

Chapter 5

Spin-spin interactions in N@C_{60}-porphyrin dyads

Following the study of effects of chemical functionalization on the stability of N@C_{60} in the previous chapter, the synthesis of "designer" N@C_{60} adducts is explored in this chapter. The prospect of using N@C_{60} in electron-spin based QIP has been demonstrated in the achievement of one-qubit operations and coherent quantum state transfer between electron spins and nuclear spins of ^{15}N@C_{60} [87,90]. To fulfil the scalability requirement, systems with controlled spin-spin interactions have to be constructed [35,48], and one feasible option is to synthesize dimers of endohedral fullerenes. Despite the successful synthesis of dimers in the type of N@C_{60}-C_{60} [100,103,104], no double filled dimer N@C_{60}-N@C_{60} has been reported yet. Correspondingly, no spin-spin interactions of N@C_{60} with other electron spins have been ever studied.

Meanwhile, dyads of C_{60} and porphyrin have been widely explored in the interests of photovoltaic energy conversion and molecular devices [139-143]. Because most of the

functionalization schemes of C_{60} are transferable to N@C_{60}, dyads of N@C_{60} and porphyrin could be synthesized in similar procedures. When a spin-active metalloporphyrin is incorporated in the dyad, a two-radical-centre system can be constructed. Therefore, an investigation on these N@C_{60}-porphyrin dyads would provide preliminary insights on the spin-spin interactions involving N@C_{60} before the achievement of a double filled dimer, such as ^{14}N@C_{60}-^{15}N@C_{60}.

5.1 Introduction

5.1.1 Spin-spin interactions

In the *weak coupling regime*, two types of spin-spin interactions, namely dipolar coupling and exchange coupling, are usually expected between two separated spin centres.

The exchange coupling (represented by tensor *J*) splits the singlet and triplet states of two electrons in energy. The spin Hamiltonian is described by:

$$\hat{H}_{exch} = \frac{1}{2}(\hat{S}_1^T \cdot J \cdot \hat{S}_2 + \hat{S}_2^T \cdot J^T \cdot \hat{S}_1) \tag{5.1}$$

where *J* is a 3×3 matrix taking into account the Coulombic interactions between the two unpaired electrons. When only the isotropic part is concerned, equation 5.1 becomes:

$$\hat{H}_{exch,iso} = J_0 \hat{S}_1^T \cdot \hat{S}_2 \tag{5.2}$$

where J_0 is the exchange coupling strength and is given by the exchange integral to a first approximation:

$$J_0 = \int \varphi_1(x_1)\varphi_2^*(x_1)\frac{1}{r_{12}}\varphi_2(x_2)\varphi_1^*(x_2)dV_1dV_2 \tag{5.3}$$

Because the products of different wave functions in equation 5.2 depend on the same coordinate, overlap between $\varphi_1(x)$ and $\varphi_2(x)$ is necessary to afford a significant J_0.

In contrast to the isotropic exchange coupling, the dipolar coupling depicts the anisotropic part of the spin-spin interactions. The dipolar coupling between two spin centres could be described as:

$$\hat{H}_{DD} = \frac{\mu_0}{4\pi} g_1 \cdot g_2 \cdot \beta_e^2 \left(\frac{\hat{S}_1^T \cdot \hat{S}_2}{r^3} - \frac{3(\hat{S}_1^T \cdot r)(\hat{S}_2^T \cdot r)}{r^5} \right) = \frac{\mu_0}{4\pi} g_1 \cdot g_2 \cdot \beta_e^2 \times$$

$$(\hat{S}_{1X} \quad \hat{S}_{1Y} \quad \hat{S}_{1Z}) \begin{pmatrix} r_{12}^2 - 3(x_1 - x_2)^2 & 3(x_1 - x_2)(y_1 - y_2) & 3(x_1 - x_2)(z_1 - z_2) \\ 3(y_1 - y_2)(x_1 - x_2) & r_{12}^2 - 3(y_1 - y_2)^2 & 3(y_1 - y_2)(z_1 - z_2) \\ 3(z_1 - z_2)(x_1 - x_2) & 3(z_1 - z_2)(y_1 - y_2) & r_{12}^2 - 3(z_1 - z_2)^2 \end{pmatrix} \begin{pmatrix} \hat{S}_{2X} \\ \hat{S}_{2Y} \\ \hat{S}_{2Z} \end{pmatrix} \tag{5.4}$$

The dipolar coupling matrix *D* could be diagonalized into a principal-axis matrix:

$$D_{dip} = \begin{pmatrix} D_{dip\,X} & 0 & 0 \\ 0 & D_{dip\,Y} & 0 \\ 0 & 0 & D_{dip\,Z} \end{pmatrix} \tag{5.5}$$

D_{dip} is normally traceless and effects of dipolar coupling would be therefore vanished in fast tumbling regime.

Spin-spin interactions affect significantly the features of CW ESR spectra of two separate electron spins. For a heterogeneous spin pair where one spin relaxes faster than the other one, the effect of spin-spin interaction on ESR spectra is determined by two physical factors. The first one is the spin relaxation time [165]. If the spin relaxation rates ($1/T_1$ and $1/T_2$) of the fast-relaxing spin are slower than the spin-spin interaction (in Hz), AB splitting patterns would be observed in the ESR spectra. When the relaxation rates increase and become comparable to the spin-spin interaction, broadening and even collapse of the ESR spectra are often observed [166,167]. Furthermore, when the relaxation rates gets much faster than the spin-spin interaction, average effects result in narrowing of the ESR spectra again. The second factor is the molecular correlation time [109]. While effects of the exchange coupling

survive in the fast tumbling regime, effects of the dipolar coupling would be averaged out because of motional narrowing.

5.1.2 Amplitude decrease and the Leigh model

To account for the decrease of ESR amplitude of nitroxyl radicals covalently bound to transitional metals in the rigid lattice, Leigh developed a model based on the Redfield theory [168]. When dipolar coupling is the only dominant spin-spin interaction, the linewidth could be described as:

$$\delta H = g\mu_B \tau[< H_{z'^2} > + < H_{y'^2} > / (1+\omega_0^2 \tau^2)] / \hbar \tag{5.6}$$

where g is electron g-factor of the observed spin, μ_B is Bohr magneton, τ is the correlation time, ω_0 is the resonance frequency, the $< H_{z'^2} >$ and $< H_{y'^2} >$ are the mean-square of the fluctuating field in the directions parallel and perpendicular to the laboratory components, respectively. If the correlation time (considered as the relaxation time of the transitional metal) satisfies $T_2 > \tau > \omega_0^{-1}$, the linewidth of the observed spin, or the slow-relaxing spin (nitroxyl radical), is dependent on the angle between the applied field and the vector joining the two spins:

$$\delta H = C(1-3\cos^2\theta'_R)^2 + \delta H_0, \text{ with } C = g\mu_B \mu^2 \tau / r^6 \hbar \tag{5.7}$$

μ effective magnetic moment of transition metal ion

τ metal relaxation time

r distance between the two electron spins

δH_0 half-weight linewidth of nitroxyl in the absence of paramagnetic metals.

The application of Leigh model has to satisfy three assumptions [165]. (a) The spin-spin interaction is solely due to dipolar coupling. Although the exchange coupling can be also collapsed by the rapid relaxation of paramagnetic metals, it is irrelevant to the inter-spin

distance. (b) The rigid lattice restriction is essential not only because a fixed orientation is considered, but also the fast tumbling can average out the effects of dipolar splitting. (c) The metal relaxation rate T_1^{-1} should be of the same order as the dipolar coupling.

The Leigh model successfully predicts a significant decrease in the ESR amplitude of the nitroxyl radicals, but later investigation argued that the decrease was caused by linewidth broadening because the double-integrated intensity kept almost unchanged [169].

5.1.3 Changes in relaxation time

The relaxation time of one spin may be changed by a second spin of more rapid relaxation. Such a change could be described as [166]:

$$\frac{1}{T_{1s}} = \frac{1}{T_{1s}^0} + S(S+1)\left[\frac{b^2 T_{2f}}{1+(\omega_f-\omega_s)^2} + \frac{c^2 T_{1f}}{1+\omega_s^2 T_{1f}^2} + \frac{e^2 T_{2f}}{1+(\omega_f+\omega_s)^2 T_{2f}^2}\right]$$

and

$$b^2 = \frac{8}{3}\left[-\frac{J}{2} - \frac{1}{4} g_s g_f \beta^2 \frac{(1-3\cos^2\theta)}{\hbar r^3}\right]^2$$

$$c^2 = 3 g_s^2 g_f^2 \beta^4 \frac{\sin^2\theta\cos^2\theta}{\hbar^2 r^6}$$

$$e^2 = 3 g_s^2 g_f^2 \beta^4 \frac{\sin^4\theta}{\hbar^2 r^6} \qquad (5.8)$$

where 'f' and 's' denote the spins with fast and slow relaxation, respectively. T_{1s}^0 T_{1s} are T_1 for the slow-relaxing spin in the absence and presence of the fast-relaxing spin. S is the spin number of the fast-relaxing centre, ω_f and ω_s are the corresponding resonant frequencies, J is the electron-electron exchange coupling strength, r is the inter-spin distance and θ is the angle between the vector and the applied magnetic field. This model assumes that relaxation rate of the second spin T_1^{-1} is fast relative to the magnitude of the spin-spin interaction.

For a spin-pair system with strong interaction or small $\omega_f - \omega_s$, the first term in equation 5.8 should be modified to:

$$\frac{b^2 T_{2f}}{1+(\omega_f - \omega_s)^2 T_{2f}^2 + b^2 T_{1f} T_{2f}} \tag{5.9}$$

with the limits of T_{1s} to be T_{1f}. The physical implication of this modification is that relaxation rate of the faster spin centre is the limits of spin-lattice relaxation rate of the slower spin due to the spin-spin interaction.

In this chapter, dyads of N@C_{60} with two different porphyrins were synthesized, and spin-spin interactions in these dyads were examined. Furthermore, a conversion of the two-radical-centre dyad into a single radical dyad was achieved by demetallation of the metalloporphyrin moiety.

5.2 Demetallation procedures and modelling parameters

Fullerene derivatives investigated in this chapter.

Synthesis of dyads **7** (**7N**) and **8** (**8N**) (Figure 5.1) were discussed in chapter 3.

Demetallation

Removal of the copper ion was carried out according to the acidification method [170]. Dyad **8** or **8N** (1.6×10^{-7} mol) was dissolved in 4 mL of CH_2Cl_2 under sonication. A mixture of trifluoroacetic acid and 2% sulphuric acid (1 mL/0.02 mL) was added and the mixture was stirred for about 5 min. Mixture of ice/water was added and the aqueous phase was extracted with CH_2Cl_2. The extraction was washed with saturated solution of $NaHCO_3$ and then with water to adjust the pH to nearly neutral. The organic phase was evaporated and redissolved in toluene or CS_2.

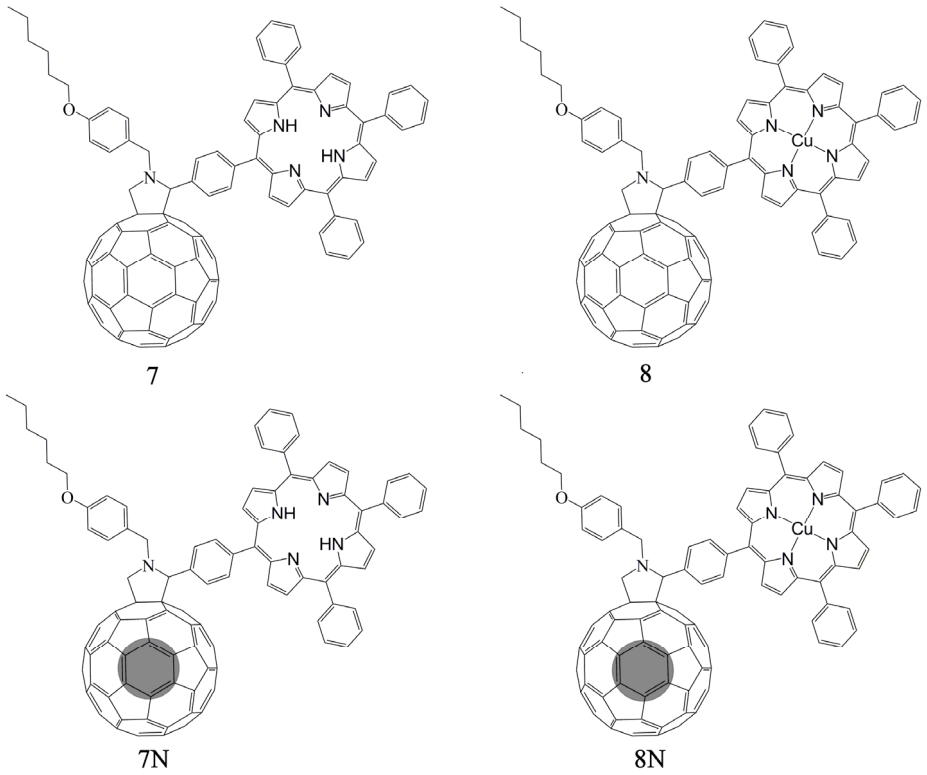

Figure 5.1: Schematic views of C_{60}-H_2TPP (**7**), C_{60}-CuTPP(**8**), N@C_{60}-CuTPP(**7N**) and N@C_{60}-CuTPP(**8N**). TPP stands for tetraphenylporphyrin.

Density functional theory calculations

Hybrid DFT calculations were carried out with the Gaussian03 programme [120] at the B3LYP level. Split-valence 6-31G basis set was used for C, H, N and O, and TZVP for the transitional metal Cu. Full geometry optimization was carried out by means of energy gradient techniques. Electron density and spin density distribution was calculated with self-consistent field (SCF) density and visualized using GaussView [156]. The electrostatic potentials are mapped with a density isosurface of 0.0004 electrons au^{-3}. All calculations were set to be in the gas phase.

5.3 Electron spin resonance of N@C_{60}-H_2TPP dyad

In the electronic ground state of most fullerene-porphyrin dyads, no significant interactions between the two moieties have been reported [139,171,172]. UV-vis absorption spectrum of

C_{60}-H_2TPP (dyad **7**) is just a combination of the constituent fullerene and H_2TPP, which confirms no significant mutual perturbation to the electronic structure of both moieties. DFT calculations also support the independence of the two moieties, with each one reserving its individual conjugation structure. As shown in Figure 5.2, the two front orbitals HOMO (highest occupied molecular orbital) and LUMO (lowest unoccupied molecular orbital) are exclusively located on the porphyrin macrocycle and the fullerene cage, respectively.

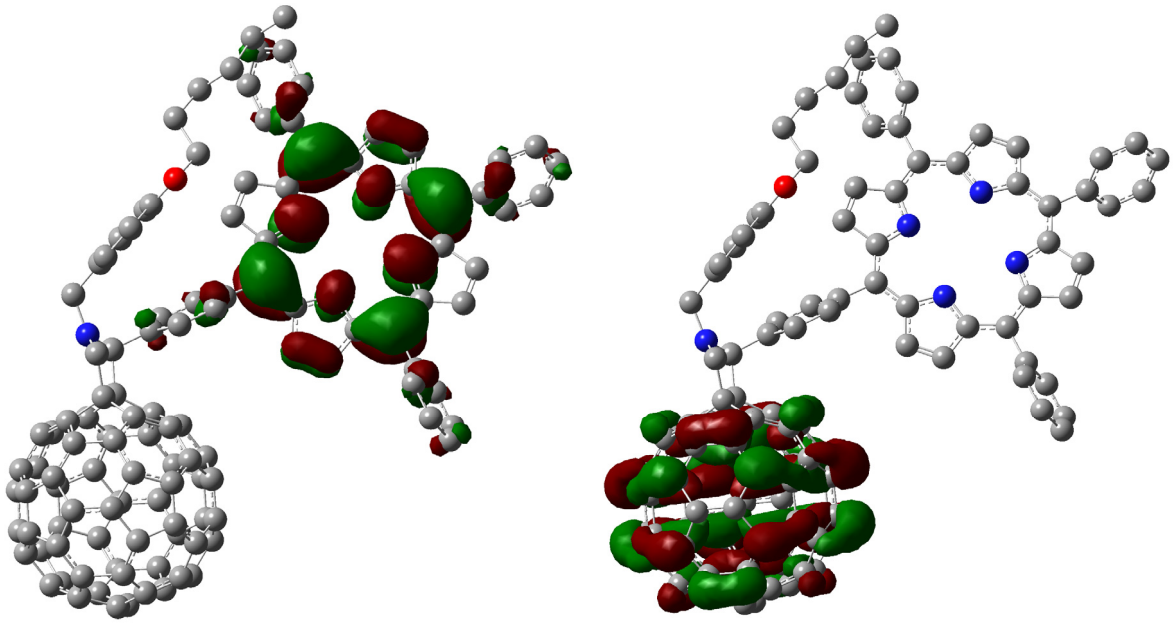

(a) (b)

Figure 5.2: Localization of the HOMO (a) and LUMO (b) orbitals of dyad **7** (hydrogen atoms are omitted). Energy level: HOMO (-4.99 eV), LUMO (-3.04 eV).

N@C_{60}-H_2TPP (dyad **7N**) exhibits similar ESR properties to other pyrrolidine derivatives of N@C_{60} [97,98]. As shown in Figure 5.3, ZFS features due to functionalization are observed in the frozen solution ESR spectrum of dyad **7N**. The consistent ZFS parameters D=16.3 MHz and E=0.4 MHz with other pyrrolidine derivatives of N@C_{60}, confirm the negligible effects of free-base porphyrin on the nitrogen spins even when they are in one molecule.

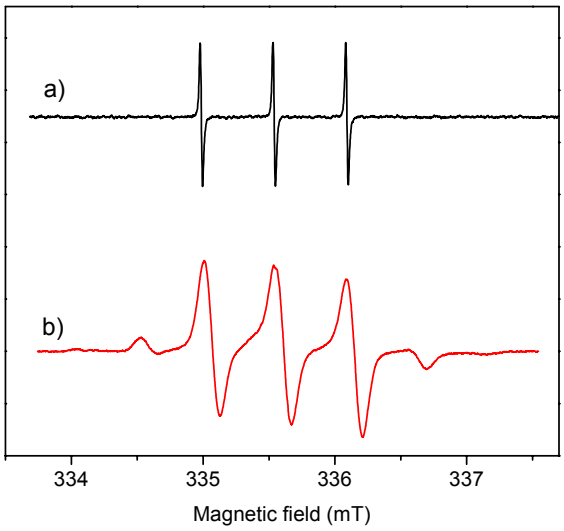

Figure 5.3: ESR spectra of dyad **7N** in toluene at room temperature (a) and 77 K (b).

5.4 Electron spin resonance of C_{60}-CuTPP dyad

The optimized geometry for C_{60}-CuTPP (dyad **8**) is similar to that for dyad **7** (Figure 5.4), where the vector joining centres of the two moieties is almost perpendicular to the normal of the porphyrin macrocycle. Similarly, no electronic interactions between the two moieties are justified based from the UV-vis absorption spectrum of dyad **8**.

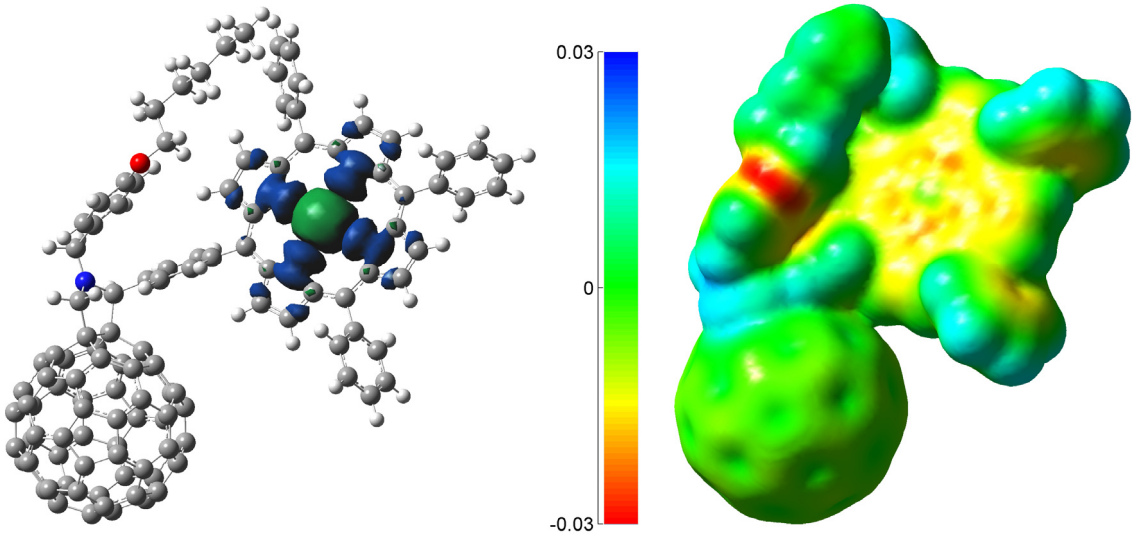

(a) (b)

Figure 5.4: Spin density distribution (a) and electrostatic potentials (b) of dyad **8**. The scale bar is in a.u..

The Cu^{2+} ion in the metalloporphyrin is spin-active because of its unpaired electron (electron configuration of d^9). In the copper (II) tetraphenylporphyrin (CuTPP), the unpaired *d* electron is coupled to four equal nitrogen atoms, and the spin system is of axial symmetry with the Hamiltonian of [173]:

$$H = \beta[g_{\parallel} H_Z S_Z - g_{\perp}(H_X S_X + H_Y S_Y)] + A_{\parallel}^{Cu} I_Z S_Z + A_{\perp}^{Cu}(I_X S_X + I_Y S_Y) + A_{\parallel}^{N} I_Z S_Z + A_{\perp}^{N}(I_X S_X + I_Y S_Y) \quad (5.10)$$

This equation is applicable to the spin system of dyad **8** as well, given the negligible interactions between the fullerene cage and the metalloporphyrin moieties (Figure 5.4a). ESR spectra of CuTPP and dyad **8** in CS_2 are shown in Figure 5.5. In the highest field component of the spectra, hyperfine splitting due to coupling with nitrogen atoms could be clearly resolved in detail. A pattern of nine lines in the ratio 1:4:10:16:19:16:10:4:1 is expected when the four nitrogen atoms are magnetically equal, which agrees well with the experimental spectra.

Simulation of both ESR spectra was performed according to equation 5.10 and the simulation parameters are listed in Table 5.1. CuTPP and dyad **8** exhibit similar *g*-factors and hyperfine interaction tensors. The different features in their ESR spectra are ascribed to the effects of molecular tumbling time, with 79 ps for CuTPP and 355 ps for dyad **8**. The attachment of a fullerene cage increases significantly the molecular size and thus the interaction with solvent molecules. Additionally, intra-molecular π-π interaction in dyad **8** may also slow down rotation of the porphyrin moiety. The phenyl group derived from the *N*-substituent of the pyrrolidine forms a stacking geometry with a phenyl group of the porphyrin moiety (Figure 5.4b), which restricts rotation of the porphyrin macrocycle.

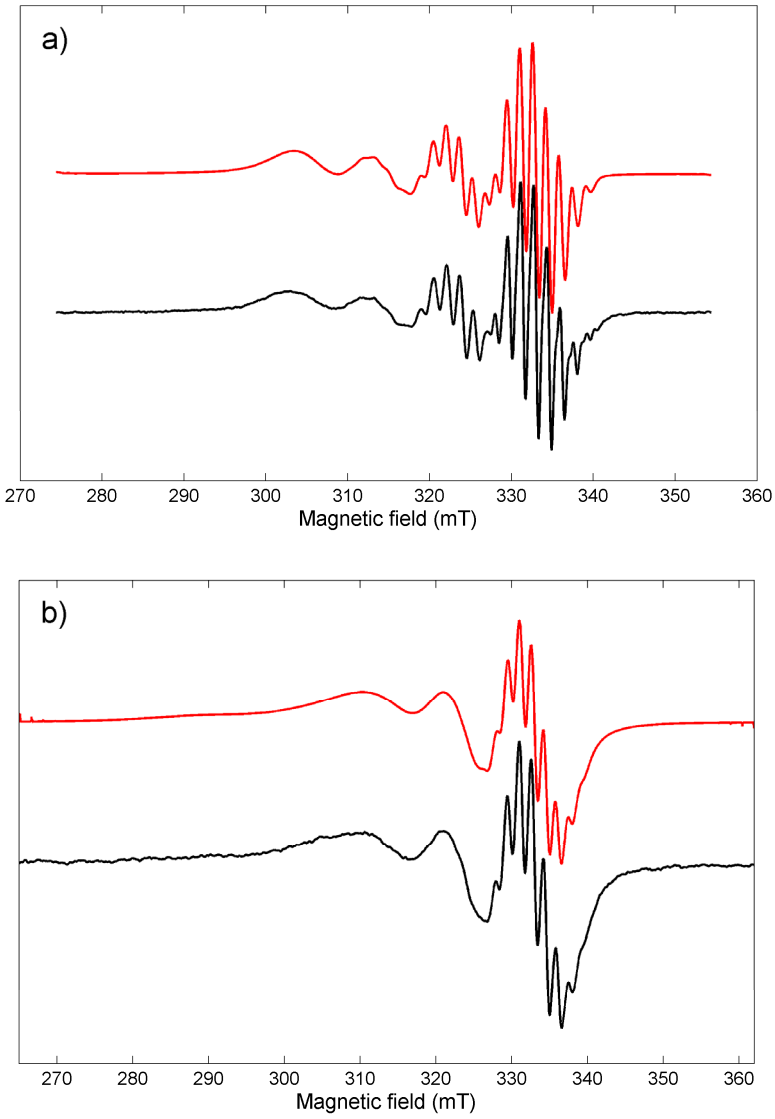

Figure 5.5: Experimental ESR spectra of CuTPP (a) and dyad **8** (b) in CS_2, and their simulation (red traces).

Table 5.1: Simulated ESR parameters for CuTPP and dyad **8**. * Hyperfine interaction tensor with nitrogen was taken from the literature, and was fixed in the simulation.

	$g_\perp, g_\parallel$	$A_\perp(^{63}Cu)$ (MHz)	$A_\parallel(^{63}Cu)$ (MHz)	$A_\perp(^{14}N)$* (MHz)	$A_\parallel(^{14}N)$* (MHz)	tumbling time (ps)
CuTPP	2.053, 2.176	-90.5	-576	43.5	49.2	79
Dyad **8**	2.053, 2.174	-90.5	-575	43.5	49.2	355

5.5 Spin-spin interactions in N@C_{60}-CuTPP

In contrast to N@C_{60}-H_2TPP (dyad **7N**), N@C_{60}-CuTPP (dyad **8N**) shows no characteristic signal of N@C_{60} in ESR spectra in either room temperature solution or frozen solution. The spectra of dyad **8N**, with features only ascribed to copper porphyrin, are the same to those of C_{60}-CuTPP (dyad **8**). The complete suppression of the spin signal of N@C_{60} indicates strong spin-spin interactions in dyad **8N**.

Based on spin counting on the dyad **7N** sample, which is synthesized from the same N@C_{60}/C_{60} mixture under the same conditions, the nitrogen filling ratio of fullerenes in the dyad **8N** sample is estimated to be 0.014%. While every N@C_{60} is bound to a porphyrin group in the same molecule, the majority of the metalloporphyrin is bound to an empty C_{60}. Therefore, effects of N@C_{60} on the metalloporphyrin could be practically neglected in the dyad **8N** sample.

In dyad **8N**, dipolar coupling should be the dominant spin-spin interaction. Exchange coupling normally requires overlap of electron density distribution, but such overlap could be excluded in dyad **8N**. Firstly, both experimental results and theoretical calculations have confirmed that approximately 98% of nitrogen spins is delocalized on the endohedral nitrogen atom in N@C_{60} [6,15]. Similarly, the copper spin is exclusively distributed on the porphyrin moiety, as revealed by the spin density distribution of dyad **8** (Figure 5.4a). Secondly, geometry of the metalloporphyrin with respect to the fullerene cage excludes possible overlap of their π orbitals. UV-vis absorption experiments on dyad **8** has already demonstrated negligible electronic interactions between the two moieties. In addition, the σ bonds that link the two moieties prevent the exchange coupling through chemical bonds. Therefore, no noticeable exchange coupling should be expected in dyad **8N**.

5.5.1 Inter-molecular or intra-molecular interactions

Both inter-molecular and intra-molecular dipolar coupling are present in the solution of dyad **8N**. The inter-molecular coupling is sensitive to sample concentrations, but the intra-molecular coupling is independent. Therefore, effects of the two types of dipolar coupling can be distinguished from concentration dependence studies of the ESR spectra.

In the mixture of N@C_{60} with CuTPP, where the inter-molecular dipolar coupling exists exclusively, an increase in sample concentration leads to both linewidth broadening and decrease of the signal amplitude (Figure 5.6a). The ESR signal of N@C_{60} disappears only in samples of very high concentrations (for instance, 4.8×10^{-3} M). The peak linewidth of N@C_{60} increases proportionally to the concentration of CuTPP, while its intensity decreases linearly (Figure 5.7a). Because the signal intensity is calculated with the double integration method, its decreasing trend is not completely justified due to the lower accuracy of dealing with peaks of lower signal/noise ratio. On the other hand, the amplitude of N@C_{60} peaks decreases exponentially with the concentration of CuTPP as shown in Figure 5.7b. Given the constant signal intensity, the signal amplitude is mainly determined by the lineshapes. Peaks with Lorentz broadening are of smaller amplitude than those with Gaussian broadening. ESR signal of pure N@C_{60} solution exhibits Gaussian broadening, and it turns into Voigtian broadening (mixed with both Gaussian and Lorentz broadening) in the mixture of N@C_{60} and CuTPP. Furthermore, the ratio of Lorentz broadening in the ESR signal of N@C_{60} increases with the CuTPP concentration.

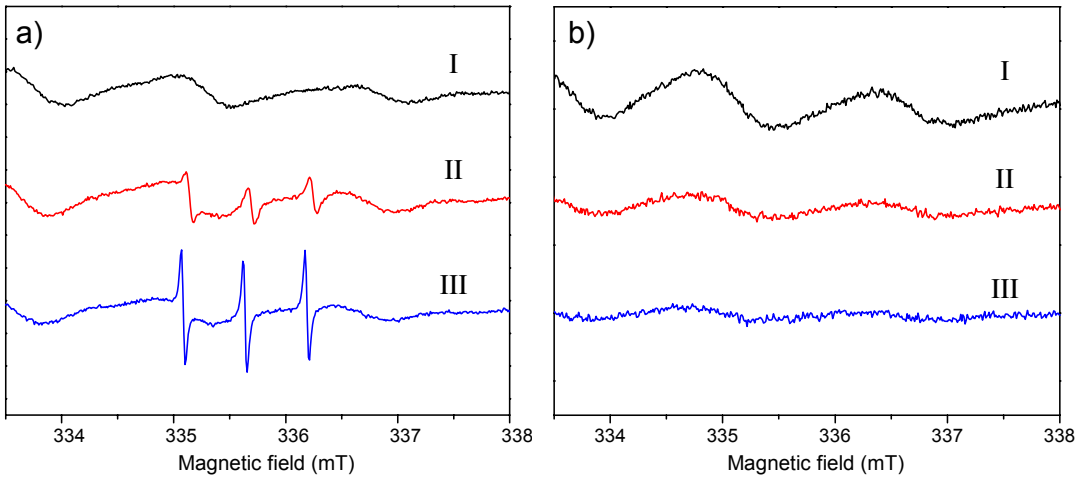

Figure 5.6: ESR spectra of a mixture of N@C_{60}/CuTPP (molar ratio 1:1) (a) and the dyad **8N** sample (b), at (I) 4.1 $\times 10^{-3}$ M, (II) 1.6 $\times 10^{-3}$ M and (III) 8.0 $\times 10^{-4}$ M. Measurements were taken at room temperature and the parameters are set to best demonstrate the signal of N@C_{60}.

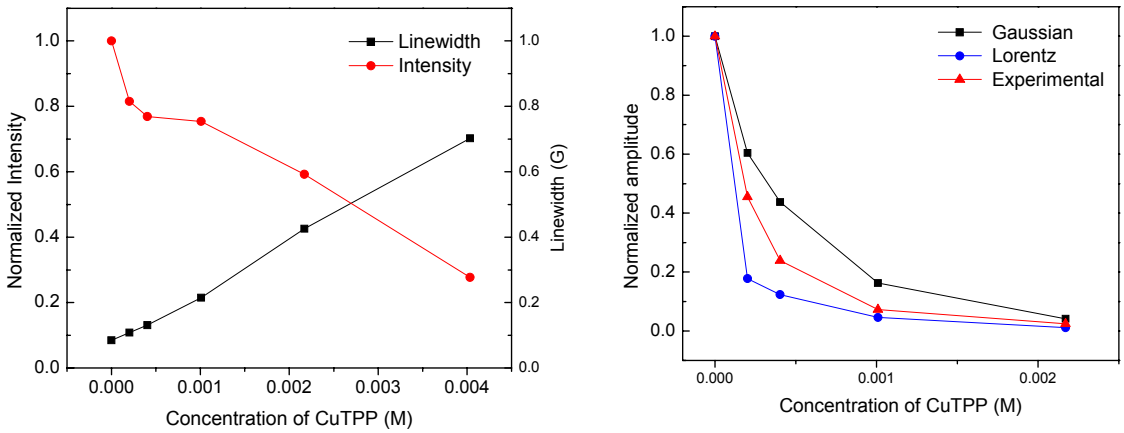

Figure 5.7: (a) Intensity and linewidth (peak to peak) of N@C_{60} mixed with CuTPP in CS_2. (b) Amplitude change and its comparison with the calculated results based on Gaussian and Lorenz broadening. Measurements were taken at room temperature (295K). Concentration of N@C_{60} and the whole volume (0.1 mL) were fixed, and the concentration of CuTPP varied as shown.

In contrast to the N@C_{60}/CuTPP mixture, no ESR signal of N@C_{60} was observed in the dyad **8N** sample at all experimental concentrations (Figure 5.6b). Because the inter-molecular dipolar coupling becomes weak when the sample concentration is low (for instance, 8.0×10^{-4} M), the intra-molecular dipolar coupling plays a dominant role in suppression of the ESR signal of N@C_{60} in dyad **8N**.

To calculate the dipolar coupling matrix, an inter-spin distance of 1.26 nm is identified from the optimized geometry of dyad **8N** (Figure 5.8). D_{dip} was then calculated according to equation 5.4 by taking g = 2.0030 for the nitrogen spins [80] and g = 2.053 for the copper spin:

$$D_{dip} = \begin{pmatrix} 27.0 & 0 & 0 \\ 0 & 27.0 & 0 \\ 0 & 0 & -54.0 \end{pmatrix} \text{(in MHz)}$$

The g = 2.053 is taken from $g_{\perp}$ of the copper spin, and $g_{\parallel}$ was excluded because it is almost perpendicular to the joining vector (Figure 5.8).

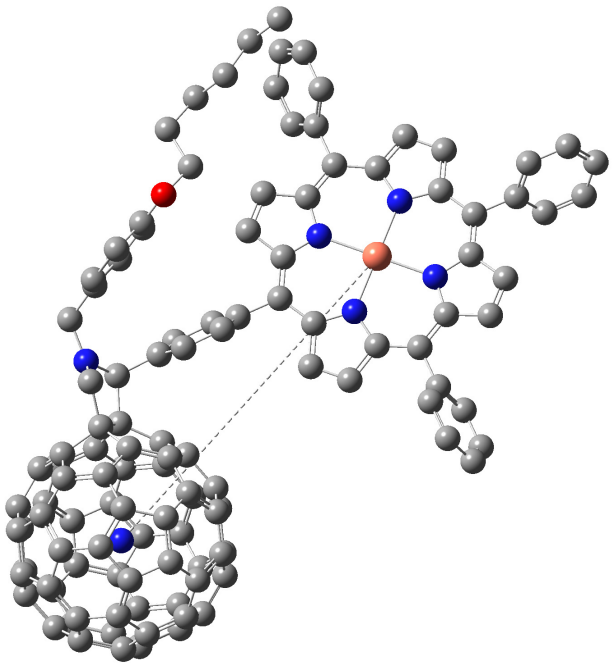

Figure 5.8: Optimized geometry of dyad **8N**. The dashed line denotes the vector joining the centre of copper ion and the endohedral nitrogen, with the length of 1.26 nm.

5.5.2 Reasons for the suppression of N@C_{60} ESR signal

Despite the argument of linewidth broadening [169], the Leigh model would be helpful to analyze suppression of N@C_{60} signal in the dyad **8N** sample from the perspective of amplitude decrease and lineshapes.

The three assumptions to satisfy the model are carefully examined in the dyad **8N**. Firstly, the dominant interaction between N@C_{60} and CuTPP in the dyad is dipolar coupling. Secondly, the rigid lattice condition needs fundamental analysis. Both the porphyrin and the pyrrolidine ring in dyad **8N** are relatively rigid groups. The copper ion stays in the symmetry centre of the porphyrin macrocycle, whose rotation would scarcely change its distance to the fullerene centre. Therefore, the joining vector is almost constant in spite of molecular vibration in solution. In addition, rotation of dyad **8N** in solution should fall within the intermediate tumbling range based on the tumbling time of 355 ps (tumbling rate of 2.8×10^9 Hz) for its counterpart dyad **8**. The relaxation time T_1 of copper ion ranges from 1000 to 3000 ps at room temperature solution [109], which is just slightly longer than the molecular tumbling time. Effects of dipolar coupling would only be partially reduced in this intermediate range. To incorporate the motional narrowing effects, the tumbling time instead of the relaxation time of copper ion was used as correlation time in the Leigh model. Consequently, similar to the Redfield theory, the C in equation 5.7 that determines the significance of the Leigh model would rely on the tumbling time as well. Such consideration for correlation time is justified in dyad **8N** because the prerequisite $\tau > \omega_0^{-1}$ is still satisfied in the X band ESR spectroscopy where the resonant microwave frequency is about 9.5 GHz. Thirdly, both relaxation rate of the copper (10^9 Hz) and the molecular tumbling rate (2.8×10^9 Hz) are faster than the dipolar coupling strength (2.7×10^7 Hz).

According to equation 5.7, the amplitude decrease is actually determined by the ratio $C/\delta H_0$ rather than the C alone. A spin system with smaller δH_0 (the intrinsic linewidth in the absence of a second spin) would be affected more significantly by a fast relaxing spin. The normalized amplitude of N@C_{60} as a function of $C/\delta H_0$ is plotted in Figure 5.9a. When the $C/\delta H_0$ ratio becomes larger than 0.1, the amplitude starts to decrease significantly.

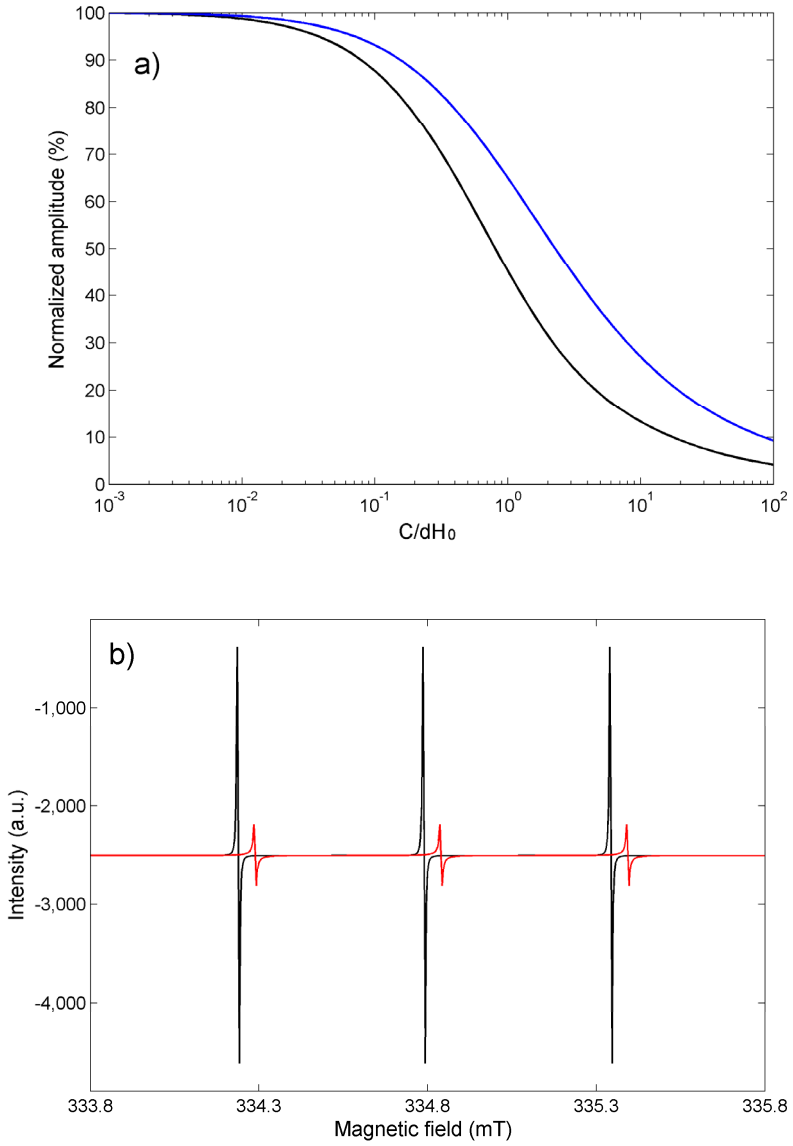

Figure 5.9: (a) Normalized amplitude of N@C_{60} as a function of $C/\delta H_0$. Blue trace: absorption amplitude; black trace: first derivative amplitude. (b) ESR spectra of N@C_{60} with $C/\delta H_0$ =0 (black trace), and $C/\delta H_0$ =15.7 (red trace).

To calculate the C for dyad **8N**, g = 2.0030 and g = 2.053 were used for the nitrogen spin and copper spin, respectively, similar to the calculation of the dipolar coupling matrix. The effective magnetic moment μ is the sum of the total spin magnetic moment and the orbital angular moment for transition metals. For dyad **8N**, μ of the copper ion is conservatively taken as 1.73 μ_B, the value of the total spin magnetic moment exclusive of the orbital angular moment. The intrinsic linewidth δH_0 was estimated from the decoherence time T_2 of the

pyrrolidine derivatives of N@C_{60}. Again, a conservative T_2 = 6.6 μs was used and the linewidth δH_0 was estimated to be 0.027 G (half of $1/T_2$) [104]. Therefore, the C is 0.425, and the ratio $C/\delta H_0$ is 15.7. Accordingly, the amplitude is reduced to be as less as 10.4% of the original signal intensity (Figure 5.9b).

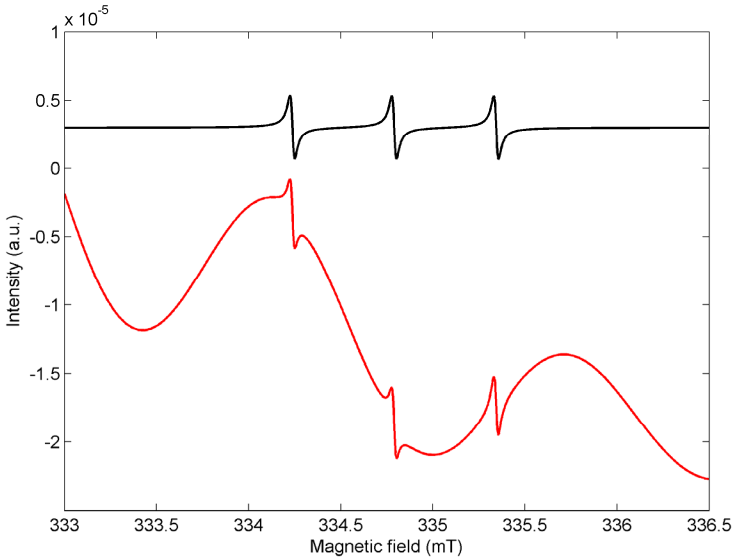

Figure 5.10: Simulated ESR spectrum of the dyad **8N** sample with $C/\delta H_0$ =15.7, linewidth of 0.1 G (peak to peak), a purity of 0.014% (red trace), and the N@C_{60} signal alone (black trace).

In addition to effects of the Leigh model, two other factors also contribute to the amplitude decrease of N@C_{60} signal in the dyad **8N** sample. Firstly, inter-molecular dipolar coupling broadens the linewidth and results in decrease of the amplitude. This broadening effect should affect the dyad **8N** sample in a similar manner to the N@C_{60}/CuTPP mixture. Linewidth of 0.1 G (peak to peak) was therefore assumed for the dyad **8N** sample at the concentration of 8×10^{-4} M according to Figure 5.7a. Secondly, the low nitrogen-filling ratio (approximately 0.014%) in the dyad **8N** sample lowers significantly the signal ratio of N@C_{60} to CuTPP. Based on all these considerations, the simulated ESR spectrum of dyad **8N** shows the relative amplitude of N@C_{60} with respect to CuTPP (Figure 5.10). The amplitude of N@C_{60} signal is much smaller than that of the CuTPP signal.

Furthermore, some realistic factors that are difficult to evaluate may cause additional broadening of the N@C_{60} peaks. For instance, the inter-spin distance is not ideally constant as assumed in the Leigh model, and anisotropy of the *g*-factor of copper ion may not be omitted. Beyond these theoretical considerations, experimental factors should be also taken into account to understand the complete suppression of the ESR signal of N@C_{60} in the dyad **8N** sample. In practice, the signal could hardly be resolved when its amplitude becomes very small. Any attempt to optimize the amplitude of N@C_{60} signal, such as increases in microwave power and modulation, may just result in a more significant increase of the CuTPP signal.

5.6 Demetallation of N@C_{60}-CuTPP

Because N@C_{60} and its derivatives can lose their electron spins due to heating or light excitation [96,126], disappearance of the ESR signal of N@C_{60} in the dyad **8N** sample could be caused by complete decomposition of N@C_{60}. Therefore, it is essential to demonstrate the existence of N@C_{60} dyads in the dyad **8N** sample. An immediate solution is to convert the metalloporphyrin into free base porphyrin by acidification [170]. If suppression of the N@C_{60} signal is caused by dipolar coupling, removal of the copper ion would definitely recover the N@C_{60} signal. In other words, dyad **8N** would be converted into dyad **7N**, from which the ESR signal of N@C_{60} could be determined.

The demetallation process was monitored by UV-vis spectroscopy. Both Copper(II) porphyrin and free base porphyrin exhibit characteristic absorptions with high extinction coefficient. As shown in Figure 5.11a, after the demetallation absorption peaks ascribed to copper (II) porphyrin disappear and peaks ascribed to free-base porphyrin emerge, which are the same to those of dyad **7N**. As expected, ESR signal of N@C_{60} was successfully recovered. The recovered N@C_{60} signal is approximately 82% of that of the dyad **7N** sample

(with the same concentration) synthesized directly from the Prato reaction. Given the possible decomposition of N@C_{60} during the acidification, nitrogen filling ratio of fullerenes in the dyad **8N** sample should be similar to that in the dyad **7N** sample (approximately 0.014%).

The recovery of N@C_{60} signal proved the presence of N@C_{60}-CuTPP in the dyad **8N** sample, which further confirms the role of dipolar coupling in suppression of N@C_{60} signal. Additionally, the similar nitrogen filling ratios in both the dyad **8N** and dyad **7N** samples exclude any effects of the CuTPP on the stability of N@C_{60} during the Prato reaction.

The demetallation, which provide a strategy to change a two-radical-centre system (dyad **8N**) into a single-radical system (dyad **7N**), may find its applications in molecular devices or electron-spin based QIP.

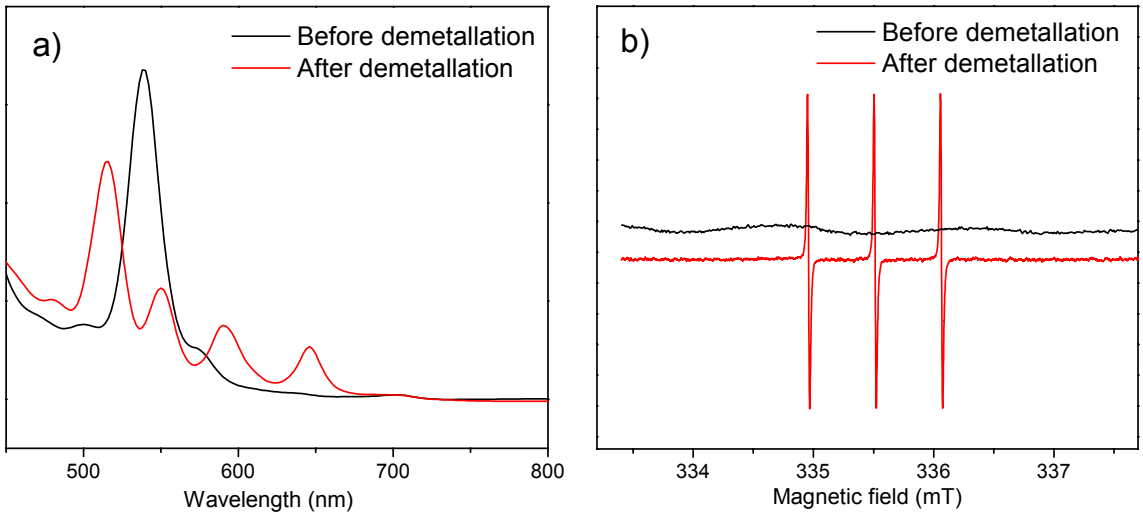

Figure 5.11: UV-vis absorption (a) and ESR spectrum (b) of dyad **8N** before and after demetallation.

5.7 Conclusions

Two dyads of endohedral fullerene N@C_{60} and porphyrin were synthesized. The free base porphyrin shows negligible effects on N@C_{60} in dyad **7N** and typical ZFS features due to functionalization were observed in the ESR spectrum measured in frozen solution. The

copper porphyrin suppressed the ESR signal of N@C_{60} in the dyad **8N** sample over a wide range of concentrations, which suggests the intra-molecular dipolar coupling between the two spin-active moieties.

The inter-spin distance between the copper ion and the encapsulated nitrogen is 1.26 nm, and the dipolar coupling strength was calculated to be 27.0 MHz. The Leigh model predicts 90% decrease of the signal amplitude, which in combination with broadening effects due to inter-molecular dipolar coupling and the low nitrogen filling ratio, explains the suppression of ESR signal of N@C_{60} in the dyad **8N** sample. In addition, effect of spin-spin interactions in suppression of ESR signal of N@C_{60} is also supported by removal of copper ion from the porphyrin moiety, with approximately 82% of the ESR signal of N@C_{60} recovered after the demetallation.

Chapter 6

Alignment of N@C_{60} derivatives in a nematic phase matrix

Intra-molecular spin-spin interactions in N@C_{60}-porphyrin dyads have been studied in the previous chapter. Two-qubit quantum gates (for instance, the controlled-NOT operation), usually require control of such interactions. According to Harneit's proposal [35], dipolar coupling is the main spin-spin interaction to be utilized for a quantum computer based on endohedral fullerenes. Anisotropy of the dipolar coupling provides the feasible means to adjust the coupling strength by controlling molecular orientations with respect to the magnetic field. Therefore, it is important to devise systems with ordered structure of fullerenes and their derivatives [48]. Herein, the nematic phase liquid crystal matrix is explored to align N@C_{60} derivatives.

6.1 Introduction

6.1.1 Alignment of endohedral nitrogen (and phosphorus) fullerenes

To date alignment of endohedral fullerenes has been achieved in anisotropic matrices including liquid crystals [174,175], single crystals [176,177] and carbon nanotubes [178-180].

The first successful example is the dispersion of N@C_{70} in a nematic phase liquid crystal *N*-(4-Methoxybenzylidene)-4-butylaniline (MBBA). The endohedral fullerene was dissolved in MBBA at room temperature using an ultrasonic bath. Alignment of the liquid crystal molecules in an external magnetic field resulted in the axial orientation of N@C_{70} molecules as revealed in ESR spectra [175].

Furthermore, co-crystallization was employed to realize an ordered arrangement of endohedral fullerenes in single crystal matrix [176]. Two crystal structures were obtained when a toluene solution of mixture of N@C_{60} and 2,4,6-tris-(4-bromophenoxy)-1,3,5-triazine (BrPOT) was slowly cooled down from 100 °C to room temperature. Although the fullerenes are only partially ordered in the hexagonal structure, they are fully ordered in the rhombohedral structure. As revealed by single crystal XRD measurements, the fullerenes are located on a centre of symmetry forming a slightly distorted cubic closed packed structure (the Wykoff position 6a, 0 0 z). Each fullerene sits in an individual pocket formed by BrPOT molecules (Figure 6.1). Similar crystal structure of P@C_{60} in BrPOT was also obtained through the same method.

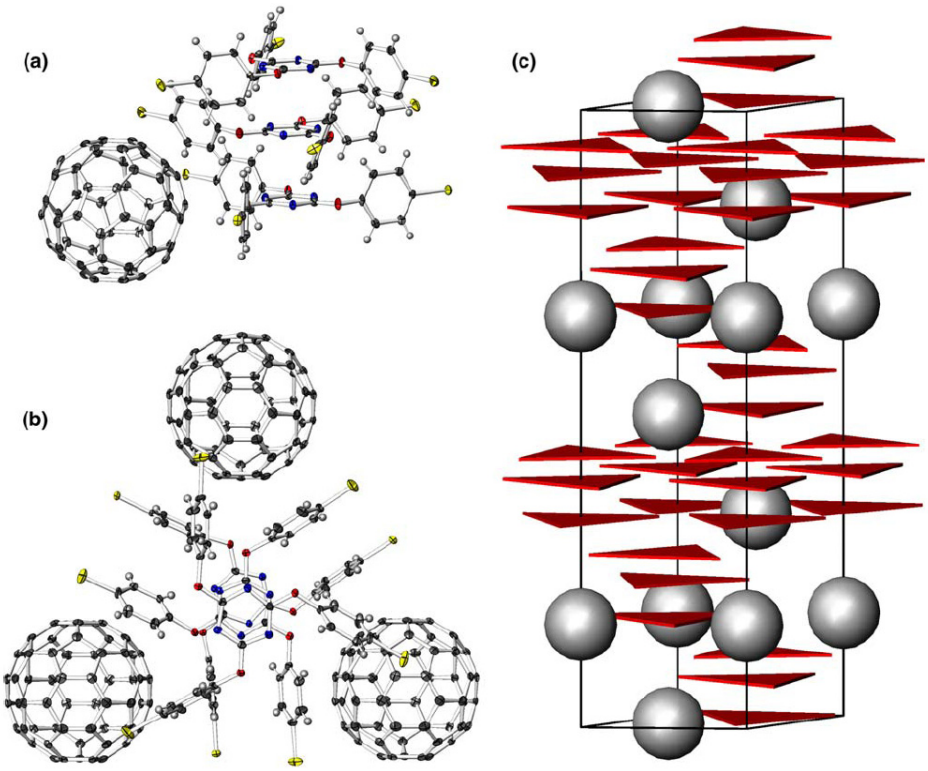

Figure 6.1: Views of the rhombohedral structure of BrPOT(C_{60}): (a) Side view of the essential building block; (b) Top view of this building block, including neighbouringC_{60} molecules; (c) Unit cell including BrPOT molecules (red triangles) of adjacent cells. Reprinted from [176].

In addition, confinement in carbon nanotubes offers another option to realize a one-dimensional array of fullerenes. The so-called *peapod* was prepared mainly through two routes. One is the vapour-filling method [180], where the fullerenes and single-walled nanotubes (SWNTs) were heated in a quartz ampoule in very high vacuum at 650 °C. The other route is the solvent-filling method [179,180], where a suspension of the fullerenes and SWNTs in hexane was sonicated and refluxed later for about 2 h. In both methods, the non-encapsulated fullerenes were removed by either sonication in toluene or dynamic vacuum treatment at 700 °C.

6.1.2 Characterization of orientations

Because all the endohedral fullerenes incorporating group-V elements are spin-active, ESR spectroscopy is a powerful technique to investigate their alignments. In previous studies

[174,175], ZFS effects were used to study the alignment of these endohedral fullerenes. Take N@C_{70} as an example, its spin Hamiltonian in high field approximation is:

$$\hat{H} = \omega_e S_z - \omega_I I_z + \hat{S} \cdot \mathbf{A} \cdot \hat{I} + \hat{S} \cdot \mathbf{D} \cdot \hat{S} \tag{6.1}$$

where **A** is the nuclear hyperfine interaction tensor and **D** is the ZFS tensor. In a high external magnetic field where the Zeeman splitting is larger than the hyperfine splitting, ZFS parameter E is negligible in axial molecules such as N@C_{70}, and the effective ZFS parameter D observed in the ESR spectrum could be represented as:

$$D_{eff} = D \cdot O_{ZZ}, \quad O_{ZZ} = (3 \cdot \overline{\cos^2 \theta} - 1)/2 \tag{6.2}$$

where O_{ZZ} is the ordering parameter that defines the orientational order of the axis Z in the liquid crystal, θ is the angle between Z and the applied magnetic field (the over bar means an average over all the molecules). When N@C_{70} is dispersed in MBBA, the non-vanishing D_{eff} results in nine sharp transitions in the ESR spectrum (Figure 6.2). According to equation 6.2, the ordering parameter O_{ZZ} was calculated to be 0.18(3) [174].

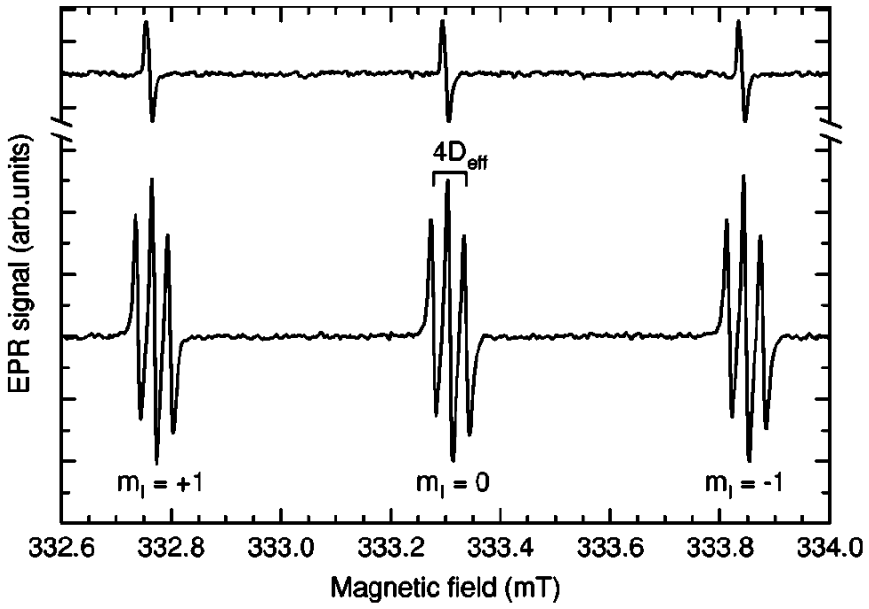

Figure 6.2: ESR spectrum of N@C_{70} in toluene solution (upper graph) and liquid crystal MBBA (lower graph) at 299K. Reprinted from [175].

In the co-crystal structure of N@C_{60} or P@C_{60} in BrPOT, large ZFS parameter of the endohedral fullerene was observed due to the strong non-covalent host-guest interaction [176]. The angular dependence of D_{eff} deduced from the line positions agrees well with equation 6.2 (Figure 6.3).

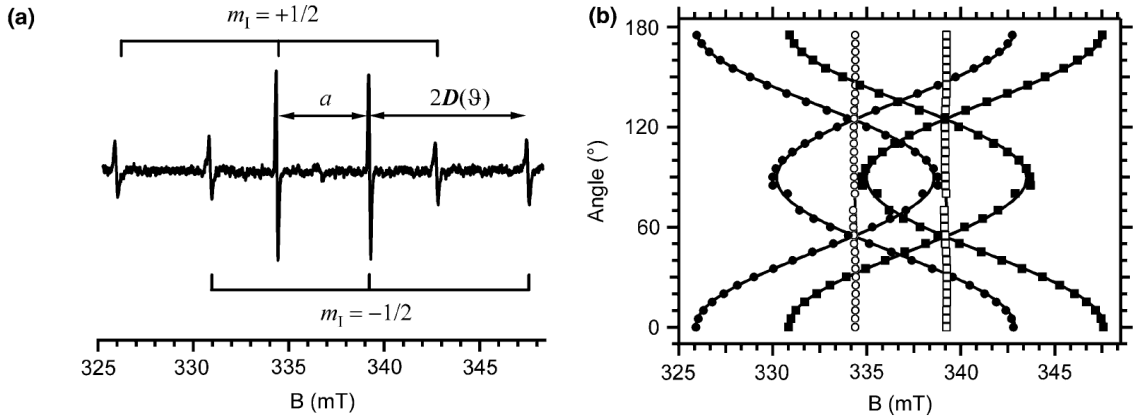

Figure 6.3: (a) ESR spectrum of rhombohedral co-crystal BrPOT(P@C_{60}) at the angle of 0°, corresponding to the maximum D_{eff} (see to equation 6.2). (b) Angular dependence of ESR line positions. Symbols: m_I =+1/2 (circles) and m_I=-1/2 (squares). Open and closed symbols denote m_S = (1/2,-1/2) and (±1/2, ±3/2) transitions, respectively. Reprinted from [176].

6.1.3 Evaluation of alignment methods

The co-crystal method is remarkably effective as N@C_{60} and P@C_{60} were fully ordered in the single crystal matrix. However, this method cannot fulfil the scalability requirement of QIP applications. As a prerequisite to control the spin-spin interactions, covalently linked fullerene dimers have to be co-crystallized with the matrix. Huge experimental challenges are then trigged by the introduction of extra chemical groups to the fullerene cage. The lowered symmetry of functionalized fullerene, especially fullerene dimers, would affect significantly the crystallization process and prohibit obtaining high quality crystals.

In terms of the confinement in nanotubes, it is not conclusively convincing that N@C_{60} retains its properties once been inserted into the nanotubes, although the *peapod* structure was confirmed by electron microscopy. The low ratio of N@C_{60} in C_{60} (usually less than 1%,

and it may be further lowered by the high temperature treatment in vapour-filling) cannot guarantee satisfactory presence of N@C_{60} in the *peapod*. In addition, a complete removal of non-encapsulated N@C_{60} from the *peapod* is challenging, which weakens reliability of the ESR spectra currently ascribed to N@C_{60} in nanotubes [179].

Compared with the other two methods, liquid crystals in their nematic phase provide readily accessible one-dimensional environment [181-183]. In the nematic phase, the molecules self-align to parallel roughly their long axes, and can be then easily aligned by an external magnetic or electric field. For MBBA, the nematic phase lies in the temperature range from 293 K to 321 K, within which the molecules have long-range directional order along the applied field. Such ambient conditions are crucial for N@C_{60} derivatives to minimize their thermal or photo-induced decomposition. Although alignment of N@C_{60} in MBBA is not pronounced [175], N@C_{60} derivatives are likely to be aligned well due to their lowered molecular symmetry. ZFS parameter D of N@C_{60} derivatives ranges from 6 to 16.5 MHz [95,97,98]. According to equation 6.2, larger parameter D (compared to 2.34 MHz for N@C_{70} [174]) indicates principally more significant effects of molecular orientations on the ESR spectra.

6.1.4 Traditional spin probes

The use of ZFS tensors to investigate the orientations of fullerenes is advantageous for *in situ* investigation with no extra labels required. However, because no alignment of N@C_{60} derivatives has been reported up to date, the traditional spin probes would be useful to confirm the orientations of fullerene derivatives in MBBA. Recently a nitroxide radical was functionalized to C_{60} to probe their orientations in nanotube [184]. Both orientation and rotational dynamics of the fullerenes could be readily revealed by analysis of the ESR spectra.

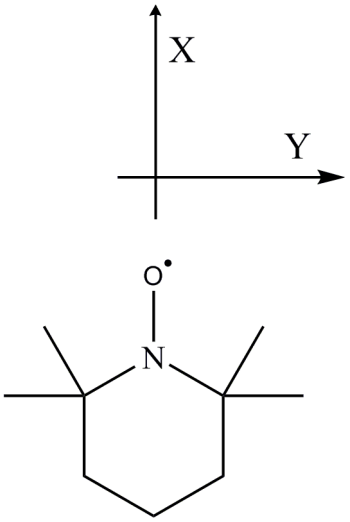

Figure 6.4: Schematic representation of 2,2,6,6-tetramethyl-1-piperidinyloxy (TEMPO).

Nitroxide radicals have been traditionally used as spin labels to probe molecular alignment due to their anisotropic *g*-factor and hyperfine interaction tensor **A** [185,186]. In the high field approximation the spin Hamiltonian for the free radical TEMPO (Figure 6.4, axis *X* is defined along the *N-O* bond) is:

$$\hat{H} = \beta_e B_0 g_{ZZ} S_Z + A_{ZZ} I_Z S_Z + [\beta_e B_0 (g_{ZX} S_X + g_{ZY} S_Y) + I_Z (A_{ZX} S_X + A_{ZY} S_Y)] \tag{6.3}$$

In the one-dimensional environment, such as nematic phase liquid crystal, where the molecules rotate around the axis *Z* at a rate faster than the spin precession frequency, the time average of equation 6.3 is:

$$\hat{H} = \beta_e B_0 (g + \Delta g) S_Z + (A + \Delta A) I_Z S_Z$$

$$g = \frac{1}{3}(g_{XX} + g_{YY} + g_{ZZ}),\ A = \frac{1}{3}(A_{XX} + A_{YY} + A_{ZZ})$$

$$\Delta g = \frac{2}{3}(O_{XX} g_{XX} + O_{YY} g_{YY} + O_{ZZ} g_{ZZ}),\ \ \Delta A = \frac{2}{3}(O_{XX} A_{XX} + O_{YY} A_{YY} + O_{ZZ} A_{ZZ}) \tag{6.4}$$

where $O_{ii}(i = X, Y, Z)$ is the ordering parameter defined as $O_{ii} = [3 \cdot \overline{\cos^2 \theta(Z,i)} - 1]/2$, with $\theta(Z,i)$ being the angle between the applied magnetic field and the principal axis *i* of TEMPO. When $A_{XX} = A_{YY} = 6$ G, $A_{ZZ} = 18$ G, $g_{xx} = 2.0089$, $g_{YY} = 2.0061$ and $g_{ZZ} = 2.0027$ are applied:

$$\Delta g = \frac{2}{3}(g_{XX} - g_{YY} - g_{ZZ})O_{XX} + \frac{1}{3}(g_{ZZ} - g_{YY})(O_{ZZ} - O_{YY}) = 0.0030 \cdot O_{XX} - 0.0011(O_{ZZ} - O_{YY})$$

$$\Delta A = \frac{2}{3}(A_{ZZ} - A_{XX})O_{ZZ} \approx 17.3 \cdot O_{ZZ} \tag{6.5}$$

If the axis *Y* and *Z* are assumed to have equal probabilities of being perpendicular to the magnetic field B_0 ($O_{YY} = O_{ZZ} = -\frac{1}{2}O_{XX}$), equation 6.4 and 6.5 could be further transformed into [185]:

$$\Delta A = -8.6 \times O_{XX}, \ \Delta g = 0.0030 \times O_{XX} \tag{6.6}$$

Because the deviation of *A* and *g* could be deduced from the ESR spectra, the ordering parameter O_{XX} is readily available according to equation 6.6.

In this chapter, the nitroxide radical TEMPO was attached to C_{60} (derivative **9** in Figure 6.5) and alignment of the resultant derivative in MBBA was firstly examined. Based on the clear experimental results that functionalized fullerenes could be aligned by liquid crystal, a series of synthesized *N*-substituted pyrrolidine derivatives of N@C_{60} (**2N** and **4N**-**6N** in Figure 6.5) were then dispersed in MBBA and their orientations were studied via the ZFS effects.

6.2 Dispersion procedures and modelling parameters

Spin-active fullerene derivatives investigated in this chapter

Synthesis and characterization of fullerene derivatives **2N** and **4N-6N** (in Figure 6.5) were described in chapter 3. Derivative **9** was provided by Dr. Maria del Carmen Gimenez-Lopez in University of Nottingham.

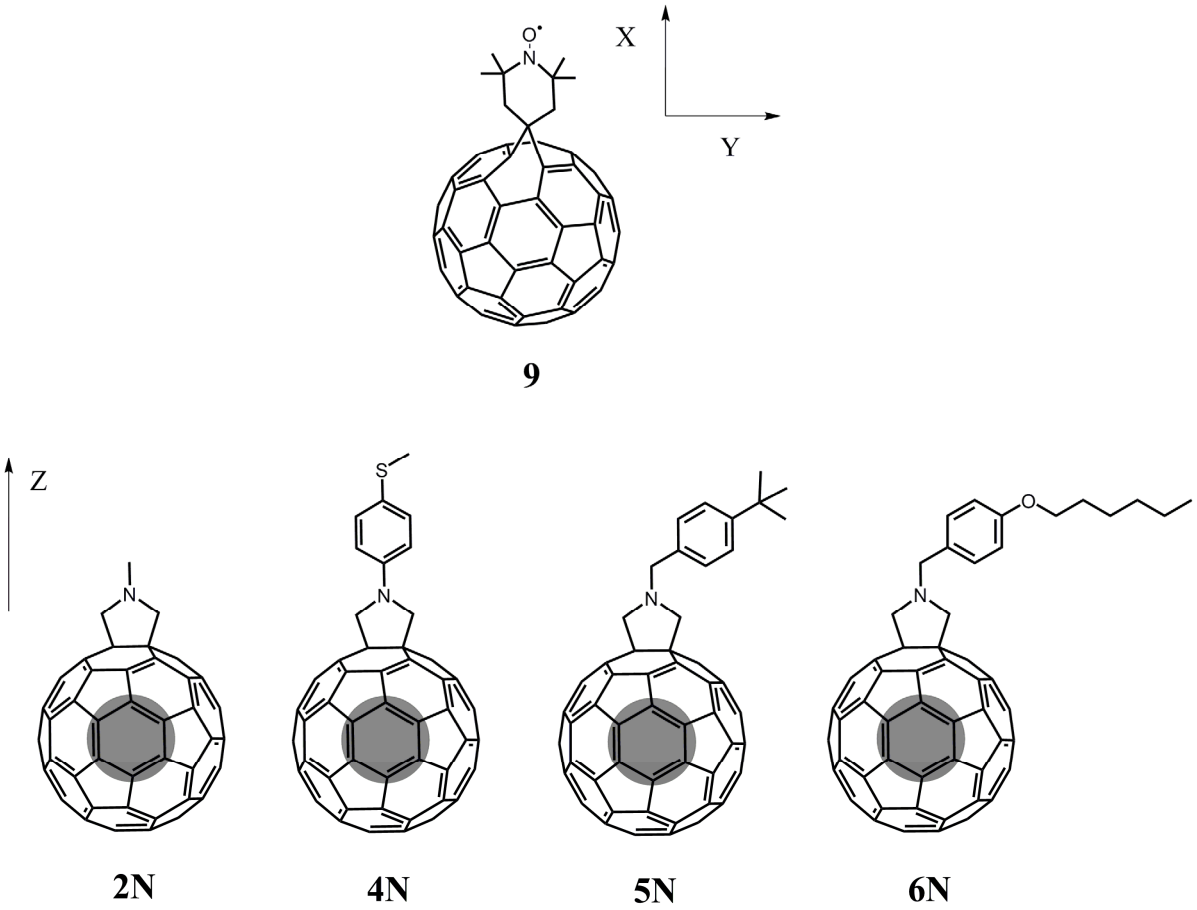

9 **2N** **4N** **5N** **6N**

Figure 6.5: Schematic representation of C_{60}(TEMPO) (**9**) and four pyrrolidine derivatives of N@C_{60}.

Dispersion of fullerene derivatives in MBBA

A solution of C_{60}(TEMPO) (**9**) or N@C_{60} derivatives (approximately 10^{-4} mmol) in toluene (0.1 mL) was evaporated to dry in a standard ESR tube under high vacuum. MBBA (0.1 mL) was then added to the powder and the tube was placed in an ultrasonic bath for 1 h at 325 K

until the sample became homogenous (temperature range for the nematic phase of MBBA is 293-321 K). After cooling down to room temperature (295 K), the samples were analyzed immediately by ESR spectroscopy.

Density Functional Theory Calculations

Hybrid DFT calculations were carried out with the Gaussian03 programme [120] at the B3LYP level. Split-valence 6-31G(d,p) basis set was used for all elements unless specified. Full geometry optimization was carried out by means of energy gradient techniques. Spin density and electrostatic potential were calculated with SCF density and visualized using GaussView [156]. The electrostatic potentials are mapped with a density isosurface of 0.0004 electrons au^{-3}. All calculations were set to be in the gas phase.

6.3 Alignment of C_{60}(TEMPO) in MBBA

As shown in Table 6.1, values of the anisotropic *g*-factor and **A** tensor of TEMPO and C_{60}(TEMPO) are simulated from their frozen solution ESR spectrum, respectively. The parameters of TEMPO are consistent with previous reports [186,187]. C_{60}(TEMPO) exhibits comparable *g*-factor to TEMPO and only slightly reduced A_{XX} and A_{ZZ} of the **A** tensor. Their similarity in ESR parameters is explained by the fact that all the spin density in C_{60}(TEMPO) is exclusively located in the functional group rather than the carbon cage (Figure 6.6c).

Table 6.1: Simulated ESR parameters for TEMPO and C_{60}(TEMPO) in toluene at 77K.

	g_{XX}	g_{YY}	g_{ZZ}	$A_{XX} = A_{YY}$ (MHz)	A_{ZZ} (MHz)
TEMPO	2.0087	2.0064	2.0018	15.7	96.3
C_{60}(TEMPO)	2.0081	2.0069	2.0021	14.8	93.9

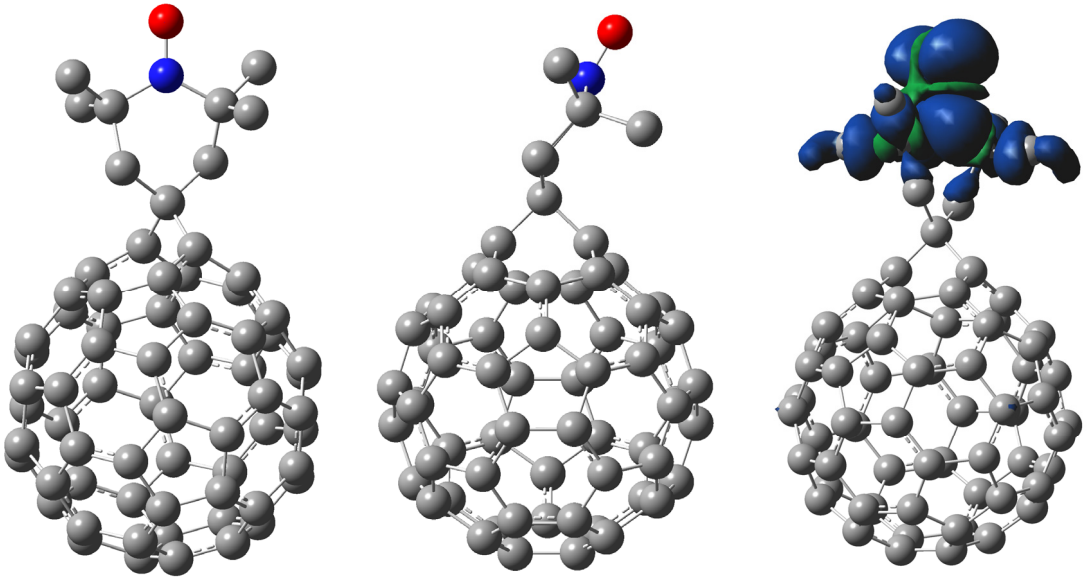

(a) (b) (c)

Figure 6.6: Two optimized conformations of C_{60}(TEMPO) (a, b) and the spin density distribution in the conformation a (c).

The molecular tumbling rate of TEMPO presents itself as m_I-dependence of the linewidth in ESR spectrum by influencing spin relaxation process. When a mixture of TEMPO and MBBA is diluted with different ratio of toluene, a change of ESR lineshapes is observed as shown in Figure 6.7a. Linewidth of the highest field transition becomes broader when less toluene is present in the mixture where molecular rotation of TEMPO gets slower. Figure 6.7b presents the simulated ESR spectra of TEMPO with different molecular tumbling time. Therefore, the tumbling time of TEMPO and C_{60}(TEMPO) in MBBA could be derived from their ESR spectra (Figure 6.7c). As listed in Table 6.2, the tumbling time of C_{60}(TEMPO) is approximately as 4 times longer as TEMPO itself. This result indicates stronger interactions between C_{60}(TEMPO) and the liquid crystal matrix, which is in good agreement with its bigger molecular size compared with TEMPO.

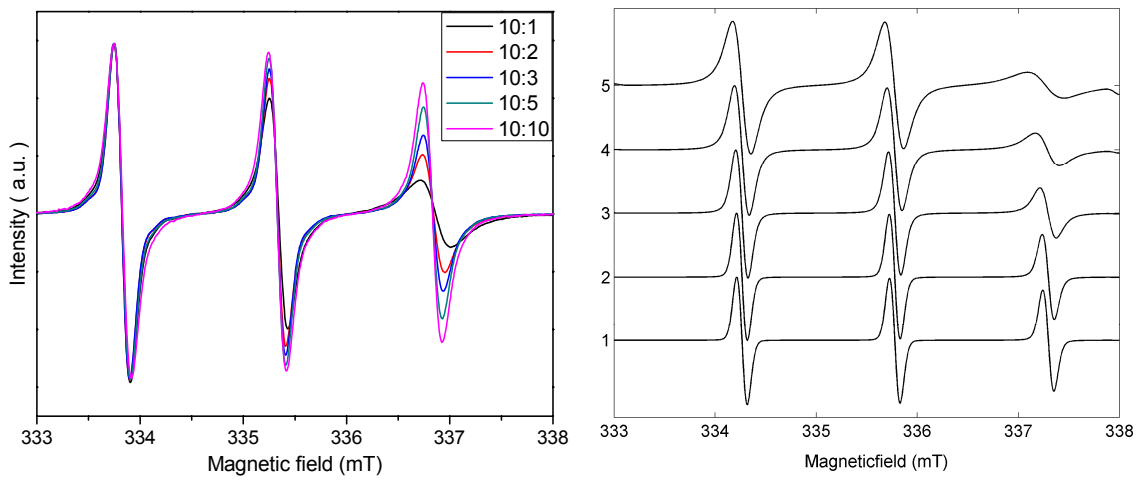

(a) (b)

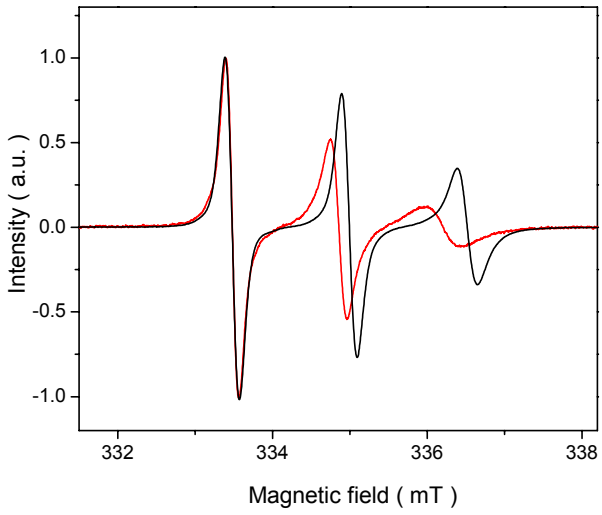

(c)

Figure 6.7: (a) Normalized ESR spectra of TEMPO dispersed in MBBA with different amount of toluene (the ratio is the volume of MBBA to toluene). (b) Simulation of TEMPO ESR spectra with correlation time 5×10^{-11}s, 1×10^{-10}s, 3×10^{-10}s, 6×10^{-10}s consecutively (starting from 1). (c) ESR spectra of TEMPO (black trace) and C_{60}(TEMPO) (red trace) in the liquid crystal matrix MBBA at room temperature.

The TEMPO radical itself exhibited negligible alignment in MBBA, based on its similar hyperfine interaction constant (hfc) *A* in both toluene and MBBA (Table 6.2). In contrast, C_{60}(TEMPO) showed preferable orientations in the liquid crystal. The hfc *A* of C_{60}(TEMPO) is significantly decreased after the medium was changed from toluene solution to liquid crystal matrix. Due to its relatively fast molecular tumbling rate, C_{60}(TEMPO) could be still

considered as an axial system in the MBBA. According to equation 6.6, the ordering parameter O_{XX} is calculated to be 0.11. The other two ordering parameters O_{YY} and O_{ZZ} could be in principle calculated as well, but an accurate shift measurement of *g*-factor required for the equation 6.5 at the scale of 0.0002 is beyond the resolution limits of our ESR spectroscopy.

Table 6.2: Simulated ESR parameters for TEMPO and C_{60}(TEMPO) in toluene and the liquid crystal matrix MBBA at room temperature.

	toluene		MBBA	
	g	*A* (MHz)	*A* (MHz)	Tumbling time (ns)
TEMPO	2.0062	43.1	42.7	0.42
C_{60}(TEMPO)	2.0061	41.7	38.7	1.58

Interpretation of the orientation would be simplified if one of the principal axes of the probing ESR tensor coincides with one major axis of the probed molecule. Unfortunately, the probing axis *X* in C_{60}(TEMPO) (defined along the *N-O* bond in Figure 6.5) deviates from the principal axis of the molecule. As shown in Figure 6.6, two conformations of C_{60}(TEMPO) were identified. Although the *N-O* bond and the principal molecular axis nearly coincide in one conformation (Figure 6.6a), they depart away by approximately 50^o in the other conformation (Figure 6.6b). Therefore, the uncertainty of the deviation in the two conformations makes it impossible to analyze the orientational distribution from the ordering parameter. However, the positive sign of O_{XX} indicates the preferential parallel orientation of C_{60}(TEMPO) molecules along the magnetic field.

To summarize, two conclusions could be drawn from the alignment of C_{60}(TEMPO) in MBBA. Firstly, fullerene derivatives rotate quickly in MBBA, and the system could not be treated as the rigid-lattice limit. Secondly, the preferential orientation of C_{60}(TEMPO) in

MBBA confirmed the suitability of liquid crystal to align fullerene derivatives. As shown below, these findings prove to be very instructive to further understand the orientations of N@C_{60} derivatives in MBBA.

6.4 Alignment of N@C_{60} derivatives in MBBA

The four synthesized pyrrolidine derivatives of N@C_{60} bear groups of various length and degrees of flexibility at the α position to the *N*-substituent (Figure 6.5). Table 6.3 lists their intrinsic ZFS parameters deduced from frozen solution ESR spectra. Dispersion of the four derivatives in MBBA gave rise to two different types of ESR spectra. Powder-like ESR spectrum with ZFS features are observed for derivatives **2N** and **4N** and solution-like spectrum are observed for derivatives **5N** and **6N.**

Table 6.3: The intrinsic ZFS parameters for pyrrolidine derivatives of N@C_{60}. The estimated uncertainties are 0.2 MHz.

	D (MHz)	*E* (MHz)
2N	16.2	0.5
4N	16.3	0.4
5N	16.3	0.6
6N	16.3	0.3

6.4.1 Distributions exhibiting powder-like ESR spectrum

As shown in Figure 6.8, derivative **2N** dispersed in MBBA exhibits powder-like spectrum that differs remarkably from its spectrum in frozen solution. As a preliminary attempt, a solid-state model with random distribution was considered, but the simulation failed to match the experimental spectrum. Firstly, this model predicts narrower linewidth and lower intensity for the minor peaks resulted from ZFS effects. Secondly, difficulty arises to

understand the simulated parameter $D_{fit} = 8.9$ MHz, which is smaller than the intrinsic value for derivative **2N** ($D_{\text{int}} = 16.2$ MHz). In addition, the solid-state model is not justified by the fact that tumbling rate of fullerene derivatives in MBBA is still far above the rigid-lattice limit.

An oriented distribution model is therefore adopted instead of the random model. Due to the much smaller value of *E* in comparison with *D*, the pyrrolidine derivative could be approximately treated as an axial system and equation 6.2 is then applicable to analyze their orientations. In contrast to C_{60}(TEMPO), axis *Z* of the ZFS tensor in derivatives **2N** and **4N**-**6N** coincides with their principal molecular axis (Figure 6.5). The ordering parameter could be therefore resolved into orientational distribution of these molecules. A Gaussian distribution is assumed for the molecular orientations [188]:

$$P(\theta) = \exp(\frac{-(\theta - \theta_0)^2}{2 \cdot \sigma^2}) / \sigma \qquad (6.7)$$

where θ is the angle between the principal molecular axis and the magnetic field, the mean angle θ_0 defines deviation of the director (the direction of preferred orientation of molecules) of the derivative from the magnetic field, and σ^2 is the variance of the distribution.

When N@C_{60} derivatives are dispersed in MBBA, their ordering parameter O_{ZZ} is assumed positive by following the result for C_{60}(TEMPO). For derivative **2N,** simulation with $\theta_0 = 44.8^o$ and $\sigma = 2.6$ fits well with the experimental spectrum (Figure 6.8). According to equation 6.2, the ordering parameter O_{ZZ} is calculated to be 0.255. For derivative **4N** dispersed in MBBA, $\theta_0 = 45.2^o$, $\sigma = 2.7$ and $O_{ZZ} = 0.245$ give the best fit in the simulation.

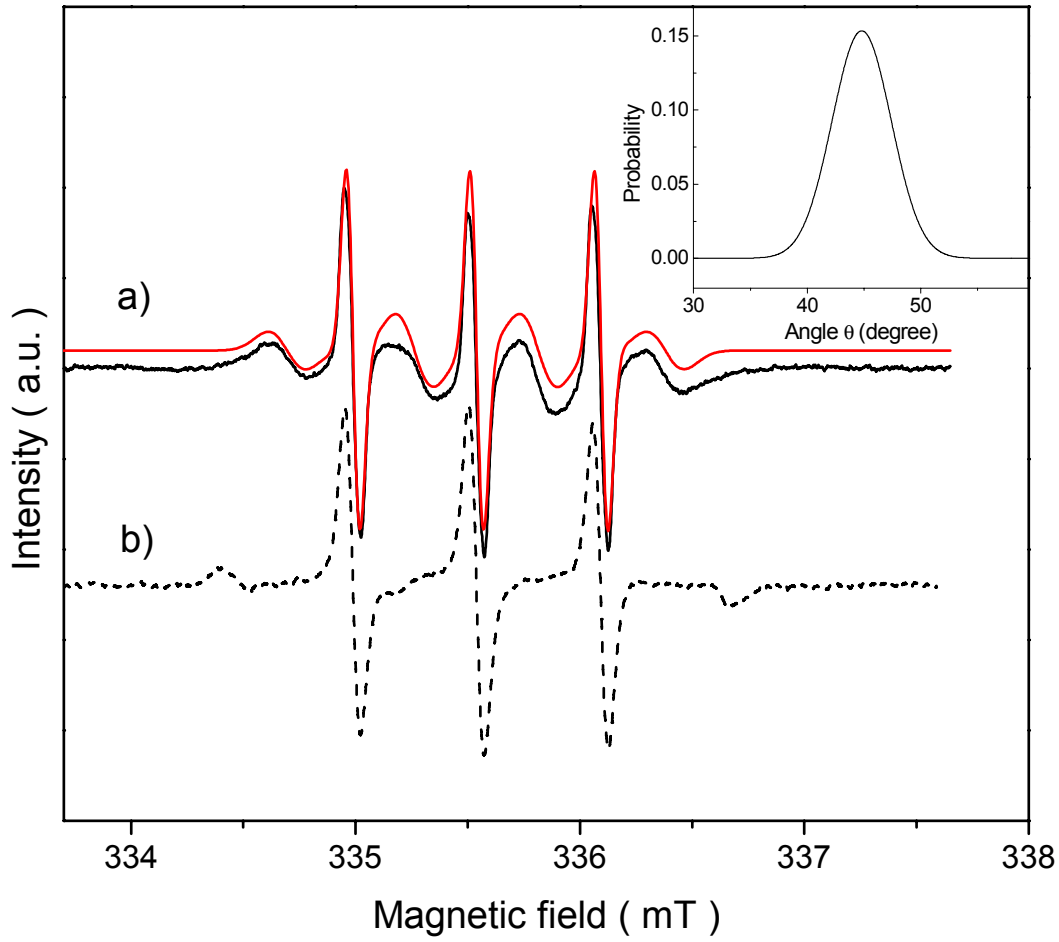

Figure 6.8: ESR spectra of derivative **2N** in MBBA (a), and in toluene at 77 K (b). Red trace is the simulated spectrum with D = 16.2 MHz, E = 0.5 MHz, $A_{XX} = A_{YY}$ = 15.4 MHz A_{ZZ} = 16.2 MHz. Inset: angle distribution employed to generate the simulation spectrum.

Because σ and θ_0 in equation 6.7 were simultaneously optimized in the simulation, reliability of their results has to be verified. The ordering parameter as a function of these two parameters is numerically plotted as 3-D surface in Figure 6.9a, which is achieved by combination of equation 6.2 and 6.7. A projection of the 3-D surface to the plane of ordering parameter and mean angle is shown in Figure 6.9b, with the two highlighted edges representing the minimum divergence ($\sigma = 0.1$) and maximum divergence ($\sigma = 20$), respectively. The highest sensitivity of ordering parameter to mean angle is achieved at 45^{o}, at which all curves have the sharpest slope.

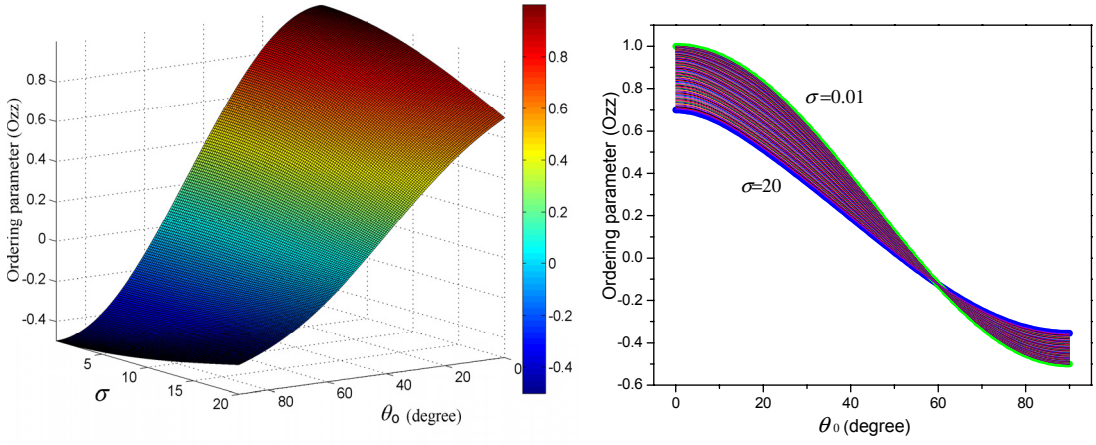

(a) (b)

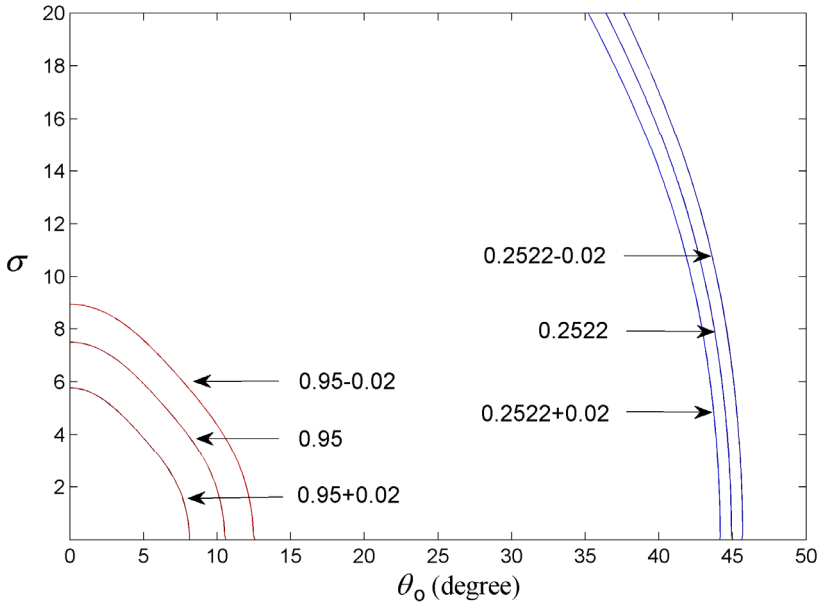

(c)

Figure 6.9: (a) The 3-D surface of the ordering parameter as a function of the mean angle θ_0 and the square root of variance σ. (b) Projection of the 3-D surface on the plane of ordering parameter and θ_0. (c) Contours of the ordering parameter on the plane of θ_0 and σ. (Values of the contours are marked in the graph).

This conclusion could be also analytically deduced from equation 6.2. When a unity distribution is assumed ($\sigma = 0$), derivative of the ordering parameter over the mean angle is:

$$\frac{dO_{ZZ}}{d\theta_0} = -3\cos\theta_0 \cdot \sin\theta_0 \qquad (6.8)$$

where the negative maximum achieves at 45°. Therefore, inaccuracy of the mean angle inherited from the ordering parameter is lower when the angle is in the range around 45°. Coincidently, both $\theta_0 = 44.8^o$ for derivative **2N** and $\theta_0 = 45.2^o$ for **4N** fall into this range. Take derivative **2N** for an example, a fluctuation (± 0.02) of the ordering parameter at $O_{ZZ} = 0.2522$ causes smaller change on the mean angle than it does at $O_{ZZ} = 0.95$ (Figure 6.9c).

Reliability of σ could be verified from the ESR spectrum simulation. As shown in Figure 6.10, intensity of the minor peaks due to ZFS effects varies with σ. When σ is larger than 5, a solution-like spectrum with nearly negligible ZFS features is predicted. The optimized simulation spectrum for derivative **2N** with $\sigma = 2.6$ is remarkably different from the spectra with $\sigma = 3.1$ and $\sigma = 2.1$.

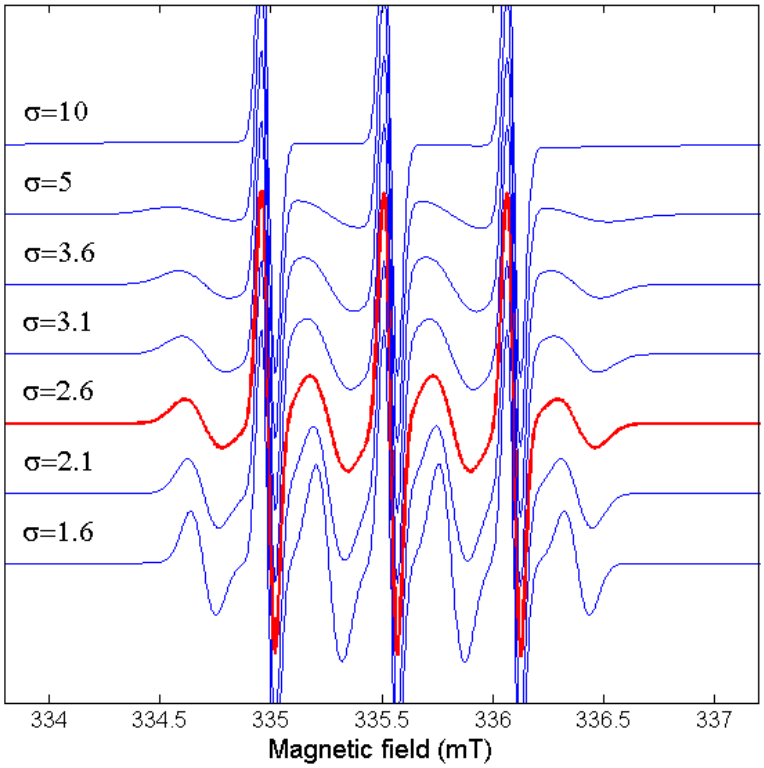

Figure 6.10: Simulation of the ESR spectrum of derivative **2N** according to the Gaussian distribution (equation 6.7), with θ_0 fixed at 44.8°. Red trace is the optimized simulation for the experimental spectrum.

6.4.2 Distributions exhibiting solution-like ESR spectrum

In contrast to derivatives **2N** and **4N**, derivatives **5N** and **6N** exhibit solution-like ESR spectrum in MBBA (Figure 6.11). The absence of ZFS features in their ESR spectra illustrates three points about the dispersion in MBBA.

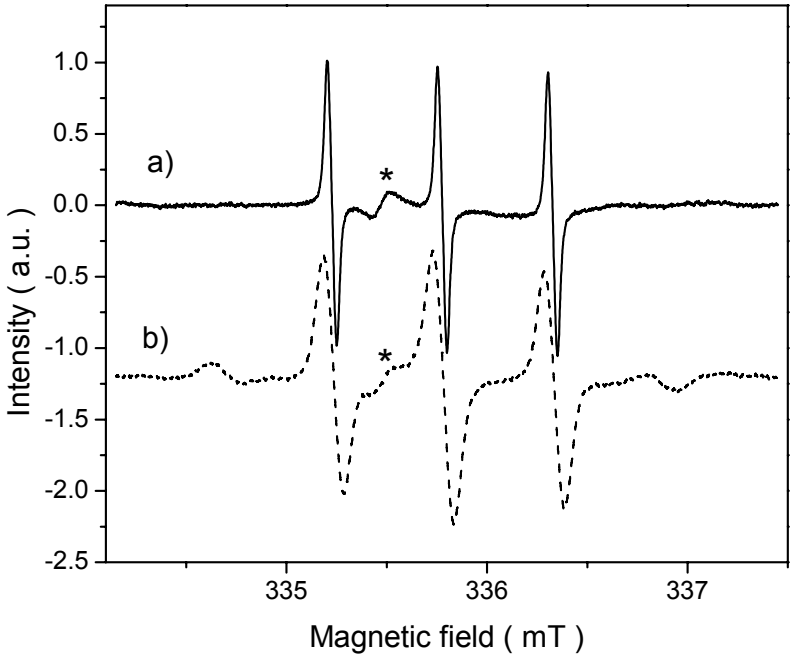

Figure 6.11: ESR spectra of derivative **5N** in MBBA (a), and in toluene at 77 K (b). * Peak from unknown impurity.

Firstly, distribution of derivatives **5N** and **6N** is nearly random. According to the simulation shown in Figure 6.10, σ of the distributions should be larger than 10. Secondly, tumbling rate of both derivatives **5N** and **6N** dispersed in MBBA is fast enough to average out their instinct ZFS effects, consistent with the finding on C_{60}(TEMPO). Finally, the solution-like ESR spectra further rationalize the alignment of derivatives **2N** and **4N** in MBBA. A matrix-induced ZFS effect was previously reported in a mixture of pristine N@C_{60} with p-ter-butylcalix[8]arene due to strong host-guest interactions [189]. However, the solution-like ESR spectra of derivatives **5N** and **6N** exclude such an effect in the MBBA matrix. This finding agrees well with the previous report that a trivial ZFS with $D = 0.090$ MHz was observed for N@C_{60} dispersed in MBBA [174]. Therefore, the ZFS features observed in ESR spectra of derivatives **2N** and **4N** dispersed in MBBA must be ascribed to

their oriented distribution. Otherwise, derivatives **2N** and **4N** dispersed in MBBA would exhibit similar solution-like ESR spectra to derivatives **5N** and **6N**.

6.4.3 Interactions between fullerene derivatives and MBBA

Since the director of MBBA in nematic phase is parallel to the magnetic field, the mean angle θ_0 in equation 6.7 is also the deviation between the director of the derivative and that of MBBA. Derivatives **2N** and **4N** are therefore aligned along MBBA with an angle of about 45^o between their principal molecular axes (Figure 6.12). This angle contrasts to the usual expectation that the solute molecules with aspect ratio larger than 1 would parallel their principal axis along the director of the liquid crystal matrix. But the result is consistent with the previous investigation on N@C_{70} dispersed in MBBA [174]. Its ordering parameter $O_{ZZ} = 0.18(3)$, as well as the nearly unitary distribution ($\sigma \approx 0$), indicates the angle between N@C_{70} and MBBA (θ_0) is about 47.7^o.

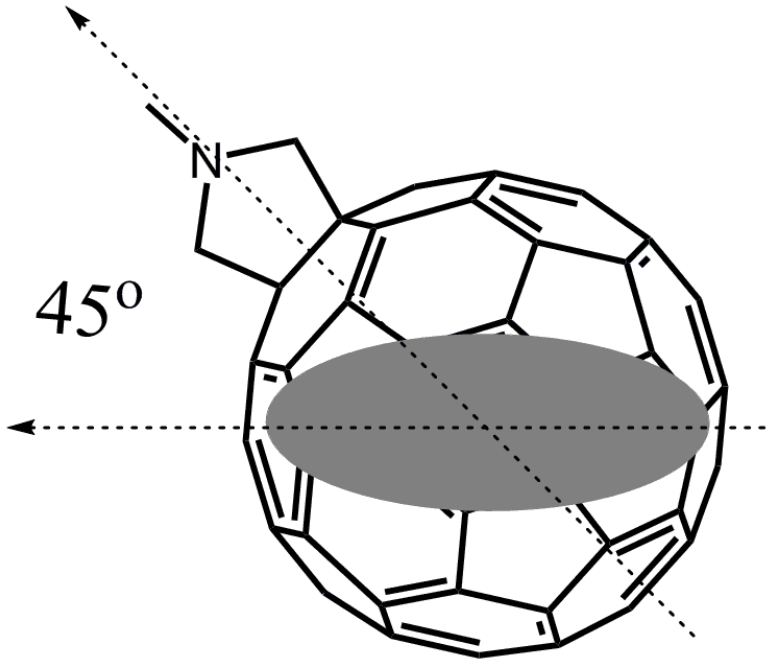

Figure 6.12: Schematic illustration of derivative **2N** aligned in MBBA. The angle 45° depicts the deviation of the director of derivative **2N** from director of MBBA or alternatively the magnetic field direction.

DFT calculations were used to further understand the orientation of fullerene derivatives in MBBA from the perspective of molecular interactions (the endohedral derivatives **2N**, **4N**-**6N** and their corresponding derivatives **2**, **4**-**6** are assumed to have the same interactions with MBBA). Derivative **2** comprises of two distinct moieties in terms of electronic structure: the conjugated fullerene cage and the non-conjugated pyrrolidine ring. The structure is confirmed by ^{13}C NMR spectrum, where 58 carbon atoms of the fullerene cage are identified as sp^2 hybridized. Due to the large surface area of fullerene cages, strong π-π interactions are expected between the fullerene derivatives and MBBA molecules. We herein propose that these π-π interactions determine the orientation of fullerene derivatives in MBBA.

Because of the small binding energies (2-3 kcal mol^{-1}) of π-π interactions, it is still rather challenging to fully understand their origins and geometrical preferences. In general, intermolecular interactions could be reduced to electrostatic, dispersion, induction and exchange-repulsion forces [190]. The fact that all these forces could play a major role in a specific system results in several different models to understand the π-π interactions [191,192]. Among them, the Hunter-Sanders model based mainly on considerations of electrostatic force is widely used due to its simplicity and broad applicability [190]. According to the Hunter-Sanders model, two opposite electrostatic forces exist simultaneously when aromatic molecules approach each other: the attraction between the negatively charged π electron clouds and the positively charged σ framework, and the repulsion between the both negatively charged π-π electron clouds. A balance between the attraction and repulsion determines both the binding energy and the geometry. Because of the strong repulsion, a face-face sandwich stacked geometry is usually not as favourable as the T-shaped and parallel-displaced geometries (Figure 6.13).

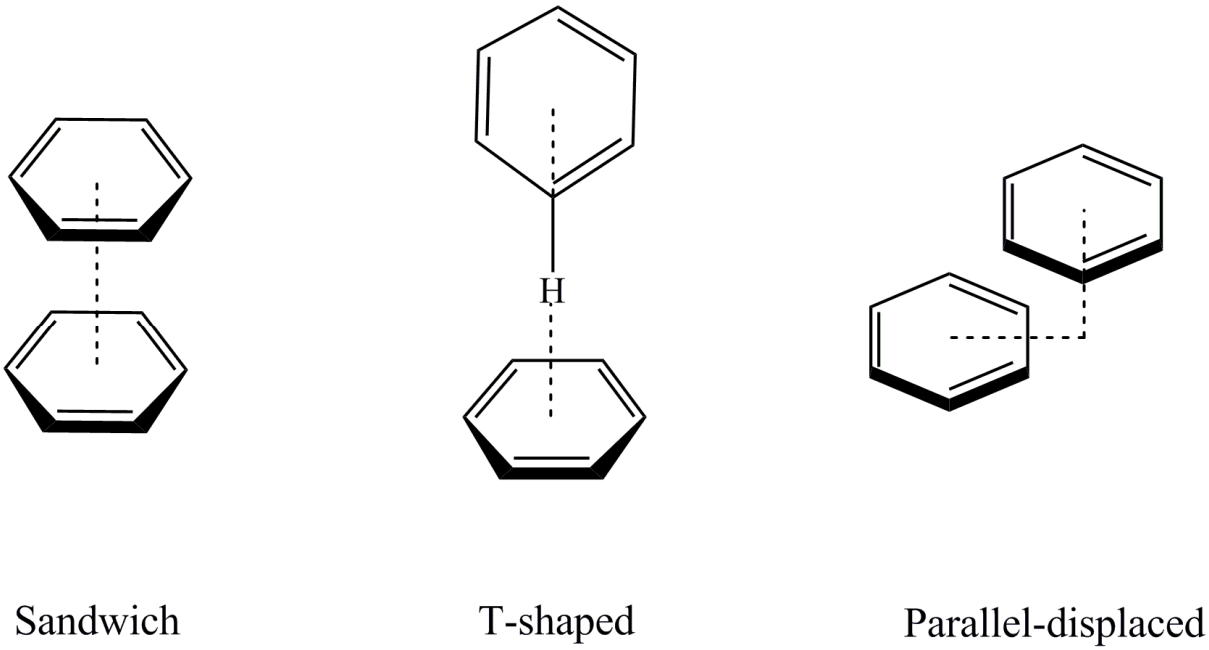

Figure 6.13: Sandwich, T-shaped and parallel-displaced configurations of two benzene rings.

Electrostatic potential maps are helpful to understand electrostatic forces between molecules. MBBA and the fullerene derivatives exhibit different charge distribution trends in their electrostatic potential maps. The π electron clouds in both phenyl ring centres of MBBA are negatively charged, and the σ frames as well as the protons are positively charged (Figure 6.14a). In contrast, centres of the hexagonal and pentagonal rings of the fullerene cage in derivative **2** are positively charged, whereas the carbon-carbon frames are negatively charged (Figure 6.14b). A face-face structure, where the positively charged fullerene ring centres point to the negatively charged MBBA phenyl centres, is the favourable geometry according to the Hunter-Santers model [190]. This face-face geometry gives rise to attraction forces between fullerene derivative and MBBA, instead of repulsion forces that are dominant in two flat aromatic molecules.

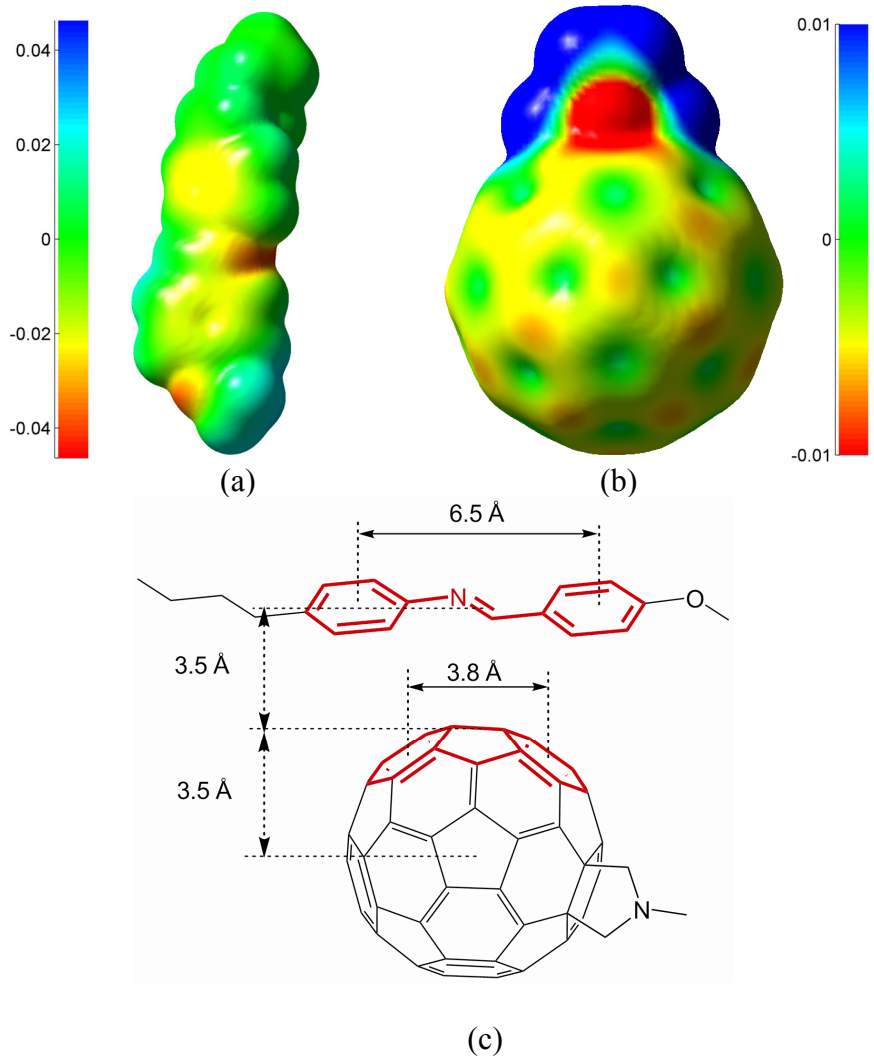

Figure 6.14: Electrostatic potentials of MBBA (a), derivative **2** (b) (The scale bars are in a.u.). (c) Schematic drawing of the interaction between a MBBA molecule and the three consecutive rings of the fullerene derivative.

If an interaction distance of 3.5 Å is assumed [193], a MBBA molecule needs to interact with three consecutive rings of the fullerene cage from the perspective of geometrical requirement (Figure 6.14c). Five possible groups of rings that match the proposed geometry are identified in the carbon cage of derivative **2** (Figure 6.15). Orientations of these triplet rings with respect to the principal axis of derivative **2** are summarized in Table 6.4. In reality, all the orientations could be experienced by the fullerene derivative given its fast molecular tumbling rate in MBBA. Averaged angle for the four non-perpendicular interaction modes (a-d in Figure 6.15) would be 50.4°, if the contribution of each mode is simply proportional

to the amount of its sub-members. This theoretical prediction is close to the experimental vale of about 45°, which qualitatively explains the deviation of directors between the fullerene derivatives and MBBA.

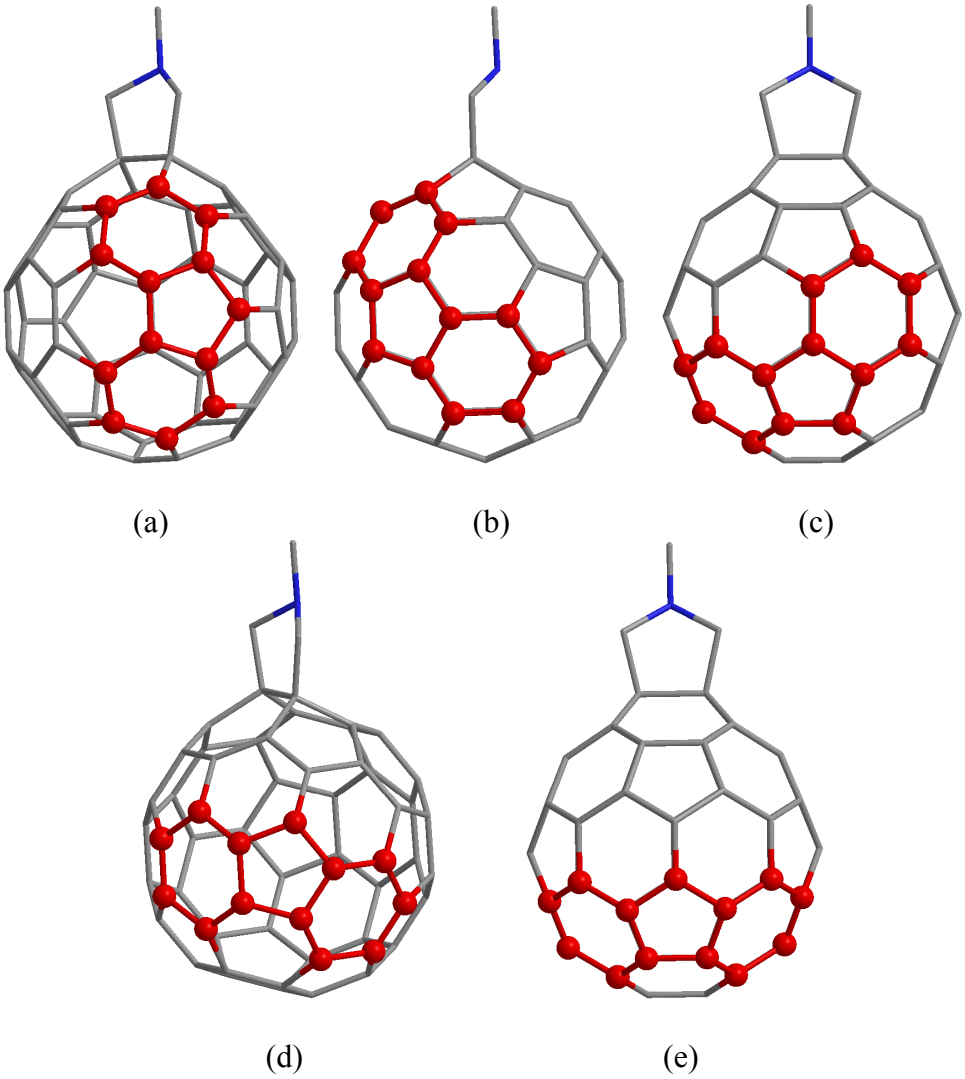

Figure 6.15: Five interaction modes in the fullerene cage with a MBBA molecule. The fullerene rings involved in the interaction are highlighted in red.

Table 6.4: Interaction modes of the fullerene cage with MBBA in derivative **2**. * With respect to the principal molecular axis of derivative **2**.

	a	b	c	d	e
Orientation of the triplet rings * (°)	0	36	60	72	90
Amount of sub-members	4	12	12	12	4

For derivative **4**, although there is a phenyl group appended to its pyrrolidine ring, no interactions between the phenyl group and the fullerene cage are observed in its both conformations (Figure 6.16). The fullerene cage should still dominate the interactions with MBBA molecules due to its larger surface area. In addition, the relatively rigid structure limits the flexibility of the phenyl group. Therefore, derivative **4N** dispersed in MBBA exhibits similar orientation to derivative **2N**.

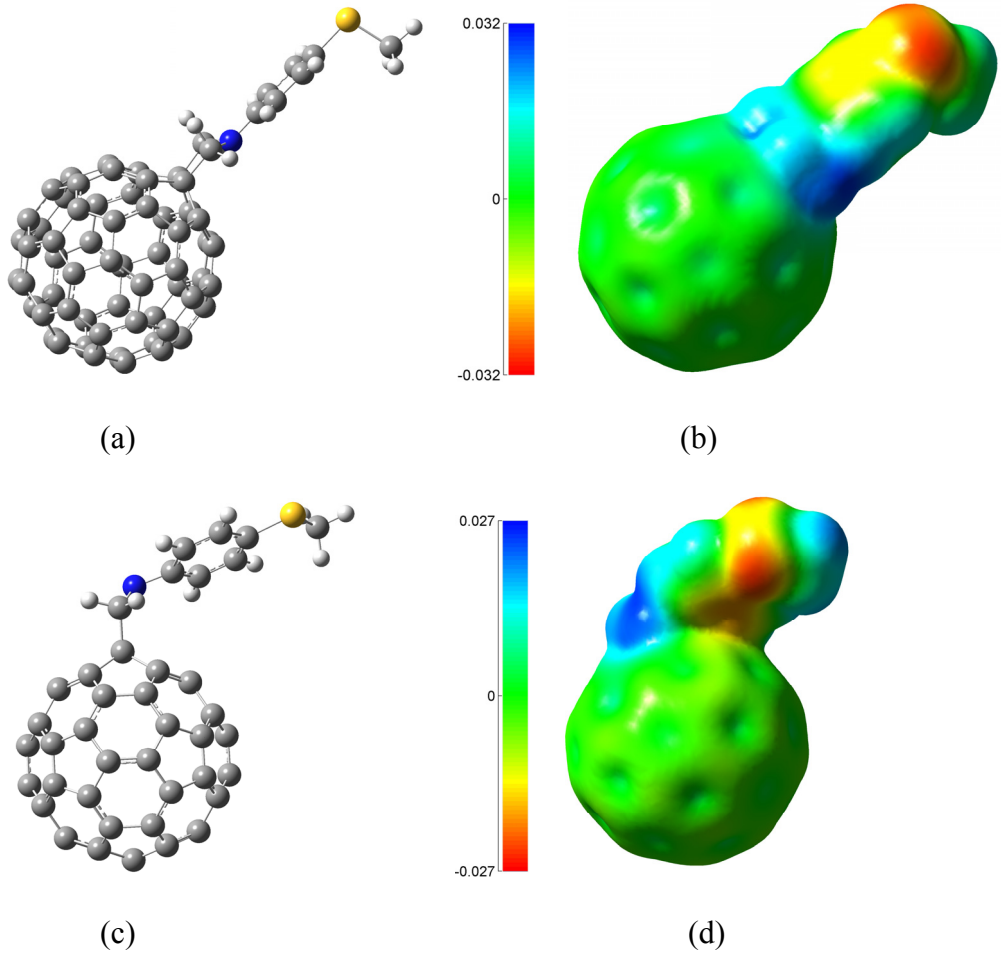

Figure 6.16: Two conformations of derivative **4** and their electrostatic potentials: the stretched (a) (b) and the folded (c) (d). The scale bars are in au.

The major structural difference between derivative **5N** (or **6N**) and derivative **4N** is the presence of a sp^3 carbon that links the pyrrolidine ring and the phenyl group. More conformations are therefore expected for derivative **5N** (or **6N**) than for derivative **4N**,

where the phenyl group orientates differently to the fullerene cage. The additional interaction between this phenyl group and MBBA molecules enables more orientations in the matrix. Moreover, a particular conformation of derivative **5** is identified with the phenyl group separated from the fullerene cage by just 3.6 Å (Figure 6.17c). An intra-molecular interaction is supported by the electrostatic potentials (Figure 6.17d), where electron density of the phenyl group is overlapped with that of the fullerene cage. Such an interaction changes the molecular symmetry and may subsequently affect the inter-molecular interaction with MBBA. Therefore, more diversified orientations of derivatives **5N** (or **6N**) in MBBA are expected, which leads to the broader distribution and solution-like ESR spectrum.

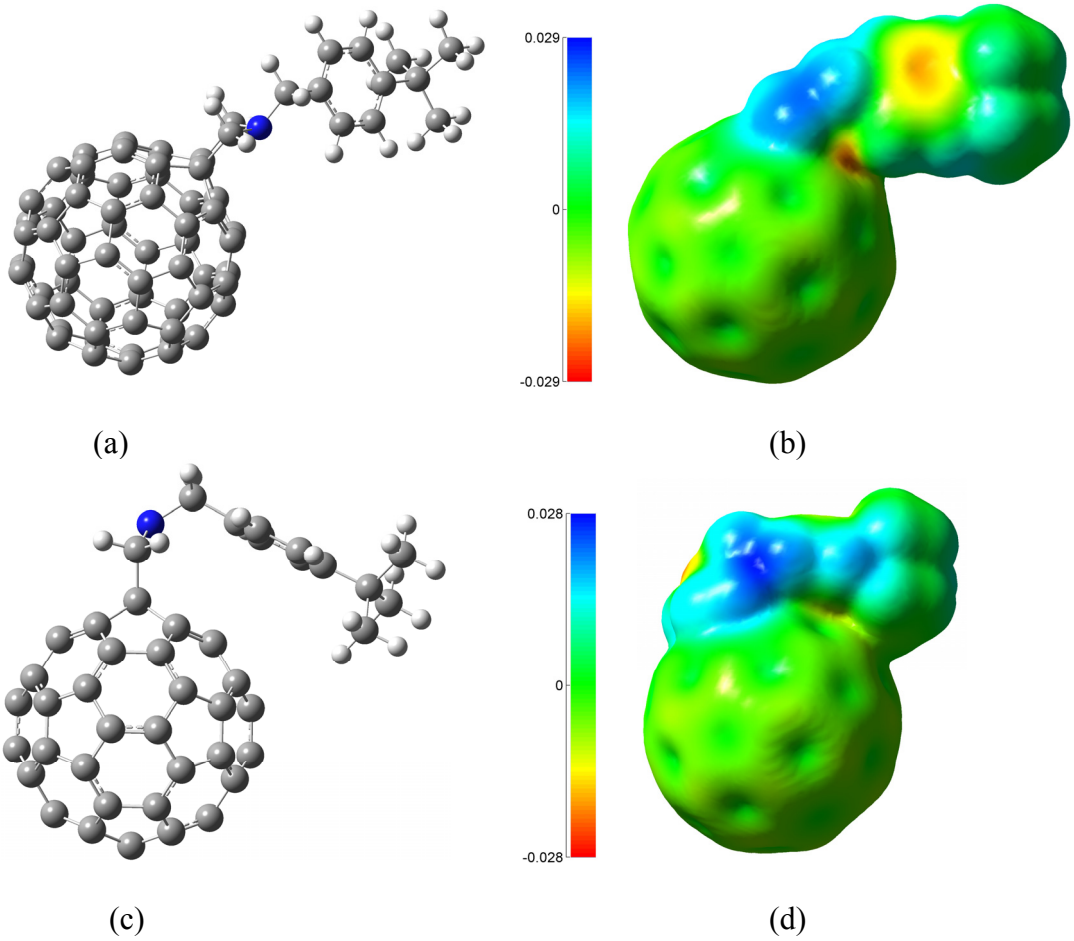

Figure 6.17: Two conformations of derivative **5** and the electrostatic potentials: the stretched (a) (b), and the folded (c) (d). The scale bars are in au.

6.5 Prospects for alignment of N@C_{60} derivatives

Although a relatively narrow distribution of orientations is achieved for derivatives **2N** and **4N** in MBBA, it is still not satisfactory concerning the low ordering parameters. According to equation 6.2, the main factor affecting the ordering parameter is the deviation of directors between the fullerene derivative and MBBA (or the mean angle θ_0 in equation 6.7). The ordering parameter would be significantly enhanced if θ_0 is reduced. As shown in Figure 6.18a, the simulation with θ_0=10^o generates sharp splitting of ESR transitions for derivative **2N** over a broad range of σ. The lift of degeneracy in transitions enables the selective addressing of individual energy level in the 12-level spin system of N@C_{60}. This would enable new refinement in information transfer between the nuclei spins and electron spins in N@C_{60} [90].

In addition to pyrrolidine derivatives, other derivatives with smaller ZFS parameter D could be similarly aligned in MBBA. Both simulations with $D = 13.4$ (Figure 6.18b) and $D = 6.0$ MHz (Figure 6.18c) exhibit good resolution of the nine transitions with the assumed θ_0=10^o. Especially, the simulation shown in Figure 6.18b is important because alignment of the fullerene dimers to control spin-spin interactions is a main target in the QIP scheme based on endohedral fullerenes.

To experimentally reduce the θ_0 between the fullerene derivatives and MBBA, further investigation is definitely required. According to findings in this work, the fullerene cage dominates the interactions with MBBA and subsequently determines the orientations in the matrix. To break up the dominance of fullerene cage, groups that would parallel to MBBA could be incorporated in the fullerene derivatives. Rigid and linear group(s), such as MBBA

itself or biphenyl esters, are possible candidates. With the parallel director of the functional group, θ_0 of the fullerene derivative may be effectively reduced.

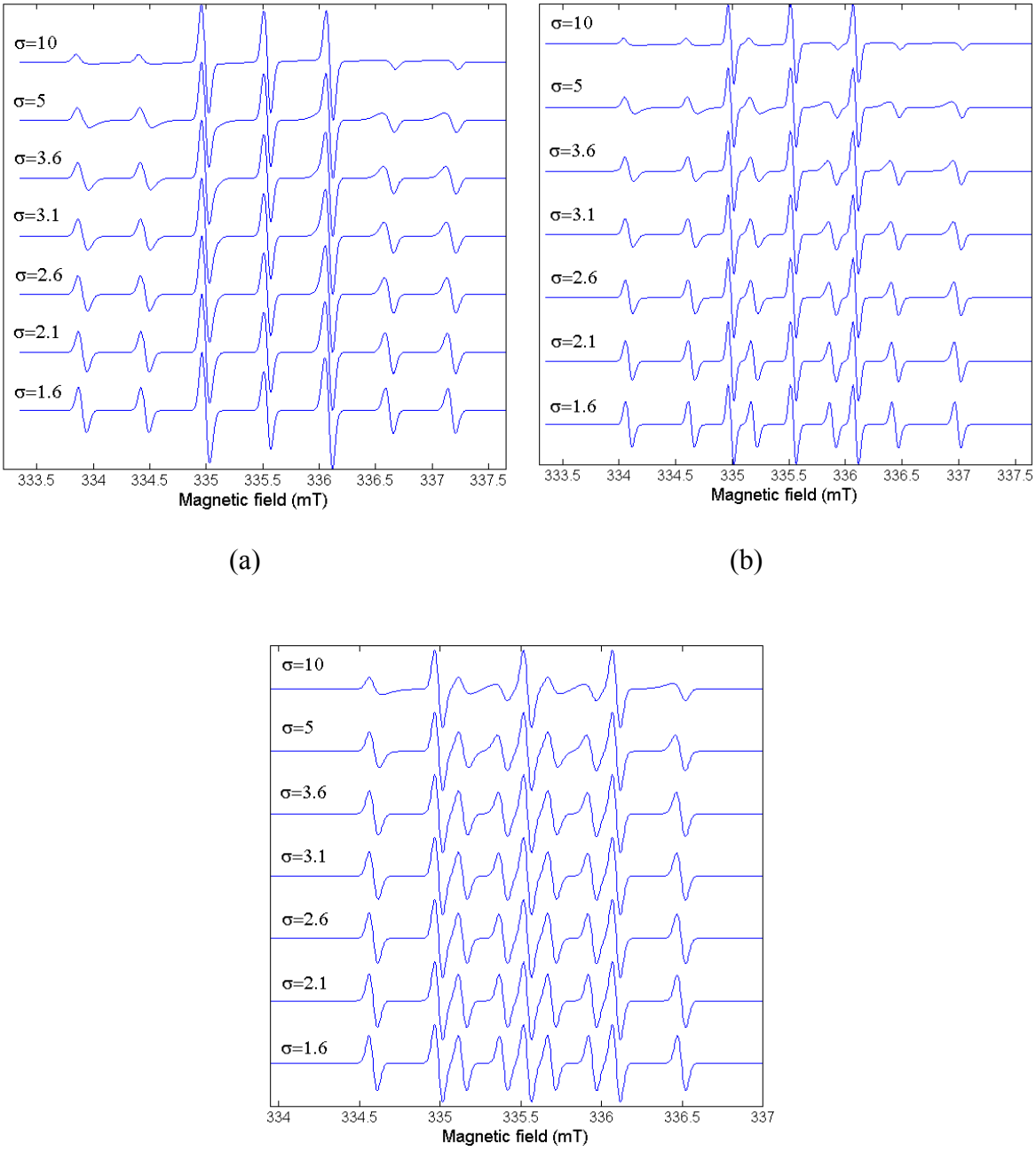

Figure 6.18: Simulation of the ESR spectra of N@C_{60} derivatives according to the Gaussian distribution (equation 6.7), with θ_0 fixed at 10 °. (a) Derivative **2N** with D = 16.2 MHz. (b) N@C_{60}-C_{60} dimer with D =13.4 MHz. (c) Cyclopropane derivatives with D = 6.0 MHz

6.6 Conclusions

The fullerene derivative labelled with a nitroxide radical was firstly investigated in the nematic phase MBBA. Ordering parameter and molecular tumbling time of 1.58 ns were determined by simulation of the ESR spectra. Orientations of four N@C_{60} pyrrolidine derivatives dispersed in MBBA were studied via their ZFS tensor. Derivatives **2N** and **4N** are preferentially oriented in the liquid crystal, with the Gaussian distribution of $\sigma = 2.6$ for derivative **2N** and $\sigma = 2.7$ for derivative **4N**. The director of the fullerene derivatives deviates from that of MBBA by an angle of about 45^o. Strong π-π interaction, with MBBA stacking over three consecutive rings of the fullerene cage, was proposed based on DFT calculations. In contrast, derivatives **5N** and **6N** (with a flexible bond linked between the phenyl group and the pyrrolidine ring) exhibit solution-like ESR spectra and random distribution in the liquid crystal. A special conformation with intra-molecular interaction was identified for derivative **5N**. In addition, matrix-induced effect on ZFS features of N@C_{60} derivatives could be excluded from consideration in these systems. Successful alignment of N@C_{60} derivatives is important for their applications in QIP.

Chapter 7

General conclusions and prospects

7.1 Conclusions

$N@C_{60}$, with its remarkably long decoherence time, has intrigued great interest in electron-spin based QIP. Although single qubit operations were achieved with high fidelity, scaling up to multiple-qubit system hindered development of the $N@C_{60}$ based architecture. The work presented here explored the feasibility of overcoming this scalability hindrance through chemical functionalization. Several fundamental issues on both the chemistry of $N@C_{60}$ and application of its derivatives were addressed.

Firstly, functionalization of C_{60} was investigated and the reaction schemes were then readily transferred to functionalize $N@C_{60}$ (described in Chapter 3). In these reactions, no difference in reactivity between $N@C_{60}$ and C_{60} was observed. The Prato reaction scheme was particularly employed due to its capability to minimize the decomposition of $N@C_{60}$ during the reaction. A variety of pyrrolidine derivatives of $N@C_{60}$ were synthesized using the specific precursors.

Stability of the encapsulated nitrogen atom is vital for any development and applications of $N@C_{60}$. In Chapter 4, the effect of functionalization on the stability of $N@C_{60}$ was studied by ESR techniques. Despite their stability in the dark, $N@C_{60}$ derivatives in a degassed solution were sensitive to light even at room temperature. It was found that photochemical stability of the $N@C_{60}$ derivatives varied with the functional groups attached to the fullerene cage. Under excitation of ambient light, the pyrrolidine derivatives of $N@C_{60}$ exhibited a half-life time approximately one fourteenth of that of the pristine $N@C_{60}$. An introduction of the pyrene chromophore to the peripheral pyrrolidine ring does not significantly change the stability of encapsulated nitrogen atom, although energy transfer from pyrene to C_{60} takes place efficiently in the excited state. In contrast to the pyrrolidine derivatives, the cyclopropane derivative of $N@C_{60}$ shows a comparable photochemical stability to pristine $N@C_{60}$.

To account for the difference in stability between the two types of $N@C_{60}$ derivatives, an escape mechanism of the encapsulated nitrogen atom was proposed based on DFT calculations. The mechanism involves bonding of the encapsulated nitrogen atom to the two carbons bearing the addends and the subsequent swinging out. The 6-membered ring formed in the decay of the pyrrolidine derivatives facilitates the inversion of the encapsulated nitrogen atom, leading to their lower stability. For the cyclopropane derivatives, no inversion of the encapsulated nitrogen atom could take place through the resultant 4-membered ring. The major decay route for cyclopropane derivatives is expected to be the same as that for pristine $N@C_{60}$. Therefore, the blocking of the C1-C2 bond by the cyclopropane addends may even enhance the stability of the encapsulated nitrogen atom.

Moreover, a particular molecular system was developed by functionalization of $N@C_{60}$ with porphyrin groups in Chapter 5. Two $N@C_{60}$-porphyrin dyads were synthesized. The dyad with free base porphyrin exhibits typical ZFS features in solid-state ESR spectrum due

to functionalization. However, the strong spin-spin interactions suppressed the ESR signal of nitrogen spins in the dyad of $N@C_{60}$ and copper porphyrin. The concentration dependence studies demonstrated strong intra-molecular dipolar coupling between the two moieties. The inter-spin distance between the copper ion and the nitrogen atom is 1.26 nm identified from DFT optimization, and the dipolar coupling strength is 27.0 MHz. The Leigh model, as well as the broadening effects due to inter-molecular dipolar coupling, was adopted to account for the suppression of ESR signals of $N@C_{60}$. To exclude the escape of nitrogen atom in the $N@C_{60}$ and copper porphyrin dyad, demetallation of the porphyrin moiety was carried out. The recovery of about 82% of the $N@C_{60}$ signal intensity confirms the effects of the dipolar coupling in the suppression of the $N@C_{60}$ signal in ESR measurement.

Finally, to prepare ordered structures, pyrrolidine derivatives of $N@C_{60}$ were dispersed in the nematic matrix MBBA (discussed in Chapter 6). Orientations of these derivatives were characterized through their ZFS tensor. The derivatives with a $-CH_3$ or phenyl group derived straightforward from the *N*-substituent of the pyrrolidine ring were preferentially oriented in the liquid crystal. Gaussian distributions with $\sigma = 2.6$ and $\sigma = 2.7$ were deduced from a simulation of their ESR spectra. The director of the fullerene derivatives deviates from that of MBBA by an angle of about 45^o. Strong π-π interactions between MBBA and the fullerene cage were proposed based on the DFT calculations of electrostatic potentials. In contrast, the $N@C_{60}$ derivatives with a $-CH_2$ group linking the phenyl group and the pyrrolidine ring were found to be nearly random in MBBA. The flexibility induced by the sp^3 carbon increases the number of conformations for these derivatives and results in more diversified orientations in the liquid crystal matrix.

7.2 Future prospects

In addition to the photochemical stability of $N@C_{60}$ derivatives, their thermal stability is equally important to develop deeper understanding on the effects of functional groups on the decay of the encapsulated nitrogen atom. Especially, the activation energy for the escape of the encapsulated nitrogen atom from these experiments could be related to the theoretical energy barrier calculated in this work.

Future work on the $N@C_{60}$-porphyrin dyad could involve improving the filling ratio of nitrogen atom in the C_{60} moiety, or replacing the $N@C_{60}$ with other spin-active metallofullerenes, such as $Y@C_{82}$ or $La@C_{82}$. These metallofullerenes are generally easier than $N@C_{60}$ to prepare in high purity the scale of several milligrams. Another reason to use metallofullerenes is their higher stability than $N@C_{60}$. For instance, $La@C_{82}$ could survive heating at 623 K for several hours [194]. This is a great advantage in technological considerations of the reliability, as well as the broader applicability of processing methods. A challenge ahead is the chemistry of metallofullerenes, which is less understood than that of C_{60}/$N@C_{60}$. These metallofullerene-porphyrin dyads can be used as unique molecular systems for further investigation. C_{60}-porphyrin has been commonly studied in the fields of photovoltaic energy conversion. The substitution of C_{60} with metallofullerene in the dyad provides a potential system for spintronic devices. The electron pair resulting from photo-induced charge separation may couple to the unpaired electron(s) of the metallofullerene. If this coupling is antiferromagnetic, the metallofullerene will become spin-silent. After a certain period, the metallofullerene will go back its original spin-active state when charge recombination has occurred. Because photo-induced charge separation and charge recombination usually happens very quickly in fullerene-porphyrin dyads, this mechanism may provide a fast-rate approach to switch on/off the spin state of metallofullerenes.

Another are of future work could involve the synthesis of hybrid $N@C_{60}$-metallofullerene systems. Fullerene-tweezers may be an alternative for multiple-qubit systems to covalently linked dimers. In this scheme (Figure 7.1), molecular tweezers are chemically attached to the host endohedral fullerene $N@C_{60}$, and a dimer will be formed after a guest endohedral fullerene $Y@C_{82}$ is trapped in the tweezers though non-covalent bonding. Synthetic procedures for this dimer are straightforward. The reaction applied to synthesize $N@C_{60}$-porphyrin dyads could be readily transferred to the synthesis of $N@C_{60}$-tweezers by using the corresponding porphyrin-tweezers molecule as a precursor.

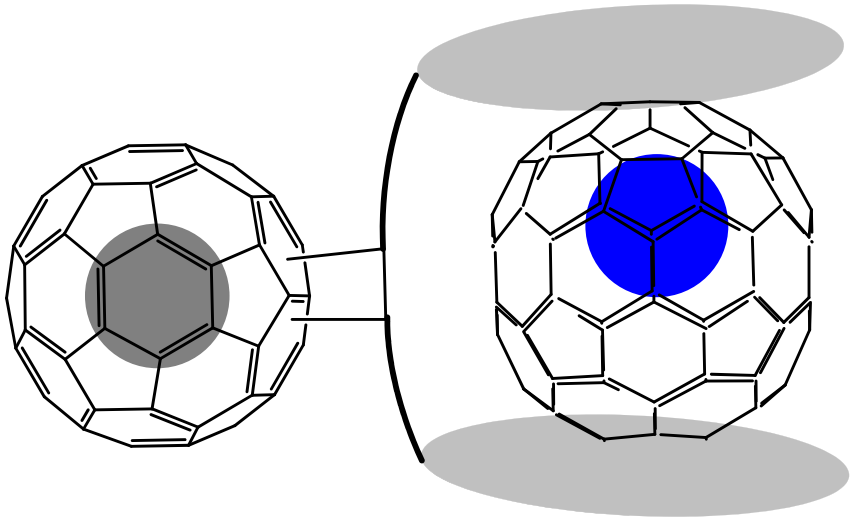

Figure 7.1: Schematic representation of $N@C_{60}$-tweezers with $Y@C_{82}$ trapped.

This scheme will mitigate several obstacles that hinder the development of endohedral fullerene dimers. Firstly, it reduces dramatically the number of potential isomers. Chemical reaction on metallofullerenes that normally gives rise to several isomers is excluded and the chemical reaction on $N@C_{60}$ could afford almost exclusively the monoadduct with a decent yield. This is very advantageous when considering the rarity of endohedral fullerenes. Secondly, it would produce asymmetric dimers. Because of their reactivity differences, asymmetric dimers are much more difficult to be synthesized. In this scheme, the

asymmetric dimers could be formed in a similar way to symmetric ones through careful selection of corresponding guest fullerenes.

Dipolar coupling would be the main spin-spin interaction between the two endohedral fullerenes, which could be investigated by ESR spectroscopy. For instance, $N@C_{60}$ and $Y@C_{82}$ exhibit distinct features in ESR spectra due to their different hyperfine interaction with nuclear spins. This difference will enable the selective addressing of individual electron spins on each fullerene. Furthermore, advanced ESR experiments may be performed on these dimers to achieve electron-electron entanglement, which is a prerequisite for quantum information processing.

In terms of the alignment of $N@C_{60}$ derivatives, further efforts could be dedicated to control of the molecular orientation in liquid crystals. As discussed in Chapter 6, groups that would be parallel to the liquid crystal could be incorporated in the derivative to diminish the dominant role of fullerene cage in determining orientations. Reduction in the mean angle of the director of the derivative with regard to the liquid crystal would significantly enhance the ordering parameter and lift the degeneracy of some ESR transitions in $N@C_{60}$. This may enable the selective addressing of individual transitions, and would allow for further quantum operations, such as coherent state transfer between the nuclear spins and the electron spins.

Bibliography

[1] D. Deutsch. Quantum-Theory, the Church-Turing Principle and the Universal Quantum Computer. *Proc. R. Soc. London, Ser. A*, 400(1818):97-117, 1985.

[2] P.W. Shor. Algorithms for Quantum Computation - Discrete Logarithms and Factoring. *35th Annual Symposium on Foundations of Computer Science, Proceedings*:124-134, 1994.

[3] P.W. Shor. Polynomial-time algorithms for prime factorization and discrete logarithms on a quantum computer. *SIAM J. Comput.*, 26(5):1484-1509, 1997.

[4] S.L. Braunstein, C.M. Caves, R. Jozsa, N. Linden, S. Popescu, R. Schack. Separability of very noisy mixed states and implications for NMR Quantum computing. *Phys. Rev. Lett.*, 83(5):1054-1057, 1999.

[5] C.Y. Lu, D.E. Browne, T. Yang, J.W. Pan. Demonstration of a compiled version of Shor's quantum factoring algorithm using photonic qubits. *Phys. Rev. Lett.*, 99(25):250504, 2007.

[6] B.P. Lanyon, T.J. Weinhold, N.K. Langford, M. Barbieri, D.F.V. James, A. Gilchrist, A.G. White. Experimental demonstration of a compiled version of Shor's algorithm with quantum entanglement. *Phys. Rev. Lett.*, 99(25):250505, 2007.

[7] D.P. DiVincenzo. The physical implementation of quantum computation. *Fortschr. Phys.*, 48(9-11):771-783, 2000.

[8] I.L. Chuang, L.M.K. Vandersypen, X.L. Zhou, D.W. Leung, S. Lloyd. Experimental realization of a quantum algorithm. *Nature*, 393(6681):143-146, 1998.

[9] J.I. Cirac, P. Zoller. Quantum Computations with Cold Trapped Ions. *Phys. Rev. Lett.*, 74(20):4091-4094, 1995.

[10] Q.A. Turchette, C.J. Hood, W. Lange, H. Mabuchi, H.J. Kimble. Measurement of Conditional Phase-Shifts for Quantum Logic. *Phys. Rev. Lett.*, 75(25):4710-4713, 1995.

[11] M.S. Sherwin, A. Imamoglu, T. Montroy. Quantum computation with quantum dots and terahertz cavity quantum electrodynamics. *Phys. Rev. A*, 60(5):3508-3514, 1999.

[12] L.M.K. Vandersypen, M. Steffen, G. Breyta, C.S. Yannoni, M.H. Sherwood, I.L. Chuang. Experimental realization of Shor's quantum factoring algorithm using nuclear magnetic resonance. *Nature*, 414(6866):883-887, 2001.

[13] N.A. Gershenfeld, I.L. Chuang. Bulk spin-resonance quantum computation. *Science*, 275(5298):350-356, 1997.

[14] B.E. Kane. A silicon-based nuclear spin quantum computer. *Nature*, 393(6681):133-137, 1998.

[15] T.D. Ladd, D. Maryenko, Y. Yamamoto, E. Abe, K.M. Itoh. Coherence time of decoupled nuclear spins in silicon. *Phys. Rev. B*, 71(1):014401, 2005.

[16] J.A. Jones, V. Vedral, A. Ekert, G. Castagnoli. Geometric quantum computation using nuclear magnetic resonance. *Nature*, 403(6772):869-871, 2000.

[17] K.V.R.M. Murali, N. Sinha, T.S. Mahesh, M.H. Levitt, K.V. Ramanathan, A. Kumar. Quantum-information processing by nuclear magnetic resonance: Experimental implementation of half-adder and subtractor operations using an oriented spin-7/2 system. *Phys. Rev. A*, 66(2):022313, 2002.

[18] E.M. Fortunato, M.A. Pravia, N. Boulant, G. Teklemariam, T.F. Havel, D.G. Cory. Design of strongly modulating pulses to implement precise effective Hamiltonians for quantum information processing. *J. Chem. Phys.*, 116(17):7599-7606, 2002.

[19] M.D. Price, S.S. Somaroo, C.H. Tseng, J.C. Gore, A.F. Fahmy, T.F. Havel, D.G. Cory. Construction and implementation of NMR quantum logic gates for two spin systems. *J. Magn. Reson.*, 140(2):371-378, 1999.

[20] J.A. Jones, M. Mosca. Approximate quantum counting on an NMR ensemble quantum computer. *Phys. Rev. Lett.*, 83(5):1050-1053, 1999.

[21] J.A. Jones, M. Mosca, R.H. Hansen. Implementation of a quantum search algorithm on a quantum computer. *Nature*, 393(6683):344-346, 1998.

[22] J.A. Jones, M. Mosca. Implementation of a quantum algorithm on a nuclear magnetic resonance quantum computer. *J. Chem. Phys.*, 109(5):1648-1653, 1998.

[23] J.A. Jones. NMR quantum computation: A critical evaluation. *Fortschr. Phys.*, 48(9-11):909-924, 2000.

[24] W.S. Warren. The usefulness of NMR quantum computing. *Science*, 277(5332):1688-1689, 1997.

[25] J.M. Elzerman, R. Hanson, L.H.W. van Beveren, B. Witkamp, L.M.K. Vandersypen, L.P. Kouwenhoven. Single-shot read-out of an individual electron spin in a quantum dot. *Nature*, 430(6998):431-435, 2004.

[26] J. Wrachtrup, C. Vonborczyskowski, J. Bernard, M. Orrit, R. Brown. Optical-Detection of Magnetic-Resonance in a Single Molecule. *Nature*, 363(6426):244-245, 1993.

[27] D. Loss, D.P. DiVincenzo. Quantum computation with quantum dots. *Phys. Rev. A*, 57(1):120-126, 1998.

[28] G. Burkard, H.A. Engel, D. Loss. Spintronics and quantum dots for quantum computing and quantum communication. *Fortschr. Phys.*, 48(9-11):965-986, 2000.

[29] H. Shinohara, H. Sato, M. Ohkohchi, Y. Ando, T. Kodama, T. Shida, T. Kato, Y. Saito. Encapsulation of a Scandium Trimer in C_{82}. *Nature*, 357(6373):52-54, 1992.

[30] H. Shinohara, H. Sato, Y. Saito, M. Ohkohchi, Y. Ando. Mass Spectroscopic and ESR Characterization of Soluble Yttrium-Containing Metallofullerenes $Y@C_{82}$ and $Y_2@C_{82}$. *J. Phys. Chem.*, 96(9):3571-3573, 1992.

[31] C.S. Yannoni, M. Hoinkis, M.S. Devries, D.S. Bethune, J.R. Salem, M.S. Crowder, R.D. Johnson. Scandium Clusters in Fullerene Cages. *Science*, 256(5060):1191-1192, 1992.

[32] J.R. Heath, S.C. Obrien, Q. Zhang, Y. Liu, R.F. Curl, H.W. Kroto, F.K. Tittel, R.E. Smalley. Lanthanum Complexes of Spheroidal Carbon Shells. *J. Am. Chem. Soc.*, 107(25):7779-7780, 1985.

[33] J.J.L. Morton, A.M. Tyryshkin, A. Ardavan, K. Porfyrakis, S.A. Lyon, G.A.D. Briggs. Electron spin relaxation of $N@C_{60}$ in CS_2. *J. Chem. Phys.*, 124(1):-, 2006.

[34] R.M. Brown, Y. Ito, J.H. Warner, A. Ardavan, H. Shinohara, G.A.D. Briggs, J.J.L. Morton. Electron spin coherence in metallofullerenes: Y, Sc, and $La@C_{82}$. *Phys. Rev. B*, 82(3):033410, 2010.

[35] W. Harneit. Fullerene-based electron-spin quantum computer. *Phys. Rev. A*, 65(3):032322, 2002.

[36] W. Harneit, C. Meyer, A. Weidinger, D. Suter, J. Twamley. Architectures for a spin quantum computer based on endohedral fullerenes. *Phys. Status Solidi B*, 233(3):453-461, 2002.

[37] D.F. Zaretsky, S.B. Sazonov. Coherent repopulation of hyperfine-structure levels with bichromatic-resonant electromagnetic fields. *Laser Physics*, 7(3):719-725, 1997.

[38] Z.L. Madi, R. Bruschweiler, R.R. Ernst. One- and two-dimensional ensemble quantum computing in spin Liouville space. *J. Chem. Phys.*, 109(24):10603-10611, 1998.

[39] A. Hirsch. Principles of fullerene reactivity. *Top. Curr. Chem.*, 1991-65, 1999.

[40] S. Lloyd. A Potentially Realizable Quantum Computer. *Science*, 261(5128):1569-1571, 1993.

[41] A. Ardavan, M. Austwick, S.C. Benjamin, G.A.D. Briggs, T.J.S. Dennis, A. Ferguson, D.G. Hasko, M. Kanai, A.N. Khlobystov, B.W. Lovett, G.W. Morley, R.A. Oliver, D.G. Pettifor, K. Porfyrakis, J.H. Reina, J.H. Rice, J.D. Smith, R.A. Taylor, D.A. Williams, C. Adelmann, H. Mariette, R.J. Hamers. Nanoscale solid-state quantum computing. *Philos. Trans. R. Soc. London, Ser. A*, 361(1808):1473-1485, 2003.

[42] M.A.G. Jones, R.A. Taylor, A. Ardavan, K. Porfyrakis, G.A.D. Briggs. Direct optical excitation of a fullerene-incarcerated metal ion. *Chem. Phys. Lett.*, 428(4-6):303-306, 2006.

[43] M.A.G. Jones, J.J.L. Morton, R.A. Taylor, A. Ardavan, G.A.D. Briggs. PL, magneto-PL and PLE of the trimetallic nitride template fullerene $Er_3N@C_{80}$. *Phys. Status Solidi B*, 243(13):3037-3041, 2006.

[44] A.N. Khlobystov, R. Scipioni, D. Nguyen-Manh, D.A. Britz, D.G. Pettifor, G.A.D. Briggs, S.G. Lyapin, A. Ardavan, R.J. Nicholas. Controlled orientation of ellipsoidal fullerene C_{70} in carbon nanotubes. *Appl. Phys. Lett.*, 84(5):792-794, 2004.

[45] A.N. Khlobystov, D.A. Britz, A. Ardavan, G.A.D. Briggs. Observation of ordered phases of fullerenes in carbon nanotubes. *Phys. Rev. Lett.*, 92(24):245507, 2004.

[46] A. Javey, J. Guo, Q. Wang, M. Lundstrom, H.J. Dai. Ballistic carbon nanotube field-effect transistors. *Nature*, 424(6949):654-657, 2003.

[47] S.J. Tans, M.H. Devoret, R.J.A. Groeneveld, C. Dekker. Electron-electron correlations in carbon nanotubes. *Nature*, 394(6695):761-764, 1998.

[48] S.C. Benjamin, A. Ardavan, G.A.D. Briggs, D.A. Britz, D. Gunlycke, J. Jefferson, M.A.G. Jones, D.F. Leigh, B.W. Lovett, A.N. Khlobystov, S.A. Lyon, J.J.L. Morton,

K. Porfyrakis, M.R. Sambrook, A.M. Tyryshkin. Towards a fullerene-based quantum computer. *J. Phys.: Condens. Matter*, 18(21):S867-S883, 2006.

[49] T.W. Chamberlain, A. Camenisch, N.R. Champness, G.A.D. Briggs, S.C. Benjamin, A. Ardavan, A.N. Khlobystov. Toward controlled spacing in one-dimensional molecular chains: Alkyl-chain-functionalized fullerenes in carbon nanotubes. *J. Am. Chem. Soc.*, 129(27):8609-8614, 2007.

[50] H.W. Kroto, J.R. Heath, S.C. Obrien, R.F. Curl, R.E. Smalley. C_{60} - Buckminsterfullerene. *Nature*, 318(6042):162-163, 1985.

[51] S. Osuna, M. Swart, M. Sola. The Diels-Alder Reaction on Endohedral $Y_3N@C_{78}$: The Importance of the Fullerene Strain Energy. *J. Am. Chem. Soc.*, 131(1):129-139, 2009.

[52] H.M. Lee, M.M. Olmstead, E. Iezzi, J.C. Duchamp, H.C. Dorn, A.L. Balch. Crystallographic characterization and structural analysis of the first organic functionalization product of the endohedral fullerene $SC_3N@C_{80}$. *J. Am. Chem. Soc.*, 124(14):3494-3495, 2002.

[53] X. Lu, X.R. He, L. Feng, Z.J. Shi, Z.N. Gu. Synthesis of pyrrolidine ring-fused metallofullerene derivatives. *Tetrahedron*, 60(16):3713-3716, 2004.

[54] L. Echegoyen, C.J. Chancellor, C.M. Cardona, B. Elliott, J. Rivera, M.M. Olmstead, A.L. Balch. X-Ray crystallographic and EPR spectroscopic characterization of a pyrrolidine adduct of $Y_3N@C_{80}$. *Chem. Commun.*(25):2653-2655, 2006.

[55] C.M. Cardona, A. Kitaygorodskiy, A. Ortiz, M.A. Herranz, L. Echegoyen. The first fulleropyrrolidine derivative of $Sc_3N@C_{80}$: Pronounced chemical shift differences of the geminal protons on the pyrrolidine ring. *J. Org. Chem.*, 70(13):5092-5097, 2005.

[56] T. Cai, Z.X. Ge, E.B. Iezzi, T.E. Glass, K. Harich, H.W. Gibson, H.C. Dorn. Synthesis and characterization of the first trimetallic nitride templated pyrrolidino endohedral metallofullerenes. *Chem. Commun.*(28):3594-3596, 2005.

[57] J.R. Pinzon, T.M. Zuo, L. Echegoyen. Synthesis and Electrochemical Studies of Bingel-Hirsch Derivatives of $M_3N@I_h$-C_{80} (M = Sc, Lu). *Chem. Eur. J.*, 16(16):4864-4869, 2010.

[58] O. Lukoyanova, C.M. Cardona, J. Rivera, L.Z. Lugo-Morales, C.J. Chancellor, M.M. Olmstead, A. Rodriguez-Fortea, J.M. Poblet, A.L. Balch, L. Echegoyen. "Open rather than closed" malonate methano-fullerene derivatives. The formation of methanofulleroid adducts of $Y_3N@C_{80}$. *J. Am. Chem. Soc.*, 129(34):10423-10430, 2007.

[59] N. Alegret, M.N. Chaur, E. Santos, A. Rodriguez-Fortea, L. Echegoyen, J.M. Poblet. Bingel-Hirsch Reactions on Non-IPR $Gd_3N@C_{2n}$ (2n=82 and 84). *J. Org. Chem.*, 75(23):8299-8302, 2010.

[60] N.B. Shustova, Y.S. Chen, M.A. Mackey, C.E. Coumbe, J.P. Phillips, S. Stevenson, A.A. Popov, O.V. Boltalina, S.H. Strauss. $Sc_3N@(C_{80}\text{-}I_h(7))(CF_3)_{14}$ and $Sc_3N@(C_{80}\text{-}I_h(7))(CF_3)_{16}$. Endohedral Metallofullerene Derivatives with Exohedral Addends on Four and Eight Triple-Hexagon Junctions. Does the Sc3N Cluster Control the Addition Pattern or Vice Versa? *J. Am. Chem. Soc.*, 131(48):17630-17637, 2009.

[61] H. Nikawa, T. Kikuchi, T. Wakahara, T. Nakahodo, T. Tsuchiya, G.M.A. Rahman, T. Akasaka, Y. Maeda, K. Yoza, E. Horn, K. Yamamoto, N. Mizorogi, S. Nagase. Missing metallofullerene $La@C_{74}$. *J. Am. Chem. Soc.*, 127(27):9684-9685, 2005.

[62] H. Nikawa, T. Yamada, B.P. Cao, N. Mizorogi, Z. Slanina, T. Tsuchiya, T. Akasaka, K. Yoza, S. Nagase. Missing Metallofullerene with C_{80} Cage. *J. Am. Chem. Soc.*, 131(31):10950-10954, 2009.

[63] S. Osuna, M. Swart, J.M. Campanera, J.M. Poblet, M. Sola. Chemical reactivity of D_{3h} C_{78} (Metallo)fullerene: Regioselectivity changes induced by Sc3N encapsulation. *J. Am. Chem. Soc.*, 130(19):6206-6214, 2008.

[64] C.M. Cardona, A. Kitaygorodskiy, L. Echegoyen. Trimetallic nitride endohedral metallofullerenes: Reactivity dictated by the encapsulated metal cluster. *J. Am. Chem. Soc.*, 127(29):10448-10453, 2005.

[65] G.Q. Liu, Y.M. Wu, K. Porfyrakis. Synthesis and Chemistry of Endohedral Fullerenes. *Curr. Org. Chem.*, 15(8):1197-1207, 2011.

[66] T. Tsuchiya, K. Sato, H. Kurihara, T. Wakahara, T. Nakahodo, Y. Maeda, T. Akasaka, K. Ohkubo, S. Fukuzumi, T. Kato, N. Mizorogi, K. Kobayashi, S. Nagase. Host-guest complexation of endohedral metallofullerene with azacrown ether and its application. *J. Am. Chem. Soc.*, 128(20):6699-6703, 2006.

[67] T. Tsuchiya, H. Kurihara, K. Sato, T. Wakahara, T. Akasaka, T. Shimizu, N. Kamigata, N. Mizorogi, S. Nagase. Supramolecular complexes of $La@C_{82}$ with unsaturated thiacrown ethers. *Chem. Commun.*(34):3585-3587, 2006.

[68] G. Gil-Ramirez, S.D. Karlen, A. Shundo, K. Porfyrakis, Y. Ito, G.A.D. Briggs, J.J.L. Morton, H.L. Anderson. A Cyclic Porphyrin Trimer as a Receptor for Fullerenes. *Org. Lett.*, 12(15):3544-3547, 2010.

[69] T. Akasaka, T. Kato, K. Kobayashi, S. Nagase, K. Yamamoto, H. Funasaka, T. Takahashi. Exohedral Adducts of La@C_{82}. *Nature*, 374(6523):600-601, 1995.

[70] T. Kato, T. Akasaka, K. Kobayashi, S. Nagase, K. Yamamoto, H. Funasaka, T. Takahashi. ESR study on the reactivity of two isomers of La@C_{82} with disilirane. *Appl. Magn. Reson.*, 11(2):293-300, 1996.

[71] T. Akasaka, T. Kato, S. Nagase, K. Kobayashi, K. Yamamoto, H. Funasaka, T. Takahashi. Chemical derivatization of endohedral metallofullerene La@C_{82} with digermirane. *Tetrahedron*, 52(14):5015-5020, 1996.

[72] S. Nagase, K. Kobayashi. The Ionization Energies and Electron-Affinities of Endohedral Metallofullerenes Mc@C_{82} (M=Sc, Y, La) - Density-Functional Calculations. *J. Chem. Soc., Chem. Commun.*(16):1837-1838, 1994.

[73] T. Suzuki, Y. Maruyama, T. Kato, T. Akasaka, K. Kobayashi, S. Nagase, K. Yamamoto, H. Funasaka, T. Takahashi. Chemical-Reactivity of a Metallofullerene - Epr Study of Diphenylmethano-La@C_{82} Radicals. *J. Am. Chem. Soc.*, 117(37):9606-9607, 1995.

[74] N. Tagmatarchis, A. Taninaka, H. Shinohara. Production and EPR characterization of exohedrally perfluoroalkylated paramagnetic lanthanum metallofullerenes: La@C_{82}-$(C_8F_{17})_2$. *Chem. Phys. Lett.*, 355(3-4):226-232, 2002.

[75] B.P. Cao, T. Wakahara, Y. Maeda, A.H. Han, T. Akasaka, T. Kato, K. Kobayashi, S. Nagase. Lanthanum endohedral metallofulleropyrrolidines: Synthesis, isolation, and EPR characterization. *Chem. Eur. J.*, 10(3):716-720, 2004.

[76] L. Feng, T. Wakahara, T. Nakahodo, T. Tsuchiya, Q. Piao, Y. Maeda, Y. Lian, T. Akasaka, E. Horn, K. Yoza, T. Kato, N. Mizorogi, S. Nagase. The bingel monoadducts of La@C_{82}: Synthesis, characterization, and electrochemistry. *Chem. Eur. J.*, 12(21):5578-5586, 2006.

[77] L. Feng, T. Nakahodo, T. Wakahara, T. Tsuchiya, Y. Maeda, T. Akasaka, T. Kato, E. Horn, K. Yoza, N. Mizorogi, S. Nagase. A singly bonded derivative of endohedral metallofullerene: La@C_{82}CBr$(COOC_2H_5)_2$. *J. Am. Chem. Soc.*, 127(49):17136-17137, 2005.

[78] Y. Maeda, Y. Matsunaga, T. Wakahara, S. Takahashi, T. Tsuchiya, M.O. Ishitsuka, T. Hasegawa, T. Akasaka, M.T.H. Liu, K. Kokura, E. Horn, K. Yoza, T. Kato, S. Okubo, K. Kobayashi, S. Nagase, K. Yamamoto. Isolation and characterization of a carbene derivative of La@C_{82}. *J. Am. Chem. Soc.*, 126(22):6858-6859, 2004.

[79] Y. Maeda, J. Miyashita, T. Hasegawa, T. Wakahara, T. Tsuchiya, T. Nakahodo, T. Akasaka, N. Mizorogi, K. Kobayashi, S. Nagase, T. Kato, N. Ban, H. Nakajima, Y. Watanabe. Reversible and regioselective reaction of La@C_{82} with cyclopentadiene. *J. Am. Chem. Soc.*, 127(35):12190-12191, 2005.

[80] T.A. Murphy, T. Pawlik, A. Weidinger, M. Hohne, R. Alcala, J.M. Spaeth. Observation of atomlike nitrogen in nitrogen-implanted solid C_{60}. *Phys. Rev. Lett.*, 77(6):1075-1078, 1996.

[81] B. Pietzak, M. Waiblinger, T.A. Murphy, A. Weidinger, M. Hohne, E. Dietel, A. Hirsch. Buckminsterfullerene C_{60}: a chemical Faraday cage for atomic nitrogen. *Chem. Phys. Lett.*, 279(5-6):259-263, 1997.

[82] H. Mauser, N.J.R.V. Hommes, T. Clark, A. Hirsch, B. Pietzak, A. Weidinger, L. Dunsch. Stabilization of atomic nitrogen inside C_{60}. *Angew. Chem., Int. Ed.*, 36(24):2835-2838, 1997.

[83] J.J.L. Morton, A.M. Tyryshkin, A. Ardavan, K. Porfyrakis, S.A. Lyon, G.A.D. Briggs. A new mechanism for electron spin echo envelope modulation. *J. Chem. Phys.*, 122(17):-, 2005.

[84] N. Weiden, H. Kass, K.P. Dinse. Pulse electron paramagnetic resonance (EPR) and electron-nuclear double resonance (ENDOR) investigation of N@C_{60} in polycrystalline C_{60}. *J. Phys. Chem. B*, 103(45):9826-9830, 1999.

[85] C. Knapp, K.P. Dinse, B. Pietzak, M. Waiblinger, A. Weidinger. Fourier transform EPR study of N@C_{60} in solution. *Chem. Phys. Lett.*, 272(5-6):433-437, 1997.

[86] J.J.L. Morton, A.M. Tyryshkin, A. Ardavan, K. Porfyrakis, S.A. Lyon, G.A.D. Briggs. Environmental effects on electron spin relaxation in N@C_{60}. *Phys. Rev. B*, 76(8):085418, 2007.

[87] J.J.L. Morton, A.M. Tyryshkin, A. Ardavan, K. Porfyrakis, S.A. Lyon, G.A.D. Briggs. High fidelity single qubit operations using pulsed electron paramagnetic resonance. *Phys. Rev. Lett.*, 95(20):200501, 2005.

[88] J.J.L. Morton, A.M. Tyryshkin, A. Ardavan, S.C. Benjamin, K. Porfyrakis, S.A. Lyon, G.A.D. Briggs. Bang-bang control of fullerene qubits using ultrafast phase gates. *Nat. Phys.*, 2(1):40-43, 2006.

[89] J.J.L. Morton, A.M. Tyryshkin, A. Ardavan, S.C. Benjamin, K. Porfyrakis, S.A. Lyon, G.A.D. Briggs. The N@C_{60} nuclear spin qubit: Bang-bang decoupling and ultrafast phase gates. *Phys. Status Solidi B*, 243(13):3028-3031, 2006.

[90] R.M. Brown, A.M. Tyryshkin, K. Porfyrakis, E.M. Gauger, B.W. Lovett, A. Ardavan, S.A. Lyon, G.A.D. Briggs, J.J.L. Morton. Coherent State Transfer between an Electron and Nuclear Spin in $N^{15}@C_{60}$. *Phys. Rev. Lett.*, 106(11):110504, 2011.

[91] T. Kaneko, S. Abe, H. Ishida, R. Hatakeyama. An electron cyclotron resonance plasma configuration for increasing the efficiency in the yield of nitrogen endohedral fullerenes. *Phys. Plasmas*, 14(11):-, 2007.

[92] T. Suetsuna, N. Dragoe, W. Harneit, A. Weidinger, H. Shimotani, S. Ito, H. Takagi, K. Kitazawa. Separation of $N_2@C_{60}$ and $N@C_{60}$. *Chem. Eur. J.*, 8(22):5079-5083, 2002.

[93] M. Kanai, K. Porfyrakis, G.A.D. Briggs, T.J.S. Dennis. Purification by HPLC and the UV/Vis absorption spectra of the nitrogen-containing incar-fullerenes i-$N@C_{60}$, and i-$N@C_{70}$. *Chem. Commun.*(2):210-211, 2004.

[94] P. Jakes, K.P. Dinse, C. Meyer, W. Harneit, A. Weidinger. Purification and optical spectroscopy of $N@C_{60}$. *Phys. Chem. Chem. Phys.*, 5(19):4080-4083, 2003.

[95] E. Dietel, A. Hirsch, B. Pietzak, M. Waiblinger, K. Lips, A. Weidinger, A. Gruss, K.P. Dinse. Atomic nitrogen encapsulated in fullerenes: Effects of cage variations. *J. Am. Chem. Soc.*, 121(11):2432-2437, 1999.

[96] M.A.G. Jones, D.A. Britz, J.J.L. Morton, A.N. Khlobystov, K. Porfyrakis, A. Ardavan, G.A.D. Briggs. Synthesis and reactivity of $N@C_{60}O$. *Phys. Chem. Chem. Phys.*, 8(17):2083-2088, 2006.

[97] L. Franco, S. Ceola, C. Corvaja, S. Bolzonella, W. Harneit, M. Maggini. Synthesis and magnetic properties of $N@C_{60}$ derivatives. *Chem. Phys. Lett.*, 422(1-3):100-105, 2006.

[98] J.Y. Zhang, J.J.L. Morton, M.R. Sambrook, K. Porfyrakis, A. Ardavan, G.A.D. Briggs. The effects of a pyrrolidine functional group on the magnetic properties of $N@C_{60}$. *Chem. Phys. Lett.*, 432(4-6):523-527, 2006.

[99] T. Wakahara, Y. Matsunaga, A. Katayama, Y. Maeda, M. Kako, T. Akasaka, M. Okamura, T. Kato, Y.K. Choe, K. Kobayashi, S. Nagase, H.J. Huang, M. Atae. A comparison of the photochemical reactivity of $N@C_{60}$ and C_{60}: photolysis with disilirane. *Chem. Commun.*(23):2940-2941, 2003.

[100] F. Hormann, A. Hirsch, K. Porfyrakis, G.A.D. Briggs. Synthesis and Magnetic Properties of a Nitrogen-Containing Fullerene Dimer. *Eur. J. Org. Chem.*(1):117-121, 2011.

[101] K. Porfyrakis, M.R. Sambrook, T.J. Hingston, J. Zhang, A. Ardavan, G.A.D. Briggs. Synthesis of fullerene dimers with controllable length. *Phys. Status Solidi B*, 244(11):3849-3852, 2007.

[102] M. Gutierrez-Nava, G. Accorsi, P. Masson, N. Armaroli, J.F. Nierengarten. Polarity effects on the photophysics of dendrimers with an oligophenylenevinylene core and peripheral fullerene units. *Chem. Eur. J.*, 10(20):5076-5086, 2004.

[103] B. Goedde, M. Waiblinger, P. Jakes, N. Weiden, K.P. Dinse, A. Weidinger. 'Nitrogen doped' C_{60} dimers ($N@C_{60}$-C_{60}). *Chem. Phys. Lett.*, 334(1-3):12-17, 2001.

[104] J. Zhang, K. Porfyrakis, J.J.L. Morton, M.R. Sambrook, J. Harmer, L. Xiao, A. Ardavan, G.A.D. Briggs. Photoisomerization of a fullerene dimer. *J. Phys. Chem. C*, 112(8):2802-2804, 2008.

[105] A. Hirsch, I. Lamparth, T. Grosser, H.R. Karfunkel. Regiochemistry of Multiple Additions to the Fullerene Core - Synthesis of a T-H-Symmetrical Hexakisadduct of C-60 with Bis(Ethoxycarbonyl)Methylene. *J. Am. Chem. Soc.*, 116(20):9385-9386, 1994.

[106] J. Zhang. *Doctoral Thesis.* University of Oxford, 2007.

[107] K. Lips, M. Waiblinger, B. Pietzak, A. Weidinger. Atomic nitrogen encapsulated in fullerenes: Realization of a chemical Faraday cage. *Phys. Status Solidi A*, 177(1):81-91, 2000.

[108] J.K. Swadesh. *HPLC: practical and indutrial applications*. CRC Press LLC, Florida, 2001.

[109] R.S. Drago. *Physical methods for chemists*. Saunders College Publishing, Florida, 1992.

[110] S.M. Bachrach. *Computational Organic Chemistry*. John Wiley & Sons, 2007.

[111] W. Koch, M.C. Holthaisen. *A Chemist's Guide to Density Functional Theory*. Wiley-VCH, Weinheim, Germany, 2000.

[112] I.H. Lee, R.M. Martin. Applications of the generalized-gradient approximation to atoms, clusters, and solids. *Phys. Rev. B*, 56(12):7197-7205, 1997.

[113] P.J. Stephens, F.J. Devlin, C.F. Chabalowski, M.J. Frisch. Ab-Initio Calculation of Vibrational Absorption and Circular-Dichroism Spectra Using Density-Functional Force-Fields. *J. Phys. Chem.*, 98(45):11623-11627, 1994.

[114] A.D. Becke. Density-Functional Thermochemistry .3. The Role of Exact Exchange. *J. Chem. Phys.*, 98(7):5648-5652, 1993.

[115] M. Ernzerhof, G.E. Scuseria. Assessment of the Perdew-Burke-Ernzerhof exchange-correlation functional. *J. Chem. Phys.*, 110(11):5029-5036, 1999.

[116] R.L. Martin, F. Illas. Antiferromagnetic exchange interactions from hybrid density functional theory. *Phys. Rev. Lett.*, 79(8):1539-1542, 1997.

[117] T. Bredow, A.R. Gerson. Effect of exchange and correlation on bulk properties of MgO, NiO, and CoO. *Phys. Rev. B*, 61(8):5194-5201, 2000.

[118] J. Muscat, A. Wander, N.M. Harrison. On the prediction of band gaps from hybrid functional theory. *Chem. Phys. Lett.*, 342(3-4):397-401, 2001.

[119] P.v.R. Schleyer. *Encyclopedia of Computational Chemistry*. John Wiley & Sons, Chichester, 1998.

[120] M.J. Frisch, G.W. Trucks, H.B. Schlegel, G.E. Scuseria, M.A. Robb, J.R. Cheeseman, J. Montgomery, J. A., T. Vreven, K.N. Kudin, J.C. Burant, J.M. Millam, S.S. Iyengar, J. Tomasi, V. Barone, B. Mennucci, M. Cossi, G. Scalmani, N. Rega, G.A. Petersson, H. Nakatsuji, M. Hada, M. Ehara, K. Toyota, R. Fukuda, J. Hasegawa, M. Ishida, T. Nakajima, Y. Honda, O. Kitao, H. Nakai, M. Klene, X. Li, J.E. Knox, H.P. Hratchian, J.B. Cross, V. Bakken, C. Adamo, J. Jaramillo, R. Gomperts, R.E. Stratmann, O. Yazyev, A.J. Austin, R. Cammi, C. Pomelli, J.W. Ochterski, P.Y. Ayala, K. Morokuma, G.A. Voth, P. Salvador, J.J. Dannenberg, V.G. Zakrzewski, S. Dapprich, A.D. Daniels, M.C. Strain, O. Farkas, D.K. Malick, A.D. Rabuck, K. Raghavachari, J.B. Foresman, J.V. Ortiz, Q. Cui, A.G. Baboul, S. Clifford, J. Cioslowski, B.B. Stefanov, G. Liu, A. Liashenko, P. Piskorz, I. Komaromi, R.L. Martin, D.J. Fox, T. Keith, M.A. Al-Laham, C.Y. Peng, A. Nanayakkara, M. Challacombe, P.M.W. Gill, B. Johnson, W. Chen, M.W. Wong, C. Gonzalez, J.A. Pople, Gaussian03, Revision E.01. Gaussian, Inc., Wallingford CT, 2004.

[121] O. Farkas, H.B. Schlegel. Methods for optimizing large molecules. II. Quadratic search. *J. Chem. Phys.*, 111(24):10806-10814, 1999.

[122] R.S. Mulliken. Electronic Population Analysis on Lcao-Mo Molecular Wave Functions .1. *J. Chem. Phys.*, 23(10):1833-1840, 1955.

[123] J.W. Ochterski. *Thermochemistry in Gaussian*. Gaussian, Inc. , Wallingford CT, 2000.

[124] C. Bingel. Cyclopropylation of Fullerenes. *Chem. Ber. Recl.*, 126(8):1957-1959, 1993.

[125] F. Diederich, L. Isaacs, D. Philp. Syntheses, Structures, and Properties of Methanofullerenes. *Chem. Soc. Rev.*, 23(4):243-255, 1994.

[126] M. Waiblinger, K. Lips, W. Harneit, A. Weidinger, E. Dietel, A. Hirsch. Thermal stability of the endohedral fullerenes N@C_{60}, N@C_{70}, and P@C_{60} (vol B 63, art. no. 045421, 2001). *Phys. Rev. B*, 6415(15):159901, 2001.

[127] M. Maggini, G. Scorrano, M. Prato. Addition of Azomethine Ylides to C_{60} - Synthesis, Characterization, and Functionalization of Fullerene Pyrrolidines. *J. Am. Chem. Soc.*, 115(21):9798-9799, 1993.

[128] M.A. Herranz, B. Illescas, N. Martin, C.P. Luo, D.M. Guldi. Donor/acceptor fulleropyrrolidine triads. *J. Org. Chem.*, 65(18):5728-5738, 2000.

[129] Y.L. Li, Z. Mao, J.H. Xu, Y.K. Yang, Z.X. Guo, D.B. Zhu, J.W. Li, B. Yin. Preparation of a novel stable nitroxide based on [60]fulleropyrrolidine and its magnetic properties. *Chem. Phys. Lett.*, 265(3-5):361-364, 1997.

[130] D.M. Guldi, M. MAggini, G. Scorrano, M. Prato. Intramolecular electron transfer in fullerene/ferrocene based donor-bridge-acceptor dyads. *J. Am. Chem. Soc.*, 119(5):974-980, 1997.

[131] A. Bianco, M. Maggini, G. Scorrano, C. Toniolo, G. Marconi, C. Villani, M. Prato. Synthesis, chiroptical properties, and configurational assignment of fulleroproline derivatives and peptides. *J. Am. Chem. Soc.*, 118(17):4072-4080, 1996.

[132] M. Maggini, A. Dono, G. Scorrano, M. Prato. Synthesis of a [60]Fullerene Derivative Covalently-Linked to a Ruthenium(Ii) Tris(Bipyridine) Complex. *J. Chem. Soc., Chem. Commun.*(8):845-846, 1995.

[133] N. Tagmatarchis, M. Prato. The addition of azomethine ylides to [60]fullerene leading to fulleropyrrolidines. *Synlett*(6):768-779, 2003.

[134] P.A. van Hal, E.H.A. Beckers, E. Peeters, J.J. Apperloo, R.A.J. Janssen. Photoinduced intermolecular electron transfer between oligo(p-phenylene vinylene)s and N-methylfulleropyrrolidine in a polar solvent. *Chem. Phys. Lett.*, 328(4-6):403-408, 2000.

[135] J.J. Apperloo, C. Martineau, P.A. van Hal, J. Roncali, R.A.J. Janssen. Intra- and intermolecular photoinduced energy and electron transfer between oligothienylenevinylenes and N-methylfulleropyrrolidine. *J. Phys. Chem. A*, 106(1):21-31, 2002.

[136] D.M. Guldi, F. Spanig, D. Kreher, I.F. Perepichka, C. van der Pol, M.R. Bryce, K. Ohkubo, S. Fukuzumi. Contrasting photodynamics between C_{60}-dithiapyrene and C_{60}-pyrene dyads. *Chem.-Eur. J.*, 14(1):250-258, 2008.

[137] J.L. Delgado, S. Osuna, P.A. Bouit, R. Martinez-Alvarez, E. Espildora, M. Sola, N. Martin. Competitive Retro-Cycloaddition Reaction in Fullerene Dimers Connected through Pyrrolidinopyrazolino Rings. *J. Org. Chem.*, 74(21):8174-8180, 2009.

[138] S. Filippone, M.I. Barroso, A. Martin-Domenech, S. Osuna, M. Sola, N. Martin. On the mechanism of the thermal retrocycloaddition of pyrrolidinofullerenes (retro-prato reaction). *Chem. Eur. J.*, 14(17):5198-5206, 2008.

[139] H. Imahori, K. Hagiwara, M. Aoki, T. Akiyama, S. Taniguchi, T. Okada, M. Shirakawa, Y. Sakata. Linkage and solvent dependence of photoinduced electron transfer in zincporphyrin-C_{60} dyads. *J. Am. Chem. Soc.*, 118(47):11771-11782, 1996.

[140] H. Imahori, Y. Sakata. Donor-linked fullerenes: Photoinduced electron transfer and its potential application. *Adv. Mater.*, 9(7):537-&, 1997.

[141] H. Imahori, K. Tamaki, H. Yamada, K. Yamada, Y. Sakata, Y. Nishimura, I. Yamazaki, M. Fujitsuka, O. Ito. Photosynthetic electron transfer using fullerenes as novel acceptors. *Carbon*, 38(11-12):1599-1605, 2000.

[142] K. Ohkubo, H. Kotani, J.G. Shao, Z.P. Ou, K.M. Kadish, G.L. Li, R.K. Pandey, M. Fujitsuka, O. Ito, H. Imahori, S. Fukuzumi. Production of an ultra-long-lived charge-separated state in a zinc chlorin-C_{60} dyad by one-step photoinduced electron transfer. *Angew. Chem., Int. Ed.*, 43(7):853-856, 2004.

[143] H. Yamada, H. Imahori, Y. Nishimura, I. Yamazaki, T.K. Ahn, S.K. Kim, D. Kim, S. Fukuzumi. Photovoltaic properties of self-assembled monolayers of porphyrins and porphyrin-fullerene dyads on ITO and gold surfaces. *J. Am. Chem. Soc.*, 125(30):9129-9139, 2003.

[144] A.D. Adler, F.R. Longo, F. Kampas, J. Kim. On Preparation of Metalloporphyrins. *J. Inorg. Nucl. Chem.*, 32(7):2443-&, 1970.

[145] J. Martensson, K. Sandros, O. Wennerstrom. Synthesis and Photophysics of Diaza-Crown Ether-Based Bisporphyrins. *J. Phys. Org. Chem.*, 7(10):534-544, 1994.

[146] O. Wennerstrom, H. Ericsson, I. Raston, S. Svensson, W. Pimlott. Meso-Tetra(Meso-Tetraphenylporphyrinyl)Porphyrin, a Macrocycle with 5 Covalently Linked Porphyrin Units. *Tetrahedron Lett.*, 30(9):1129-1132, 1989.

[147] K.L. Cunningham, K.M. McNett, R.A. Pierce, K.A. Davis, H.H. Harris, D.M. Falck, D.R. McMillin. EPR spectra, luminescence data, and radiationless decay processes of copper(II) porphyrins. *Inorg. Chem.*, 36(4):608-613, 1997.

[148] G.D. Dorough, F.M. Huennekens. The Spectra of Alpha,Beta,Gamma,Sigma-Tetraphenylchlorin and Its Metallo-Derivatives. *J. Am. Chem. Soc.*, 74(16):3974-3976, 1952.

[149] G.D. Dorough, J.R. Miller, F.M. Huennekens. Spectra of the Metallo-Derivatives of Alpha,Beta,Gamma,Omega-Tetraphenylporphine. *J. Am. Chem. Soc.*, 73(9):4315-4320, 1951.

[150] Y.V. Ishkov, Z.I. Zhilina. Porphyrins and Their Derivatives .12. Synthesis of Isomeric Formylphenylporphyrins. *Zh. Org. Khim.*, 26(6):1339-1344, 1990.

[151] S.R. Plant. *Doctoral Thesis.* University of Oxfored, 2010.

[152] T. DaRos, M. Prato, F. Novello, M. Maggini, E. Banfi. Easy access to water-soluble fullerene derivatives via 1,3-dipolar cycloadditions of azomethine ylides to C_{60}. *J. Org. Chem.*, 61(25):9070-9072, 1996.

[153] G.H. Barnett, M.F. Hudson, K.M. Smith. Concerning Meso-Tetraphenylporphyrin Purification. *J. Chem. Soc., Perkin Trans. 1*(14):1401-1403, 1975.

[154] R. Shimshi, A. Khong, H.A. JimenezVazquez, R.J. Cross, M. Saunders. Release of noble gas atoms from inside fullerenes. *Tetrahedron*, 52(14):5143-5148, 1996.

[155] M. Saunders, R.J. Cross, H.A. JimenezVazquez, R. Shimshi, A. Khong. Noble gas atoms inside fullerenes. *Science*, 271(5256):1693-1697, 1996.

[156] R. Dennington, T. Keith, J. Millam, GaussView, Version 5. Semichem Inc., Shawnee Mission KS, 2009.

[157] T. Gareis, O. Kothe, J. Daub. Chromophore-appended C_{60} and C_{70} fullerenes: Anthracene and pyrene derivatives - Syntheses, cyclic voltammetry and spectra. *Eur. J. Org. Chem.*(8):1549-1557, 1998.

[158] A.S.D. Sandanayaka, Y. Araki, O. Ito, G.R. Deviprasad, P.M. Smith, L.M. Rogers, M.E. Zandler, F. D'Souza. Photoinduced electron transfer in fullerene triads bearing pyrene and fluorene. *Chem. Phys.*, 325(2):452-460, 2006.

[159] R.B. Martin, K.F. Fu, Y.P. Sun. Efficient intramolecular excited-state energy transfer in pyrenes-fullerene macromolecule. *Chem. Phys. Lett.*, 375(5-6):619-624, 2003.

[160] J.C. Greer. The atomic nature of endohedrally encapsulated nitrogen $N@C_{60}$ studied by density functional and Hartree-Fock methods. *Chem. Phys. Lett.*, 326(5-6):567-572, 2000.

[161] J. Lu, X.W. Zhang, X.G. Zhao. Electronic structures of endohedral $N@C_{60}$, $O@C_{60}$ and $F@C_{60}$. *Chem. Phys. Lett.*, 312(2-4):85-90, 1999.

[162] K.G. Thomas, V. Biju, M.V. George, D.M. Guldi, P.V. Kamat. Excited-state interactions in pyrrolidinofullerenes. *J. Phys. Chem. A*, 102(28):5341-5348, 1998.

[163] K. Kordatos, T. Da Ros, M. Prato, S. Leach, E.J. Land, R.V. Bensasson. Triplet state properties of N-mTEG[60]fulleropyrrolidine mono and bisadduct derivatives. *Chem. Phys. Lett.*, 334(4-6):221-228, 2001.

[164] J.W. Arbogast, A.P. Darmanyan, C.S. Foote, Y. Rubin, F.N. Diederich, M.M. Alvarez, S.J. Anz, R.L. Whetten. Photophysical Properties of C_{60}. *J. Phys. Chem.*, 95(1):11-12, 1991.

[165] S.S. Eaton, G.R. Eaton. Interaction of Spin Labels with Transition-Metals .2. *Coord. Chem. Rev.*, 8329-72, 1988.

[166] M.H. Rakowsky, K.M. More, A.V. Kulikov, G.R. Eaton, S.S. Eaton. Time-Domain Electron-Paramagnetic-Resonance as a Probe of Electron-Electron Spin-Spin Interaction in Spin-Labeled Low-Spin Iron Porphyrins. *J. Am. Chem. Soc.*, 117(7):2049-2057, 1995.

[167] J.M. Burchfield, J.L. Du, K.M. More, S.S. Eaton, G.R. Eaton. Enhancement of electron spin relaxation rates of metalloporphyrins due to interaction with a faster relaxing metal bound to an appended bipyridyl. *Inorg. Chim. Acta*, 263(1-2):23-33, 1997.

[168] J.S. Leigh. ESR Rigid-Lattice Line Shape in a System of Two Interacting Spins. *J. Chem. Phys.*, 52(5):2608-&, 1970.

[169] S.S. Eaton, M.L. Law, J. Peterson, G.R. Eaton, D.J. Greenslade. Metal-Nitroxyl Interactions .7. Quantitative Aspects of Epr-Spectra Resulting from Dipolar Interactions. *J. Magn. Reson.*, 33(1):135-141, 1979.

[170] K. Tan, L. Jaquinod, R. Paolesse, S. Nardis, C. Di Natale, A. Di Carlo, L. Prodi, M. Montalti, N. Zaccheroni, K.M. Smith. Synthesis and characterization of beta-fused porphyrin-BODIPY (R) dyads. *Tetrahedron*, 60(5):1099-1106, 2004.

[171] D. Kuciauskas, S. Lin, G.R. Seely, A.L. Moore, T.A. Moore, D. Gust, T. Drovetskaya, C.A. Reed, P.D.W. Boyd. Energy and photoinduced electron transfer in porphyrin-fullerene dyads. *J. Phys. Chem.*, 100(39):15926-15932, 1996.

[172] D.I. Schuster, K. Li, D.M. Guldi, A. Palkar, L. Echegoyen, C. Stanisky, R.J. Cross, M. Niemi, N.V. Tkachenko, H. Lemmetyinen. Azobenzene-linked porphyrin - Fullerene dyads. *J. Am. Chem. Soc.*, 129(51):15973-15982, 2007.

[173] J.M. Assour. Electron Spin Resonance of Tetraphenylporphine Chelates. *J. Chem. Phys.*, 43(7):2477-2489, 1965.

[174] P. Jakes, N. Weiden, R.A. Eichel, A. Gembus, K.P. Dinse, C. Meyer, W. Harneit, A. Weidinger. Electron paramagnetic resonance investigation of endohedral fullerenes N@C_{60} and N@C_{70} in a liquid crystal. *J. Magn. Reson.*, 156(2):303-308, 2002.

[175] C. Meyer, W. Harneit, K. Lips, A. Weidinger, P. Jakes, K.P. Dinse. Alignment of the endohedral fullerenes N@C_{60} and N@C_{70} in a liquid-crystal matrix. *Phys. Rev. A*, 65(6):061201, 2002.

[176] B. Naydenov, C. Spudat, W. Harneit, H.I. Suss, J. Hulliger, J. Nuss, M. Jansen. Ordered inclusion of endohedral fullerenes N@C_{60} and P@C_{60} in a crystalline matrix. *Chem. Phys. Lett.*, 424(4-6):327-332, 2006.

[177] B. Naydenov, C. Spudat, M. Scheloske, H.I. Suess, J. Hulliger, W. Harneit. N@C_{60} and N@C_{70} oriented in a single-crystalline matrix. *Phys. Status Solidi B*, 243(13):2995-2998, 2006.

[178] B. Corzilius, A. Gembus, N. Weiden, K.P. Dinse, K. Hata. EPR characterization of catalyst-free SWNT and N@C_{60}-based peapods. *Phys. Status Solidi B*, 243(13):3273-3276, 2006.

[179] S. Toth, D. Quintavalle, B. Nafradi, L. Korecz, L. Forro, F. Simon. Enhanced thermal stability and spin-lattice relaxation rate of N@C_{60} inside carbon nanotubes. *Phys. Rev. B*, 77(21):214409, 2008.

[180] F. Simon, H. Kuzmany, H. Rauf, T. Pichler, J. Bernardi, H. Peterlik, L. Korecz, F. Fulop, A. Janossy. Low temperature fullerene encapsulation in single wall carbon nanotubes: synthesis of N@C_{60}@SWCNT. *Chem. Phys. Lett.*, 383(3-4):362-367, 2004.

[181] C.F. Polnaszek, J.H. Freed. Electron-Spin Resonance Studies of Anisotropic Ordering, Spin Relaxation, and Slow Tumbling in Liquid-Crystalline Solvents. *J. Phys. Chem.*, 79(21):2283-2306, 1975.

[182] K. Ohno, J. Sohma. Analysis of Magnetic-Field-Induced Distribution Using Electron-Spin-Resonance Parallel-Edge Lines of a Slow Tumbling Spin Probe in a Rigid Liquid-Crystal. *J. Magn. Reson.*, 58(1):1-13, 1984.

[183] J.I. Spielberg, E. Gelerinter. Electron-Paramagnetic-Res Probe Study of the Molecular-Dynamics of the Supercooled Liquid, the Glass State, and the Glass-Transition in

Liquid-Crystalline Mbba [Normal-(Para-Methoxybenzlidene)-Para-Butylaniline]. *Phys. Rev. A*, 32(6):3647-3660, 1985.

[184] S. Campestrini, C. Corvaja, M. De Nardi, C. Ducati, L. Franco, M. Maggini, M. Meneghetti, E. Menna, G. Ruaro. Investigation of the inner environment of carbon nanotubes with a fullerene-nitroxide probe. *Small*, 4(3):350-356, 2008.

[185] P. Ferruti, D. Gill, M.A. Harpold, M.P. Klein. Esr of Spin-Labeled Nematogenlike Probes Dissolved in Nematic Liquid Crystals. *J. Chem. Phys.*, 50(10):4545-&, 1969.

[186] J.S. Hwang, M.A. Morsy, G.A. Oweimreen. Nonmesomorphic Solute-Mesomorphic Solvent Interaction Studies .1. Visual and Esr Studies on Nitroxide Radicals in the Nematic and Isotropic Phases of 4-Cyano-4'-N-Pentylbiphenyl (5cb) Liquid-Crystalline Solvent. *J. Phys. Chem.*, 98(36):9056-9062, 1994.

[187] H. Kobayashi, T. Ueda, K. Miyakubo, T. Eguchi, A. Tani. Spin-spin interaction of TEMPO molecular chains formed in an organic one-dimensional nanochannel as studied by electron spin resonance (ESR). *Bull. Chem. Soc. Jpn.*, 80(4):711-720, 2007.

[188] S.V. Savenko, M. Dijkstra. Accuracy of measuring the nematic order from intensity scatter: A simulation study. *Phys. Rev. E: Stat. Phys., Plasmas, Fluids,*, 70(1):01170, 2004.

[189] B. Paci, G. Amoretti, G. Arduini, G. Ruani, S. Shinkai, T. Suzuki. Vibrational spectrum of C_{60} in the p-tert-butylcalix[8]arene(1:1)C_{60} complex. *Phys. Rev. B*, 55(9):5566-5569, 1997.

[190] C.A. Hunter, J.K.M. Sanders. The Nature of Pi-Pi Interactions. *J. Am. Chem. Soc.*, 112(14):5525-5534, 1990.

[191] H.J. Schneider, K. Philippi, J. Pohlmann. Host-Guest Chemistry .2. Structure-Dependence and Solvent-Dependence in the Complexation of Lipophilic Substrates in a Water-Soluble Azacyclophane. *Angew. Chem., Int. Ed.*, 23(11):908-910, 1984.

[192] A.V. Muehldorf, D. Vanengen, J.C. Warner, A.D. Hamilton. Aromatic Aromatic Interactions in Molecular Recognition - a Family of Artificial Receptors for Thymine That Shows Both Face-to-Face and Edge-to-Face Orientations. *J. Am. Chem. Soc.*, 110(19):6561-6562, 1988.

[193] T. Dahl. The Nature of Stacking Interactions between Organic-Molecules Elucidated by Analysis of Crystal-Structures. *Acta Chem. Scand.*, 48(2):95-106, 1994.

[194] P. Jakes, A. Gembus, K.P. Dinse, K. Hata. Electron paramagnetic resonance investigation of metalloendofullerene derived carbon nanotube peapods. *J. Chem. Phys.*, 128(5), 2008.

Publications

Chapter 1

1. G. Liu, Y. Wu, K. Porfyrakis. Synthesis and chemistry of endohedral fullerenes. *Curr. Org. Chem.*, 15(8):1197-1207, 2011.

Chapter 4

2. G. Liu, A. N. Khlobystov, A. Ardavan, G. A. D. Briggs K. Porfyrakis. Photochemical stability of N@C_{60} and its pyrrolidine derivatives. *Chem. Phys. Lett.*, 508:187-190, 2011.
3. G. Liu, A. N. Khlobystov, G. A. D. Briggs K. Porfyrakis. Catalytic and non-catalytic roles of pendant groups in the decompostion of N@C_{60}: a DFT investigation. Submitted, 2012.

Chapter 5

4. G. Liu, A. N. Khlobystov, G. Charalambidis, A. G. Coutsolelos, G. A. D. Briggs, and K. Porfyrakis. N@C_{60}-porphyrin: a dyad of two radical centers. *J. Am. Chem. Soc.*, 134 (4) 1938-1941, 2012.

Chapter 6

5. G. Liu, M. del C. Gimenez-Lopez, M. Jevric, A. N. Khlobystov, G. A. D. Briggs and K. Porfyrakis. Alignment of N@C_{60} derivatives in a liquid crystal matrix. Submitted, 2012.